Kinetics and mechanisms of solid-state phase transitions and reactions

Thesis

UNRESTRICTED

KINETICS AND MECHANISMS OF SOLID-STATE PHASE TRANSITIONS AND REACTIONS

Beatrice Purser-Hallard

A Thesis submitted for the Degree of

Doctor of Philosophy

The Open University

Department of Chemistry
The Open University
July 2005

DATE OF SUBMISSION: 20 JULY 2005
DATE OF AWARD: 19 OCTOBER 2005

ProQuest LLC.
789 East Eisenhower Parkway
P.O. Box 1346
Ann Arbor, MI 48106 – 1346

Abstract

The phase transition of ζ_α- to ζ_β-ferrosilicon has been studied, both with and without a doping of 1% aluminium, at high temperature by time-resolved simultaneous X-ray powder diffraction and iron K-edge EXAFS at four temperatures, and also by high temperature time-resolved Mössbauer spectroscopy at two temperatures. The extent of the phase transition and its evolution with time has been determined using a novel method. The results have been analysed in terms of theories of solid state kinetics. Some tentative conclusions for the mechanism of the phase transition have been drawn. Approximate values for the activation energy of the phase transitions, with and without 1% aluminium doping, have been derived. The structures of the phases, with and without 1% aluminium doping, have been examined by techniques including X-ray powder diffraction, Fe K-edge EXAFS and Si K-edge EXAFS and Mössbauer spectroscopy, in order to gain insight on how the presence of the dopant might affect the phase transition.

The formation of mullite from precursors formed by the hydrothermal processing of aluminium- and silicon-acetates, both undoped and with the inclusion of iron and vanadium dopants, has been investigated using flat-plate room temperature X-ray powder diffraction of samples heated at a variety of temperatures and for different durations of time. The structures of the precursors and the mullite formed have been examined by techniques including X-ray powder diffraction, Fe K-edge EXAFS, Mössbauer spectroscopy and MAS NMR. The formation of 5% iron-doped mullite from a precursor formed by the hydrothermal processing of aluminium-, silicon- and iron acetates has also been monitored by time-resolved X-ray powder diffraction.

Acknowledgements

I have been indebted in the preparation of this thesis to my supervisors Prof Frank Berry and Dr Michael Mortimer of The Open University, whose patience and support as well as academic expertise have been invaluable to me. My sincerest thanks also to CCLRC for funding my research, and to the Institute of Physics for further funding during the writing-up stage. I am also indebted to Bob Bilsborrow, Andy Dent, Fred Mosselmans and many others at Daresbury Laboratory for assistance and advice during my Daresbury experiments. My heartfelt gratitude further to Örn Helgason and Birgir Johannesson of the University of Iceland for their support, assistance and hospitality during my stay in Iceland performing the time-resolved Mössbauer spectroscopy experiments. I would also like to thank my contemporaries who during my time at The Open University were very helpful in assisting with experiments and providing useful feedback on the progress of my work, especially Karl Whittle, Paul Wynn and Julia McManus. My thanks also to former University of Iceland student Thordur Magnusson whose MSc dissertation on ferrosilicon was very helpful in preparing for my own work on the ferrosilicon phase transition, and to The Open University student Mark Booth whose thesis on the characterisation of mullite was instrumental in conceiving the potential for the experiments on the formation of mullite.

The support of those closest to me has been indispensable in finding the courage to complete this thesis. My parents Martin and Jenny Purser, my parents-in-law Terry and Margaret Hallard, my sisters, my grandparents, my best friend Rachel and most of all my husband Phil have provided me with heroic quantities of love, support and encouragement during my labours. I thank them all from the bottom of my heart.

The journey is noble, and adventure is sweet

But wine by the fireside is sweeter, and knowing one's home

- Rihansu Proverb

Contents

Chapter One: Introduction

1.1 Aims

The aims of the work reported in this thesis have been:

a) to use simultaneous high-temperature time-resolved X-ray powder diffraction (XRPD) and extended X-ray absorption fine structure (EXAFS) to investigate *in situ* the kinetics and mechanisms of:

   i) the phase transition of ζ_{α}- to ζ_{β}-ferrosilicon.

   ii) the synthesis of mullite from a gel formed by the hydrothermal processing of aluminium- and silicon- acetates.

b) to complement the investigation of the ζ_{α}- to ζ_{β}-ferrosilicon phase transition by the use of high-temperature time-resolved ^{57}Fe Mössbauer spectroscopy.

c) to examine the effects of dopants on the kinetics and mechanisms of the two systems, and to investigate the structures of the doped materials in order to understand these effects.

d) to examine the structure of metastable ζ_{β}-ferrosilicon containing excess silicon to identify the position occupied by the additional silicon within the unit cell.

e) to interpret the experimental data in terms of established theories of solid-state kinetic reactions.

1.2 Literature survey

1.2.1 Ferrosilicon

1.2.1.1 Ferrosilicon and its uses

Ferrosilicon is any alloy of iron and silicon. The work reported in this thesis is concerned only with silicon-rich ferrosilicon in which the silicon content exceeds 50 atomic percent (at%).

The major use of ferrosilicon is in the steel industry. So called "cast iron" is formed by heating a mixture of iron ore and coke to temperatures exceeding 2270 K in a process known as smelting. Cast iron contains up to 10 % carbon and 10 % oxygen, as well as other impurities, and is brittle and lacks the strength and hardness required for structural purposes. However, pure iron is soft and lacks the qualities of a useful structural material. It is the presence of other elements alloyed with the iron which improves many properties such as strength, hardness, corrodibility and elasticity. Steel is cast iron which has had most of the carbon and oxygen removed and has been alloyed with other elements, such as silicon, zirconium and various transition metals[1]. The addition of silicon to molten steel promotes graphitization, which is the precipitation of the excess carbon present due to the smelting process, and also acts as a reducing agent by reacting with any oxygen present and precipitating in the form of quartz. Precipitates of graphite and quartz may then be removed from the molten steel. The presence of silicon as an alloying element in steel increases the hardenability, strength and electrical resistivity of the material[2]. Silicon also increases the corrosion resistance of steel by forming a non-porous protective layer on the surface of steel materials[3]. Ferrosilicon, an alloy of iron and silicon, is often used in order to add silicon to molten steel.

Ferrosilicon with 65 – 75 at% silicon is commonly manufactured by reducing (using coke) either a mixture of a quartz and iron ore, or a mixture of quartz and scrap iron[4]. The

ferrosilicon formed during the process contains significant proportions of the high temperature ζ_α phase, which is less dense than ferrosilicon with the ζ_β phase structure. The phase transition to ζ_β within regions of ζ_α phase material leads to tensile stresses in the brittle matrix. The tensile stresses lead to fines, which make the ferrosilicon liable to cracking and crumbling during transportation and storage. This decomposition of ferrosilicon causes wastage of material. The industrial manufacture from impure starting materials naturally leads to impurities, particularly aluminium and phosphorous, in the ferrosilicon. During the decomposition phosphine gas can be released which has caused fatalities in the industry[5]. A better understanding of the ζ_α to ζ_β phase transition would enable industrial processes to be developed to minimise these effects.

1.2.1.2 Compositions of the ferrosilicon phases

Figure 1.1 shows the silicon-rich part of the binary alloy phase diagram for the iron-silicon system[6].

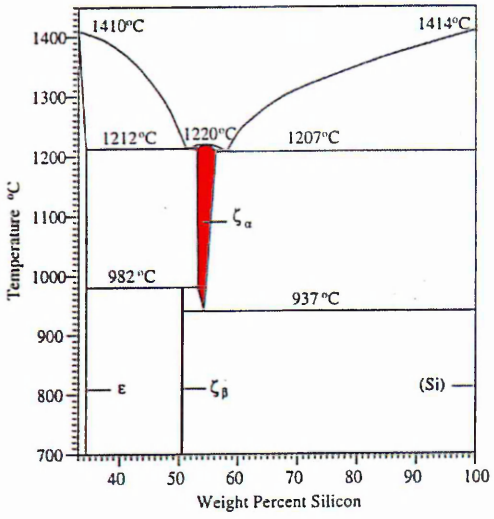

Figure 1.1: Binary alloy phase diagram for iron-silicon

The significant phases are the ζ_α and ζ_β phases at 50 – 56 weight percent (wt%) silicon, equivalent to 67 – 72 at% silicon. The region of stability of the ζ_α phase is the central area marked with red. The region of stability of the ζ_β phase is more limited, and is marked by the

vertical line below this area in blue. There is no stable phase containing greater than ~56 wt% silicon. Thus, ferrosilicon containing > 56 wt% silicon will be a mixture of ζ ferrosilicon and silicon.

The ζ_α phase is non-stoichiometric at temperatures above 1210 K, and can contain between 52 and 56 wt% silicon. However, at 1210 K the composition of the pure ζ_α phase structure is less variable, and is close to 54 wt% silicon. Hence, in the majority of the experiments carried out in the present work, ferrosilicon with 54 wt% silicon (equivalent to 70 at% silicon and thus referred to as $FeSi_{2.33}$) has been used.

1.2.1.3 Structures of the ferrosilicon phases

The crystal structures of pure ζ_α- [7] and ζ_β-ferrosilicon[8] are described in the Inorganic Crystal Structures Database (ICSD)[9]:

i) dimensions of the unit cell

ζ_α-$FeSi_{2.33}$:	$a = 2.6901(1)$ Å	ζ_β-$FeSi_2$:	$a = 9.863(7)$ Å
	$b = 2.6901(1)$ Å		$b = 7.791(6)$ Å
	$c = 5.134(2)$ Å		$c = 7.833(6)$ Å
	$\alpha = \beta = \gamma = 90°$		$\alpha = \beta = \gamma = 90°$

ii) location of atoms in the cell

Atom type	x	y	z
Fe	0.000	0.000	0.000
Si	0.500	0.500	0.270

space group: P4/MMM

3 atoms per unit cell

Atom type	x	y	z
Fe	0.2146(2)	0.0	0.0
Fe	0.5	0.3086(2)	0.1851(2)
Si	0.1282(2)	0.2746(3)	0.0512(4)
Si	0.3727(2)	0.0450(3)	0.2261(3)

space group: CMCA

48 atoms per unit cell

These data have been used to generate a diagram of the unit cells using the CrystalMaker[10] software package. The results are shown in Figures 1.2:

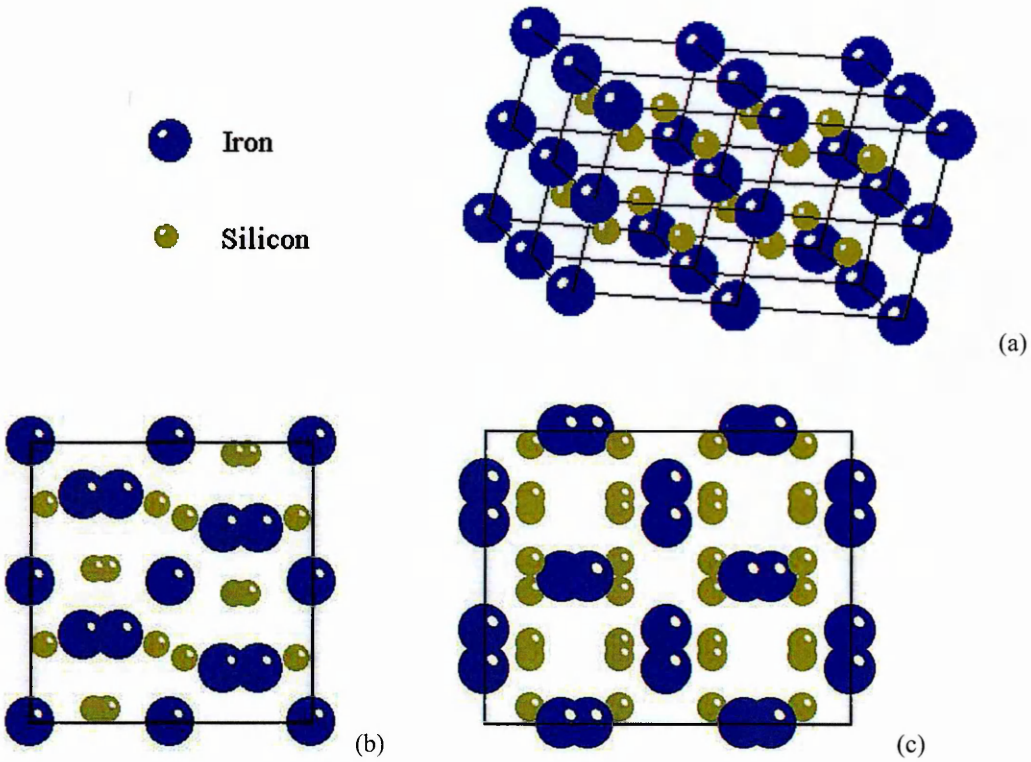

Figures 1.2: (a) Structure of ζ_α-$FeSi_{2.33}$ (b) Structure of ζ_β-$FeSi_2$ looking along *b*-axis (c) Structure of ζ_β-$FeSi_2$ looking along *c*-axis

The unit cell of ζ_α-ferrosilicon contains one iron atom and two silicon atoms – which implies 50 wt%, 67 at% silicon. However, the lowest possible silicon content for ζ_α-ferrosilicon shown on the phase diagram is 52 wt%, 68 at% silicon. Therefore ζ_α-ferrosilicon always contains iron vacancies in the unit cell. This may be a key to explaining some details of the kinetics and mechanisms of the phase transition.

1.2.1.4 The ζ_α to ζ_β phase transition

As described in Section 1.2.1.1, the phase transformation of non-stoichiometric ζ_α-ferrosilicon to ζ_β-ferrosilicon causes some problems in the steel industry. The kinetics and mechanisms of the transition are unknown, although some limited work on the rate of the

phase transition has been reported[11 12].

Until the mid-twentieth century it was believed that there was only one ζ phase, also known as leboite. Workers in Russia established that there were two phases[13], and that at temperatures below 1210 K eutectoid decomposition takes place in the metallic ζ_α phase

$$\zeta_\alpha\text{-}FeSi_x \longrightarrow \zeta_\beta\text{-}FeSi_2 + (x\text{-}2)Si$$

where x can be between 2.15 (equivalent to 52 wt%) and 2.53 (equivalent to 56 wt%). Examination of single crystals of ferrosilicon using scanning electron microscopy by van den Boomgaard[14] led him to revise this equation to include a metastable pre-beta transitional phase which then precipitates out the excess silicon which he observed in the form of rods.

$$\text{i) } \zeta_\alpha\text{-}FeSi_x \longrightarrow \zeta_\beta\text{-}FeSi_x$$

$$\text{ii) } \zeta_\beta\text{-}FeSi_x \longrightarrow \zeta_\beta\text{-}FeSi_2 + (x\text{-}2)Si$$

The structure of the metastable pre-beta phase is unknown. Silicon rods are not always observed in samples where they might reasonably be expected to be present[15], and details of the conditions for their precipitation are sketchy. The location of the excess silicon in the metastable phase ζ_β-$FeSi_{2.33}$ may be relevant in determining the mechanism of the phase transition. However, the paper by van den Boomgaard notes that there are significant differences in the results obtained using powdered samples as compared to using single crystals.

Previous workers[11] have performed a series of experiments in which pieces of ζ_α-$FeSi_{2.33}$ were heated at various temperatures, and the relative abundances of the ζ_α and ζ_β phases present measured at room temperature by Mössbauer spectroscopy. The transformation-time-temperature (TTT) diagram produced from these results is shown in Figure 1.3.

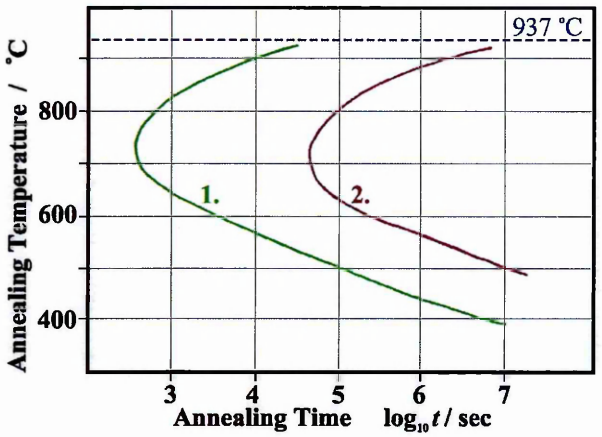

Figure 1.3: Transformation-time-temperature (TTT) diagram for the ζ_α- to ζ_β-phase transition. Line 1 shows the time taken for a recording of 5% ζ_β-$FeSi_2$ to be observed. Line 2 shows the time taken for 95% ζ_β-$FeSi_2$ to be observed.

The TTT diagram shows that the phase transition occurs fastest at *ca.* 970 K (*ca.* 700 °C). At higher temperatures, the ζ_α-$FeSi_{2.33}$ approaches the temperatures at which it is stable, and so the phase transition occurs less readily. At lower temperatures it is presumed that there is insufficient thermal energy to effectively drive the phase transformation.

Previous workers[16] have investigated the rates of the phase transition of ferrosilicon at various temperatures using Mössbauer spectroscopy. The extent of the reaction was observed to follow the standard sigmoidal form for nucleation and growth at an interface[17]:

$$P(t) = P_0 \,.\, \exp(-k \,.\, t^n) \qquad \text{Equation 1.1}$$

where $P(t)$ is the percentage of ζ_α-ferrosilicon remaining in the sample, P_0 is the percentage of ferrosilicon present at $t = 0$, k is a rate constant, t is time and n is a constant which was observed to be equal to 2.1 ± 0.2 at 808 K and equal to 1.4 ± 0.1 at 840 K – see Section 1.3 for discussion of the theory behind this equation. However, the meaning and temperature dependence of the constants k and n were not discussed in any detail.

1.2.2 Mullite

1.2.2.1 Mullite and its uses

Mullite is a non-stoichiometric aluminosilicate ceramic. It was discovered as a naturally occurring mineral on the isle of Mull[18] and was first synthesised in 1865 by passing SiF_4 over a mixture of alumina and silica at a "bright red heat"[19].

Mullite is not ideal for high strength applications at room temperature because its low fracture toughness limits its strength to 200-500 MPa[20]. However, mullite can retain this strength at temperatures up to 1770 K[21]. This strength retention is dependent on the purity of the mullite phase, the particle size and the absence of any glassy phase[22]. Hence, the method of preparation is very important.

Mullite has also been shown to have very good creep resistance – *i.e.* the ability of a material to resist plastic deformation, especially at high temperature. Examination of mullite formed at 1770 K[21] showed that there was no plastic deformation at stress levels up to 900 MPa. If, however, mullite does contain an amorphous boundary, the creep resistance has been observed to decrease by two orders of magnitude[23].

A comprehensive review on the uses of mullite has been published by Tummala[24], relevant points of which are summarised here. The main use described is in the electronics packaging industry – *i.e.* the interconnecting, powering, protecting and cooling of semiconductor circuits. This is a vital technology on which the computer industry depends. A good packaging material has a low dielectric constant to prevent electric and magnetic fields from different parts of a circuit from adversely affecting the operation of the circuit. The dielectric constant of mullite ($\varepsilon = 6.5$) is low compared to that of alumina ($\varepsilon = 9.4$) which

has previously been widely used for packaging. Another important property of a packaging material is the possibility of soldering a chip to it. The fatigue life of the solder is dependent on the difference between the thermal coefficient of expansion of the ceramic and the thermal coefficient of expansion of the silicon in the chip, the smaller the difference the better. Mullite substrates have a thermal coefficient more similar to that of silicon than alumina substrates. Mullite-based glass ceramics have a thermal coefficient even closer to that of silicon, and hence are seen as a possible choice for high performance packaging applications.

1.2.2.2 Composition of mullite.

The composition of mullite varies according to x in the formulation

$$Al^{VI}_{2}(Al^{III}_{2+2x}Si^{IV}_{2-2x})O_{10-x}$$

where x denotes the average number of oxygen vacancies in the unit cell. All experiments performed in the present work used a ratio of aluminium to silicon such as to make mullite with x = 0.25, which is known as 3:2 mullite because, substituting into the formulation above, $Al_{4.5}Si_{1.5}O_{9.75}$ is equivalent to $3Al_2O_3 : 2SiO_2$. Naturally occurring mullite is always of this form, and other commonly made forms, such as 2:1 mullite (x = 0.4) easily degrade to this form[25]. The variation in composition occurs because of oxygen loss when tetravalent silicon is replaced in the structure by trivalent aluminium as x increases. The oxygen vacancies on the tetrahedral linking sites within the structure thus caused were initially thought to be randomly distributed[26], but it has since been asserted that certain situations are avoided, *e.g.* two holes adjacent to one another[27]. Due to these oxygen losses, there is no one crystal system that can describe mullite.

1.2.2.3 *Structure of mullite*

The ICSD gives the following structural data for mullite with x = 0.25 ($Al_{4.5}Si_{1.5}O_{9.75}$)[28]

i) dimensions of the unit cell :

$a = 7.54336(6)$ Å $\qquad \alpha = \beta = \gamma = 90°$

$b = 7.69276(6)$ Å

$c = 2.88402(2)$ Å

ii) location of atoms in the unit cell :

Atom type	*x*	*y*	*z*	Occupancy
Al	0.000	0.000	0.000	1
Al or Si	0.1485(1)	0.3407(1)	0.500	0.867(4)
Al or Si	0.2610(7)	0.2073(7)	0.500	0.133(4)
O	0.3577(2)	0.4235(2)	0.500	1
O	0.500 or 0.4635(2)	0.000 or 0.0465(2)	0.500	0.673(7)
O	0.1265(2)	0.2197(2)	0.000	1

space group: PBAM

22 atom sites per unit cell (not all occupied)

The compositional limits of mullite in the above formulation result in the structure having similarities with that of silimanite $Al_4Si_2O_{10}$ (x = 0) at one extreme and ι-alumina at the other (x = 1). The silimanite structure consists of columns of AlO_6 octahedra, which run parallel to the *c*-axis[27]. The octahedral columns are cross-linked by vertex-sharing pairs of tetrahedrally coordinated silicon and aluminium. These tetrahedra form double chains, which also run parallel with the *c*-axis. A single layer of the silimanite structure, looking down on the *c*-axis, is shown in Figure 1.4a. In mullite, Al^{3+} ions are replaced by Si^{4+} ions, giving rise to oxygen vacancies. It is thought that oxygen vacancies occur only at the tetrahedral linking sites[26 29]. This causes the neighbouring tetrahedra to relocate,

giving rise to a hole in the structure, as shown in Figure 1.4b.

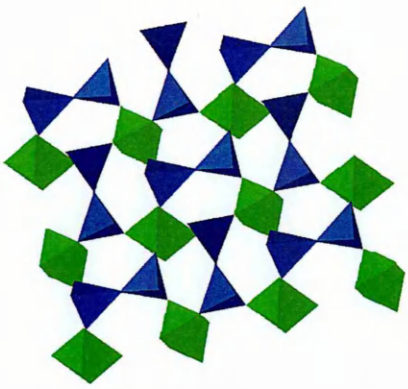

Figure 1.4a: the silimanite structure

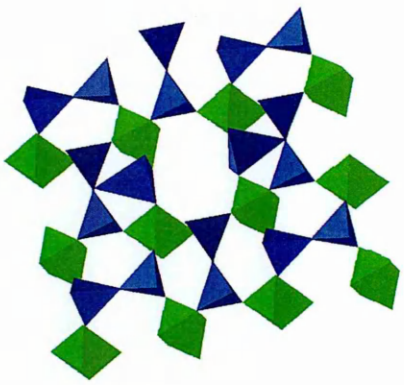

Figure 1.4b: the mullite structure showing an oxygen vacancy.

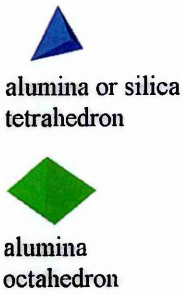

1.2.2.4 Synthesis of mullite

The conventional method of synthesising mullite has been to grind together alumina and silica in the required stoichiometry and fire the mixture at temperatures exceeding 1870 K. This was found to be an unsatisfactory route[30]. The temperature is excessively high for industrial processes, the lack of intimate association between the reactants leads to inhomogeneity of crystallite size, and long sintering times are required for complete reaction. It is the second of these problems which has caused the most concern, as an inhomogeneous crystallite size can adversely influence most of the beneficial properties of mullite described in Section 1.2.2.1.

Alternative methods of mullite synthesis have been developed to try to overcome these problems. The transformation of minerals such as kaolinite ($SiO_2.Al_2O_3.2H_2O$) or staurolite ($Fe^{2+}Al_{18}Si_8O_{46}(OH)_2$) can be successful[31], and tend to take place at lower temperatures than those required by the conventional method. However, these methods tend not to give a single phase product[32].

A detailed study by previous workers[33] has investigated various synthesis techniques, including those mentioned above as well as co-precipitation, spray drying, chemical vapour deposition and sol-gel techniques, and also methods using the hydrothermal processing technique in the initial stage of the synthesis before firing. The study also investigated the effect of varying the environment of the metals in the starting materials, *e.g.* using aluminium- and silicon- acetates, alkoxides, polymerics and salts. The hydrothermal processing technique was found to be highly effective in the production of single-phase mullite with homogenous low particle size (~50 nm), such as to optimise the beneficial properties of mullite as described in Section 1.2.2.1. Further study of the processes involved will ultimately enable the control and optimisation of high quality mullite formation.

This work investigates further the formation of mullite using hydrothermal processing of metal acetates in the initial stage of the synthesis. The instrumentation and techniques of the hydrothermal processing of mullite precursors are described in Section 2.6. In previous work it has been reported[34] that the product of hydrothermal processing of aluminium- and silicon-containing precursors, when dried by filtration, is a fine white powder, the X-ray powder diffraction pattern of which shows broad peaks at positions similar to those characteristic of pseudoboehmite, γ-AlOOH.nH_2O, although clearly the substance must also contain silicon in some form. When heated at temperatures exceeding 1370 K this substance forms mullite.

1.2.2.5 Boehmite and pseudoboehmite

The ICSD gives the following data on the structure of boehmite γ-AlOOH[35] :

i) dimensions of the unit cell :

$a = 2.86$ Å $\qquad \alpha = \beta = \gamma = 90°$

$b = 12.24$ Å

$c = 3.69$ Å

ii) location of atoms in the unit cell :

Atom type	*x*	*y*	*z*
Al	0.250	0.684(8)	0.0
O	0.250	0.287(5)	0.0
O	0.250	0.083(5)	0.0

space group: AMAM

12 atoms per unit cell

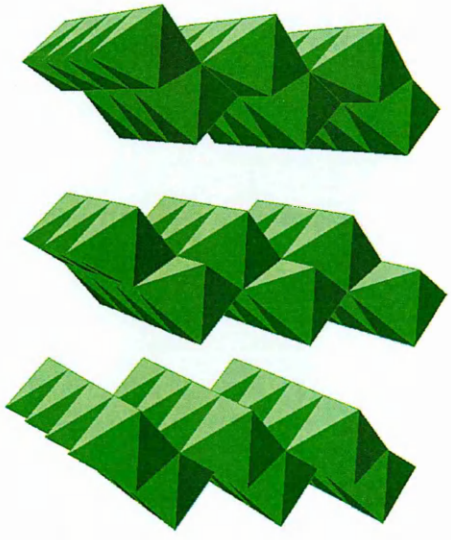

Figure 1.5: The structure of boehmite.

The structure of boehmite, shown in Figure 1.5, consists of planes of edge-sharing aluminium octahedra, linked by hydrogen bonds[36]. Pseudoboehmite is described as boehmite with a small particle size and intercalated water, which causes the structure to be more disordered[37].

Uncertainty still remains on the exact composition of the pseudoboehmite phase[38] formed by the hydrothermal processing technique in the synthesis of mullite as described in Section 1.2.2.4. There may be a separate but amorphous silicon-containing phase, or the silicon may be incorporated into the pseudoboehmite structure. However, the powder formed by this technique forms mullite at temperatures much lower than is achieved by conventional mixing and heating of reactants.

1.2.2.6 Metal-doped mullite

Metal dopants can improve the beneficial properties of mullite[39], and some dopants can further reduce the temperature and timescale of mullite formation. Commonly used dopants include manganese, iron, thallium, and chromium. The dopants chosen for this work were iron and vanadium. Previous workers[40] have shown that both these dopants significantly reduce the time and temperature required for mullite formation. Recent work[39] has also suggested that some dopants form a solid solution in the mullite lattice causing expansion of the *b*- and *c*-axes and contraction of the *a*-axis.

1.3 Theory of the kinetics of solid state phase transitions and reactions

This work is substantially concerned with investigating the kinetics of two solid state processes, and therefore it is appropriate to give an overview of the field of kinetics of solid state reactions and phase transitions. This is a field in which there are still significant uncertainties, although there are many texts that provide an introduction to the subject. The derivations in this section have been taken from the comprehensive text by Christian[41] as well as the Bamford and Tipper[42 43] series. Lecture notes provided by J Anwar[44] have also been useful.

1.3.1 Types of transformation

Heterogeneous reactions and phase transitions in the solid state have traditionally been regarded as falling into two main categories – "nucleation and growth" and "martensitic". A nucleation and growth transformation is considered in terms of the initiation of the change, which is known as nucleation, and the process of the change spreading throughout the material, which is known as growth. Individual atoms migrate independently to their place in the new structure, and given sufficient time the transformation will, in principle, continue until complete. The nucleation and growth process is thermally activated. A martensitic transformation is virtually independent of time, occurring almost instantaneously. Transformations of this type occur only when the composition of the original phase is the same as that of the product, such that no diffusion is involved. They involve the cooperative movements of many atoms rather than the independent movements of single atoms, as a small number of unit cells deform to the new phase in a single process. The extent to which the transformation occurs is dependent on temperature. More recent work has demonstrated that many transformations share characteristics of both nucleation and growth and martensitic models.

Nucleation and growth transformations may be further classified as either interface-controlled or diffusion-controlled. In the former, the compositions of the phases either side of the boundary are the same, albeit with different arrangements. The rate of growth of the new phase is determined by atomic processes in the immediate vicinity of the interface. In diffusion-controlled transformations, the composition of the product is not identical to the initial phase, so the rate of change depends on the speed with which atoms can diffuse towards or away from the growth boundary.

The processes which take place during nucleation and growth, and their relative dominances, vary considerably in different systems. However, it is possible to make some generalisations which do not require detailed knowledge of the mechanisms of nucleation and growth in order to model the kinetics of a change.

1.3.2 Kinetics of nucleation

Nucleation, or the initiation of a change, occurs when the local energy becomes sufficient to provide the necessary free energy of activation for nucleus formation. It is not necessary to have knowledge of the mechanism of nucleation in order to derive a useful model of the kinetics of the process. Nucleation is more likely to occur at localised points of crystallographic disorder, known as potential nucleation sites, such as grain boundaries, stacking faults, dislocations and other defects where the free energy of activation is lower. The following derivation assumes that:

(i) there are a limited number of potential nucleation sites,

(ii) the nucleation process is an instantaneous one-step occurrence,

(iii) the free energy of activation for the formation of a nucleus is equal for all sites.

If these assumptions hold, then the rate of nucleation will be directly proportional to the number of potential nucleation sites remaining at a given time in the process:

$$\frac{dS}{dt} = k_S(S_0 - S) \qquad \text{Equation 1.2}$$

where dS / dt is the rate of nucleation, S_0 is the total number of potential nucleation sites and S is the number of such sites where nucleation has occurred by time t, and k_S is an unknown rate constant governing nucleation which depends upon the free energy of activation required for nucleation and the energy supplied. Integration leads to a standard exponential dependence

$$S = S_0(1 - \exp^{-k_S t}) \qquad \text{Equation 1.3}$$

If the growth of the new phase causes cracking and the formation of new defect points, then the assumption that the total number of potential nucleus-forming sites is constant does not hold, and the above equations will not be valid. This effect is taken into account in Section 1.3.5 and 1.3.7.

1.3.3 Kinetics of growth

As with the phenomenon of nucleation, the kinetics of growth may be considered without knowledge of the mechanisms causing it, provided that the distinction between interface-controlled and diffusion-controlled processes is made. In an interface-controlled transformation, there is continuous growth at all points on the interface[45]. Direct microscopic observations of a large number of diverse interface-controlled solid state reactions have shown that nuclei generally grow at a constant rate. However, it is only possible to observe growth microscopically once the nuclei have reached a certain minimum size. Some reactions have been observed to have an initial linear growth rate slower than the final linear growth rate, and it is possible that this actually occurs in many systems.

In a diffusion-controlled process the change relies on the diffusion of atoms through the solid to the interface and the growth rate will be strongly dependent on diffusion rates, the exact shape of the particles of the material, and other factors. This type of process is considered in Section 1.3.5.

In some processes the nuclei may grow more readily in one crystallographic direction than in another. In these cases, three linear growth rate constants exist, one for each crystallographic direction. If one growth rate constant is much greater than the other two, the domains of new phase or reaction product will have a rod-like shape. If two growth rate constants are much greater than the other one, the domains of new phase or reaction product will have a plate-like shape. If all three constants are similar the domains of new phase or reaction product will be spherical.

1.3.4 The Avrami Erofe'ev equation

If a volume V of material undergoing a nucleation-and-growth transformation can be considered as having a nucleation rate per unit volume k_U then in a period of time $(t\text{-}\tau)$ the number of new nuclei formed, S, is:

$$S = k_U.V.(t-\tau) \qquad \text{Equation 1.4}$$

The volume v_i of an individual region of growth in the material can be generally defined as:

$$v_i = \varsigma.r^D \qquad \text{Equation 1.5}$$

where ς is a shape factor (*e.g.* $^{4\pi}/_3$ for a spherical growth), D is the dimensionality of the growth and r is the radial size of the region. If a growth rate k_G is the rate of increase of the radius r then the volume after time $(t\text{-}\tau)$ is:

$$v_i = \varsigma.k_G{}^D(t-\tau)^D \qquad \text{Equation 1.6}$$

In time dt the volume of the new phase transformed, V_{new}, will be the incremental growth of each growth region (defined in Equation 1.6) multiplied by the number of nuclei created (defined in Equation 1.4) thus, assuming that k_U is constant:

$$dV_{new} = \varsigma . k_G{}^{D} . k_U . V \int_0^{\tau} (t - \tau) dt \qquad \text{Equation 1.7}$$

On integration, this becomes

$$V_{new} = \frac{\varsigma . k_G{}^{D} . k_U}{D+1} . V . t^{D+1} \qquad \text{Equation 1.8}$$

However, this simple model assumes that new nuclei may be formed throughout the volume of the material. In practice, potential nucleation sites are absorbed into the transformed region of material before nucleation occurs. Also, growth is restricted when areas of growth springing from two neighbouring nuclei impinge upon one another and thus there is no further growth in that direction.

Johnson and Mehl[46] and Avrami[47] proposed a geometrical solution to this problem by considering an "extended" volume V_e of transformed material, being the volume of material that would have transformed if unimpeded by volumes already having been transformed. V_{new} described above in Equation 1.8 is equal to this extended volume rather than the volume of the new phase.

If γ is defined as the fraction of material which has transformed into the new phase (*i.e.* V_β / V) and γ_e as the equivalent for the "extended" volume V_e, then in time dt a small fraction dγ_e will transform into the new phase, of which γ will be material which has already transformed. Therefore,

$$d\gamma = (1 - \gamma) d\gamma_e \qquad \text{Equation 1.9}$$

and on integration this gives

$$\gamma_e = -\ln(1-\gamma) \qquad \text{Equation 1.10}$$

which can be substituted into Equation 1.8 to give

$$-\ln(1-\gamma) = \frac{\varsigma.k_G{}^{D}.k_U}{D+1}t^{D+1} \qquad \text{Equation 1.11}$$

This may be re-arranged to a form similar to that of Equation 1.1 proposed as a model for the kinetics of the phase transition of ζ_α-$FeSi_{2.33}$ to ζ_β-$FeSi_2$, as described in Section 1.2.1.4. This equation is known as the Avrami Erofe'ev equation and is normally expressed in the form

$$k.t = N[-\ln(1-\gamma)]^{1/N} \qquad \text{Equation 1.12}$$

where k is a general rate constant incorporating rate constants for both nucleation and growth and N is referred to as either the Avrami constant or the nucleation constant. The above derivation assumes that k_U is constant. Similar derivations exist for cases where k_U is increasing or decreasing, but in both cases the resulting expressions can be generalised into the same form as Equation 1.12. The physical interpretations of different values of N are given in Section 1.3.6.

The rate constant k will depend on various factors. In terms of temperature, the Arrhenius equation,

$$k = C.\exp\left(-\frac{\varepsilon}{RT}\right) \qquad \text{Equation 1.13}$$

where ε is the activation energy and R is the gas constant, has been shown experimentally[48] to govern the variation in the rate constant for many solid state reactions and phase transitions. However, the determination of the Arrhenius parameters provides only a limited description of the kinetics of the process and these parameters may well be influenced by reaction conditions.

1.3.5 Kinetics of nucleation and growth for diffusion-controlled transformations

Bamford and Tipper[49] state that the simplest kinetic law obeyed in many diffusion-controlled transformations is the parabolic law. If the surface area of each particle is constant and the diminishing reaction rate is a consequence of an increasing thickness of barrier layer through which diffusion must take place, then

$$\gamma = (k_D t)^{1/2} \qquad \text{Equation 1.14}$$

This expression may be combined with a similar derivation to that described in Section 1.3.4, along with an expression for the shape of the particle, to give a range of expressions equivalent to that given by Equation 1.12 for the interface-controlled transformations which apply to diffusion-controlled transformations:

$$-\ln(1-\gamma) = (kt)^M \qquad \text{Equation 1.15}$$

The exponent M is the sum of a factor indicating whether the nucleation is instantaneous (= 0), constant (= 1) or decelatory (between 0 and 1) plus a factor indicating whether the growth is in one dimension (= 0.5), two dimensions (= 1) or 3 dimensions (= 1.5). Hence the largest value for the exponent M in a diffusion-controlled transformation is 2.5.

1.3.6 Deriving the transformation type from a sigmoid curve

If the curve describing the extent of a transformation $\gamma(t)$ is obtained experimentally, the values of k and N may be extracted from the data mathematically. The value of N may be used to consider the mechanism type for the transformation. However, most possible values of N can be indicative of more than one transformation type, as shown in Table 1.1 below.

Condition		Value of N (interface-controlled transformation)	Value of M (diffusion-controlled transformation)
Increasing nucleation rate		> 4	n/a
Constant nucleation			
a)	3 dimensional growth	4	2.5
b)	2 dimensional growth	3	2.0
c)	1 dimensional growth	2	1.5
Decreasing nucleation rate			
a)	3 dimensional growth	3 – 4	1.5 – 2.5
b)	2 dimensional growth	2 – 3	1.0 – 2.0
c)	1 dimensional growth	1 – 2	0.5 – 1.5
Zero nucleation rate (instant saturation)			
a)	3 dimensional growth	3	1.5
b)	2 dimensional growth	2	1.0
d)	1 dimensional growth	1	0.5

Table 1.1: Possible values of the exponent in sigmoid equations[50]

Clearly therefore an experimentally derived value of the constant N does not provide a unique description of the kinetics of a phase transition or reaction, unless details are known (or can be estimated) of the time dependence of the nucleation rate or the dimensionality of growth.

1.3.7 The Prout-Tompkins kinetic model

An alternative model for the kinetics of solid state transformations is the "chain-type" model[51]. These are so-called because the original formulation of the theory assumed that the transformation took place via a kind of "chain reaction" in which the energy released from a transformation at one point in the structure provided the energy to initiate the transformation in a neighbouring point. This aspect of the theory has since been shown to be not generally applicable. However, the theory is still useful for certain types of

transformation, especially those where the rate of nucleation is initially strongly acceleratory, followed by termination of the nucleation rate upon saturation.

The model envisages either (i) the development of needle or laminar nuclei, which undergo branching and hence rapidly multiply or (ii) the development of cracks in the reactant phase due to strains at each reactant-product contact point, thus creating new nuclei. Although these both lead to reasonable kinetic expressions it is not normally possible to verify either model through observation or measurement.

If the rate of spontaneous creation of new nuclei is constant, k_U, and there is a constant rate of increase of existing nuclei, k_G, the expression for nucleation as a whole will be:

$$\frac{dS}{dt} = k_U S_0 + k_G S \qquad \text{Equation 1.16}$$

which has similarities with Equation 1.2. However, this cannot hold throughout a transformation, as eventually the reactant will be consumed. Equation 1.16 must therefore be altered to take this into account by adding a term for the termination of nucleation:

$$\frac{dS}{dt} = k_U S_0 + \{k_G - k_T(\gamma)\}S \qquad \text{Equation 1.18}$$

It is assumed that in this model the second part of this equation will dominate, therefore the expression may be approximated by:

$$\frac{dS}{dt} \approx \{k_G - k_T(\gamma)\}S \qquad \text{Equation 1.19}$$

Integration of this expression requires some knowledge of the relationship between k_G, k_T, and γ, where γ is the extent of the transformation and is equal to S / S_0. The Prout-Tompkins theory assumes that the extent of the transformation γ plotted against time t will

be a curve sigmoid in shape with rotational symmetry in which the point of inflection is at γ_i = 0.5. The boundary conditions allowing for integration of the above expression can therefore be assumed to be that when $t = 0$, $\gamma_0 = 0$ and $k_T = 0$, and when $t = t_i$ (the point of inflection), $\gamma_i = 0.5$ and $d\gamma / dt$ is at a maximum. Hence:

$$\frac{d\gamma}{dt} = k_G \gamma (1-\gamma) \qquad \text{Equation 1.20}$$

which integrates to:

$$\ln\left[\frac{\gamma}{(1-\gamma)}\right] = k_G t + c \qquad \text{Equation 1.21}$$

which is known as the Prout-Tompkins equation, also occasionally as the Austin-Rickett equation.

References for Chapter One

1 *New Encyclopædia Britannica* 15th Edition, pub. USA 1995 **21** p.426.

2 E. C. Bain, H. W. Paxton *Alloying Elements in Steel* 2nd Edition, pub. ASM International Ohio 1966 p. 244.

3 J. Baszkiewicz, J. A. Kozubowski, D. Krupa, M. Kaminski, A. Barcz, G. Gawlik, J. Jagielski *J. Mat. Sci.* 1998 **33** 4561.

4 J. R. Lampman, A. T. Peters (eds.) *Ferroalloys and Other Additives to Liquid Iron and Steel* ASTM Publications Philadelphia USA 1981 p. 51.

5 H. Holdhus *J. Iron & Steel Institute* 1962 p.1024.

6 T. B. Massalski *Binary Alloy Phase Diagrams* ASM International Ohio 1990.

7 ICSD ref. 42561 (54380). F.A. Sidorenko, P.V. Gel'd, L.B. Dubrovskaya, *Fizika Metallov i Metallovedenie* 1959 **8** 88.

8 ICSD ref. 9119 (3440). Y. Dusausoy & J. Protas *Acta Crystallographica B* 1971 **27** 1209.

9 © FIZ Karlsruhe and NIST. http://cds.dl.ac.uk/icsd/

10 © 1999 CrystalMaker Software P.O. Box 183, Bicester, Oxfordshire, OX6 7BS, UK.

11 Th. I. Sigfusson, Ö. Helgason *Hyperfine Interactions* 1990 **54** 861.

12 Th. Magnusson, M.Sc. Thesis *Silicon Rich Ferrosilicon* University of Iceland 1996.

13 History summarised in H. Holdhus *J. Iron & Steel Institute* 1962 p.1024.

14 J. van den Boomgaard *J. Iron & Steel Institute* 1962 p. 276.

15 B. Johannesson, Technological Institute of Iceland, Keldnaholt, 112 Reykjavik, Iceland.

16 Th. Magnusson, M.Sc. Thesis *Silicon Rich Ferrosilicon* University of Iceland 1996.

17 Ö. Helgason, Th. Magnusson, Th.I. Sigfusson *Hyperfine Interactions* 1998 **111** 215.

18 N. L. Bowen, J. W.Greig, E. G. Zeiss *J. Washington Ac. Sci.* 1924 **14** 183.

19 H. S. Deville, H. Caron *Ann. Chem. Phys.* 1865 p.114.

20 F. Orgaz. *Proc. Third Euro-Ceramics Conf.* P. Duran & J.F. Fernandez. Pub. Faenza Editrice Iberica S.L. Spain 1993 **1** 377.

21 T. Mah, K. S. Mazdiyasni *J. Am. Ceram. Soc.*1983 **66** 699.

22 P. C. Dokko, J.A. Pask, K.S. Mazdiyasni *J. Am. Ceram. Soc.*1977 **60** 150.

[23] R. D. Nixon, S. Chevacharoenkul, R.F. Davis, T.N. Teigs *Ceram. Trans.* 1990 **6** 579.

[24] R. R. Tummala *J. Am. Ceram. Soc.*1991 **74** 895.

[25] H. Schneider, K. Okada, J. Pask *Mullite & Mullite Ceramics* Wiley 1994 ch. 1.

[26] B. D. Butler, T.R. Welberry, R.L. Withers *Phys. Chem. Minerals* 1993 **20** 323.

[27] R. J. Angel, C.T.Prewitt *Am. Mineral.* 1986 **71** 1476.

[28] ICSD ref 74008 (38582). D. Balzar, H. Ledbetter *Am. Mineral.* 1993 **78** 1192.

[29] H. Schneider, K. Okada, J. Pask *Mullite & Mullite Ceramics* Wiley 1994 ch. 2.

[30] M. W.Booth, Ph.D. Thesis *The Characterisation of Mullite* The Open University 1986 p.7.

[31] G. W. Brindley, M. Nakahira *J. Am. Ceram. Soc.*1959 **42** 311.

[32] J. A. Pask, A.P. Tomisia *J. Am. Ceram. Soc.*1991 **74** 2367.

[33] M. W. Booth, Ph.D. Thesis *The Characterisation of Mullite* The Open University 1986 Ch4&5.

[34] M. W. Booth, Ph.D. Thesis *The Characterisation of Mullite* Open University 1986 p.72.

[35] ICSD ref. 15696 (5914). W.O. Milligan, J.L. McAtee *J. Phys. Chem.* 1956 **60** 273.

[36] A. F. Wells *Structural Inorganic Chemistry* 5th ed. O.U.P. 1984 p.641.

[37] R. C. T. Slade, J.C. Southern, I. M. Thomson *J. Mater. Chem.* 1991 **1** 875.

[38] F. J. Berry, M. W. Booth, P. M. Marquis, M. Mortimer, M. R. Piramoon, C. B. Ponton *J. Mater. Chem.* 1993 **3**(9) 965.

[39] S. P. Chaudhuri, S. K. Patra *Brit. Ceram. Trans.* 1997 **96** No.3 105-111.

[40] M. W. Booth, Ph.D. Thesis *The Characterisation of Mullite* The Open University 1986 p.125&147.

[41] J. W. Christian *The Theory of Transformations in Metals and Alloys* Pergamon Press 1975 Oxford UK.

[42] C. H. Bamford, C. F. H. Tipper (eds.) *Comprehensive Chemical Kinetics vol. 2 : The Theory of Kinetics* 1st ed. Elsevier Scientific Publishing 1969 The Netherlands Ch5.

[43] C. H. Bamford, C. F. H. Tipper (eds.) *Comprehensive Chemical Kinetics vol. 22 : Reactions in the Solid State* 1st ed. Elsevier Scientific Publishing 1980 The Netherlands.

[44] J. Anwar *Kinetics of Solid State Reactions* BCA Industrial Group Meeting: High Temperature Powder Diffraction, Middlesborough 1998.

[45] J. W. Christian *The Theory of Transformations in Metals and Alloys* Pergamon Press 1975 Oxford UK p.476.

[46] W. A. Johnson, R. F. Mehl *Trans. Am. Inst. Min. (Metall.)* 1939 **135** 416.

[47] M. Avrami *J. Chem. Phys.* 1939 **7** 1103.

[48] C. H. Bamford, C. F. H. Tipper (eds.) *Comprehensive Chemical Kinetics vol. 22 : Reactions in the Solid State* 1st ed. Elsevier Scientific Publishing 1980 The Netherlands pp.87-91.

[49] C. H. Bamford, C. F. H. Tipper (eds.) *Comprehensive Chemical Kinetics vol. 22 : Reactions in the Solid State* 1st ed. Elsevier Scientific Publishing 1980 The Netherlands p.69.

[50] C. H. Bamford, C. F. H. Tipper (eds.) *Comprehensive Chemical Kinetics vol. 22 : Reactions in the solid state* 1st ed. Elsevier Scientific Publishing 1980 The Netherlands p.71.

[51] C. H. Bamford, C. F. H. Tipper (eds.) *Comprehensive Chemical Kinetics vol. 22 : Reactions in the solid state* 1st ed. Elsevier Scientific Publishing 1980 The Netherlands p.67.

Chapter Two: Theory and Instrumentation of Techniques

This Chapter describes the measurement and analysis techniques used in this work.

2.1 Generation of X-rays

Several of the techniques described in this chapter use X-rays for structural measurements, and therefore a description of the techniques used for generating X-rays is given here. X-rays, discovered by Röntgen in 1895[1], are high-energy electromagnetic radiation with wavelengths between 0.01 Å and 10 Å. X-ray diffraction experiments are usually carried out using X-rays with wavelengths between 0.5 Å and 2.5 Å.

Photons are produced whenever charged particles, usually electrons, experience a change in energy, either through a change of energy state within an atom, or an acceleration, or a deceleration. When this change in energy state produces photons within the range $10^3 - 10^5$ eV, these photons are known as X-rays. Two most common means of generating X-rays are outlined below, as described in the texts by Als-Nielsen and McMorrow[2], and Duke[3].

2.1.1 Copper anode X-ray tube

X-rays may be generated in an evacuated tube containing a tungsten filament which acts as a cathode, emitting electrons which are accelerated through a potential difference of ~30 kV before striking a metal anode target. The deceleration of the electrons by collisions within the anode causes energy to be released in the form of high-energy photons, or X-rays (known as brehmstrahlung 'braking' radiation) which are emitted as white radiation at all energies up to the energy of the accelerating potential difference. However, at certain energies, the energy of an electron transferred to an atom within the anode in one collision is sufficient to release an electron from an inner shell, ionising the atom. An electron from an outer shell then drops into the lower orbital, thus releasing energy in the form of a

photon. This phenomenon leads to sharp peaks in the X-ray spectrum. Figure 2.1 shows the idealised form of the spectrum of photons typical of a copper anode. Each peak represents a different transition of electrons within the copper atom. If an electron is ejected from the 1s shell and an electron drops from a 2p shell into the empty orbital, the transition is known as K_α. Close examination of the X-ray spectrum in the K_α region shows that the peak is made up of two barely resolvable peaks. These are the K_{α^1} peak at 1.54056 Å and the K_{α^2} peak at 1.54439 Å, which are generated by transitions from the 2p orbitals with spin $j = {}^3/_2$ and $j = {}^1/_2$ respectively. If the empty 1s orbital is filled by an electron from the 3p orbital the transition is known as K_β and the radiation produced has a wavelength of 1.39217 Å.

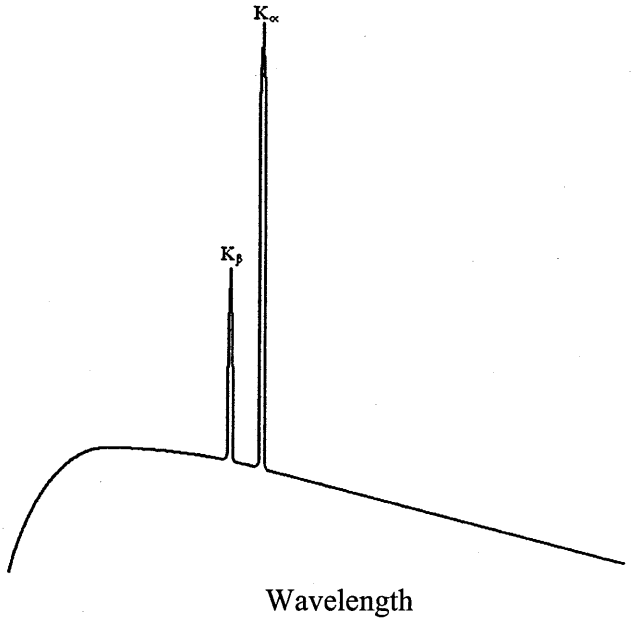

Figure 2.1: Typical spectrum from a copper anode X-ray source

If monochromatic X-rays are required, a nickel filter is usually used to remove the K_β peak from the X-ray spectrum. However, the difference between the wavelengths of the K_{α^1} peak and the K_{α^2} peak is small enough not to affect results under most circumstances. The Brehmstrahlung radiation at other wavelengths is not usually removed and leads to a low level of background noise at all angles. Thus a reasonably monochromatic beam of

wavelength 1.54 Å is produced. If a monochromatic beam at another wavelength is required, a different metal anode may be used in the X-ray tube, or a monochromator (see Section 2.3.5) may be used to select a particular wavelength from the lower intensity Brehmstrahlung radiation.

2.1.2 Synchrotron radiation

Synchrotron radiation was first observed in 1947[4], and was developed for experimental application in the 1960s. As the availability of large-scale synchrotron sources has increased, it has become the preferred tool for X-ray studies due to the high quality and brilliance of the electromagnetic radiation produced.

When an electron (charge e) travelling through vacuum with velocity $\boldsymbol{v}$ passes through a magnetic field $\boldsymbol{B}$ which is oriented in a direction perpendicular to $\boldsymbol{v}$, the magnetic field associated with the electron interacts with the field $\boldsymbol{B}$, which results in a force $\boldsymbol{F}$

$$\boldsymbol{F} = e\boldsymbol{v} \times \boldsymbol{B} \qquad \text{Equation 2.1}$$

which acts upon the electron in a direction perpendicular to its velocity and the field $\boldsymbol{B}$. This causes the electron to move in a circle with radius ρ,

$$\rho = \frac{mv}{Be} \qquad \text{Equation 2.2}$$

where m is the mass of the electron. Any acceleration of a charged particle generates electric and magnetic fields, and therefore electromagnetic radiation. This propagates in all directions from the electron with a wide range of energies. At relativistic electron velocities, the propagation in all directions occurs only in the electron frame of reference, but in the laboratory frame Lorentz contraction is such that the bulk of the electromagnetic radiation propagates over a small angular distribution in a direction tangential to the circular path of the electron[5 6].

Several techniques have been developed to provide the conditions needed for circular acceleration of electrons, of which the synchrotron accelerator is only one. Properly, the term synchrotron applies only to an apparatus with a uniform magnetic field such that the electron path is actually circular. The most common large-scale radiation sources using the principles of synchrotron radiation are storage rings, which consist of a number of bending magnets arranged in a circle. The electron path is not circular, as the electrons travel in straight lines between each bending magnet. Some of the magnetic sections in the ring may be "wigglers" or "undulators" rather than simple bending magnets, which constrain the electron pathway to a series of semi-circular arcs, generating a radiation beam of even greater brilliance. However, common usage refers to all radiation generated according to these principles as synchrotron radiation.

The experiments using synchrotron radiation reported in this work were carried out using the Synchrotron Radiation Source (SRS) at Daresbury Laboratory. The Daresbury SRS is a storage ring consisting of sixteen bending magnets arranged in a circle. Electrons are emitted from a cathode and accelerated using a linear accelerator to an energy of 12 MeV before passing into a small booster ring which accelerates the electrons to an energy of 600 MeV. Electrons are then injected into the storage ring, at which stage the energy is brought up to approximately 2 GeV.

An idealised graph of the typical spectrum of electromagnetic radiation obtained from a storage ring bending magnet is shown in Figure 2.2. The intensities of radiation produced from the circular acceleration of stored electrons are far greater than those obtainable using conventional metal anode techniques. The electromagnetic radiation produced is also coherent and, in the plane of the electron circle, unpolarised. The intensity is not quite

uniform over different wavelengths. However, the variation is small, and so experiments over a wide range of wavelengths are viable.

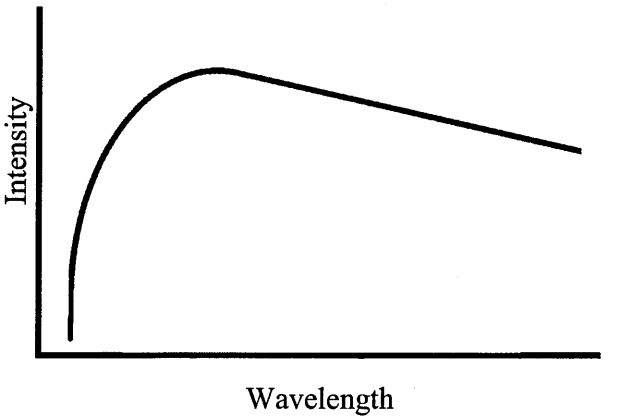

Figure 2.2: The shape of the spectrum of electromagnetic radiation from a storage ring bending magnet.

2.2 X-ray powder diffraction

X-ray diffraction crystallography was first suggested by von Laue in 1912, and developed as a usable technique for structural analysis by Bragg and Bragg in 1913[7]. Since then, and especially recently with very high resolution X-ray diffraction being made available, it has been used extensively both to characterise and identify crystalline materials. There are many texts providing a description of the theory and techniques pertaining to X-ray diffraction available. That by Azároff and Buerger[8] provides a good basic introduction to the technique sufficient for the depth of this work.

2.2.1 Scattering

When an electromagnetic wave is incident upon a system of electrons, the electrons are disturbed by the electrical field and will vibrate with the same frequency as the radiation. The accelerating electrons generate electromagnetic radiation. This radiation propagates in all directions, and thus the electrons are said to scatter the radiation.

If a beam of electromagnetic radiation is incident on a plane of atoms, every atom in the beam will scatter the radiation in all directions. However, in most directions destructive interference between electromagnetic radiation scattered from neighbouring atoms will prevent the scattered radiation from propagating. In order for constructive interference to occur there must be an equal path length from a wave front before the beam reaches the plane to a wave front after the beam has passed the plane, for all atom locations on that plane, as shown in Figure 2.3. This occurs in only two directions, firstly the direction of the continuation of the beam, and secondly the direction of the specular reflection of the beam in the plane (green lines). In all other directions (e.g. red lines) there will be a difference between the distance to the wavefront (solid black line) and the line of equal distance

(dashed black line) and the radiation will not propagate.

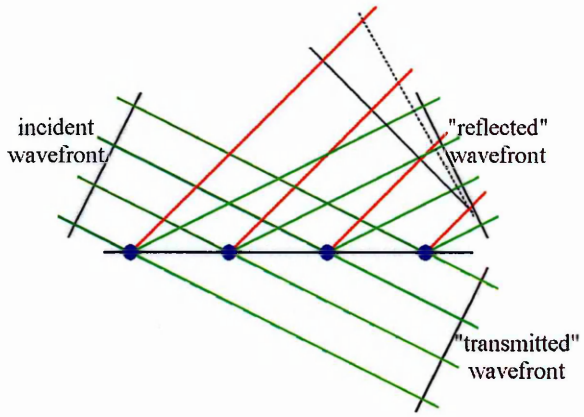

Figure 2.3: The scattering of electromagnetic radiation from a plane of atoms

Thus, a plane of atoms within a crystalline structure reflects radiation only at an angle equal to the angle of incidence, yet allows some radiation to pass through with direction unchanged. Therefore, in considering theories of X-ray diffraction in crystals, a plane of atoms may be treated as a semi-silvered mirror.

2.2.2 X-ray diffraction in crystals

When electromagnetic radiation is incident on a crystalline solid, it is partially specularly reflected by all of the planes within the structure. When the radiation is of a wavelength comparable with the distance between adjacent planes in the structure, there will be constructive and destructive interference between radiation reflected from different planes. A diffraction pattern will be seen, from which structural details about the crystal structure may be determined. If the wavelength of the electromagnetic radiation is much smaller than the distance between planes the diffraction angles will be very small, making resolution difficult. If the wavelength is much larger, the detailed structure cannot be resolved, although some average interaction does occur, as is seen with visible light. The

distance between atoms in most crystal structures is ~2 Å, and thus electromagnetic radiation in the X-ray region of the spectrum is most useful for diffraction techniques.

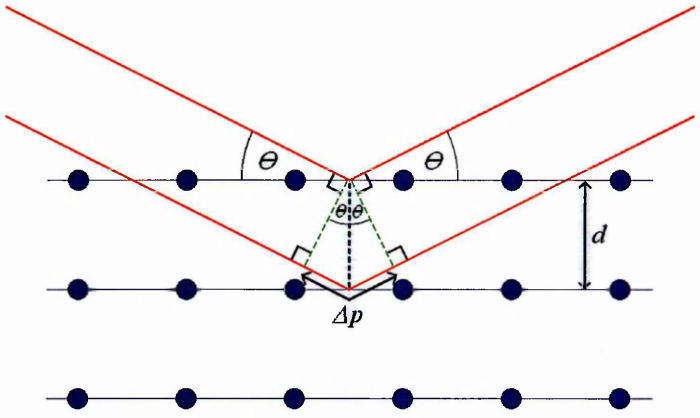

Figure 2.4: Defining the Bragg angle

The path difference, Δp, of electromagnetic radiation reflected from two adjacent planes in a crystal is shown in Figure 2.4. When Δp is a whole number of wavelengths, constructive interference will be seen. The angle at which this occurs is known as the Bragg angle and is defined by the condition:

$$n\lambda = 2d.\sin\theta \qquad \text{Equation 2.3}$$

where n is a positive integer, λ is the wavelength of the X-rays, d is the distance between the planes of atoms in the crystal, and θ is the Bragg angle. Equation 2.3 is commonly known as Bragg's Law.

2.2.3 X-ray powder diffraction

Most analytical X-ray diffraction experiments use monochromatic X-rays. In order to satisfy the Bragg condition for a fixed wavelength, it is necessary to have a continuous distribution of angles of the crystal planes relative to the incident beam, so that all planes will reflect. A powdered crystalline material consists of a large number of randomly oriented small crystals,

known as crystallites. When placed in an incident beam of X-rays, a small fraction of crystallites will be oriented so that they satisfy the condition for θ as defined by the Bragg equation for one or more of the crystal planes. Each crystallite will diffract a beam at an angle of 2θ from the incident beam, as shown in Figure 2.5.

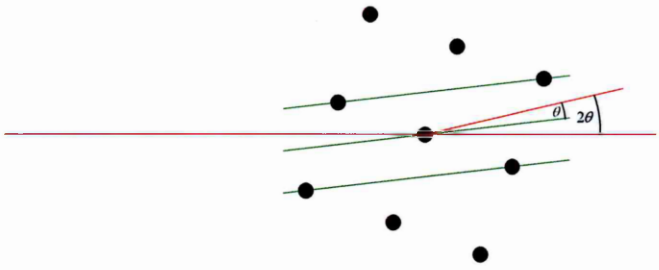

Figure 2.5: Angles of diffraction

As only the angle between the incident beam of X-rays and the crystallite planes is significant, the orientation of the crystallite about the axis of the incident beam is irrelevant. Each crystallite will diffract at an angle of 2θ to the incident beam regardless of this orientation, and thus the locus of diffracted X-rays for each set of crystal planes will be a cone with the apex at the sample and semi-apex angle 2θ. A separate cone of X-rays will be formed for each set of lattice planes, thus the diffraction pattern recorded by placing photographic film perpendicularly to the incident X-ray beam would consist of a series of concentric circles. This is shown in Figure 2.6a.

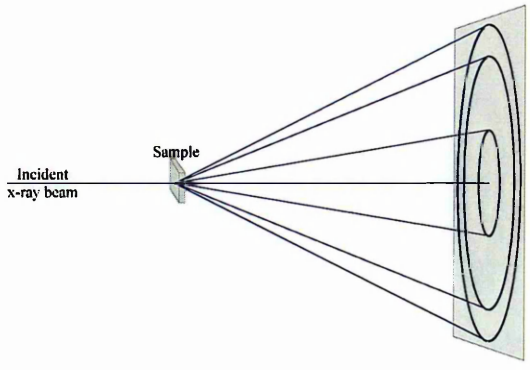

Figure 2.6a: The formation of a cone of diffracted radiation.

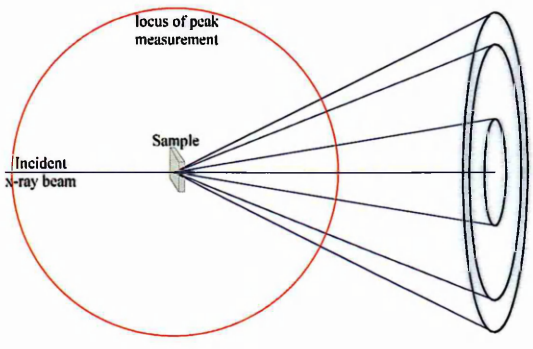

Figure 2.6b: The locus of where measurements are taken.

Generally, measurements are not taken of the entire set of concentric rings, but rather

measurements are taken along a single line in a circle around the sample (Figure 2.6b), which intersects with each cone of diffracted X-rays such that the diffraction angle 2θ may be calculated. For phase identification it is not necessary to record the entire pattern, but only to record the positions of the strongest peaks. These may then be compared with known patterns stored in a database. If structural refinement is required then a much larger portion of the pattern will be recorded to a much higher resolution and accuracy than is used for phase identification.

2.2.4 Crystal structure

The values of *d*, the distance between planes, which are calculated from each value of the peaks in intensity of radiation recorded at angles 2θ using Equation 2.3, must then be related to the crystal structure. Crystals are thought of as being made up of a very large number of blocks, known as unit cells, which are packed together. There are seven possible shapes of unit cell, which can pack together in three dimensions. A unit cell may contain various atoms at various locations within the unit cell, but because all unit cells are identical the distances between planes depends only on the shape and dimensions of the unit cell. The seven possible shapes are shown in Figure 2.7.

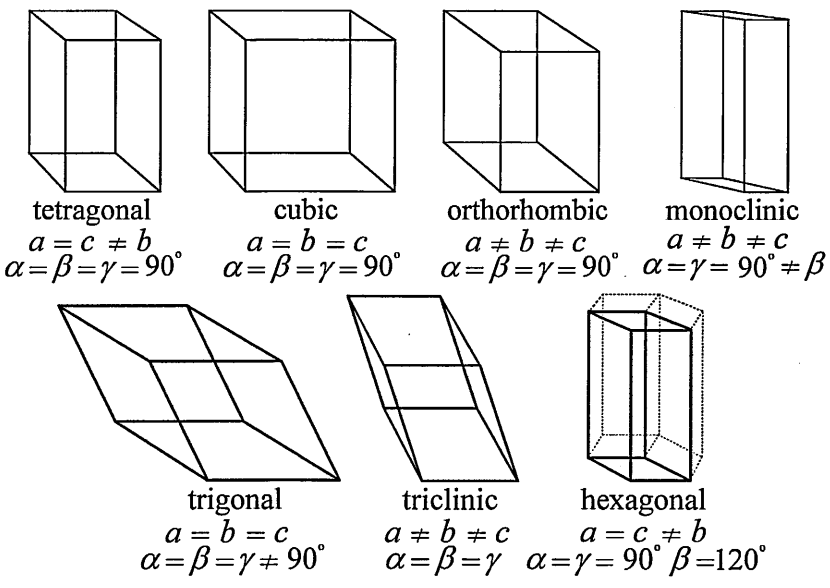

Figure 2.7: Possible shapes for a crystal unit cell

The shape of a unit cell is described in terms of the lengths, usually expressed in Angstroms (Å), of the three axes, which are known as *a*, *b*, and *c*, and the angles between each pair of axes, which are expressed in degrees and known as α, β, and γ. α is the angle between the *b* and *c* axes, β is the angle between the *a* and *c* axes, and γ is the angle between the *a* and *b* axes.

Crystals contain planes in many orientations, which cut the axes of unit cells at rational fractions of the dimension of the unit cell along each axis, and are defined in terms of their Miller indices. The Miller index is the reciprocal of the point at which the plane cuts the axis. Three Miller index numbers (generally *h*, *k*, *l*) are required to describe a plane, which relate to the intercepts on the *a*, *b* and *c* axes respectively. Figures 2.8a-e illustrate the use of Miller indices to describe crystal planes.

A Miller index of zero indicates an intercept point at infinity and thus describes a plane parallel to that axis. A Miller index with a bar above indicates that the intercept is in the negative direction along that axis.

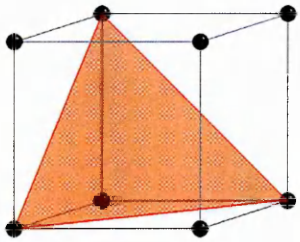

(a) Crystallographic plane with Miller indices (111)

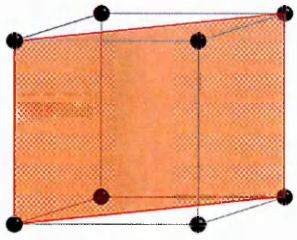

(b) Crystallographic plane with Miller indices (110)

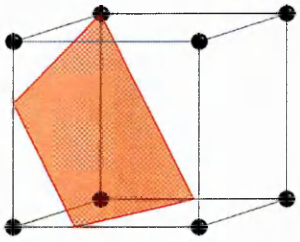

(c) Crystallographic plane with Miller indices (163)

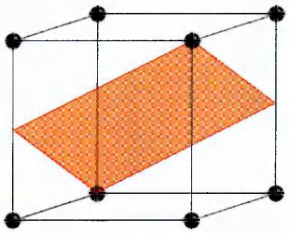

(d) Crystallographic plane with Miller indices $(11\bar{2})$

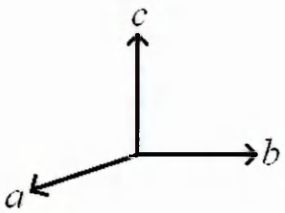

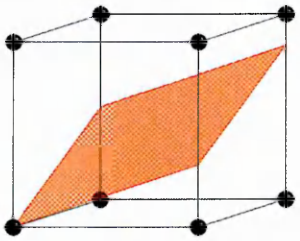

(e) Crystallographic plane with Miller indices $(\bar{3}2\bar{6})$

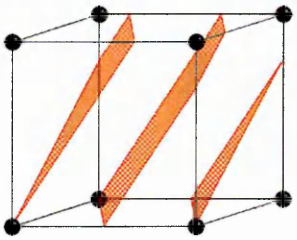

(f) Set of crystallographic planes with Miller indices $(3\bar{6}4)$

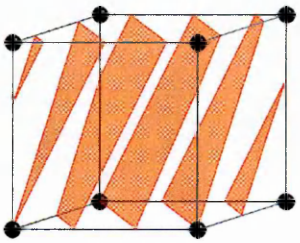

(g) Set of crystallographic planes with Miller indices $(\bar{4}6\bar{3})$

Figures 2.8: Illustrating Miller indices

For a unit cell with $\alpha = \beta = \gamma = 90°$ the value of d, the distance between planes, can be calculated by the formula

$$d_{hkl} = \left[\frac{h^2}{a^2} + \frac{k^2}{b^2} + \frac{l^2}{c^2} \right]^{-1/2} \qquad \text{Equation 2.4}$$

If α, β, or γ are not equal to 90° this equation is more complicated. However, the materials used in this work all have unit cells with $\alpha = \beta = \gamma = 90°$. Thus, the values of the diffraction angles θ calculated from an X-ray powder diffraction pattern may, if h, k, and l can be identified for each peak, be easily used to calculated values for the unit cell dimensions a, b and c.

While the positions of the diffracted X-ray beams are dictated solely by the shape, size and

crystal system of the unit cell, the intensities of the diffracted beams are dependent on the nature of the atoms themselves. The theory of X-ray diffraction presented in Sections 2.2.1 and 2.2.2 treats atoms as single points. However, on the scale of crystal structures, ~2 Å, the positions of the electrons, which are distributed throughout the atom volume, become significant. Electromagnetic radiation scattered from one side of an atom will not be perfectly in phase with that scattered from the other side of the same atom, and so partial destructive interference will occur.

The efficiency of an atom to scatter X-rays is described by a form factor *f*, which largely depends on the number of electrons in the atom. The effects of the form factor are more significant as the Bragg angle θ increases, and so a general decrease in peak intensity is seen at high angles in diffraction patterns. Also, the relatively low electron density in smaller atoms makes them difficult to detect. The intensity of diffracted X-rays crucially depends on the arrangement of atoms within the unit cell, which is described by a function known as the structure factor, which takes into account the contribution of all atoms within the unit cell to the overall amplitude of a wave diffracted from a given set of *hkl* planes.

Other effects which influence the intensity of the diffracted X-rays are the partial absorption of some of the photons by the atoms (described by the absorption factor); the Lorentz polarisation effect; the thermal vibrations of atoms at higher temperatures which both decrease the intensity of the diffracted X-rays and increase the line broadening due to an uncertainty in the position of the atoms.

2.2.5 X-ray powder diffraction for phase identification

When X-ray powder diffraction is used only to identify the phases present in a material, detailed structural analysis is not required. The Joint Committee on Powder Diffraction

Standards (JCPDS) issues a database of the known X-ray powder diffraction patterns of over 60000 compounds. The peak positions and relative intensities of recorded patterns may be compared with patterns in the JCPDS database in order to find a match. As no two compounds give identical patterns, this is a reliable method of phase identification.

2.2.6 Rietveld refinement

When detailed structural information about a phase is required, the analysis must be very thorough in order to accurately identify the positions of each atom within the unit cell. The analysis of X-ray powder diffraction patterns for structural purposes was developed by Rietveld in 1969[9]. The Rietveld method of refinement uses the method of least squares to fit a calculated diffraction profile to the measured diffraction profile. Instead of simple phase-identification, this method enables structural details of the unit cell, including any effects of impurities, to be determined.

The calculation of structure provided by the analysis program includes a reliability factor R_{wp} (or R-weighted-pattern) expressed as a percentage. The value of R_{wp} which can be taken as indicating that a good fit has been found is dependent on data quality. Therefore, the analysis includes a figure R_{exp} which is the reliability factor which would be expected for a perfect fit with that level of data quality. The actual R_{wp}-factor achieved should be within 20% of this value for a fit to be acceptable.

2.2.7 Recording of X-ray powder diffraction data at The Open University

The instrument used for X-ray powder diffraction at The Open University is a Siemens D5000 1988 model using Cu-K_α radiation with a rotating flat disc sample plate and a θ–2θ arm.

As with most diffractometers, this apparatus detects diffracted X-rays using a detector mounted on an arm, which is rotated about the specimen. When the sample is mounted on a flat plate, the plate is also rotated so as to keep the angle made by the X-ray beam to the surface of the sample plate equal to the angle from the surface of the sample plate to the detector. The detector is a proportional counter (ionising chamber) in which X-rays generate current pulses. The magnitude of the current is then proportional to the intensity of the diffracted X-ray beam.

2.2.8 Recording of X-ray powder diffraction data at Daresbury Laboratory

X-ray powder diffraction using synchrotron radiation can provide data of a much higher quality than that which can be obtained using a conventional metal anode diffractometer. Diffraction patterns may be recorded at almost any wavelength, the wavelength can be selected to be highly monochromatic, and the high flux means that a smaller beam size may be used, increasing resolution whilst maintaining an excellent signal to noise ratio.

X-ray powder diffraction patterns were recorded using the equipment on Station 9.1 at Daresbury Laboratory. X-rays are generated as described in Section 2.1.2 and passed through a monochromator as described in Section 2.3.5. The sample is placed in a capillary tube which rotates about its long axis in the beam – this provides a better distribution of crystallite positions. The detector arm is a proportional counter mounted on a moving arm which rotates about the sample to record diffraction intensity over the required range of angle 2θ, at a resolution of 0.01° in 2θ.

Details of the collection of X-ray diffraction data at high temperature using Station 9.3 may be found in Section 2.4.

2.3 The EXAFS technique

The principles of extended X-ray absorption spectroscopy fine structure (EXAFS) have been understood for most of the twentieth century. However, the practical application of the technique has been hindered until more recent times by the lack of good quality tuneable sources of white radiation. EXAFS is theoretically possible using traditional X-ray tube radiation, but it is only with the advent of synchrotron radiation that the technique has become a reliable and useful structural tool.

The phenomenon of EXAFS was first observed by Kronig[10] in 1931, but the structural analysis to be gained from the phenomenon was not discovered until 1975 by Stern, Sayers and Lytle[11]. More recent developments in the theory, practice and analysis of EXAFS have enabled the development of the technique into a powerful analytical tool. Several accounts of the theory exist, that by Teo[12] is particularly useful.

2.3.1 X-ray absorption

The photoelectric effect was explained by Einstein in 1905 in terms of photons impinging on a material and being absorbed by the atoms of the material, which transfer the energy to their electrons. If the photon is of sufficient energy, an electron is released from its atomic orbital and becomes free. This leads to very sharp steps in the absorption spectrum, known as absorption edges. In the X-ray region of the electromagnetic spectrum the photon energies are great enough (1 – 40 keV) to release electrons from core K (1s) or L (2s or 2p) shells of the heavier elements.

Figure 2.9 shows a simplified and idealised X-ray absorption spectrum, such as that which

would be recorded from a monatomic gas in perfect, noiseless conditions. There is very little absorbance at energies below that required to eject an electron from an inner shell, but when the photons are tuned to the binding energy of a core electron, there is a sharp increase in absorption. After the absorption edge the absorbance remains high, but decreases monotonically as the higher energy electrons are less likely to be absorbed by the material.

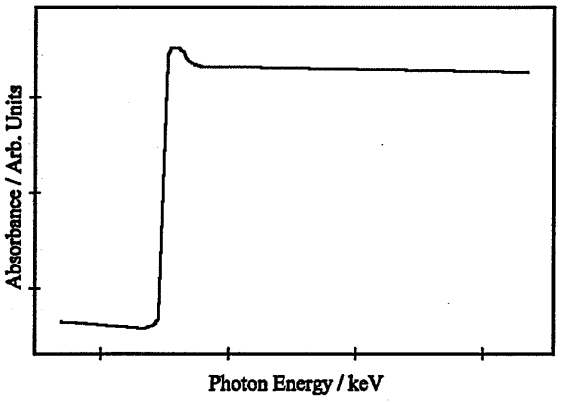

Figure 2.9: Idealised X-ray absorption spectrum of a monatomic gas.

2.3.2 EXAFS spectroscopy

In a molecule or in a condensed phase, all atoms are in an environment of other atoms. An outgoing photoelectron emitted from an absorbing atom scatters from the surrounding atoms, and can be reflected back towards the origin. The electron may be treated as a spherical wave originating from the absorbing atom. The reflected and phase-shifted wave undergoes constructive and destructive interference with the outgoing wave from the absorbing atom. This modifies the absorption cross-section of the absorbing atom, leading to a variation in the absorbance of the material.

Figure 2.10 shows an idealised raw absorption spectrum from a simple solid. When an X-ray absorption spectrum is recorded from a sample, oscillations are seen in the spectrum

after the absorption edge. These oscillations (the EXAFS) may be related back to details about the local environment of the absorbing atom, and structural information about the material may be deduced.

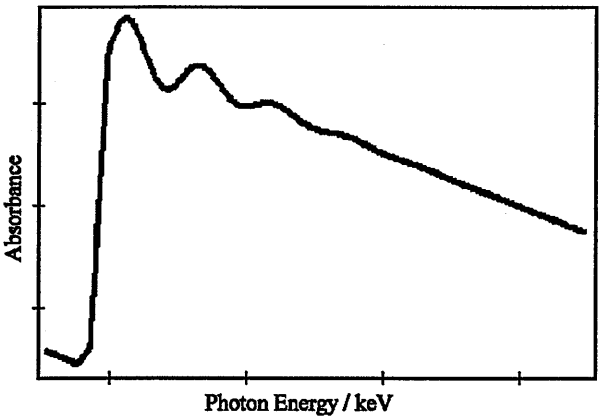

Figure 2.10: Idealised EXAFS raw data for a simple solid

2.3.3 EXAFS theory

The absorbance of a material, usually expressed in terms of an absorption coefficient μ, is measured by observing the attenuation of a beam of X-rays due to their passage through the material. The event of a photon, of sufficient energy that it is absorbed and a core electron emitted, colliding with an atom will occur randomly with a constant probability dependent on the material. Therefore the difference in the intensity of an impinging beam of photons (∂I) after passing through a material will be proportional to the initial intensity (I) and the thickness (∂x) of the material through which the beam must travel. The constant of proportionality is known as the absorbance, μ. This may be expressed mathematically as

$$\partial I = -\mu . I . \partial x \qquad \text{Equation 2.5}$$

This expression integrates to

$$\mu.x = \ln\left(\frac{I_0}{I}\right) \qquad \text{Equation 2.6}$$

Therefore the absorbance can be measured by recording and comparing the intensity of the beam of photons before and after it passes through the material, and it is this technique which is used for transmission EXAFS. If EXAFS data are to be recorded on very dilute samples, or at an absorption edge with a low energy such that general absorption by the surrounding material may totally eliminate the transmitted beam, the absorbance is measured by other means (see Section 2.3.5.2).

The absorbance data, normalised to the free-atom background, yields a function $\chi(E)$ which is the oscillatory part of the spectrum.

$$\chi(E) = \frac{\mu(E) - \mu_0(E)}{\mu_0(E)} \qquad \text{Equation 2.7}$$

The ejected photoelectron is treated as a spherical wave originating at the absorbing atom, with wavenumber k defined as

$$k = \sqrt{\frac{2m}{\hbar^2}(E - E_0)} \qquad \text{Equation 2.8}$$

A simple short-range, single-electron, single-scattering treatment of $\chi(E)$ formulated by Stern, Sayers and Lytle[11] relates $\chi(E)$ to structural parameters through a transform into k space such that

$$\chi(k) = \sum_j N_j S_i(k) F_j(k) e^{-2\sigma_j^2 k^2} e^{-2r_j/\lambda_j(k)} \frac{\sin\left(2kr_j + \phi_{ij}(k)\right)}{kr_j^2} \qquad \text{Equation 2.9}$$

where $F_j(k)$ is the amplitude of the electron wave backscattered from each of the N_j neighbouring atoms of type j and at distance r_j, with a Debye-Waller factor σ_j accounting for thermal and static disorder in the system. The term $e^{-2r_j/\lambda_j(k)}$ accounts for inelastic scattering losses in which a photoelectron is not ejected, which may be due to neighbouring

atoms or the surrounding medium, and is determined by the electron mean free path λ_j. $S_i(k)$ is an amplitude reduction factor due to many-body effects such as shake-up/off processes at the central atom i. The sinusoidal term contains an expression, dependent on r, which describes the periodicity of the structure, and a term ϕ_{ij}, describing the phase shift experienced by the electron wave due to backscattering. ϕ_{ij} is sometimes divided into two terms, $\phi_{ij}(k) = 2\delta_i(k) + \theta_j(k)$, being the phase shift due to the absorbing atom and the phase shift due to the j^{th} neighbouring atom respectively. Several derivations for this equation may be found in the text by Teo[13].

However, this theory is not general. The derivation requires the assumption that all atoms are small compared to interatomic differences and as such the spherical electron wave may be treated as a plane wave. Unless the atom size is indeed very small, or the distance between atoms very large such as to match the plane wave approximation more reasonably, this approximation is not valid. A curved-wave theory must therefore be adopted.

The exact curved-wave theory of EXAFS, derived by Lee and Pendry[14] in 1975 and Gurman and Pettifer[15] in 1979, is mathematically complicated and not suited to practical use. A simplified curved-wave theory, known as the rapid curved-wave theory, was published by Gurman, Binstead and Ross[16] in 1984. The rapid curved-wave theory retains the accuracy of the exact curved-wave theory while vastly reducing the computational time required to perform the calculations by removing the necessity to define the direction to the scattering atom, and averaging the angles throughout.

Under most circumstances the rapid curved-wave, single-electron, single-scattering theory is sufficient for structural analysis, and this theory is the basis for the analysis programs

used for the data collected in connection with this work. Occasionally, it may be necessary to modify the theory to incorporate the possibility of multiple scattering, which is the effect of the electron wave impinging upon a third atom after reflection from the scattering atom. In this case the exact curved-wave theory must be used.

2.3.4 EXAFS analysis

All the EXAFS data recorded as part of this work were analysed with the following software programs: calibration was performed using Excalib[17], background subtraction was performed using Exbrook[18] and final analysis was performed using the Excurv97 program[19], all based on the xrsserv1 server at Daresbury Laboratory.

2.3.4.1 Calibration

The raw data from an EXAFS experiment consists of beam intensity measurements from scintillation counters which are placed in the X-ray beam path before and after it passes through the sample, the time of recording, and the angle of the monochromator at the time of the reading. The data are calibrated using measured "dark current" readings taken from the scintillation counters when no beam is present, any glitches or obviously erroneous data points are removed. Ideally a number of data sets will have been collected from each sample, and these are summed after calibration. During time-resolved experiments this is not usually possible unless the experiment conditions are such that the rate of transformation is low. The output is a file containing the energies of the X-ray beam and the absorbance, μ, of the sample at that energy.

2.3.4.2 Background subtraction

The data, such as depicted in Figure 2.10, are then background subtracted in order to reject the parts of the data that are due to the structureless absorption edge and achieve data for $\chi(E)$, the oscillatory part of the data. When the Exbrook program is used for

background subtraction, the procedure is as follows:

1) The absorption energy, E_0, is identified and used as a reference point for further calculations.
2) The monotonic decrease in absorbance, μ, which is due to the decrease in absorption cross section at higher energies of X-rays, is fitted to two polynomials, one which applies at energies less than E_0 and one which applies at energies greater than E_0.
3) The smoothed atomic absorption factor, $\mu_0(E)$, is approximated by a polynomial, which passes as closely as possible through the centre of each oscillation.
4) The polynomials found in (2) and (3) are subtracted from the data to give $\chi(E)$, the x-axis is converted from E to k (Equation 2.8) and a k^3 weighting is introduced, as the oscillations at high k are small in magnitude but are significant in the structural analysis.

Figure 2.11 shows a simplified data set after background subtraction and k^3 weighting.

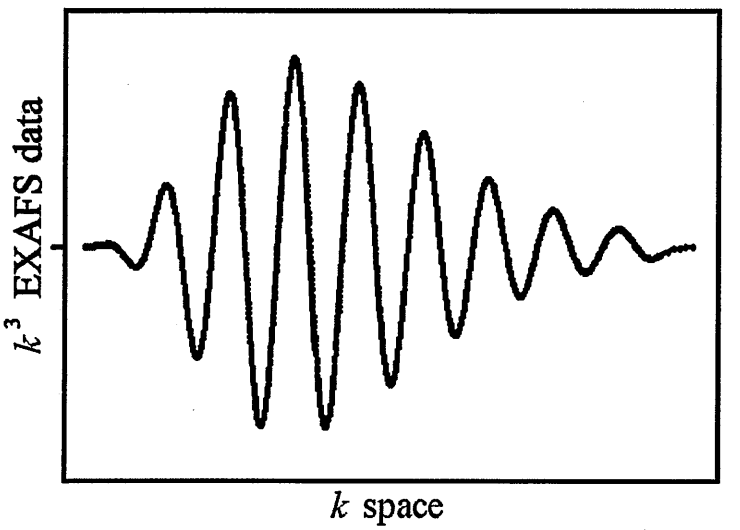

Figure 2.11: Idealised EXAFS dataset after background subtraction and k^3 weighting

2.3.4.3 Structure fitting

The Excurv97 program is then used to model the number, type and distance of atoms

surrounding the central absorbing atom, and a unique Debye-Waller factor (quantifying thermal and structural disorder) is calculated for each shell of the fit. The various constants mentioned in Section 2.3.3 and phase-shift functions for each atom used in the fit are calculated automatically by the software. The software generates the spectrum which would be expected from the fitted model, and the parameters of the model are refined until the fitted model follows the experimental data as closely as possible.

The Fourier transform of the background-subtracted data into normal space can be used as a guide to the local environment of the absorbing atom. Figure 2.12 shows the Fourier transform of the simplified EXAFS data shown in Figure 2.11.

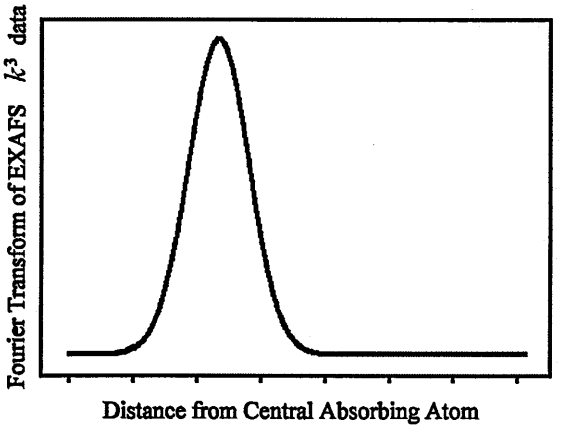

Figure 2.12: Fourier transform of idealised EXAFS data

The positions of peaks in the Fourier transform are useful for indicating the likely positions of shells in the fit, although the apparent position of a peak in the Fourier transform is often significantly different from the final fitted distance of the shell. The intensities of peaks in the Fourier transform are dependent on the occupation number of the shell, the type of atom in the shell (heavier elements produce stronger peaks) and the Debye-Waller factor. Therefore although it is a useful tool in the process of understanding the EXAFS spectrum of a material, it is inadvisable to place undue weight on features in

the Fourier transform of a spectrum. The fitting is based solely on how well the fitted model fits the experimental spectrum in the k^3 weighted untransformed data.

2.3.4.4 *Interpretation of results*

EXAFS is an "average" technique – in that the results show the average environment of all the absorbing atoms in the beam cross section. In a multi-phase sample, results can frequently show a fractional number of atoms surrounding the central absorbing atom – meaning that some fraction of the absorbing atoms in the sample are in one surrounding environment, and the remainder of the absorbing atoms are in a different environment.

EXAFS is also a non-directional technique. Results may show that there are six atoms of a particular type surrounding the absorbing atom at a particular distance, but no information is immediately available about the arrangement of those atoms. The arrangement of the atoms may be modelled using backscattering theory, which takes into account the secondary reflection of the electron wave by a third atom, but this cannot always be used. Therefore, EXAFS is not a suitable tool for identifying entirely unknown structures. In order to interpret EXAFS results successfully, it is necessary to have a good idea as to what the structure will be.

2.3.4.5 *Accuracy of fit*

The Excurv97 software includes in the analysis two measures of accuracy, the fit-index and the reliability factor (R). The reliability factor is usually taken as the most meaningful indication of the quality of fit. It is calculated by

$$R_{exafs} = \sum_i^N \Big/ \sigma_i \left(\left| \chi_i^{\exp}(k) - \chi_i^{theo}(k) \right| \right) \qquad \text{Equation 2.10}$$

and then expressed as a percentage. With very good data and a well-described structure, an *R*-factor of 20 % can be achieved. Values significantly lower than 20 % are exceptional. Values between 20 % and 40 % are considered acceptable. Values between 40 % and 60 % may be acceptable where data quality is poor (e.g. due to high temperatures and/or short recording times).

Due to the nature of the EXAFS fitting process, values for errors are not usually specifically derived for each shell unless particularly in-depth structural calculations are being made with very high quality data. For more general measurements, the error in the co-ordination number (i.e. the number of atoms in each "shell") is taken as ± 20%, and the error in the distance from the absorbing atom is taken as ± 0.02 Å. The Debye-Waller factor, σ_j, which is a measure of the thermal and static disorder of the structure, is also a helpful indicator of the error values inherent in an EXAFS fit.

2.3.5 Instrumentation for the collection of EXAFS data

The room-temperature EXAFS data used for this work were collected using Stations 3.4, 7.1 and 8.1 at the SRS at Daresbury Laboratory. Details of the collection of high-temperature EXAFS using Station 9.3 may be found in Section 2.4.

2.3.5.1 Instrumentation for achieving a monochromatic beam

Each Station is attached to a "beamline" which leaves the storage ring tangentially at one of the bending magnets. The white radiation from the ring passes through a single-crystal monochromator, which consists of two parallel single crystals of silicon, which are cut and polished along a defined crystallographic plane, as illustrated in Figure 2.13.

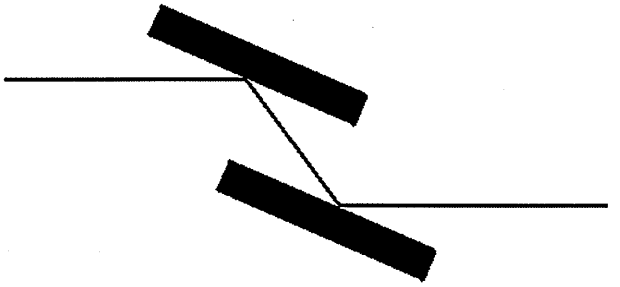

Figure 2.13: A single-crystal monochromator

According to the principles of X-ray diffraction described in Section 2.2.2, only the wavelengths from the incident radiation defined by Equation 2.3 ($n\lambda = 2d.\sin\theta$) will be passed by the first crystal. The second crystal then diffracts the radiation a second time, such that the direction of the radiation to be used in the experiment is constant. However, this second crystal is often offset slightly from the angle θ, which has the effect of cutting out any second or third order harmonics from the beam (i.e. where $n \neq 1$), thus providing an excellent monochromatic beam.

2.3.5.2 Collection of data

The collection of raw EXAFS data is the accurate measurement of how much of the impinging radiation a sample absorbs at a range of frequencies around the absorption edge. This may be achieved through several methods, the most common of which is known as Transmission EXAFS. However, other techniques, known as Fluorescence EXAFS and Total Electron Yield EXAFS may also be used, particularly for dilute or highly absorbing samples.

(i) Transmission EXAFS

This technique measures absorbance simply by measuring the intensity of the X-ray beam

before and after it passes through the sample. The X-ray beam from the synchrotron ring is first passed through an ion chamber, which measures the incident intensity of the beam. The beam then passes through the sample, which is positioned in the window of a sample holder. A second ion chamber is then used to measure the intensity of the beam after having passed through the sample.

(ii) Fluorescence EXAFS

This technique collects scattered photons re-emitted by the sample, which will be proportional to the amount of radiation absorbed, and compares the intensity of these photons with the intensity of the incident X-ray beam to produce the absorption spectrum. This spectrum may then be analysed in the same way as transmission EXAFS. This technique is sometimes called FLEXAFS.

(iii) Total electron yield EXAFS

The sample is formed into a pellet (mixed with graphite if the sample is not an electrical conductor) and an electrode is then attached. The current, which is produced by the scattered electrons as the sample absorbs the incident X-rays, is measured. This current is proportional to the absorbance of the sample and can be analysed in the same way as transmission EXAFS.

2.4 Combined time-resolved X-ray powder diffraction and EXAFS

Time-resolved experiments collecting both X-ray powder diffraction and EXAFS data are possible at Daresbury Laboratory using Station 9.3 which is equipped with the instrumentation for both techniques as well as with a small furnace which can be placed in the radiation beam. This enables the collection of data during a phase transition, reaction or other dynamic change of state. The technique is described as simultaneous; however, the apparatus actually alternates between recording an X-ray powder diffraction pattern and then recording an EXAFS spectrum.

2.4.1 X-ray diffraction

X-ray powder diffraction patterns were recorded using the equipment at Daresbury Laboratory Station 9.3 using highly monochromatic synchrotron radiation as described in Section 2.2.8. However, the data collection method is a fixed detector rather than a rotating arm. The detector gives a resolution of 0.1° in 2θ and is capable of data collection between *ca.* 10° and 65° 2θ. The data quality is therefore less than that given by other methods, but is sufficient for phase identification. During the course of time-resolved experiments, the intensity of the synchrotron radiation gradually decreases, therefore the X-ray diffraction patterns must be normalised against beam intensity.

2.4.2 EXAFS

Transmission EXAFS data may be recorded using the equipment at Daresbury Laboratory Station 9.3 using the methods described in Section 2.3.5.

2.4.3 Combined XRD and EXAFS

The equipment is set to alternately record an X-ray diffraction pattern for a set length of time (for instance, 100 seconds) and then collect a transmission EXAFS spectrum. Because both the XRD and EXAFS data must be collected at speed, due to the ongoing changes in the sample, the data quality is less than might otherwise be achieved.

2.5 Mössbauer spectroscopy

In 1958 Rudolf Mössbauer[20] discovered the phenomenon of recoil-free nuclear resonance fluorescence, which was later developed into the technique now known as Mössbauer spectroscopy. The application of Mössbauer spectroscopy has had an important influence in many branches of physics and chemistry and is used for a wide variety of purposes. Texts covering the theory and practice of the technique have been published by Greenwood and Gibb[21] and Dickson and Berry[22].

2.5.1 Recoil-free nuclear resonance fluorescence

When the nuclei of atoms of certain radioactive isotopes undergo radioactive decay, they will first emit an α- or β-particle to decay to an excited state of the daughter element. The nuclei will release their excitation energy by emitting a γ-ray and will then be in the relaxed state. The energy of the γ-rays thus emitted will be constant for a particular radioactive isotope, and can potentially be used as a source of highly monochromatic radiation. However, this can only occur if the nuclei do not suffer recoil (often compared to that which might be expected if a person fired a gun whilst standing in a boat) on emission of the γ-ray, which would modify the energy of the photon. If the radioactive nuclei are incorporated into a crystal lattice, and the energy of the emitted γ-rays are small compared to the lowest quantised lattice vibration, recoil will not occur as the atoms are rigidly held in place. The most commonly used isotopes for which this condition is possible are ^{57}Fe and ^{119}Sn, for which the γ-ray energies are 14.4 keV and 23.8 keV respectively. Since these energies are relatively small, nuclear recoil may be disregarded.

2.5.2 Mössbauer absorption spectroscopy

The monochromatic γ-rays emitted by an exited ^{57}Fe nucleus are used in Mössbauer

spectroscopy to investigate the environments of iron nuclei in other materials. The surrounding electrons of iron in any material will subtly alter the nuclear energy levels of both ground and excited states, and absorption will only occur when the energy of the incident γ-ray is identical to the excitation energy of the absorbing atom. This only occurs when the source and the sample are in the same electronic environment.

To perform Mössbauer spectroscopy, the radioactive source is vibrated back and forth over a small range of velocities of the order of millimetres per second. The Doppler shift thus affects the frequency of the γ-rays emitted by the source. A sample of the material to be analysed is placed near the source along the same line as the vibration. The sample will absorb γ-rays over the range of frequencies to give an absorption spectrum dependent on the hyperfine electric monopole-, electric quadrupole- and magnetic dipole-interactions of the absorbing atoms in the sample.

2.5.3 Understanding the Mössbauer spectrum

The Mössbauer spectrum typical of a sample containing absorbing atoms in the same cubic environment as the source is shown in Figure 2.14.

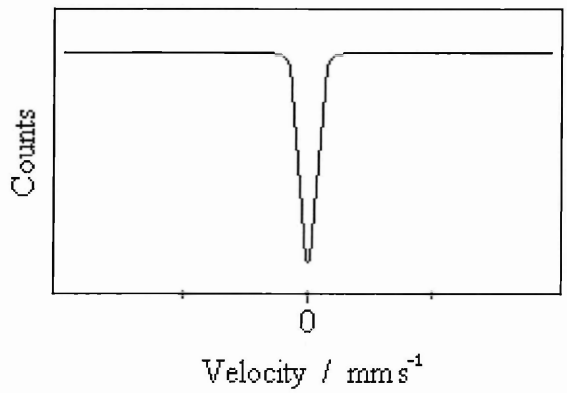

Figure 2.14: Mössbauer spectrum with sample and source in the same cubic environment.

Where the source and sample are in different electronic environments, the electric monopole interaction affects the spectrum. There is shifting of the energy levels in the nucleus created by the coulombic attraction of the surrounding electrons. The ground- and excited-state energies of the emitting nucleus in the source are represented in Figure 2.15a, with difference in energy levels E. The ground- and excited-state energies of the absorbing nucleus in the sample are represented in Figure 2.15b, with difference in energy levels E^*.

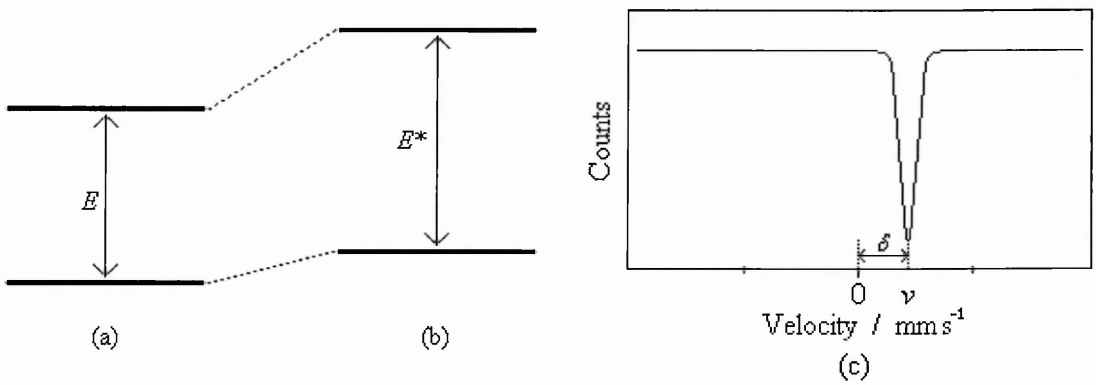

Figures 2.15: (a) Energy levels of emitting nucleus (b) Energy levels of absorbing nucleus (c) Resultant Mössbauer spectrum

The energy E of the emitted γ-radiation is modified by the Doppler shift at velocity v to match the absorption energy of the sample E^*, and the γ-radiation is absorbed. The shift in peak position in the spectrum (illustrated in Figure 2.15c) is known as the isomer shift, and is denoted δ.

If the energy state of a nucleus has a spin I greater than $^1/_2$, the asymmetric nuclear charge distribution gives rise to a nuclear quadrupole moment. In the presence of an electric field gradient this gives rise to a splitting of the nuclear energy levels, as illustrated in Figure 2.16a. There are therefore two possible energies at which incident γ-rays may be absorbed, and the Mössbauer spectrum will contain two peaks, shown in Figure 2.16b.

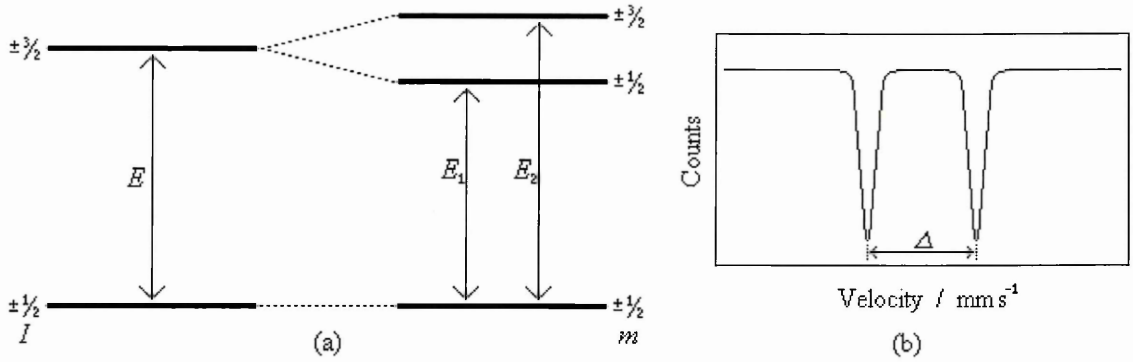

Figures 2.16: (a) Nuclear energy levels split by the electric quadrupole interaction (b) Resultant Mössbauer spectrum

The difference in the position of the two peaks in the Mössbauer spectrum due to this electric quadrupole interaction is known as the quadrupole splitting and is denoted Δ. The width of each peak is denoted by Γ.

A nucleus of spin $I > 0$ has a magnetic moment and will interact with a magnetic field via a magnetic dipole interaction. The nuclear energy levels are split: the degeneracy of the nuclear states is removed by the interaction of the nucleus with the magnetic field, and each level splits into $2I + 1$ substates. In ^{57}Fe the nuclear ground state splits into 2 sub-states ($m = {}^{1}/_{2}$ and $m = -{}^{1}/_{2}$) and the nuclear excited state splits into 4 sub-states ($m = {}^{3}/_{2}$, ${}^{1}/_{2}$, $-{}^{1}/_{2}$ and $-{}^{3}/_{2}$). However, transitions between energy states may only occur where Δm is 0 or ± 1, therefore there are six possible energy transitions in the absorption spectrum, as shown in Figure 2.17a. This then gives a Mössbauer spectrum with six peaks, although with differing intensities, as illustrated in Figure 2.17b.

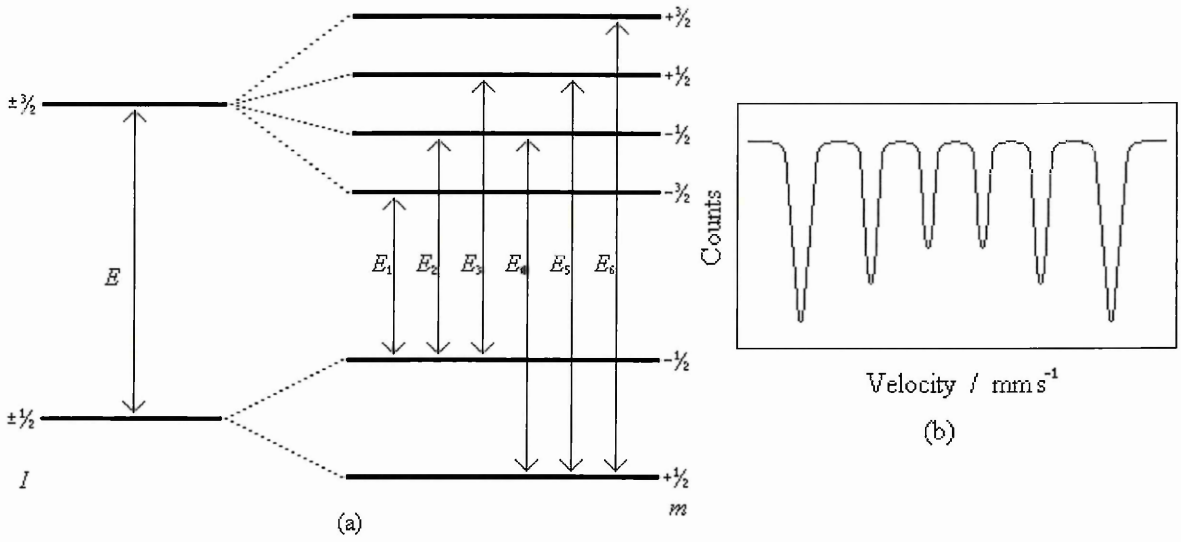

Figure 2.17: (a) Nuclear energy levels split by the magnetic hyperfine interaction (b) Resultant Mössbauer spectrum

Detailed knowledge of magnetic hyperfine splitting is not relevant to the results presented in this work, therefore this phenomenon is not examined further here.

2.5.4 Mössbauer spectra of mixed-state compounds

When the compound being examined contains more than one type of location for the absorbing atom in the lattice, the spectrum consists of an addition of the spectra for the two sites. This is illustrated in Figure 2.18 for two doublets (as in Figure 2.16b) with slightly different values of isomer shift and quadrupole splitting.

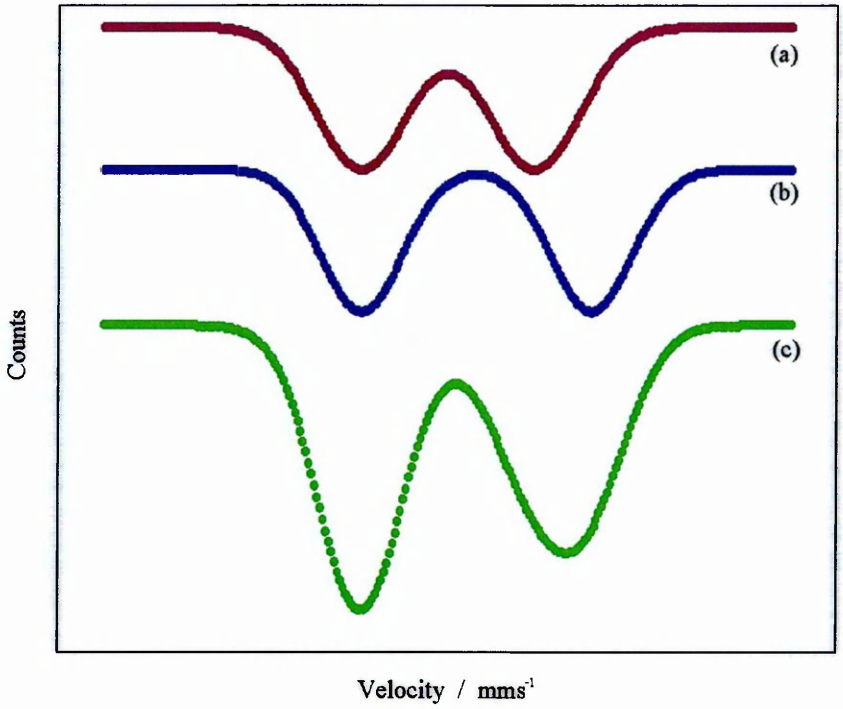

Figure 2.18: An asymmetric Mössbauer spectrum (c) which can be interpreted in terms of the addition of the two symmetrical spectra (a) and (b) attributable to the two sites in the sample

2.5.5 Instrumentation for Mössbauer spectroscopy

The apparatus required to perform Mössbauer spectroscopy is shown schematically in Figure 2.19.

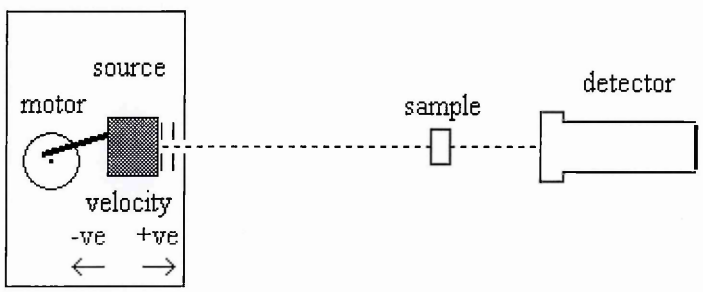

Figure 2.19: Schematic of Mössbauer spectroscopy apparatus

The radioactive source is held in a lead-lined case. A motor provides the vibration of the source along a defined axis. A series of slits along the axis ensure a single beam of γ-rays from the source to the sample. The powdered sample is held in a plastic case in the path of the radiation beam. The intensity of the γ-rays is recorded beyond the sample, using an

Ar/CO_2 filled proportional counter. The γ-rays not absorbed by the sample ionise the Ar gas in the detector, the electric current thus produced being proportional to the intensity of the transmitted γ-rays. The signal from the detector is passed through a multi-channel analyser, which translates the signal into a Mössbauer spectrum.

2.5.6 Instrumentation for high-temperature Mössbauer spectroscopy

The measurement of Mössbauer spectra at temperatures up to 900 K can be performed in a furnace designed for the purposed as illustrated in Figure 2.20.

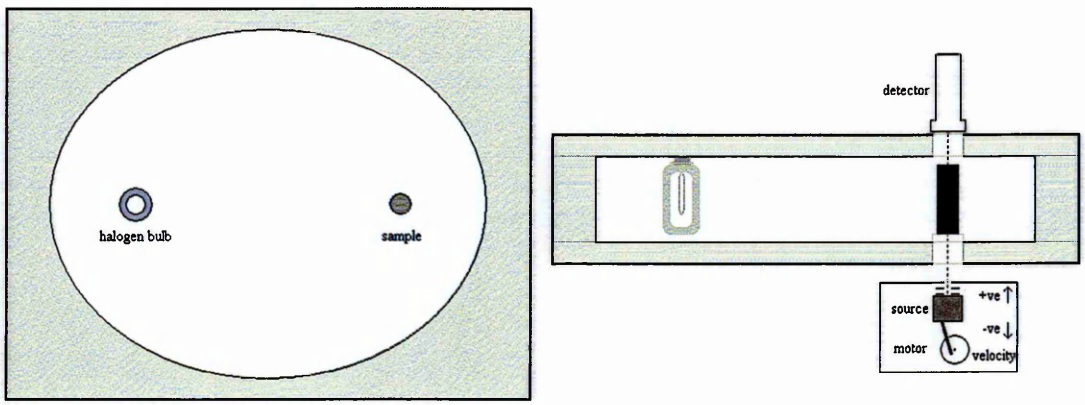

Figure 2.20: Schematic of high-temperature Mössbauer spectroscopy apparatus

The furnace consists of a block of aluminium containing an elliptical cylinder space, the inner surface of which is highly polished. A 250 W halogen lamp is placed at one focal point of the ellipse. The sample is placed between two beryllium oxide disks within a black-painted copper cylinder at the other focal point. The temperature of the sample is monitored by a thermocouple, the signal from which is used to control the temperature by modulating the power of the lamp. Aluminised Mylar® windows above and below the sample allow the passage of γ-rays. The instrumentation as described above in Section 2.5.5 is arranged on a vertical axis, with the lead case containing the radioactive source, the slits and the motor

being placed below the furnace and the detector above.

2.5.7 Analysis of Mössbauer spectra

The data collected as described above in Sections 2.5.5 and 2.5.6 are analysed using the MFIT software[23] which uses linear regression to fit the peaks of the spectrum to lorentzian lines and determine the Mössbauer parameters δ and Δ. Where the sample contains a mixture of two structures, the known Mössbauer spectrum of each structure can be fitted with the relative intensities varied to find the best fit. The ratio of the intensities of the fits then gives the ratio of amounts of the two structures present in the sample.

2.6 Hydrothermal processing

A general definition of hydrothermal synthesis is "the chemical interaction between hydrolysable precursor materials and water, either directly or catalytically, under hyperatmospheric pressure at temperatures above the boiling point of water, to produce, in general, oxides"[24].

2.6.1 Instrumentation for hydrothermal processing

The autoclave used for the hydrothermal processing is a Teflon[25]-lined beaker (into which the reactants are placed) which is inserted into a chamber made from a chromium nickel and molybdenum stainless steel. The beaker used has been treated by an isostatic pressing process to reduce porosity, which the manufacturers assert gives thermal expansion properties similar to those of steel, thus minimising any possible problems of stress in the materials due to differences in thermal expansion during experiments. The effects of high temperatures and pressures on the corrosion properties of most materials are not fully known, and so it is important to have an unreactive material as the autoclave lining. Teflon resists corrosion even by hydrogen fluoride, and is ideal for this purpose. The steel chamber is surrounded by an electric heating mantle. The steel lid has a Teflon seal which fits over the Teflon beaker, and a Teflon tube leading down from the lid contains a NiCr/Ni thermocouple which is in contact with the reactants. The lid is secured to the base by means of two large semicircular steel clamps, which are joined together with steel bolts. The upper limits of conditions for the Teflon lining are a temperature of 550 K and a pressure of 350 bar.

References for Chapter Two

1 A. R. Bleich *The Story of X-Rays* Dover Publications 1960 New York.

2 J. Als-Nielsen and D. McMorrow *Elements of Modern X-Ray Physics* Wiley 2001 Chichester.

3 P. J. Duke *Synchrotron Radiation: Production and Properties* Oxford University Press 2000 Oxford.

4 J. P. Blewett *J Synchrotron Radiation* 1998 **5** 135.

5 J. Als-Nielsen and D. McMorrow *Elements of Modern X-Ray Physics* Wiley 2001 Chichester p34.

6 P. J. Duke *Synchrotron Radiation: Production and Properties* Oxford University Press 2000 Oxford pp 79-87.

7 W. H. Bragg and W. L. Bragg *X-Rays and Crystal Structure* G Bell & sons 1915 London.

8 L. V. Azároff and M. J. Buerger *The Powder Method in X-Ray Crystallography* McGraw-Hill 1958 New York.

9 H. M. Rietveld *J. Appl. Cryst.* 1969 **2** 65-71.

10 R. DeL. Kronig *Z. Phys.* 1931 **70** 317.

11 E. A. Stern, D. E. Sayers, F. W. Lytle *Phys. Rev. B* 1975 **11** 4836.

12 B. K. Teo *EXAFS : Basic Principles and Data Analysis* Springer-Verlag 1986 Berlin.

13 B. K. Teo *EXAFS : Basic Principles and Data Analysis* Springer-Verlag 1986 Berlin Ch 2&4.

14 P. A. Lee, J. B. Pendry *Phys. Rev. B* 1975 **11** 2795.

15 S. J. Gurman, R. F. Pettifer *Phil. Mag. B* 1979 **40** 345.

16 S. J. Gurman, N. Binstead, I. Ross *J. Phys. C* 1984 **17** 143.

17 Excalib Software © CCLRC Daresbury http://srs.dl.ac.uk/xrs/Computing/Programs/excalib

18 Exbrook Software © CCLRC Daresbury http://srs.dl.ac.uk/xrs/Computing/Programs/exbrook

19 Excurv97 Software, CCLRC Daresbury. Author N. Binstead 1997.

20 R. L. Mössbauer *Z. Physik* 1958 **151** 1189.

[21] N. N. Greenwood and T.C. Gibb *Mössbauer Spectroscopy* Chapman and Hall 1971 London.

[22] D. P. E. Dickson and F. J. Berry (eds) *Mössbauer Spectroscopy* Cambridge University Press 1986 Cambridge.

[23] Software © Science Institute, University of Iceland. Author K. Jónsson.

[24] C. B. Ponton *Proc. Third Euro-Ceramics Conf.* P. Duran & J.F. Fernandez. Pub. Faenza Editrice Iberica S.L. Spain 1993 **1** 189.

[25] Teflon™ (which is also known as PTFE or polytetrafluoroethylene) is a registered trademark of E.I. du Pont de Nemours and Company.

Chapter Three: Experimental Procedures

Except where otherwise stated, all procedures were carried out by the author of this thesis.

3.1 Preparation of starting materials

3.1.1 Preparation of ferrosilicon

3.1.1.1 Preparation of high-temperature-phase ferrosilicon (ζ_α-$FeSi_x$)

The ζ_α-ferrosilicon used for the experiments described in this work was supplied (a) by the University of Iceland and (b) by the Metals Crystals and Oxides Laboratory (MCO), Cambridge. The first experiments to be carried out as part of this work were the high-temperature time-resolved Mössbauer spectroscopy experiments described in Section 3.3.2, the results of which are presented in Section 4.3. These experiments used the samples of ferrosilicon prepared as described in (i) below. All other measurements and experiments were carried out using the samples of ferrosilicon prepared as described in (ii) below.

i) ζ_α-ferrosilicon supplied by the University of Iceland

Samples of ζ_α-ferrosilicon prepared by Thórdur Magnússon at the University of Iceland were prepared in an induction furnace consisting of a Radyne Model RD 150/E high impedance current generator, a Thyristor AC Power regulator and a copper coil, which wraps around a sample-making unit. Argon was used to provide an inert atmosphere. 99.8 %+ pure iron supplied by Goodfellow Cambridge Ltd and 99.9999 % pure silicon supplied by Johnson Matthey plc were weighed, washed in acetone, and heated in an alumina crucible within the induction furnace under a flow of argon. The sample was kept at approximately 1575 K for five minutes and the power decreased slowly until the sample started to solidify. The power was turned off and the sample quenched in flowing argon[1].

The quantities of reactants used in the preparation of ζ_α-ferrosilicon by this method are shown in Table 3.1

	Iron / g	wt % Fe	Silicon / g	wt % Si	atomic Fe:Si	Aluminium /g	wt % Al
Undoped ζ_α-ferrosilicon	2.797	45.1	3.409	54.9	1 : 2.423	-	-
Al-doped ζ_α-ferrosilicon	2.060	44.5	2.518	54.4	1 : 2.430	0.0484	1.0

Table 3.1: Quantities of reactants used to make undoped and Al-doped ferrosilicon at the University of Iceland

ii) ζ_α-ferrosilicon purchased from Metal Crystals and Oxides Laboratory

Ferrosilicon samples prepared by and purchased from the Metal Crystals and Oxides Laboratory (MCO) Cambridge were prepared by mixing hydrogen-reduced cold-crucible-cast low carbon iron supplied by Johnson Matthey with 99.994 % purity and 99.99998 % pure silicon metal and heating in an RF (radio frequency) source in a high purity argon atmosphere to approximately 1675 K. The melt was then cast in a water-cooled copper crucible[2]. The quantities of the reactants used to make the four samples supplied by MCO are given in Table 3.2:

	Iron / g	wt % Fe	Silicon / g	wt % Si	atomic Fe:Si	Aluminium / g	wt % Al
Undoped ζ_α-ferrosilicon (54 wt% Si, batch one)	2.302	46.0	2.698	54.0	1 : 2.330	-	-
Undoped ζ_α-ferrosilicon (54 wt% Si, batch two)	4.605	46.1	5.395	54.0	1 : 2.330	-	-
Undoped ζ_α-ferrosilicon (50 wt% Si)	4.986	49.9	5.014	50.1	1 : 2.000	-	-
Al-doped ζ_α-ferrosilicon (53 wt% Si)	4.559	45.6	5.341	53.4	1 : 2.329	0.10	1.0

Table 3.2: Quantities of reactants used to make undoped and Al-doped ferrosilicon at the MCO Laboratory

The compositions of batches one and two of undoped ζ_α-ferrosilicon with a silicon content of 54 wt% are effectively identical therefore in this work no distinction is made between them.

3.1.1.2 Preparation of low-temperature-phase ferrosilicon (ζ_β-$FeSi_x$)

Samples, approximately 2 g of each, of undoped ζ_α-ferrosilicon with silicon contents of 54 % and 50 % by weight, and 1 % Al-doped ferrosilicon with a silicon content of 53 % by weight (each prepared by MCO as detailed in Section 3.1.1.1(ii)) were ground to a fine powder using an agate pestle and mortar. Portions of each powder were heated in alumina crucibles at 973 K for 10 hours in air.

3.1.1.3 Preparation of intermediate samples for phase evolution analysis.

(i) Preparation of intermediate samples of ferrosilicon

A portion of undoped ζ_α-ferrosilicon with a silicon content of 54 % by weight (prepared by MCO as detailed in Section 3.1.1.1(ii)) was ground, and a series of graded sieves were used to separate the material into samples of grain sizes 60-125 μm, 125-250 μm and 250-500 μm. Portions of material of each grain size range were heated at 898 K for 2, 4, 6, 9 and 21 hours.

(ii) Preparation of a sample containing equal quantities of ζ_α- and ζ_β-ferrosilicon

Equal masses of unheated undoped ζ_α-ferrosilicon with a silicon content of 54 % by weight, and ζ_β-ferrosilicon, made by heating a portion of undoped ζ_α-ferrosilicon with a silicon content of 54 % by weight as described in Section 3.1.1.2, were ground together using an agate pestle and mortar, mixed with dry boron nitride and pressed into a pellet.

3.1.2 Preparation of mullite precursors, mullite and related materials.

3.1.2.1 Preparation of doped and undoped materials by hydrothermal processing

Experiments performed to observe the phase evolution of the formation of mullite used a precursor material made by hydrothermal processing, using the apparatus described in Section 2.6.1. The individual compounds used in this process were also hydrothermally

processed alone.

The compound, or mixture of compounds in stoichiometric proportions were dispersed in 300 ml distilled water and transferred to the Teflon beaker of the autoclave. The beaker was placed into the stainless steel sleeve, and the lid was put in place, ensuring that no droplets of water were trapped between the beaker and the stainless steel sleeve or the lid. The lid was clamped onto the base, and the heating current was switched on. The assembly usually took approximately 2 – 3 hours to reach its maximum temperature of 463 K at autogenous pressure, and was then left for 5 hours. In each case the resulting sol was filtered and dried under an I-R lamp and ground to a powder using an agate pestle and mortar.

As described in Section 1.2.2.2, the proportions of aluminium and silicon acetates used was such as to make 3:2 mullite $Al_{4.5}Si_{1.5}O_{9.75}$, so the ratio of aluminium to silicon in the starting materials was 3:1. Where iron or vanadium, in the form of iron(II) acetate or vanadium(III) acetylacetonate, was added to the mixture of aluminium or silicon acetates the quantities were such as to give a molar ratio of aluminium to the dopant metal of 1:0.07.

The compounds and mixtures of compounds which were hydrothermally processed as described above were:

i. aluminium acetate
ii. silicon acetate
iii. iron(II) acetate
iv. vanadium(III) acetylacetonate
v. aluminium acetate and silicon acetate
vi. aluminium acetate, silicon acetate and iron(II) acetate
vii. aluminium acetate, silicon acetate and vanadium(III) acetylacetonate

3.1.2.2 Preparation of doped mullite precursor by mixing

Portions of the dry undoped precursor prepared by hydrothermal processing of aluminium- and silicon-acetates as described in Section 3.1.2.1, were mixed with either iron(III) oxide or vanadium(V) oxide using an agate pestle and mortar in appropriate

proportions to result in a molar ratio of aluminium to the dopant metal of 1:0.07.

3.1.2.3 Preparation of mullite from precursors

A small quantity (*ca.* 1 g) of mullite precursors prepared as described in Sections 3.1.2.1 and 3.1.2.2 (i) by hydrothermal processing of aluminium- and silicon-acetates (ii) prepared by hydrothermal processing of aluminium-, silicon- and iron(II)-acetates (iii) prepared by hydrothermal processing of aluminium-, and silicon-acetates with vanadium(III) acetylacetonate (iv) prepared by mixing iron(III) oxide with the precursor prepared by hydrothermal processing of aluminium- and silicon-acetates and (v) prepared by mixing vanadium(V) oxide with the precursor prepared by hydrothermal processing of aluminium- and silicon-acetates, were placed in alumina crucibles in a pre-heated furnace at 1623 K for 3 hours.

3.1.2.4 Preparation of intermediate samples in the phase evolution of mullite

A small quantity (*ca.* 1g) of mullite precursors (i) to (v) as listed in Section 2.1.2.3 were placed in alumina crucibles in a pre-heated furnace for 3 hours at 623, 723, 873, 973, 1173, 1423, or 1623 K.

3.1.2.5 Preparation of further samples for the purposes of comparison

Samples of (i) the material prepared by hydrothermal processing of aluminium acetate and (ii) the material prepared by hydrothermal processing of silicon acetate, as described in Sections 3.1.2.1, were placed in alumina crucibles in a pre-heated furnace for 3 hours at 623, 873, 1173, 1273, or 1623 K.

3.2 Analysis of samples

3.2.1 X-ray powder diffraction

Flat-plate X-ray powder diffraction patterns were recorded with a Siemens D5000 X-ray diffractometer using Cu K_α radiation. Phase identification was achieved using the Joint Committee on Powder Diffraction Standards (JCPDS) database on CD-ROM. Typically, data were recorded between 10 and 70° of 2θ using a step size of 0.05° and a recording time of 2 seconds per point.

3.2.2 High resolution X-ray powder diffraction

High resolution X-ray powder diffraction patterns were recorded at Station 9.1 at Daresbury Laboratory. The sample holders were 0.5 mm glass capillary tubes. Radiation of wavelength 0.692 Å was used. The data were recorded using a radial-arm mounted solid-state detector, with a step size of 0.01° of 2θ. The intense radiation provided by the synchrotron results in a diffraction pattern of a quality high enough to analyse the structure of a sample beyond simple phase identification. Analysis using Rietveld refinement was carried out by Dr Mark Roberts of Daresbury Laboratory.

3.2.3 Iron K-edge EXAFS

Iron K-edge EXAFS were recorded in transmission mode at 298 K at Station 7.1 at Daresbury Laboratory using radiation energies between 6962 and 8080 eV (λ between 1.781 and 1.534 Å). A silicon 111 double crystal order-sorting monochromator was used.

Data were also recorded at *ca.* 77 K at Station 8.1 at Daresbury Laboratory using radiation energies between 6900 and 7760 eV (λ between 1.797 and 1.598 Å). A silicon 220 double crystal monochromator with automatic harmonic rejection adjustment was used. Samples were cooled using a bucket cryostat and liquid nitrogen.

3.2.4 Silicon K-edge EXAFS

A 13 mm diameter pellet of approx. 3 mm thickness was made from equal quantities of the sample and graphite, and fixed with conducting tape to the electrode sample holder at Station 3.4 at Daresbury Laboratory. Silicon K-edge total-electron yield EXAFS under vacuum at 298 K were recorded with radiation energies between 1810 and 2450 eV using an InSb 111 double crystal monochromator.

3.2.5 Mössbauer spectroscopy

Mössbauer spectra were recorded using either (a) a Cryophysics microprocessor-controlled Mössbauer Spectrometer with a 25mCi ^{57}Co-Rh source at room temperature, as described in Section 2.5.4, calibrated using an iron foil; or (b) the Mössbauer spectrometer furnace described in Section 2.5.5. All isomer shift data are quoted relative to metallic iron, all spectra were computer fitted to Lorentzian lines using the MFIT software package[3].

3.2.6 Magic-angle-spinning nuclear magnetic resonance (MAS NMR)

^{27}Al MAS NMR spectra were recorded on a JEOL EX-400 spectrometer operating at 104.05 MHz and equipped with a 5 mm high-speed DOTY probe head. All experiments employed single-pulse excitation with pulse widths less than $\pi/6$; rotor spinning frequencies were in the region of 9 kHz. Spectra were referenced to external $Al(H_2O)_6^{3+}$ and are presented with exponential filtering selected to have minimum effect on overall linewidth. All analysis of MAS NMR spectra was performed by Dr M Mortimer of The Open University.

3.2.7 Tables summarising measurements carried out

Tables 3.4 and 3.5 show which techniques were used to examine the various samples prepared as described in Section 3.1 where X denotes that a measurement was made.

Sample	X-ray powder diffraction	High resolution X-ray powder diffraction	*ca.*295 K Fe K-edge EXAFS	*ca.*77 K Fe K-edge EXAFS	*ca.*295 K Si K-edge EXAFS	Mössbauer Spectroscopy
Unheated undoped ferrosilicon 54.9 wt% Si (Table 3.1 line 1)	X	-	-	-	-	X
" " heated at 855 K for 60 hours	-	-	-	-	-	X
Unheated undoped ferrosilicon 54.0 wt% Si (Table 3.2 lines 1 / 2)	X	X	X	-	-	-
" " heated at 973 K for 10 hours	X	X	X	X	X	-
" " heated at 898 K for various times 2 - 10 hours	X	-	-	-	-	-
Unheated undoped ferrosilicon 50.1 wt% Si (Table 3.2 line 3)	X	-	-	-	-	-
" " heated at 973 K for 10 hours	X	X	X	-	X	-
Unheated ferrosilicon 54.4 wt% Si doped with 1 % Al (Table 3.1 line 2)	X	-	-	-	-	-
Unheated ferrosilicon 53.4 wt% Si doped with 1 % Al (Table 3.2 line 4)	X	X	-	X	-	-
" " heated at 973 K for 10 hours	X	-	-	X	-	-

Table 3.3: Details of the techniques used to examine ferrosilicon samples

Sample	X-ray powder diffraction	*ca.* 295 K Fe K-edge EXAFS	MAS NMR	Mössbauer Spectroscopy
Gel made by hydrothermal processing of aluminium acetate - (i) unheated and (ii) heated for 3 hours at various temperatures	X	-	-	-
Gel made by hydrothermal processing of silicon acetate - (i) unheated and (ii) heated for 3 hours at various temperatures	X	-	-	-
Gel made by hydrothermal processing of iron(II) acetate - unheated	X	-	-	-
Gel made by hydrothermal processing of vanadium(III) acetylacetonate - unheated	X	-	-	-
Gel made by hydrothermal processing of aluminium- and silicon-acetates - unheated	X	-	X	-
Gel made by hydrothermal processing of aluminium- and silicon acetates - heated at various temperatures for three hours	X	-	-	-

Table 3.4 (i): Details of the techniques used to examine samples of mullite and mullite precursors.

Sample	X-ray powder diffraction	c.295K Fe K-edge EXAFS	MAS - NMR	Mössbauer Spectroscopy
Gel made by hydrothermal processing of aluminium-, silicon- and iron(II)-acetates - unheated	X	X	X	X
Gel made by hydrothermal processing of aluminium-, silicon- and iron(II)-acetates - heated at various temperatures for three hours	X	-	-	-
Gel made by hydrothermal processing of aluminium- and silicon-acetates and vanadium(III) acetylacetonate - (i) unheated and (ii) heated for 3 hours at various temperatures	X	-	-	-
Gel made by hydrothermal processing of aluminium- and silicon-acetates mixed with 5% iron(III) oxide - heated at various temperatures for three hours	X	-	-	-
Gel made by hydrothermal processing of aluminium- and silicon-acetates mixed with 5% vanadium(V) oxide - heated at various temperatures for three hours	X	-	-	-
Gel made by hydrothermal processing of aluminium-, silicon- and iron(II)-acetates - heated at 1323K for 15 hours	-	X	-	-
Gel made by hydrothermal processing of aluminium-, silicon- and iron(II)-acetates - heated at 1623K for 6 hours	-	X	-	-

Table 3.4 (ii): Details of the techniques used to examine samples of mullite and mullite precursors.

3.3 Time-resolved experiments

3.3.1 High-temperature time-resolved combined X-ray powder diffraction and Fe K-edge EXAFS

These experiments used the equipment described in Section 2.4. A mixture of dry boron nitride and a small amount of sample were ground to a very fine powder using an agate pestle and mortar and pressed into a pellet using a standard 13 mm diameter KBr pellet press. The grain size of powder required in order for a uniform pellet to be formed was <10 μm (see Sections 4.3.3 and 4.5 for the relevance of this). The pellet was placed in the ceramic sample holder in the centre of the furnace on the beamline and heated to 773 K at a rate of 20 $Kmin^{-1}$, then to the experiment temperature at a rate of 10 $Kmin^{-1}$ under a flow of nitrogen, and held at that temperature until the experiment was complete.

X-ray powder diffraction data using radiation at a wavelength of 1.779 Å, and Fe K-edge EXAFS data using radiation with energies between 6976 and 7756 eV (λ = 1.777 to 1.599 Å) were collected alternately throughout the duration of the experiment, with an average current of 200 mA at 2 GeV. X-ray diffraction peaks characteristic of boron nitride were deleted from all X-ray diffraction patterns.

The collection time for XRD data was typically 300 seconds, though times of 180 seconds or less were used where the transition was expected to be faster. EXAFS data were collected with a step size equivalent to 4.4 eV in the pre-edge region, 0.4 eV in the region around the edge and 1.0 – 2.2 eV in the region after the edge with a step size of between 0.5 and 5.0 seconds per point.

In all cases the value for time associated with the experimental results is calculated as the

mid-point of the collection period compared with the time that the experiment reached the target temperature.

3.3.2 High-temperature time-resolved Mössbauer spectroscopy.

Approximately 90 mg of unheated undoped ferrosilicon with a silicon content of 54.9 % by weight was placed in the sample holder of the Mössbauer spectroscopy furnace described in Section 2.5.5. A room temperature Mössbauer spectrum was recorded for at least 12 hours before the sample was heated to either 855 or 873 K at a rate of 100 $Kmin^{-1}$ and held at that temperature until the phase transition was complete. Mössbauer data were recorded using a microprocessor-controlled constant-acceleration Mössbauer Spectrometer with a ^{57}Co-Rh source calibrated using an iron foil. The data collection time for each spectrum varied between 2 and 10 hours. The value for time associated with the experimental results is calculated as the mid-point of the collection period compared with the time that the experiment reached the target temperature.

References for Chapter Three

1 Th. Magnusson, MSc Thesis, University of Iceland, 1996, p32.

2 Personal Communication, M. Good. Metal Crystals and Oxides Laboratory Unit B5, Button End, Cambs. CB2 5NX.

3 Supplied by K. Jónsson, Science Insititute, University of Iceland.

Chapter Four: Results and Discussion – Ferrosilicon

4.1 Structural characterisation of undoped and aluminium-doped ζ_α- and ζ_β-ferrosilicon used in subsequent experiments.

4.1.1 Structure of undoped ζ_α-ferrosilicon.

4.1.1.1 Flat-plate X-ray powder diffraction

The flat-plate X-ray powder diffraction patterns, using Cu-K_α radiation (λ = 1.54 Å), recorded at *ca.* 295 K from samples of ζ_α-ferrosilicon with a silicon content of (i) 54.9 wt%[a] (ii) 54.0 wt%[b], and (iii) 50.1 wt%[b] are shown in Figure 4.1. The red lines indicate the positions of the peaks characteristic of ζ_α-ferrosilicon[1]. The blue lines indicate the positions of the peaks characteristic of ε-FeSi[2].

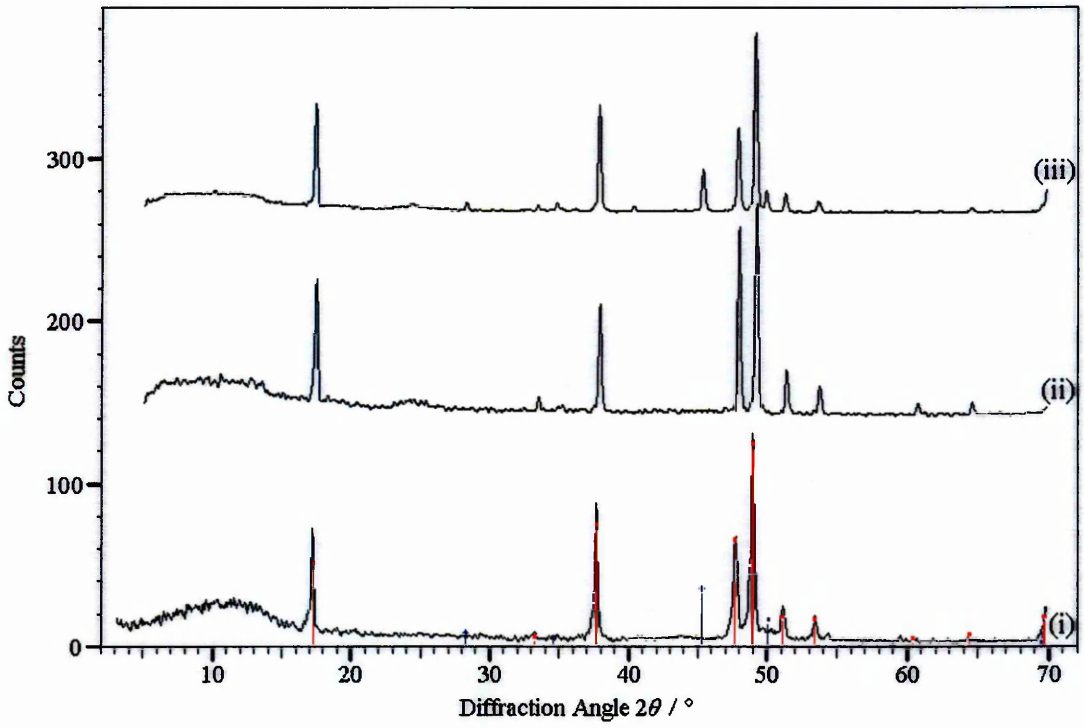

Figure 4.1: X-ray powder diffraction patterns recorded from samples of ζ_α-ferrosilicon with silicon content (by weight) (i) 54.9 %, (ii) 54.0 %, and (iii) 50.1 %

Patterns (i) and (ii) indicate that each sample has the structure of ζ_α-ferrosilicon given in

[a] Prepared at the University of Iceland as described in Section 3.1.1.1(i)

[b] Prepared by MCO Cambridge as described in Section 3.1.1.1(ii)

the literature. Pattern (i) includes a very small unexpected peak at $2\theta = 54.3°$, which could be due to some impurity in this particular sample. This was a sample made at the University of Iceland (see Section 3.1.1.1i) and other workers have found that samples such as this often contained small regions of oxides. However, there is insufficient data to make a positive identification. Pattern (ii) shows no unexpected peaks, which indicates that there are no crystalline impurities detectable in the material. Pattern (iii) indicates that the sample with a silicon content of 50.1 % consists of a mixture of ζ_α-ferrosilicon and ε-FeSi, as would be expected as indicated by the phase diagram in Section 1.2.1.2.

The increased background level at low angle seen in these, and most other X-ray powder diffraction patterns presented in this work, is a reflection from the sample plate which is a common effect with the apparatus used for these measurements, especially where a very small amount of sample is used. It is therefore disregarded throughout.

4.1.1.2 High-resolution X-ray powder diffraction

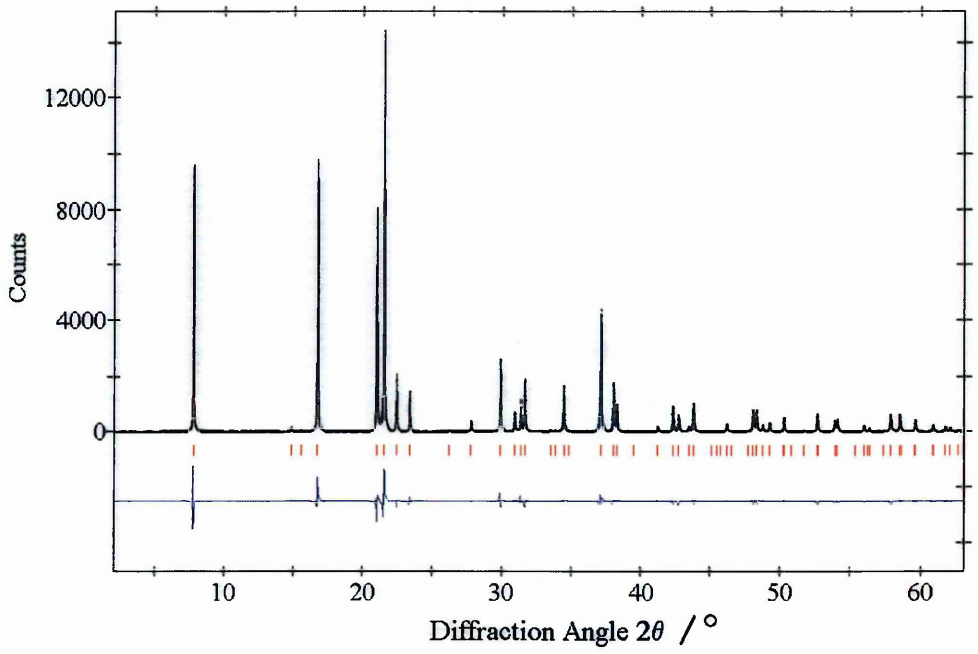

Figure 4.2: High-resolution X-ray powder diffraction pattern recorded from the sample of ζ_α-ferrosilicon with a silicon content of 54.0 %

The high-resolution X-ray powder diffraction pattern recorded at *ca.* 295 K on Station 9.1 at Daresbury Laboratory as described in Section 3.2.2 from the sample of ζ_α-ferrosilicon with a silicon content of 54.0 % using radiation of wavelength $\lambda = 0.696$ Å is shown in Figure 4.2.

The black line shows the experimental data; the blue line shows the difference between the model and the recorded data. The theoretical model used is the structure of ζ_α-ferrosilicon as described in Section 1.2.1.3, with 14.2 % iron vacancies (as would be expected for $FeSi_{2.33}$) randomly distributed within the structure. Refinement of the model using the Rietveld method gives values for the unit cell dimensions, of $a = b = 2.691$ Å, $c =$ 5.135 Å, (± 0.002 Å). These dimensions are all within 0.001 Å of those reported in the literature[3]. The computer-predicted R_{exp}-factor expected from the data quality was 9.19, the R_{wp}-factor for this fit is 11.41. This is within 20 % of the expected value so meets the criteria for acceptability described in Section 2.2.6, indicating that the data are in good agreement with the structure reported in the literature.

4.1.1.3 Iron K-edge EXAFS

The background-subtracted k^3 weighted Fe K-edge EXAFS and Fourier transform recorded at *ca.* 295 K from the sample of ζ_α-ferrosilicon with a silicon content of 54.0 % on Station 7.1 at Daresbury Laboratory are shown in Figures 4.3a and 4.3b.

These data were fitted using the structure of ζ_α-ferrosilicon given in the literature[3] and described in Section 1.2.1.3. The theoretical values for coordination numbers and distances used in this and all subsequent EXAFS fits were calculated using the software programme CRAD on the Crystals Database Server at Daresbury Laboratory[4].

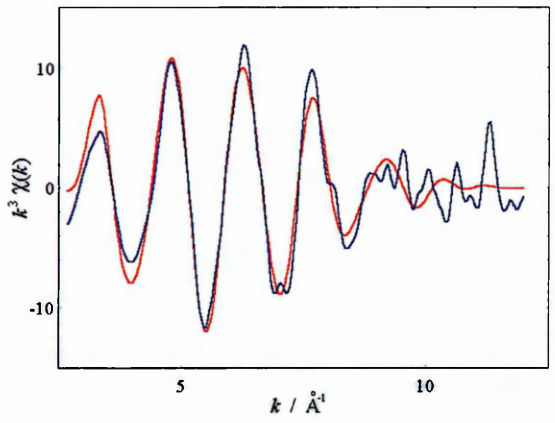

Figure 4.3a: k^3weighted Fe K-edge EXAFS of ζ_α-ferrosilicon

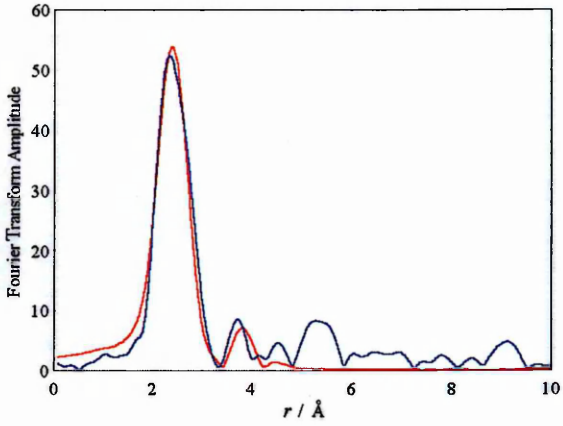

Figure 4.3b: Fourier transform of Fe K-edge EXAFS of ζ_α-ferrosilicon

The blue lines show the experimental data; the red lines show the fitted model.

The fitted model consists of three shells, as described in Table 4.1. This fit carries a fit index of 0.00065 and an *R*-factor of 32.42 %. The data are in good agreement with the structure reported in the literature and with the results obtained by X-ray powder diffraction.

Coordination Number	Atom Type	Theoretical Distance / Å	Fitted Distance / Å	Debye-Waller $2\sigma^2$ / Å^2
8	Silicon	2.384	2.38 ± 0.02	0.026
3.4	Iron	2.690	2.64 ± 0.02	0.023
3.4	Iron	3.804	3.86 ± 0.02	0.028

Table 4.1: Best fit of Fe K-edge EXAFS data shown in Figures 4.3

4.1.1.4 Mössbauer spectroscopy

^{57}Fe Mössbauer spectra were recorded using the apparatus described in Section 2.5.6 from ζ_α-ferrosilicon with a silicon content of 54.9 % (a) at *ca.* 295 K and (b) at 855 K. The spectrum recorded at 855 K has the most relevance to this work and is shown in Figure 4.4.

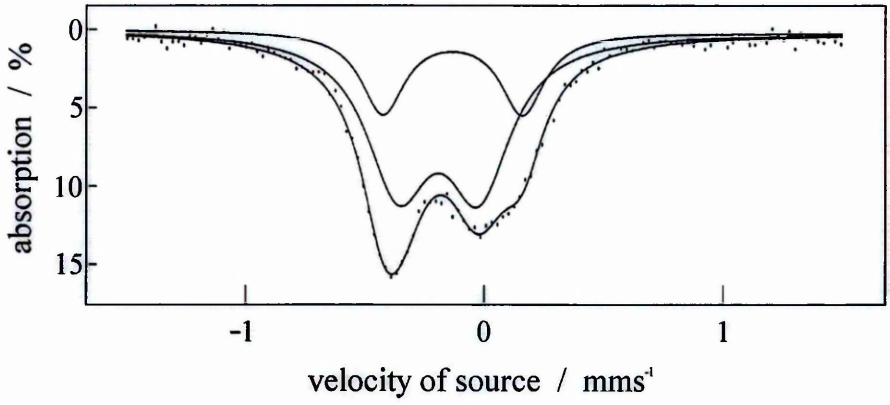

Figure 4.4: ^{57}Fe Mössbauer spectrum of ζ_α-ferrosilicon recorded at 855 K

The spectra were each fitted to two doublets, the values of the isomer shift and quadrupole splitting of the doublets are shown in Table 4.2. Uncertainties are ± 2 %.

		δ / mms^{-1}	Δ / mms^{-1}	Γ / mms^{-1}
ca. 295 K	Doublet 1	0.19	0.44	0.39
	Doublet 2	0.29	0.75	0.30
855 K	Doublet 1	-0.18	0.34	0.34
	Doublet 2	-0.13	0.59	0.22

Table 4.2: ^{57}Fe Mössbauer parameters for ζ_α-ferrosilicon

These values are consistent with those reported in the literature[5] [6]. Each doublet corresponds to an iron site in the structure of ζ_α-ferrosilicon. Doublet 2 corresponds to the spectrum that would be expected for the structure of ζ_α-ferrosilicon as shown in Section 1.2.1.3 with no iron vacancies. Doublet 1 has broader and asymmetric peaks, which are indicative of a heterogeneity of iron species in structurally similar sites contributing to this component of the spectrum. This corresponds to the distribution of iron sites, which are due to the different combinations of iron vacancies in the structure. The reduction in isomer shifts in the spectrum recorded at 855 K is indicative of the elevated energy state which would be expected at high temperature. After recording the Mössbauer spectrum at 855 K, a second spectrum was recorded at *ca.* 295 K to ensure that no phase transition had taken place while the sample was at elevated temperature. There was no significant difference in the second spectrum.

4.1.2 Structure of ζ_α-ferrosilicon doped with 1% aluminium.

4.1.2.1 Flat plate X-ray powder diffraction

The flat-plate X-ray powder diffraction patterns, using Cu-K_α radiation (λ = 1.54 Å), recorded at *ca.* 295 K from the samples of ζ_α-ferrosilicon with aluminium content of 1 % by weight and silicon content of (i) 54.4 %[a] and (ii) 53.4 %[b] by weight are shown in Figure 4.5. The red lines are the positions of the peaks characteristic of ζ_α-ferrosilicon[1]. The green lines (at 2θ = 28.4°, 47.3° and 56.1°) are the positions of the peaks characteristic of metallic silicon[7].

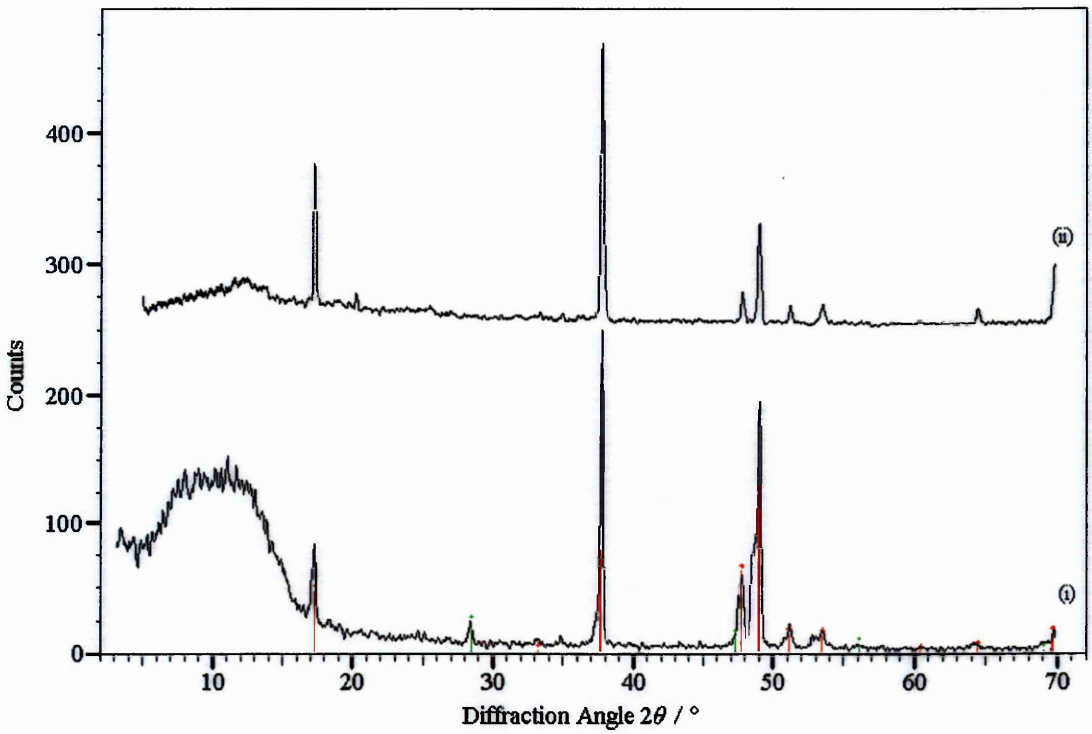

Figure 4.5: X-ray powder diffraction patterns recorded from ζ_α-ferrosilicon with an aluminium content of 1% by weight and a silicon content of (i) 54.4% and (ii) 53.4% by weight

Pattern (i) indicates that the sample with a silicon content of 54.4% by weight has the structure of ζ_α-ferrosilicon, and that some metallic silicon is also present. Pattern (ii) indicates that the sample with a silicon content of 53.4 % by weight has the structure of

---

[a] Prepared in Iceland as described in Section 3.1.1.1(i)

[b] Prepared by MCO Cambridge as described in Section 3.1.1.1(ii)

ζ_α-ferrosilicon, with no evidence of the presence of metallic silicon. It is interesting to compare these with the patterns in Figure 4.1, which indicate that the samples of undoped ζ_α-ferrosilicon with silicon contents of 54.9, 54.0 and 50.1 % show no evidence of the presence of metallic silicon. This may indicate that the addition of aluminium reduces the range of silicon content over which the ζ_α-ferrosilicon phase is stable. These results are comparable to work published by Sabirzyanov *et al*[8] in which it was stated that the addition of 0.8 – 0.9 % aluminium to ζ_α-ferrosilicon caused precipitation of a new optically active phase of unknown composition.

4.1.2.2 High-resolution X-ray powder diffraction

The high-resolution X-ray powder diffraction pattern recorded at *ca.* 295 K on Station 9.1 at Daresbury Laboratory as described in Section 3.2.2 from a sample of ζ_α-ferrosilicon with an aluminium content of 1 % by weight and a silicon content of 53.4 % by weight using radiation of wavelength λ = 0.696 Å is shown in Figure 4.6.

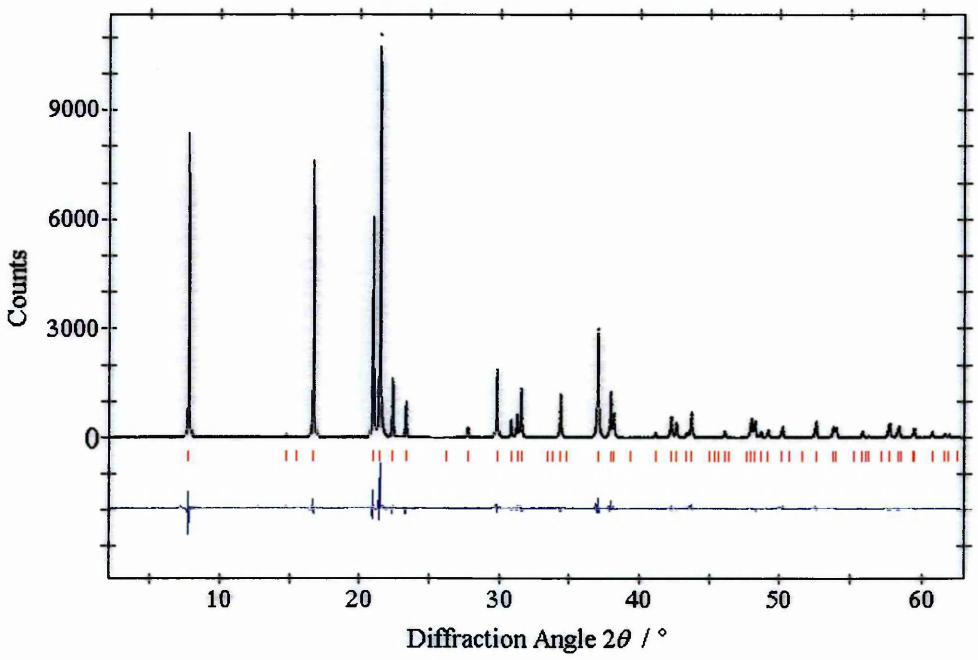

Figure 4.6: High-resolution X-ray powder diffraction pattern recorded from ζ_α-ferrosilicon with an aluminium content of 1 % and a silicon content of 53.4 %

The black line shows the experimental data; the blue line shows the differences between the theoretical model and the recorded data. The initial theoretical model used is the structure of undoped ζ_α-ferrosilicon described in Section 1.2.1.3, with 14.2% iron vacancies (as would be expected for $FeSi_{2.33}$) randomly distributed within the structure. Rietveld refinement of the model gives values for the unit cell dimensions of $a = b = 2.694$ Å, $c = 5.133$ Å, (± 0.002 Å). The computer-predicted R_{exp}-factor expected from the data quality was 11.55. The R_{wp}-factor for this fit was 13.97. This is over 20% difference so the fit is on the limits of acceptability according to the criteria described in Section 2.2.6. However, attempts to improve the fit by introducing the presence of aluminium into the undoped theoretical model have not resulted in any significant improvement to the quality of fit.

The presence of aluminium does not appear to have had any significant effect on the lattice parameters, as these unit cell dimensions are almost identical to those given in Section 4.1.1.2 for the undoped sample. There are no unexpected peaks in the X-ray diffraction pattern, the blue line in Figure 4.6 shows that the differences between the fitted model and the recorded data are only in the intensities and widths of the diffraction peaks, not their positions. The aluminium dissolved within the ζ_α-ferrosilicon structure could have the effect of changing the diffraction peaks in this way by introducing a level of disorder into the structure. However, a more detailed view of the effect of the addition of aluminium to the structure of ζ_α-ferrosilicon is not quantifiable with these data.

4.1.2.3 Low-temperature iron K-edge EXAFS

The background subtracted k^3 weighted EXAFS and Fourier transform recorded on Station 8.1 at Daresbury Laboratory from ζ_α-ferrosilicon with an aluminium content of 1 % by

weight and a silicon content of 53.4 % by weight and cooled to *ca.* 77 K with liquid nitrogen are shown in Figures 4.7a and 4.7b.

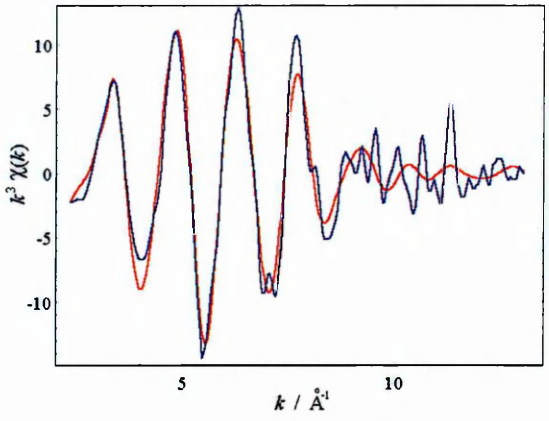

Figure 4.7a: k^3 weighted EXAFS of ζ_α-ferrosilicon containing 1 % Al

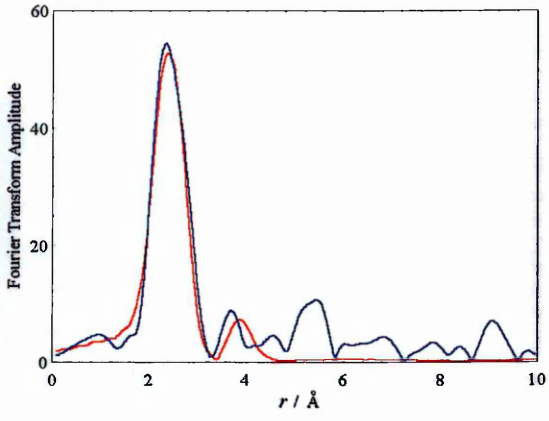

Figure 4.7b: Fourier transform of EXAFS of ζ_α-ferrosilicon containing 1 % Al

The blue lines show the experimental data; the red lines show the fitted model.

These data were fitted using the structure of ζ_α-ferrosilicon given in the literature[3] and described in Section 1.2.1.3, with aluminium atoms occupying iron vacancy positions. The fit is described in Table 4.3 below. This fit carries a fit index of 0.00062 and an *R*-factor of 31.43 %.

Coordination Number	Atom Type	Theoretical Distance[3] / Å	Fitted Distance / Å	Debye-Waller $2\sigma^2$ / Å^2
8	Silicon	2.384	2.36 ± 0.02	0.025
3.4	Iron	2.690	2.64 ± 0.02	0.021
0.04	Aluminium	2.690	2.64 ± 0.02	0.021
3.4	Iron	3.804	3.85 ± 0.02	0.027

Table 4.3: Best fit of Fe K-edge EXAFS data shown in Figures 4.7

The aluminium shell was constrained to the same distance and Debye-Waller factor as the first iron shell. However, the values of the fit index and *R*-factor showed very little variance upon the removal of the fitted aluminium shell, therefore this fit is not sufficient evidence for the aluminium dopant location on the vacant iron site. Figures 4.8a and 4.8b show compar-

isons of the data shown in Figures 4.3a and 4.7a and Figures 4.3b and 4.7b respectively.

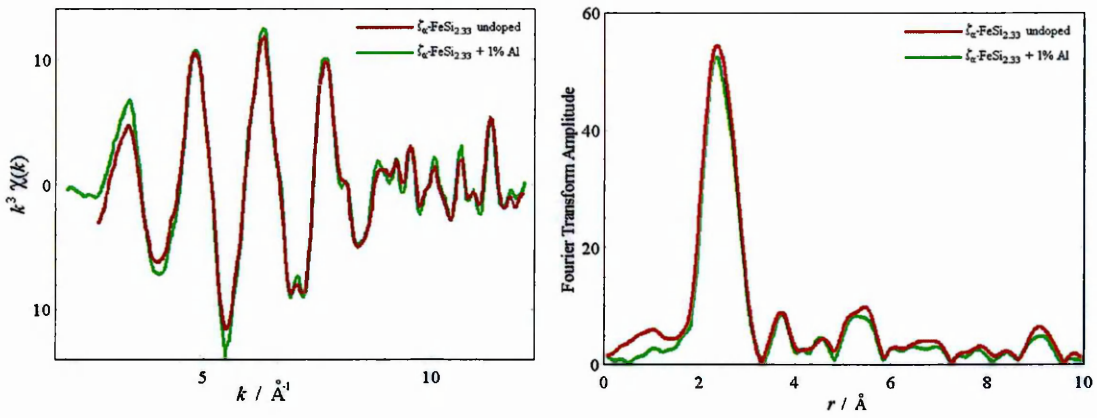

Figures 4.8: Comparisons of (a) k^3 weighted EXAFS and (b) Fourier transforms of EXAFS, both of ζ_α-ferrosilicon with and without 1 % aluminium doping

The Fourier transforms shown in Figure 4.8b shows that the intensity of the first peak is slightly reduced for the sample with 1 % aluminium doping, which would be consistent with the presence of Al on Fe sites. However, the difference is very small and could equally be attributed to differences in experimental conditions, data quality, and in statistical noise. Therefore, it appears that the effect of the presence of 1 % aluminium on the structure of ζ_α-ferrosilicon cannot be quantified with these data.

4.1.3 Structure of undoped ζ_β-$FeSi_2$

The structure of ζ_β-ferrosilicon with a silicon content of 50.1% (thus ζ_β-$FeSi_2$) was examined in order to investigate the effect of the additional silicon in the structure of ζ_β-$FeSi_{2.33}$ which will be discussed in Section 4.1.4.

4.1.3.1 Flat plate X-ray powder diffraction

The flat-plate X-ray powder diffraction pattern, using Cu-K_α radiation (λ = 1.54 Å), recorded at *ca.* 295 K from ζ_β-$FeSi_2$ prepared by heating ferrosilicon with a silicon content of 50.1% as described in Section 3.1.1.2 is shown in Figure 4.9. The red lines indicate the positions of the peaks characteristic of ζ_β-$FeSi_2$[9].

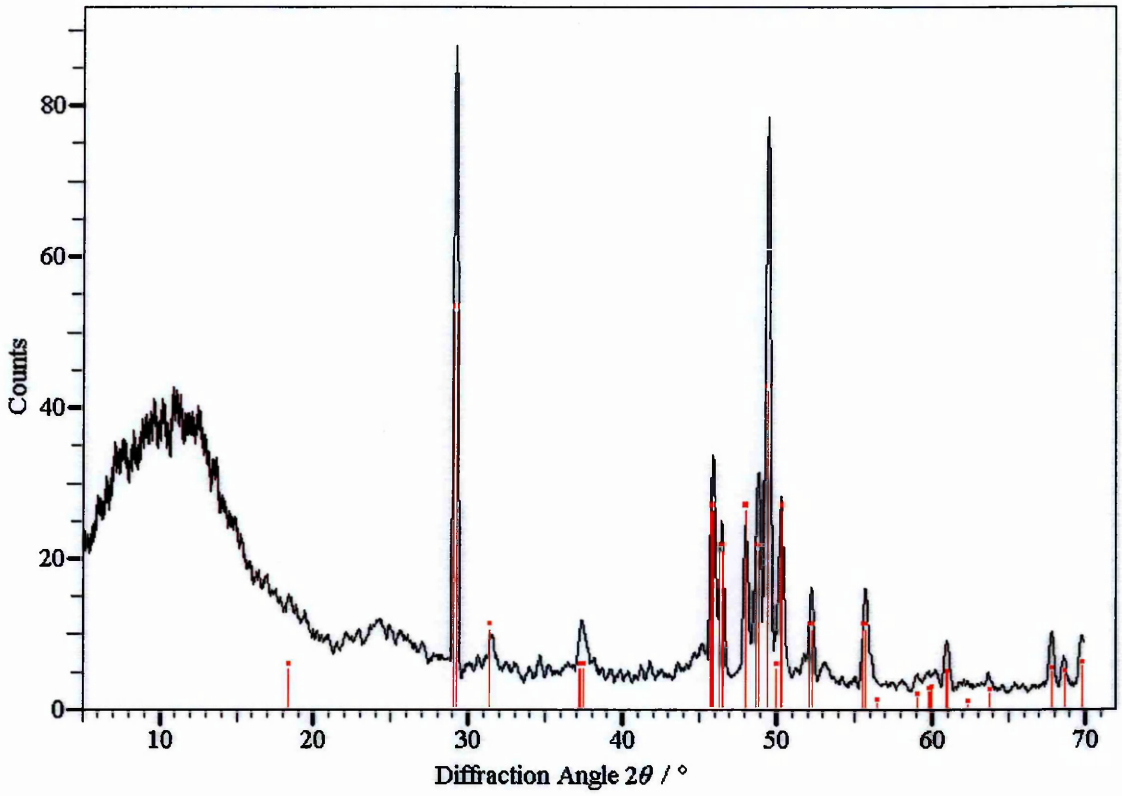

Figure 4.9: X-ray powder diffraction pattern recorded from heated ferrosilicon with silicon content 50.1%

There is no evidence of the presence of ζ_α-ferrosilicon or ε-FeSi and the pattern shows no unexpected peaks. The pattern indicates that the sample has the structure of ζ_β-$FeSi_2$ given in the literature.

4.1.3.2 High-resolution X-ray powder diffraction

The high-resolution X-ray powder diffraction pattern recorded at *ca.* 295 K on Station 9.1 at Daresbury Laboratory as described in Section 3.2.2, using radiation of wavelength λ = 0.696 Å, from the sample of ζ_β-$FeSi_2$ prepared by heating ζ_α-ferrosilicon with silicon content 50.1 % as described in Section 3.1.1.2 is shown in Figure 4.10. The black line shows the experimental data; the blue line shows the differences between the theoretical model and the recorded data. The theoretical model used is the structure of ζ_β-$FeSi_2$ as described in Section 1.2.1.3.

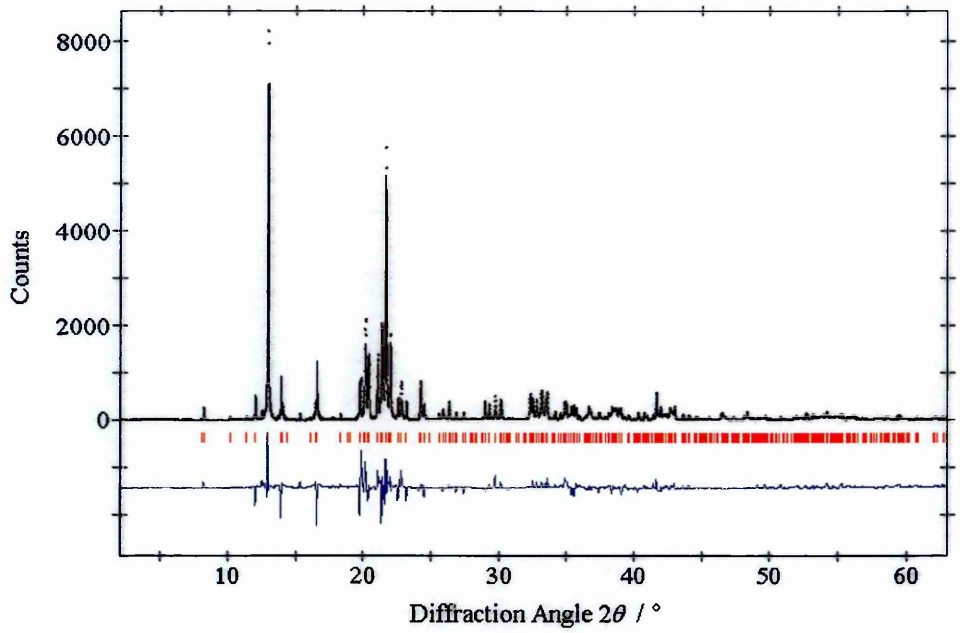

Figure 4.10: High resolution X-ray powder diffraction pattern recorded from a heated sample of ferrosilicon with silicon content 50.1%

Refinement of the model using the Rietveld method gives values for the unit cell dimensions of a = 9.879 Å, b = 7.804 Å, c = 7.836 Å, (± 0.003 Å). These are all slightly higher than those reported in the literature (as detailed in Section 1.2.1.3) albeit within less than 1 % of the expected values. The R_{wp}-factor for this fit was 31.70, as compared with a computer-predicted expected R_{exp}-factor of 17.12, therefore this cannot be said to be an acceptable fit according to the criteria described in Section 2.2.6. This means that although these data are consistent with the structure of ζ_{β}-$FeSi_2$ reported in the literature and there is no indication of the presence of impurities or a second phase, the data cannot be used for more in-depth structural analysis.

4.1.3.3 Iron K-edge EXAFS

The background subtracted k^3 weighted EXAFS and Fourier transform recorded at *ca.* 295 K on Station 7.1 at Daresbury Laboratory from ζ_{β}-$FeSi_2$ prepared by heating ferrosilicon with a silicon content of 50.1 % as described in Section 3.1.1.2 are shown in Figures 4.11a and 4.11b.

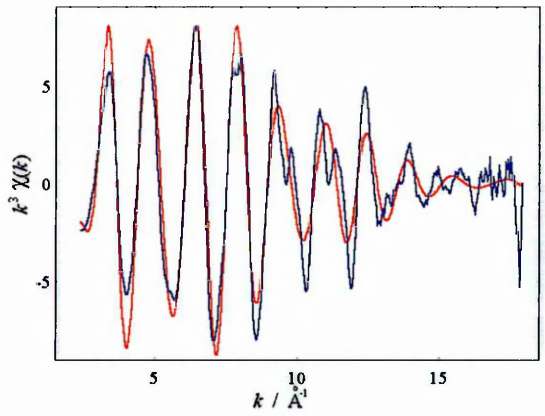

Figure 4.11a: k^3 weighted Fe K-edge EXAFS of ζ_β-$FeSi_2$

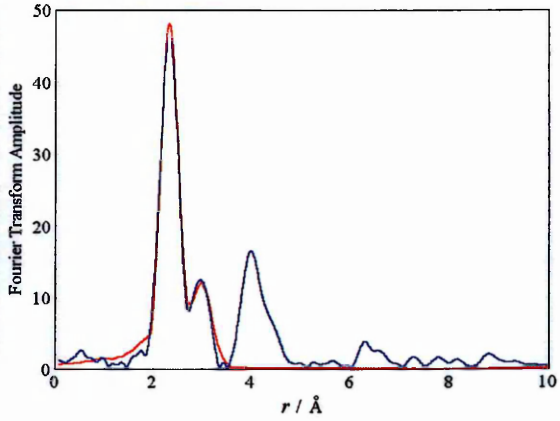

Figure 4.11b: Fourier transform of Fe K-edge EXAFS of ζ_β-$FeSi_2$

The blue lines show the experimental data; the red lines show the fitted model.

These data were fitted using the structure of ζ_β-$FeSi_2$ given in the literature[10]. The model fitted consists of two shells, as described in Table 4.4 below. This fit carries a fit index of 0.00065 and an *R*-factor of 32.42 %. The data are in good agreement with the structure reported in the literature and in general agreement with the findings of the high-resolution X-ray powder diffraction investigation described in Section 4.1.3.2.

Detailed Theoretical Model Calculated by CRAD[4] from ICSD data[10]			Simplified Theoretical Model Average of Detailed Theoretical Model			Fitted Model	
Coordination Number	Atom Type	Theoretical Distance / Å	Coordination Number	Atom Type	Theoretical Distance / Å	Fitted Distance / Å	Debye-Waller $2\sigma^2$ / Å^2
8	Silicon	2.333 ; 2.335 2.338 ; 2.338 2.377 ; 2.386 2.428 ; 2.436	8	Silicon	2.371	2.33 ± 0.02	0.027
2	Iron	2.967	2	Iron	2.967	2.97 ± 0.02	0.018

Table 4.4: Best fit of Fe K-edge EXAFS data shown in Figures 4.11

4.1.3.4 Silicon K-edge EXAFS

The background-subtracted k^3 weighted Si K-edge EXAFS and Fourier transform data recorded at *ca.* 295 K from the sample of ζ_β-$FeSi_2$ prepared by heating ζ_α-ferrosilicon with a

silicon content of 50.1 % as described in Section 3.1.1.2, using Station 3.4 at Daresbury Laboratory, are shown in Figures 4.12a and 4.12b.

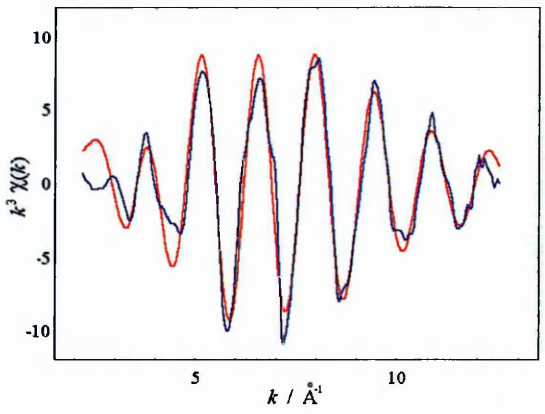

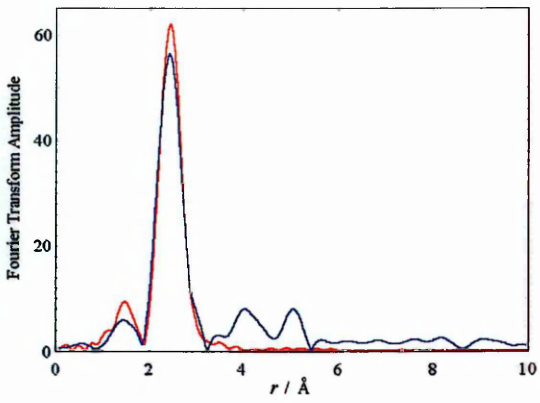

Figure 4.12a: k^3 weighted Si K-edge EXAFS of ζ_β-$FeSi_2$ Fig. 4.12b: Fourier transform of Si EXAFS of ζ_β-$FeSi_2$ The blue lines show the experimental data; the red lines show the fitted model.

These data were collected using Total Electron Yield EXAFS (as described in Sections 2.3.5.2 (iii) and 3.2.4) rather than transmission EXAFS because at the low energies required for collected EXAFS data at the silicon K-edge, transmission EXAFS data of acceptable quality would only be obtainable if the sample was less than one micron thick.

Initial attempts to fit these data using the structure of ζ_β-$FeSi_2$ as described in Section 1.2.1.3 were unsuccessful. This was probably due to the fact that in Total Electron Yield EXAFS atoms on the surface of the sample absorb the majority of the incident radiation, therefore surface phenomena, which can be ignored in transmission EXAFS, become highly significant. Any material that has been prepared or stored in air is likely to show surface oxidation. Even if this accounts for a small fraction of one percent of the bulk material, oxidised atoms can make up a significant proportion of the absorbing atoms on the surface of the sample in TEY EXAFS.

Therefore, the best fit for the Si K-edge TEY EXAFS data shown in Figure 4.12 was found

using the structure ζ_{β}-$FeSi_2$ as described in Section 1.2.1.3 and also the structure characteristic of α-SiO_2 (quartz)[11]. This is not evidence that there is a separate SiO_2 phase in the sample but only that a proportion of the silicon atoms on the surface of the sample have bonded to an oxygen atom.

(i) Theoretical EXAFS characteristic of ζ_{β}-$FeSi_2$

Table 4.5 shows how the structure of ζ_{β}-$FeSi_2$ given in the literature can be simplified to two shells for the purpose of EXAFS fitting.

Coordination Number	Atom Type	Theoretical Distances / Å Calculated by CRAD[4] from ICSD data[10]	Average Distance / Å	Max. Variance
4	Fe	2.334, 2.338, 2.382, 2.432	2.371	0.065
5	Si	2.449, 2.499, 2.512, 2.529, 2.579	2.525	0.076

Table 4.5: Expected shells around silicon characteristic of ζ_{β}-$FeSi_2$

(ii) Theoretical EXAFS characteristic of SiO_2

Table 4.6 shows how the structure of α-SiO_2 given in the literature[11] can be simplified to two shells for the purpose of EXAFS fitting.

Coordination Number	Atom Type	Theoretical Distances / Å Calculated by CRAD[4] from ICSD data[11]	Average Distance /Å	Max. Variance
4	O	1.609, 1.616	1.613	± 0.004
4	Si	3.065	3.065	-

Table 4.6: Expected shells around silicon characteristic of α-SiO_2

The best fit to the EXAFS data shown in Figures 4.12 is given in Table 4.7. The fit was found by combining the data in the above tables and refining the coordination numbers in order to find what proportion of the absorbing silicon was oxidised.

Coordination Number	Atom Type	Theoretical Distance / Å From Tables 4.5 and 4.6	Fitted Distance / Å	Debye-Waller $2\sigma^2$ / Å^2
0.69 ± 0.04	O	1.613	1.62 ± 0.02	0.011
3.31 ± 0.04	Fe	2.371	2.37 ± 0.02	0.013
4.14 ± 0.04	Si	2.525	2.54 ± 0.02	0.027
0.69 ± 0.04	Si	3.065	3.05 ± 0.02	0.026

Table 4.7: Best fit to Si K-edge EXAFS data shown in Figures 4.12

The fit index was 0.00061, and the *R*-factor was 34.15 %. This analysis indicates that 17.3 % ± 1.0 % of the absorbing silicon atoms on the surface are in an oxidised environment, and that the remaining silicon is in a ζ_β-$FeSi_2$ structure. To examine the structure using Si K-edge EXAFS without any surface oxidation, it would be necessary to prepare and examine the sample in the absence of oxygen. However, it is possible that other surface phenomena would also affect the analysis.

4.1.4 Structure of undoped ζ_β-$FeSi_{2.33}$

A scanning electron microscopy image of a sample of ferrosilicon prepared by heating a piece of ferrosilicon of *ca.* 1 cm diameter with a silicon content of 54.0 %, for 74 hours is shown in Figure 4.13.

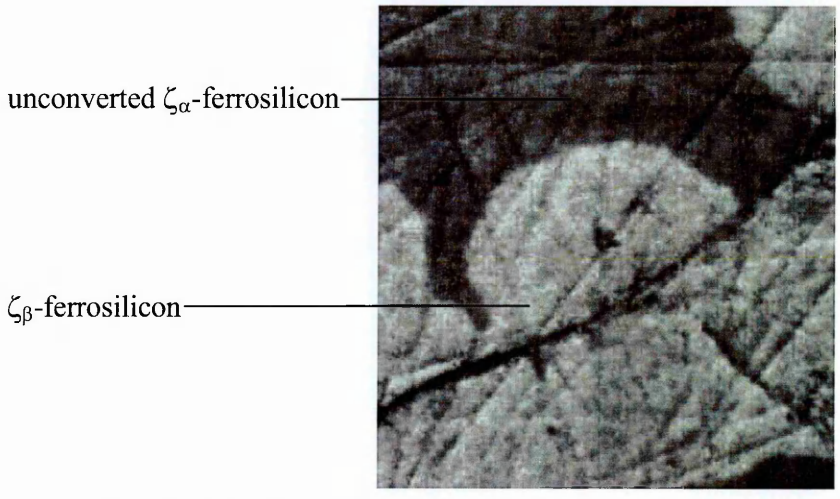

Figure 4.13: SEM view of sample of ferrosilicon prepared by heating a portion of ferrosilicon with silicon content 54.0%

The darker region is unconverted ζ_α-ferrosilicon. There is no evidence of a precipitated

phase of silicon, as observed by Boomgaard[12], which would appear as very dark or black thin rods within the pale area. This sample may therefore be the metastable ζ_{β}-$FeSi_{2.33}$.

4.1.4.1 Flat plate X-ray powder diffraction

The flat-plate X-ray powder diffraction patterns, using Cu-K_{α} radiation (λ = 1.54 Å), recorded at *ca.* 295 K from a sample of ζ_{β}-$FeSi_{2.33}$ prepared by heating ferrosilicon with a silicon content of 54.0 wt% supplied by MCO Cambridge as described in Section 3.1.1.1(ii) as described in Section 3.1.1.2 is shown in Figure 4.14 (i) immediately after heating and (ii) several days after heating. The red lines indicate the positions of the peaks characteristic of ζ_{β}-$FeSi_2$[9]. The green lines indicate the positions of the peaks characteristic of metallic silicon[7].

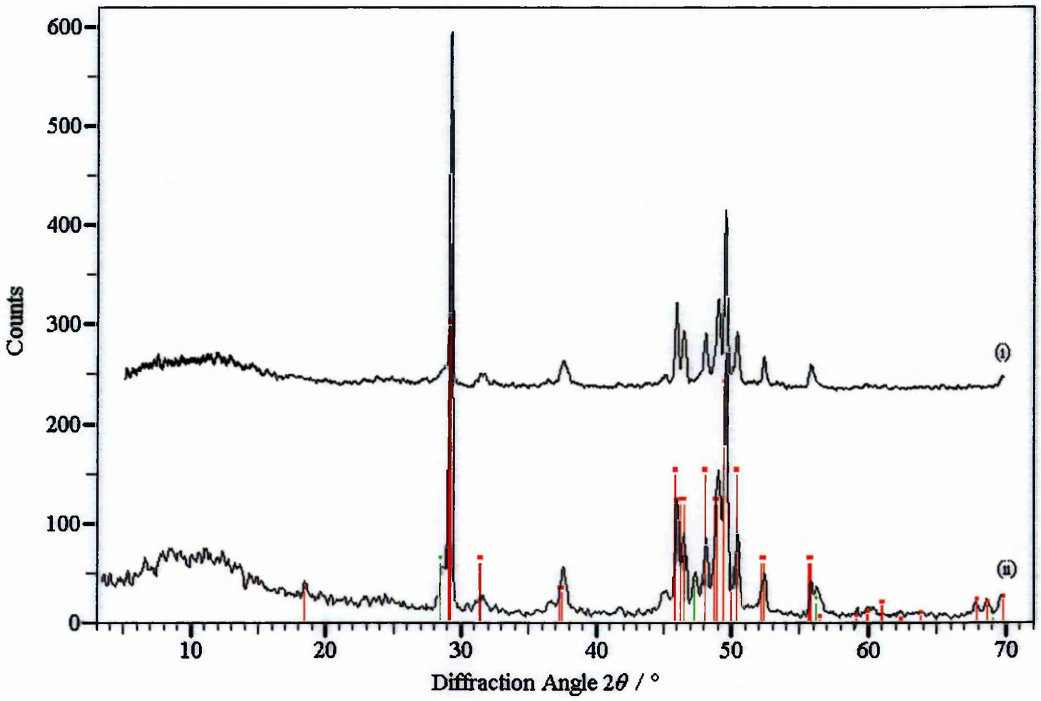

Figure 4.14: XRD pattern recorded from sample of ζ_{β}-$FeSi_{2.33}$ prepared by heating ferrosilicon with silicon content 54.0 % by weight (i) immediately after heating and (ii) several days after heating

Pattern (i) indicates that the sample has the structure of ζ_{β}-$FeSi_2$. There is no indication of the presence of a separate crystalline metallic silicon phase, indicating that the excess silicon may be incorporated into the ζ_{β}-$FeSi_2$ structure to form the metastable ζ_{β}-$FeSi_{2.33}$ proposed by Boomgaard[12]. Pattern (ii) shows peaks characteristic of metallic silicon,

indicating that some of the excess silicon has precipitated from the metastable ζ_{β}-$FeSi_{2.33}$. In pattern (i) some of the low-intensity peaks characteristic of ζ_{β}-$FeSi_2$ at $2\theta > 59°$ are barely detectable, whereas they are more intense in pattern (ii). The reduction in intensity in pattern (i) may be due to the additional silicon within the unit cell in metastable ζ_{β}-$FeSi_{2.33}$ causing disruptions in the crystallographic planes corresponding to these peaks and reducing the amount of radiation diffracted in these directions by destructive interference.

4.1.4.2 High-resolution X-ray powder diffraction

The high-resolution X-ray powder diffraction pattern recorded at *ca.* 295 K on Station 9.1 at Daresbury Laboratory as described in Section 3.2.2 from a sample of ζ_{β}-$FeSi_{2.33}$ prepared by heating ferrosilicon with a silicon content of 54.0 % by weight using radiation of wavelength $\lambda = 0.696$ Å is shown in Figure 4.15.

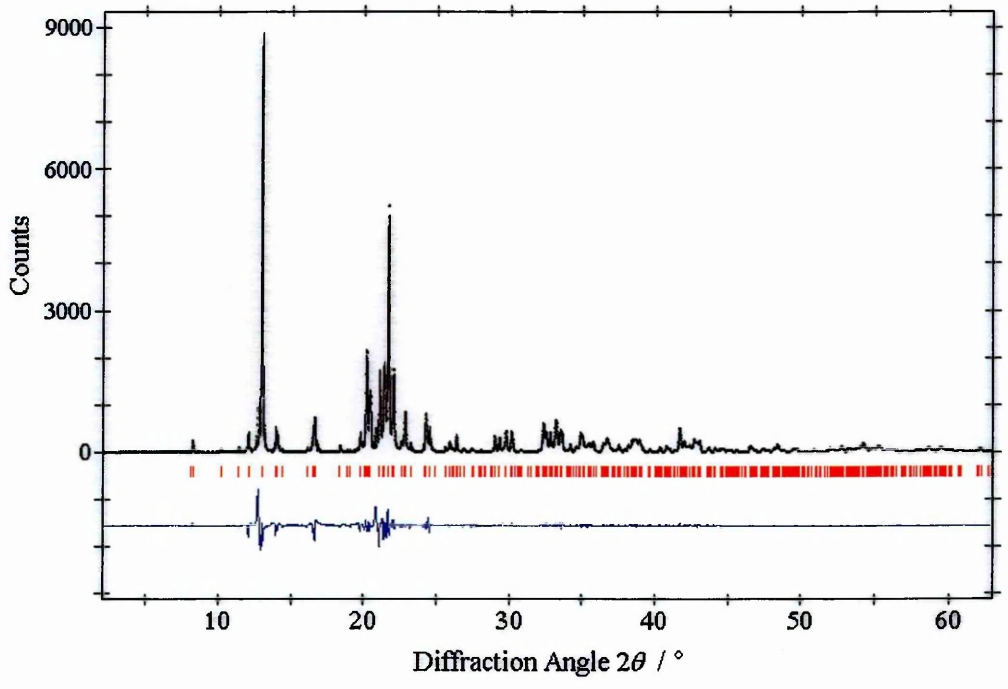

Figure 4.15: High-resolution X-ray powder diffraction pattern recorded from a sample of ζ_{β}-$FeSi_{2.33}$ prepared by heating a portion of ferrosilicon with silicon content 54.0 % by weight

The black line shows the experimental data; the blue line shows the differences between the theoretical model and the recorded data. The theoretical model used is the structure of ζ_β-$FeSi_2$ described in Section 1.2.1.3. Refinement of the model using the Rietveld method gives unit cell dimensions of a = 9.882 Å b = 7.801 Å, c = 7.833 Å, (± 0.002 Å). The computer-predicted R_{exp}-factor expected from the data quality was 14.65, the R_{wp}-factor for this fit, which excludes any parameters to account for the extra silicon in the structure, was 21.69. The difference is almost 50 %, which is not acceptable according to the criteria described in Section 2.2.6, so a better model is needed. The blue line in Figure 4.15 does not indicate the presence of any peaks at unexpected positions so there is no evidence for the presence of a second phase (for instance metallic silicon or ζ_α-ferrosilicon). However, all attempts to introduce fitting parameters that indicate the presence of the additional silicon were not successful. This is mainly attributed to the lack of a fit of suitable quality for ζ_β-$FeSi_2$ as discussed in Section 4.1.3.2.

Despite the difficulties associated with an in-depth analysis of these data, it is interesting to note that the intensity of the peak at *ca.* 13.0° (corresponding to crystal planes (202) and (220)) relative to the majority of the other peaks in the pattern is greater in Figure 4.15 than in Figure 4.10, the pattern recorded from ζ_β-$FeSi_2$. The shape of the blue line in Figure 4.15 at this position also indicates that the position and width of this diffraction peak is very slightly different from the theoretical model. Putting aside any effects due to preferential alignment in sample preparation, this could be evidence that the extra silicon in ζ_β-$FeSi_{2.33}$ contributes strongly to the intensities of reflections from the (202) and (220) planes.

4.1.4.3 Iron K-edge EXAFS

The background subtracted k^3 weighted EXAFS and Fourier transform data recorded on Station 7.1 at Daresbury Laboratory at *ca.* 295 K from ζ_β-$FeSi_{2.33}$ prepared by heating

ferrosilicon with a silicon content of 54.0 % by weight as described in Section 3.1.1.2 are shown in Figures 4.16a and 4.16b.

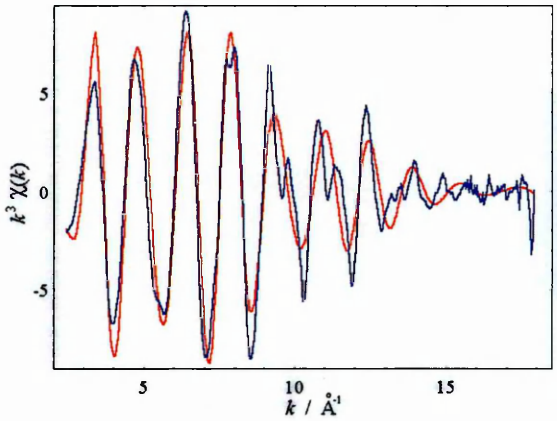

Figure 4.16a: k^3 weighted Fe K-edge EXAFS of sample of ζ_β-$FeSi_{2.33}$: first fit.

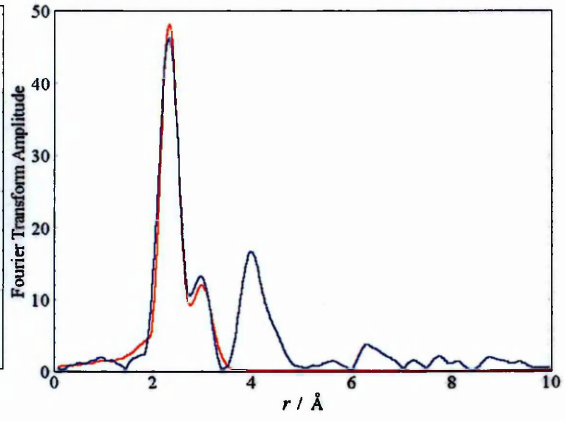

Figure 4.16b: Fourier transform of Fe K-edge EXAFS of sample of ζ_β-$FeSi_{2.33}$: first fit.

The blue lines show the experimental data; the red lines show the fitted model.

These data were initially analysed using the fit calculated in Section 4.1.3.3, relating to ζ_β-$FeSi_2$ with silicon content 50.1 wt%. This model consists of 2 shells, as given in Table 4.4 and below in Table 4.8. With these parameters, the fit carries a fit index of 0.00082 and an *R*-factor of 45.7 %.

Detailed Theoretical Model Calculated by CRAD[4] from ICSD data[10]			Simplified Theoretical Model Average of Detailed Theoretical Model			Fitted Model	
Coord. Number	Type	Expected Distance / Å	Coord. Number	Type	Expected Distance / Å	Fitted Distance / Å	Debye-Waller $2\sigma^2$ / Å^2
8	Silicon	2.333 ; 2.335 2.338 2.338 2.377 ; 2.386 2.428 ; 2.436	8	Silicon	2.371	2.33 ± 0.02	0.027
2	Iron	2.967	2	Iron	2.967	2.97 ± 0.02	0.018

Table 4.8: Initial EXAFS fit of data shown in Figures 4.16 (these are the same values as given in Table 4.4)

The model was then altered to take into account the presence of the additional silicon in ζ_β-$FeSi_{2.33}$. With the hypothesis that the additional silicon is dissolved within the crystalline structure of ζ_β-$FeSi_2$, and the suggestion from XRD data that this silicon contributes strongly to the intensities of reflections from the (202) and (220) planes, it was

postulated that silicon atoms could be located in the large spaces in the unit cell near the eight (±0.25, ±0.25, ±0.25) positions.

The unit cell of ζ_β-$FeSi_2$ contains 16 iron atoms and 32 silicon atoms (see Section 1.2.1.3). In metastable ζ_β-$FeSi_{2.33}$ there are an additional 0.33 silicon atoms dissolved within the structure for every 2 silicon atoms in the normal unit cell positions. Therefore, each unit cell of ζ_β-$FeSi_{2.33}$ will contain on average an additional 5.28 silicon atoms (= 0.33 x 32 / 2). This is equivalent to a 66% occupancy level of the eight (±0.25, ±0.25, ±0.25) positions.

If the eight (±0.25, ±0.25, ±0.25) positions were occupied at 100 % with extra silicon atoms, one of the iron sites would have a shell of 4 such silicon atoms at a distance of 2.784 Å, and the other iron site would have a shell of 2 such silicon atoms at a distance of 2.559 Å. The average effect would therefore be a shell of 3 silicon atoms at a distance of 2.709 Å. At 66% occupancy, the effect would be of an average of 1.98 silicon atoms at a distance of 2.709Å from the absorbing iron atom.

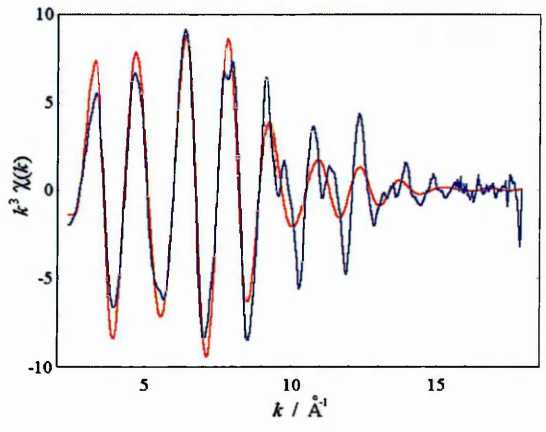

Figure 4.17a: k^3 weighted Fe K-edge EXAFS of sample of ζ_β-$FeSi_{2.33}$: second fit

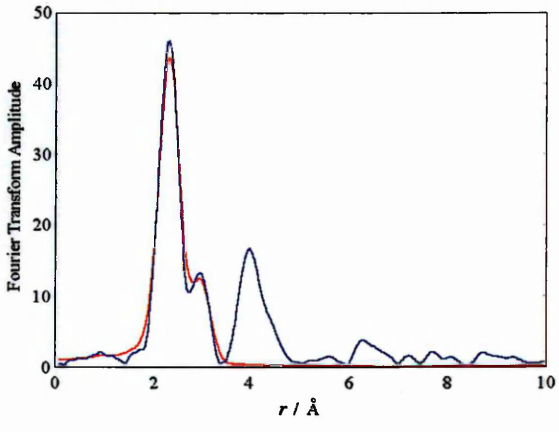

Figure 4.17b: Fourier transform of Fe K-edge EXAFS of sample of ζ_β-$FeSi_{2.33}$: second fit

The blue lines show the experimental data; the red lines show the fitted model.

The background-subtracted k^3 weighted EXAFS and Fourier transform data for the model including this shell are shown in Figures 4.17a and 4.17b. The best fit consists of three shells, as described in Table 4.9.

Detailed Theoretical Model Calculated by CRAD[4] from ICSD data[10] with additional Si shell as described above			Simplified Theoretical Model Average of Detailed Theoretical Model			Fitted Model	
Coord. Number	Type	Expected Distance / Å	Coord. Number	Type	Expected Distance / Å	Fitted Distance / Å	Debye-Waller $2\sigma^2$ / Å^2
8	Silicon	2.333 ; 2.335 2.338 2.338 2.377 ; 2.386 2.428 ; 2.436	8	Silicon	2.371	2.37 ± 0.02	0.020
1.98	Silicon	2.709	1.98	Silicon	2.709	2.72 ± 0.02	0.026
2	Iron	2.967	2	Iron	2.967	2.98 ± 0.02	0.019

Table 4.9: EXAFS fit of data shown in Figures 4.17

This fit carries a fit index of 0.00058 and an *R*-factor of 36.7 % – indicating a better fit than that shown previously in Table 4.8. It would be unreasonable to expect an *R*-factor significantly better than this without adding further shells to the model in the 3.5 – 5 Å region. The structure of ζ_β-ferrosilicon is such that at least 4 additional shells would be needed to successfully model this region. Without significantly better data quality, this could not be attempted.

4.1.4.4 Low-temperature iron K-edge EXAFS

The background subtracted k^3 weighted EXAFS and Fourier transform recorded on Station 8.1 at Daresbury Laboratory from ζ_β-$FeSi_{2.33}$ prepared by heating ferrosilicon with a silicon content of 54.0 % by weight as described in Section 3.1.1.2 and cooled to *ca.* 77 K with liquid nitrogen are shown in Figures 4.18a and 4.18b.

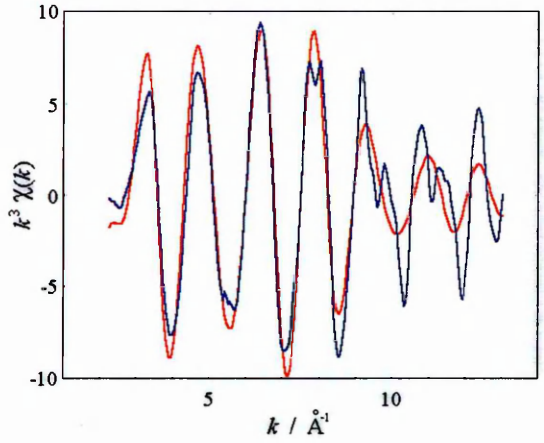

Figure 4.18a: k^3 weighted low temperature Fe K-edge EXAFS of ζ_β-$FeSi_{2.33}$

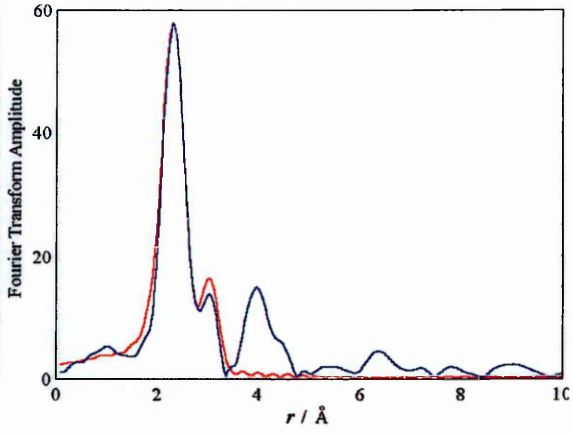

Figure 4.18b: Fourier transform of low temperature Fe K-edge EXAFS of ζ_β-$FeSi_{2.33}$

The blue lines show the experimental data; the red lines show the fitted model.

The data were fitted using the model described in Section 4.1.4.3 above. However, with this model the value of the Debye-Waller factor for the shell of 1.98 silicon atoms at *ca.* 2.7 Å was significantly higher than expected. It was postulated that some of the excess silicon in the sample may have precipitated out from the structure as described in Section 1.2.1.4. Therefore, the coordination number of this shell was included as a variable in the refinement of the fit. The resulting fit is described in Table 4.10. This fit carries a fit index of 0.00077 and an *R*-factor of 36.6 %.

Detailed Theoretical Model Calculated by CRAD[4] from ICSD data[10] with additional Si shell			Simplified Theoretical Model Average of Detailed Model			Fitted Model		
Coord. Number	Type	Expected Distance (Å)	Coord. Number	Type	Expected Distance / Å	Coord. Number	Distance / Å	Debye-Waller $2\sigma^2$ / Å^2
8	Silicon	2.333 2.335 2.338 2.338 2.377 2.386 2.428 2.436	8	Silicon	2.371	8	2.37 ± 0.02	0.018
1.98	Silicon	2.709	1.98	Silicon	2.709	1.44	2.69 ± 0.02	0.019
2	Iron	2.967	2	Iron	2.967	2	2.98 ± 0.02	0.016

Table 4.10: EXAFS fit of data shown in Figures 4.18

This fit supports the suggestion that the extra silicon in the ζ_β-$FeSi_{2.33}$ structure is located

in the (±0.25, ±0.25, ±0.25) positions. However, in this sample a considerable amount of this excess silicon had precipitated out of the structure. The refined value for the coordination number of the shell corresponding to the (±0.25, ±0.25, ±0.25) positions is 1.44, indicating that in this sample, 27% of the excess silicon had precipitated out of the ζ_β-$FeSi_2$ structure.

4.1.4.5 Silicon K-edge EXAFS

Silicon K-edge EXAFS data were recorded using the Total Electron Yield method (as described in Sections 2.3.5.2 (iii) and 3.2.4) at *ca.* 295 K from the sample of ζ_β-$FeSi_{2.33}$ prepared by heating ζ_α-ferrosilicon with a silicon content of 54.0 % as described in Section 3.1.1.2, using Station 3.4 at Daresbury Laboratory.

The data were initially fitted using the same model as was found in Section 4.1.3.4 for ζ_β-$FeSi_2$ as presented in Table 4.7. However, this model could not be refined to a satisfactory fit, indicating that the environment of silicon in ζ_β-$FeSi_{2.33}$ is significantly different from that in ζ_β-$FeSi_2$.

The second model used to fit the data was to modify the fit given in Table 4.7 with the addition of a shell of silicon atoms at a radius of 2.341 Å, which would be expected if the excess silicon was not incorporated into the ζ_β-ferrosilicon structure but formed a separate metallic silicon phase[13]. This also could not be refined to a satisfactory fit. The shape of the Fourier transform of the EXAFS data indicated that the model required the addition of a shell in the region of radii *ca.* 1.8-2.0 Å. The model for the structure of metastable ζ_β-$FeSi_{2.33}$ with the excess silicon located in the (±0.25, ±0.25, ±0.25) positions includes a shell of silicon atoms at a radius of 1.99 Å indicating that this model should be

included in the analysis.

The final model used to fit these data was constructed by combining the structures of ζ_β-ferrosilicon (with a variable amount of silicon in the (±0.25, ±0.25, ±0.25) positions), α-SiO_2 (quartz) to take into account any oxidised atoms on the surface of the sample, and metallic silicon to take into account any silicon which had precipitated out from the ζ_β-ferrosilicon structure. The theoretical parameters for the fit are given in Table 4.11. The variable x refers to the amount of silicon atoms which are located within the ζ_β structure in the (±0.25, ±0.25, ±0.25) positions. That is, x = 0.33 if all of the excess silicon is in the (±0.25, ±0.25, ±0.25) positions and x = 0 if all of the excess silicon has precipitated out of the structure. The quantity A refers to the proportion of the absorbing silicon which is not oxidised.

Structure	Coordination Number	Atom Type	Distances / Å	Average Distance / Å
ζ_β-ferrosilicon with additional silicon in the (±0.25, ±0.25, ±0.25) positions	$\frac{6}{2.33}xA$	Si	1.976 ; 2.013	1.995
	$\frac{8}{2.33}A$	Fe	2.333 ; 2.335 ; 2.338 ; 2.338 ; 2.377 ; 2.386 ; 2.428 ; 2.436	2.371
	$\frac{(10+6x)A}{2.33}$	Si	2.449 ; 2.499 ; 2.511 ; 2.513 ; 2.529 ; 2.562 ; 2.587 ; 2.604 ; 2.654	2.534 ± 0.009 *
	$\frac{6}{2.33}xA$	Fe	2.559 ; 2.784	2.709
SiO_2	$4-4A$	O	1.613	1.613
	$4-4A$	Si	3.065	3.065
Si (metallic)	$\frac{4(0.33-x)A}{2.33}$	Si	2.341	2.341

Table 4.11: Theoretical parameters for fitting EXAFS data shown in Figures 4.19, as calculated by CRAD[4] from ICSD data[10 11 13]

The variability in the expected distance of the 3rd shell characteristic of ζ_β-ferrosilicon (marked *) is because the contribution to this average distance of the shells at 2.604 and 2.654 Å will vary according to the value of x. The background-subtracted k^3 weighted Si K-edge EXAFS and Fourier transform data are shown in Figures 4.19a and 4.19b. The best fit to the EXAFS data is presented in Table 4.12.

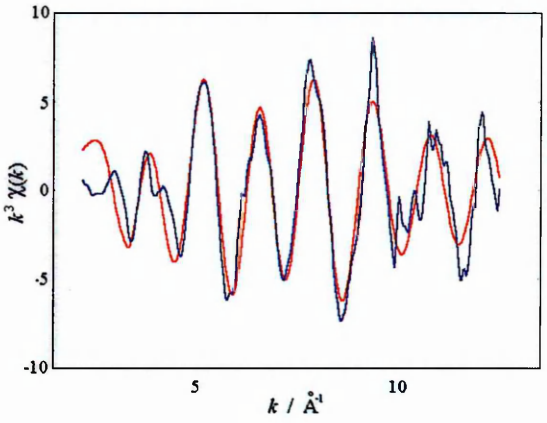

Figure 4.19a: k^3 weighted Si K-edge EXAFS of ζ_β-$FeSi_{2.33}$

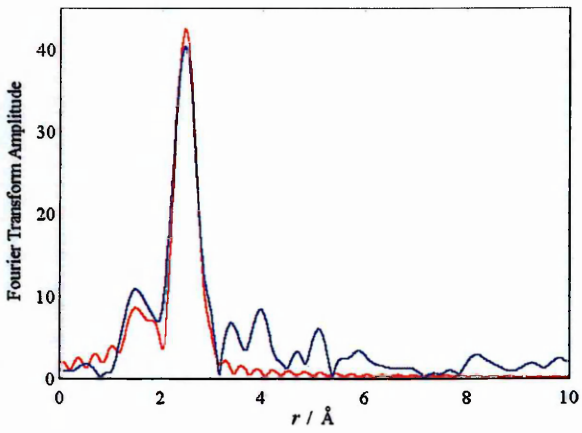

Figure 4.19b: Fourier transform of Si K-edge EXAFS of ζ_β-$FeSi_{2.33}$

The blue lines show the experimental data; the red lines show the fitted model.

Structure	Coordination Number	Atom Type	Expected Distance / Å	Fitted Distance / Å	Debye-Waller $2\sigma^2$ / Å^2
ζ_β-ferrosilicon with additional silicon in the (±0.25, ±0.25, ±0.25) positions	0.18 ± 0.004	Si	1.995	1.92 ± 0.04	0.012
	2.95 ± 0.06	Fe	2.371	2.40 ± 0.04	0.015
	3.87 ± 0.08	Si	2.534	2.51 ± 0.04	0.015
	0.18 ± 0.004	Fe	2.709	2.61 ± 0.04	0.012
SiO_2	0.57 ± 0.07	O	1.613	1.61 ± 0.04	0.009
	0.57 ± 0.07	Si	3.065	3.01 ± 0.04	0.009
Si (metallic)	0.36 ± 0.01	Si	2.341	2.38 ± 0.04	0.008

Table 4.12: EXAFS fit of data shown in Figures 4.19

This fit carries a fit index of 0.00111 and an R-factor of 46.67 %. The fit quality is low

because rules were used to restrict the refinement in this model, rather than allowing free refinement which is unfeasible with such a large number of parameters. This fit indicates that 14.2 % ± 1.7 % of the absorbing silicon is in an oxidised environment, which compares favourably with the value of 17.3 % obtained from the analysis of silicon K-edge EXAFS of ζ_{β}-$FeSi_{2.33}$ presented in Section 4.1.3.4. The value of x is 0.083 ± 0.0003 which means that 74.8 % of the excess silicon in the metastable ζ_{β}-$FeSi_{2.33}$ has precipitated out to form a metallic silicon phase representing 9.1 % of the total absorbing silicon in the sample, the remaining 25.2 % ± 1.0 % of the excess silicon is located in the (±0.25, ±0.25, ±0.25) positions in the metastable ζ_{β}-ferrosilicon structure.

This fit supports the suggestion that the additional silicon in metastable ζ_{β}-$FeSi_{2.33}$ is located in the (±0.25, ±0.25, ±0.25) positions and that this silicon then precipitates out to form a metallic silicon phase such as that observed by van den Boomgaard[12]. It would be worthwhile to repeat this measurement using a sample prepared and kept in an inert atmosphere to remove the effect of surface oxidation. It would also be interesting to observe the precipitation of the silicon from the metastable ζ_{β}-$FeSi_{2.33}$ by time-resolved silicon K-edge EXAFS.

4.1.4.6 Mössbauer spectroscopy

^{57}Fe Mössbauer spectra were recorded, using the apparatus described in Section 2.5.6, from ζ_{β}-$FeSi_{2.33}$ prepared by heating ferrosilicon with a silicon content of 54.0 % by weight as described in Section 3.1.1.2 (a) at *ca.* 295 K and (b) at 855 K. The spectrum recorded at 855 K has the most relevance to this work and is shown in Figure 4.20.

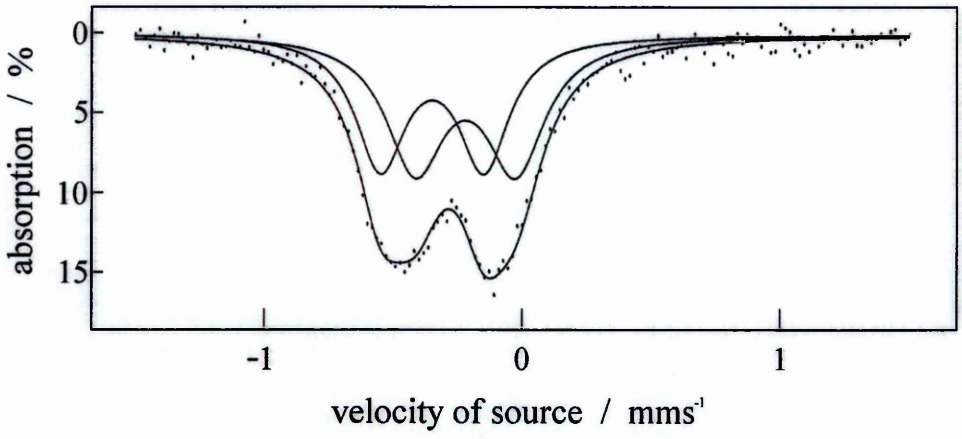

Figure 4.20: ^{57}Fe Mössbauer spectrum of ζ_β-$FeSi_{2.33}$ recorded at 855 K

The spectra were each fitted to two doublets, the values for the isomer shifts and quadrupole splittings of the doublets are shown in Table 4.13. Uncertainties are ± 2 %.

		δ / mms^{-1}	Δ / mms^{-1}	Γ / mms^{-1}
ca. 295 K	Doublet 1	0.15	0.42	0.28
	Doublet 2	0.02	0.44	0.27
855 K	Doublet 1	-0.23	0.39	0.27
	Doublet 2	-0.35	0.40	0.25

Table 4.13: ^{57}Fe Mössbauer parameters for ζ_β-$FeSi_{2.33}$

These values are consistent with those reported in the literature[5] [6]. Each doublet corresponds to one of the two iron sites in the structure of ζ_β-$FeSi_2$ as described in Section 1.2.1.3. The reduction in isomer shifts in the spectrum recorded at 855 K is indicative of the elevated energy state which would be expected at high temperature.

4.1.5 Structure of ζ_β-$FeSi_{2.33}$ doped with 1 % aluminium

4.1.5.1 Flat-plate X-ray powder diffraction

The flat-plate X-ray powder diffraction pattern, recorded at *ca.* 295 K using Cu-K_α radiation (λ = 1.54 Å), from Al-doped ζ_β-$FeSi_{2.33}$ prepared by heating ferrosilicon with a silicon content of 53.4 % and an aluminium content of 1 % by weight as described in

Section 3.1.1.2 is shown in Figure 4.21.

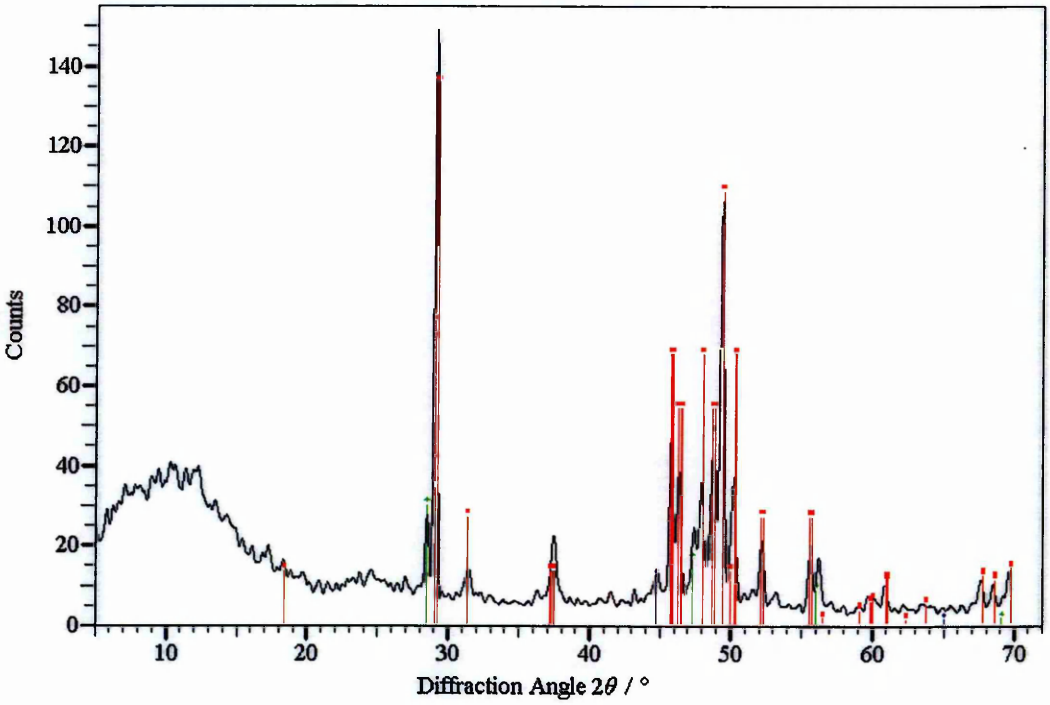

Figure 4.21: X-ray powder diffraction pattern recorded from 1 % aluminium-doped ζ_{β}-$FeSi_{2.33}$

The red lines indicate the positions of the peaks characteristic of ζ_{β}-$FeSi_2$[9]. The green lines indicate the positions of the peaks characteristic of metallic silicon[7]. The blue lines indicate the positions of the peaks characteristic of metallic iron[14]. There is no evidence of a separate aluminium-containing phase. The apparent presence of metallic iron and silicon is unexpected, but may indicate that the presence of aluminium has affected the stability of the ferrosilicon.

4.1.5.2 Low-temperature iron K-edge EXAFS

The background subtracted k^3 weighted EXAFS and Fourier transform data recorded on Station 8.1 at Daresbury Laboratory from Al-doped ζ_{β}-$FeSi_{2.33}$ prepared by heating ferrosilicon with a silicon content of 53.4 % and an aluminium content of 1 % by weight as described in Section 3.1.1.2 and cooled to *ca.* 77 K using liquid nitrogen are shown in Figures 4.22a and 4.22b.

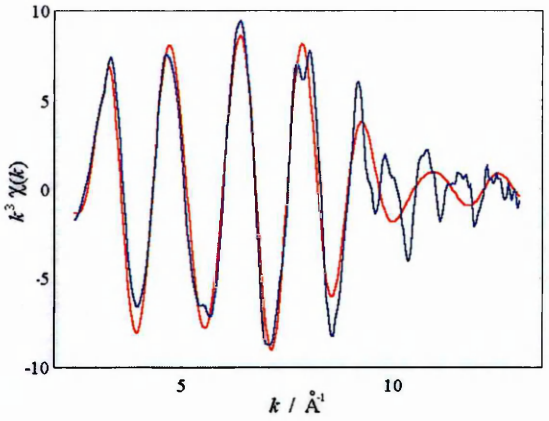

Figure 4.22a: k^3 weighted Fe K-edge EXAFS of 1 % Al-doped ζ_β-$FeSi_{2.33}$

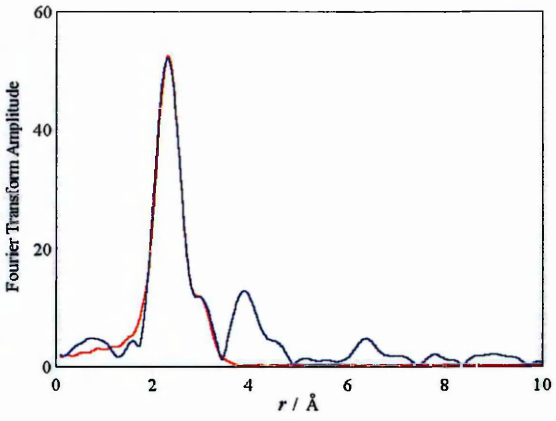

Figure 4.22b: Fourier transform of Fe K-edge EXAFS of sample of 1 % Al-doped ζ_β-$FeSi_{2.33}$

The blue lines show the experimental data; the red lines show the fitted model.

These data were initially fitted using the same model and parameters as described in Section 4.1.4.4 Table 4.9, which was calculated for undoped ζ_β-$FeSi_{2.33}$. Refinement of this fit resulted in the parameters detailed in Table 4.14.

Detailed Theoretical Model Calculated by CRAD[4] from ICSD data[10] with additional Si shell as described above			Simplified Theoretical Model Average of Detailed Theoretical Model			Fitted Model	
Coord. Number	Type	Expected Distance / Å	Coord. Number	Type	Expected Distance / Å	Fitted Distance / Å	Debye-Waller $2\sigma^2$ / Å^2
8	Silicon	2.333 ; 2.335 2.338 2.338 2.377 ; 2.386 2.428 ; 2.436	8	Silicon	2.371	2.37 ± 0.02	0.021
1.98	Silicon	2.709	1.98	Silicon	2.709	2.78 ± 0.02	0.022
2	Iron	2.967	2	Iron	2.967	2.95 ± 0.02	0.022

Table 4.14: EXAFS fit of data shown in Figures 4.22

This fit has a fit index of 0.00056 and an *R*-factor of 29.98 %. The distances for the second and third shells in this fit diverge from the expected values, and the Debye-Waller values are higher than are typical for a cooled sample. This behaviour could be attributable to disorder brought about by the inclusion of aluminium. However, these data could not be fitted with the inclusion of aluminium atoms with any confidence due to the low concentration of aluminium.

A comparison plot showing the experimental data recorded at *ca.* 77 K from undoped ζ_{β}-$FeSi_{2.33}$ as well as that recorded at *ca.* 77 K from ζ_{β}-$FeSi_{2.33}$ doped with 1% aluminium is shown in Figures 4.23a and 4.23b.

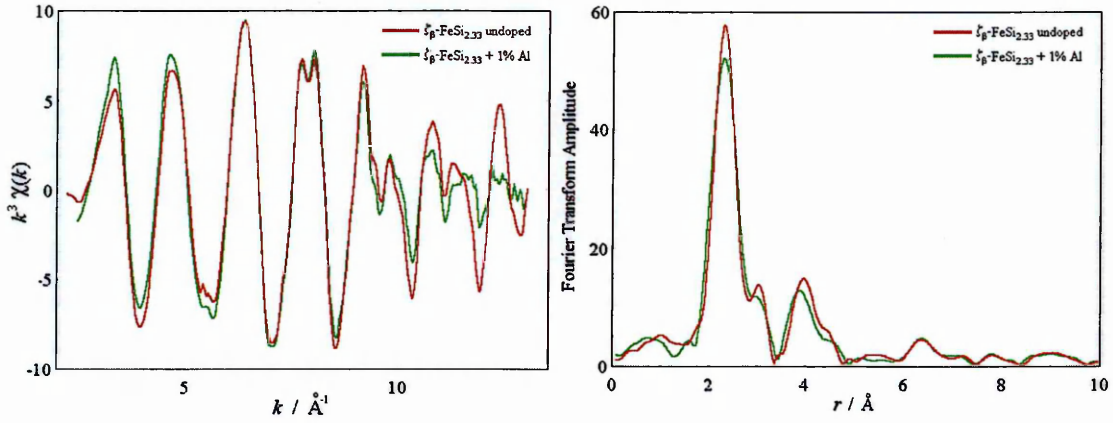

Figures 4.23: Comparisons of (a) k^3 weighted EXAFS and (b) Fourier transforms of EXAFS, both of ζ_{β}-ferrosilicon with and without 1 % aluminium doping recorded at *ca.*77 K

The Fourier transform for the Al-doped ζ_{β}-$FeSi_{2.33}$ shows a smaller height of the first peak and the second peak is less distinct than seen in the Fourier transform for the undoped ζ_{β}-$FeSi_{2.33}$. This indicates that there is greater structural disorder in the aluminium-doped sample. However, as similarly discussed in Section 4.1.2.3 relating to the Fe K-edge EXAFS recorded from alumnium-doped ζ_{α}-ferrosilicon, the differences are not sufficiently significant to provide evidence for a firm conclusion. Therefore these data cannot be used to discern with certainty the effect of the presence of aluminium on the structure of ζ_{β}-$FeSi_{2.33}$.

4.1.6 Summary of structural characterisation sections

The results presented in Section 4.1 have shown that the ζ_{α}- and ζ_{β}-ferrosilicon samples used for this work conform to the crystal structures reported in the literature[3] [10]. It appears from a search

of the literature that results of the examination of the structure of ζ_α- and ζ_β-ferrosilicon by EXAFS recorded from a powder sample have not previously been published.

The in-depth investigations by XRD and EXAFS of the position of the excess silicon in metastable ζ_β-$FeSi_{2.33}$ are new results. This work shows evidence that silicon atoms temporarily locate in the large spaces in the unit cell at the eight (±0.25, ±0.25, ±0.25) positions before precipitating out to form a separate silicon phase.

The conclusions which can be drawn from this work are discussed further in Section 6.1.

4.2 High-temperature time-resolved combined X-ray powder diffraction and iron K-edge EXAFS.

4.2.1 Measurement of the extent of a phase transition

In Sections 4.2.2 and 4.2.3, combined X-ray powder diffraction and Fe K-edge EXAFS data recorded at high temperature are presented. These were used to observe the progress of the phase transition of ζ_α- to ζ_β-ferrosilicon, and therefore the accuracy of the techniques in measuring the composition of a mixed-phase sample must be established. In this section, the analysis technique is presented in detail using a mixed-phase sample of known composition.

4.2.1.1 Investigation of mixed 50 % ζ_α- and 50 % ζ_β-ferrosilicon

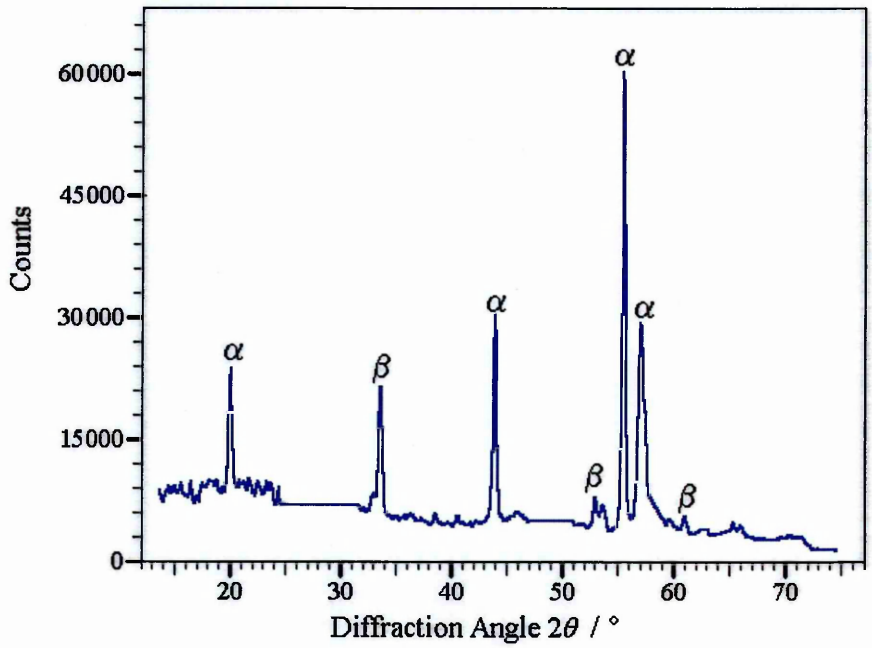

Figure 4.24: XRD pattern recorded from sample of 50 % ζ_α- and 50 %ζ_β-ferrosilicon

The X-ray powder diffraction pattern recorded on Station 9.3 at Daresbury Laboratory at *ca.* 295 K using radiation of wavelength 1.779 Å from a pellet containing boron nitride and a 50:50 mixture of ζ_α- and ζ_β-ferrosilicon prepared as described in Section 3.1.1.3 is shown in Figure 4.24. Peaks characteristic of ζ_α-ferrosilicon are marked with an α; peaks characteristic of ζ_β-ferrosilicon are marked with a β.

As discussed in Section 2.3.4.4, in EXAFS analysis it is important to start with a reasonably accurate theoretic model of the structure. The X-ray diffraction data recorded in these experiments are of insufficient quality to allow for accurate quantitative analysis of the amounts of the two phases present. However, the relative areas of X-ray diffraction peaks characteristic of ζ_α- and ζ_β-ferrosilicon may be used as a rough estimate to provide a starting point for the EXAFS analysis.

Figure 4.24 shows that at room temperature and when the fraction of ζ_β-ferrosilicon present is known to be 0.5, the ratio of the area of the ζ_α-ferrosilicon peak at $2\theta = 44°$ (referred to below as A_α) to the area of the major ζ_β-ferrosilicon peak at $2\theta = 34°$ (referred to below as A_β) is approximately 1.3, where area is calculated by maximum peak height multiplied by the full width of the peak at half the maximum. Therefore in the analysis of EXAFS data recorded at high temperature presented in Sections 4.2.2 and 4.2.3 an approximate value for γ, the fraction of ζ_α-ferrosilicon transformed to ζ_β-ferrosilicon was estimated as

$$\gamma_{\text{estimated}} = \frac{A_\beta}{A_\alpha / 1.3 + A_\beta}$$

from the X-ray diffraction patterns recorded immediately before and after the recording of each EXAFS spectrum. The average of these two values was used as a starting point for the analysis of the EXAFS data. Occasionally the peaks identified above were not amenable to analysis by this method. In these case either different peaks characteristic of the two phases were used, or a single peak exhibiting a clear variance with time over the course of the experiment was chosen, and an estimated value of γ was found by comparing the area under that peak with the area at the beginning or the end of the

experiment.

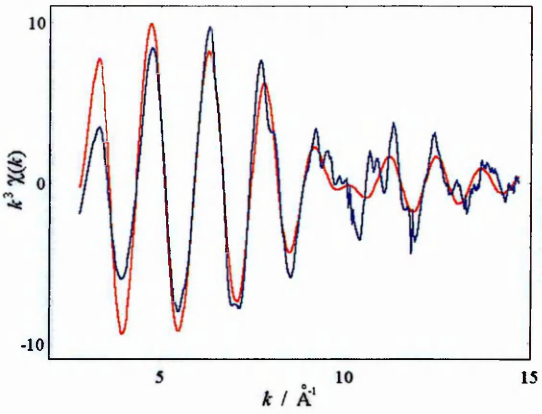

Figure 4.25a: k^3 weighted Fe K-edge EXAFS of 50 % ζ_α- and 50 % ζ_β-ferrosilicon

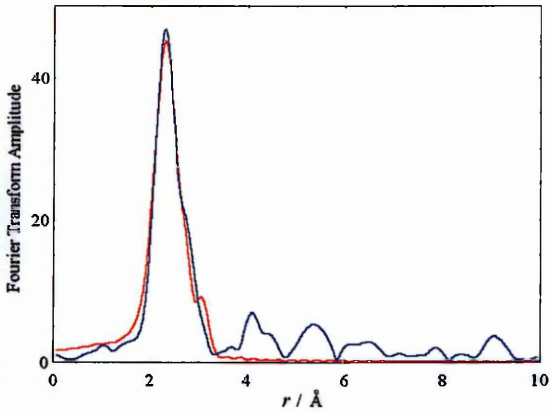

Figure 4.25b: Fourier transform of Fe K-edge EXAFS of 50 % ζ_α- and 50 % ζ_β-ferrosilicon

The blue lines show the experimental data; the red lines show the fitted model.

The background-subtracted k^3 weighted Fe K-edge EXAFS and Fourier transform data recorded at *ca.* 295 K on Station 9.3 at Daresbury Laboratory from a 50:50 mixture of ζ_α- and ζ_β-ferrosilicon prepared as described in Section 3.1.1.3 are shown in Figures 4.25a and 4.25b.

Detailed Theoretical Model Calculated by CRAD[4] from ICSD data[3] [10]			Simplified Theoretical Model Average of Detailed Theoretical Model			Fitted Model	
Coord. Number	Atom Type	Expected Distance / Å	Coord. Number	Atom Type	Expected Distance / Å	Fitted Distance / Å	Debye-Waller $2\sigma^2$ / Å^2
4	Silicon	2.333 ; 2.335 2.338 ; 2.338 2.377 ; 2.386 2.428 ; 2.436	8	Silicon	2.378	2.37 ± 0.02	0.023
4	Silicon	2.384					
1.7	Iron	2.690	1.7	Iron	2.690	2.68 ± 0.02	0.026
1	Iron	2.967	1	Iron	2.967	2.97 ± 0.02	0.009

Table 4.15: Best fit of the Fe K-edge EXAFS of mixed-phase 50 % ζ_α- and 50 % ζ_β-ferrosilicon at *ca.* 295 K

A model to fit these data was constructed using the shells characteristic of ζ_α-ferrosilicon

with a site occupancy level of 50 %, and also the shells characteristic of ζ_β-ferrosilicon with a site occupancy level of 50 %. Table 4.15 shows this model, a simplified version in which nearby shells are considered as a single shell, and the fitted model.

This fit gives a fit index of 0.000516 and an *R*-factor of 39.6 %. The *R*-factor is high due to the approximation of a single shell of silicon instead of fitting individual shells at slightly separated distances. However, as the data quality of EXAFS spectra recorded at high temperatures with short recording times is low, such a detailed fit would introduce an unreasonable number of degrees of freedom into the refinement. For the same reason, no shell indicative of the presence of silicon at 2.709 Å, as discussed in Section 4.1.4, is included in the fit. The effect of these simplifications is to reduce the accuracy of the fitting of the silicon shells. However, this is not significant for the purposes of the analysis following the progress of the phase transition from ζ_α- to ζ_β-ferrosilicon, as the iron shells have a much greater impact on the EXAFS fit and it is these which are used to measure the extent of the phase transition.

The contour plot function of Excurv97, which is used in Sections 4.2.2 and 4.2.3 to evaluate the progress of the phase transition from ζ_α- to ζ_β-ferrosilicon, was applied to this fit to investigate the accuracy of the contour plot function for the purpose of phase analysis.

The contour plot function takes two variables in the fit (in this case the coordination numbers of the ζ_α-ferrosilicon shell at $d = 2.69$ Å and the ζ_β-ferrosilicon shell at $d = 2.97$ Å) and calculates the fit-indices for a large number of possible combinations. The function then produces a contour plot indicating at which combination of the two variables the best fit-index may be found. The contour plot thus derived for the mixed-phase sample is shown

in Figure 4.26.

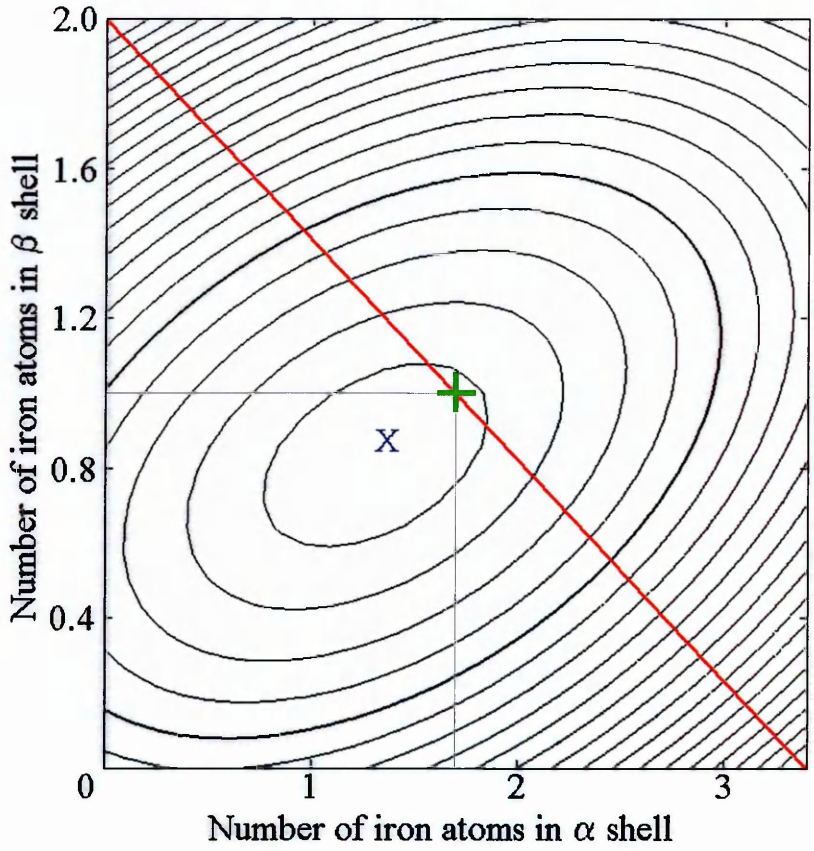

Figure 4.26: Fit index contour plot of the fit of the Fe K-edge EXAFS data recorded from mixed-phase 50 % ζ_α- and 50 % ζ_β-ferrosilicon at *ca.* 295 K

The contour plot shown in Figure 4.26 indicates that the best fit, indicated by the blue X, is found when the coordination number of the shell characteristic of the ζ_α phase at 2.69 Å is 1.36 and the coordination number of the shell characteristic of the ζ_β phase at 2.97 Å is 0.88. The green cross marks the known actual composition of the mixed phase sample.

4.2.1.2 Technique for analysis of EXAFS recorded at high temperature

The contour plot function described above was used in the interpretation of the EXAFS data recorded at high temperature presented in Sections 4.2.2 and 4.2.3. X-ray powder diffraction data were used to provide a starting point for the EXAFS fitting process by comparing the areas under peaks characteristic of ζ_α- and ζ_β-ferrosilicon, and then a contour

plot was generated. To simplify the analysis and allow useful information to be extracted from the data, it is assumed that the sum of the fraction of ζ_α-ferrosilicon and the fraction of ζ_β-ferrosilicon is 1, thus the point on the contour plot nearest to the line where

$$\frac{\text{Coordination Number of } \alpha\text{-ferrosilicon shell at } d = 2.69\text{Å}}{3.4} + \frac{\text{Coordination Number of } \beta\text{-ferrosilicon shell at } d = 2.97\text{Å}}{2} = 1$$

is chosen as the best fit point – this is the diagonal line marked in red. From this point a value γ, which is the fraction of ζ_α-ferrosilicon transformed to ζ_β-ferrosilicon, is calculated. The values of the coordination numbers are taken from the point on the red diagonal line closest to the blue X.

$$\gamma = \frac{\text{Coordination Number of } \beta\text{-ferrosilicon shell at } d = 2.97\text{Å}}{2} \quad \text{or, coming to the same result,} \quad \gamma = 1 - \frac{\text{Coordination Number of } \alpha\text{-ferrosilicon shell at } d = 2.69\text{Å}}{3.4}$$

The assumption above would require analysis beyond the scope of this work to verify, and it could be the case that a proportion of the material may be in neither the ζ_α- nor the ζ_β-ferrosilicon structure. However, (a) it is necessary to make some assumption about the relationship between the coordination numbers in order to translate the EXAFS data into a measurement of the extent of the phase transition and (b) even if the assumption is not valid, the value of γ thus calculated will still be a good measure of the extent of the phase transition.

In each contour plot measurement presented in Sections 4.2.2 and 4.2.3, the uncertainty in the value of γ is operationally estimated as half of the average radius of the first circle in the contour plot.

4.2.1.3 Comment on the fitting technique

The technique described above was novel at the time that these experiments were carried

out. The contour plot function of the Excurv fitting programme has been routinely used to investigate relationships between fitting parameters across a wide range of materials[15 16], but a search of the literature has not revealed evidence of its use in time-resolved measurements other than in reports relating to the present work[17 18].

There are limitations in the range of systems which can be examined using this technique. The ζ_{α}- and ζ_{β}-ferrosilicon phase transition is suitable because the simple EXAFS fits of the two phases differ in the radial positions and occupancies of a single shell, thus a simple refinement between the shells characteristic of the two phases is possible.

Since the time when these experiments were performed, further developments in the Excurv software have automated this process in the "cluster" function whereby structures of two or more phases may be defined, and a refinement process used to calculate the relative abundances of these phases. The cluster method is more flexible as phase transitions in which the structures have significant differences, and are thus unsuitable for the contour plot method, may be examined. However, it has disadvantages in the context of data which has been recorded at high temperature with short recording times. The use of two models which are refined with respect to one another almost doubles the number of parameters used. Unless data quality is high, the number of parameters in an EXAFS fit should be kept as low as possible, because with a higher number of parameters a much wider range of fit parameters can be refined to seem acceptable, thus rendering conclusions less meaningful. Therefore under these circumstances, results obtained by the contour plot method are likely to be more reliable.

4.2.2 High-temperature time-resolved combined X-ray powder diffraction and Fe K-edge EXAFS recorded from the undoped phase transition of ζ_α- to ζ_β-ferrosilicon.

4.2.2.1 Experiment at 855 K

A three-dimensional plot of the X-ray powder diffraction patterns collected using λ = 1.779 Å during the heating at 855 K of undoped ζ_α-ferrosilicon, prepared as described in Sections 3.1.1.1(ii) and Section 3.3.1, is shown in Figure 4.27.

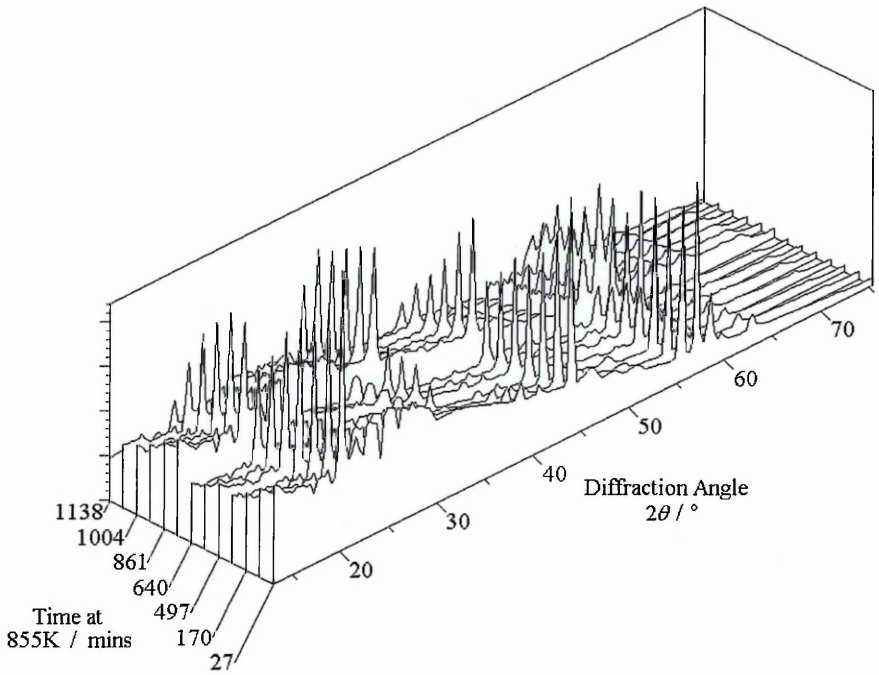

Figure 4.27: 3D view of the XRD patterns recorded during the phase transition of ζ_α- to ζ_β-ferrosilicon at 855 K

There is a discontinuity in the patterns after *ca.* 700 minutes at 855 K, which is due to a refill of the synchrotron ring. The peak characteristic of ζ_α-ferrosilicon at 2θ = 44° decreases steadily up to this point, but after the refill the intensity appears increased, despite the data being normalised against beam intensity. There is a similar discontinuity in the increasing intensity of the peak characteristic of ζ_β-$FeSi_2$ at 2θ = 34°. These differences may be due to the beam passing through two slightly different parts of a non-uniform sample pellet before and after the refill. The last pattern indicates that the phase

transition was not complete by the end of the experiment, as peaks characteristic of ζ_α-ferrosilicon are still visible.

Figure 4.28 shows a three-dimensional plot of the Fourier transforms of the Fe K-edge EXAFS recorded during the same experiment.

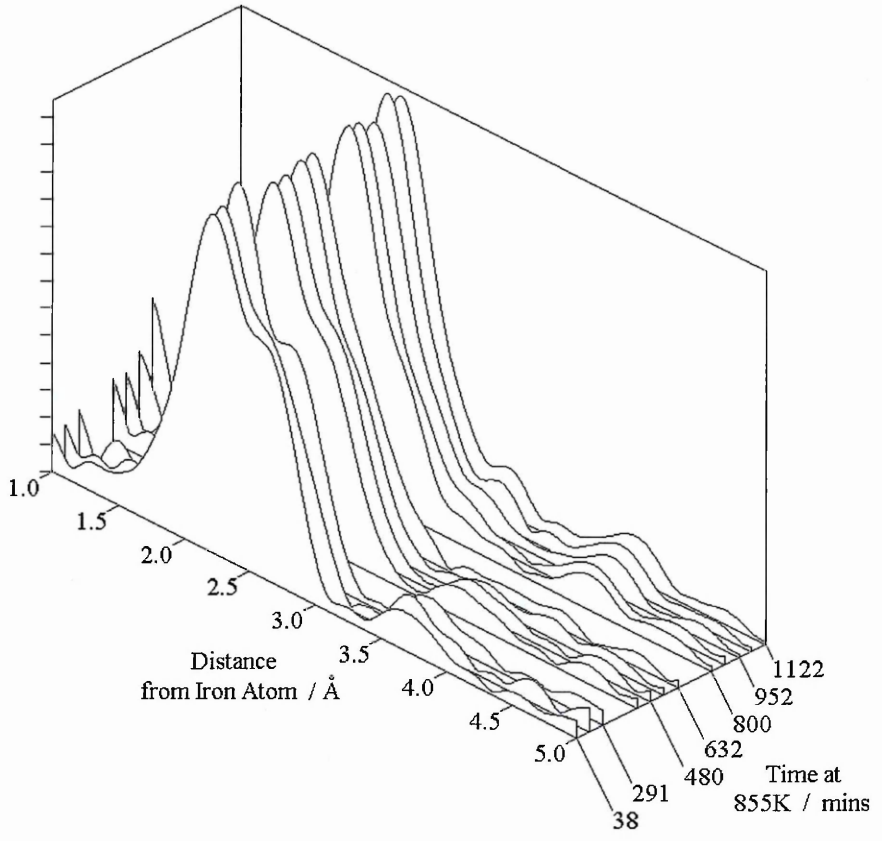

Figure 4.28: 3D view of the Fourier transforms of Fe K-edge EXAFS data recorded during the phase transition of ζ_α- to ζ_β-ferrosilicon at 855 K

The shoulder to the right of the first shell peak, which is indicative of the second shell characteristic of ζ_α-ferrosilicon at d = 2.69 Å (see Table 4.1), is seen to decrease with time, while the separate peak at about 3 Å characteristic of ζ_β-ferrosilicon (see Table 4.4) becomes distinct in the Fourier transform of the EXAFS spectrum recorded at 952 minutes and is seen to increase in intensity with increasing time.

Each EXAFS file was analysed using the method demonstrated in Section 4.2.1. The map contour plots for each EXAFS file are shown in Figures 4.29a-l.

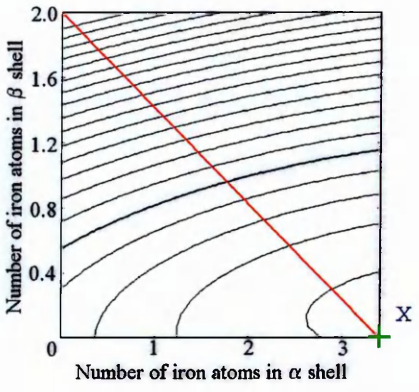

(a) Time = 38 mins ; $\gamma = 0.00$

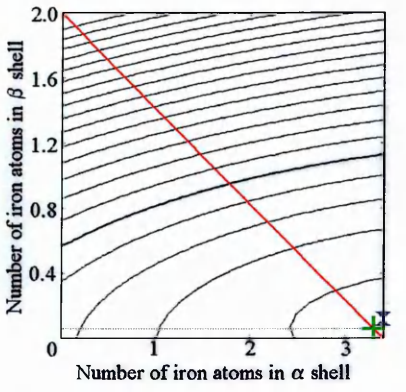

(b) Time = 172 mins ; $\gamma = 0.03 \pm 0.05$

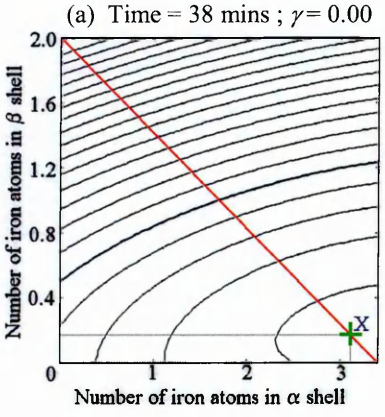

(c) Time = 291 mins ; $\gamma = 0.09 \pm 0.05$

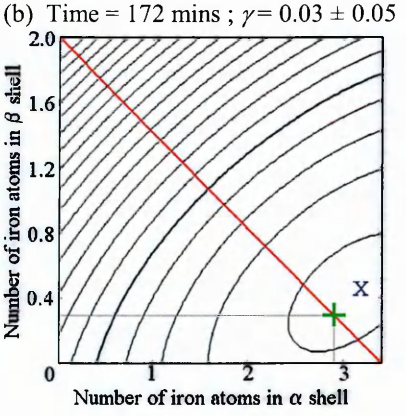

(d) Time = 380 mins ; $\gamma = 0.15 \pm 0.06$

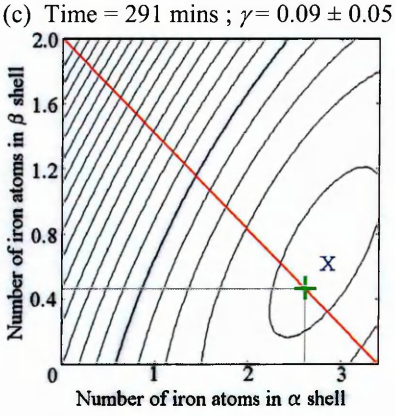

(e) Time = 480 mins ; $\gamma = 0.23 \pm 0.06$

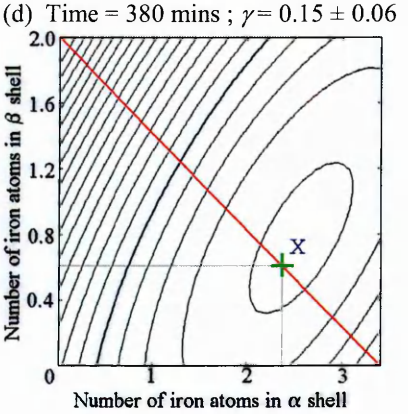

(f) Time = 561 mins ; $\gamma = 0.30 \pm 0.05$

Figures 4.29a-f: Map contour plots relating to Fe K-edge EXAFS data recorded during the phase transition of ζ_α- to ζ_β-ferrosilicon at 855 K

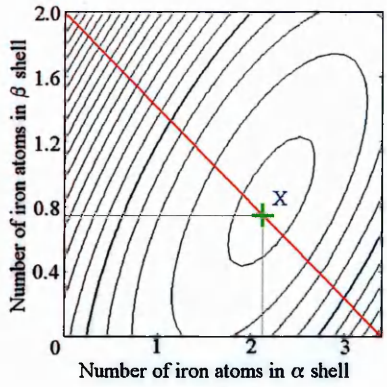

(g) Time = 632 mins ; $\gamma = 0.37 \pm 0.05$

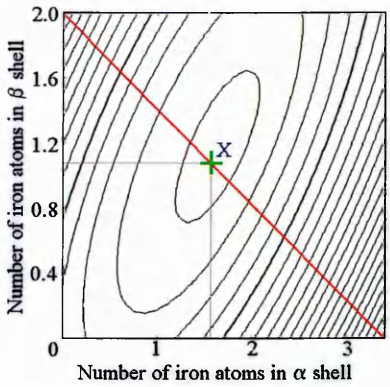

(h) Time = 800 mins ; $\gamma = 0.54 \pm 0.04$

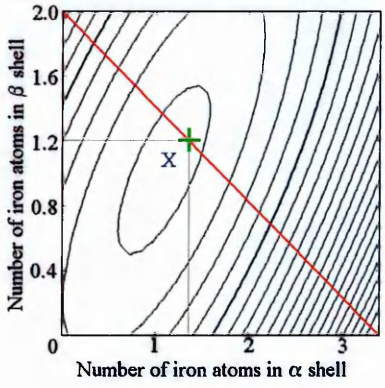

(i) Time = 872 mins ; $\gamma = 0.60 \pm 0.05$

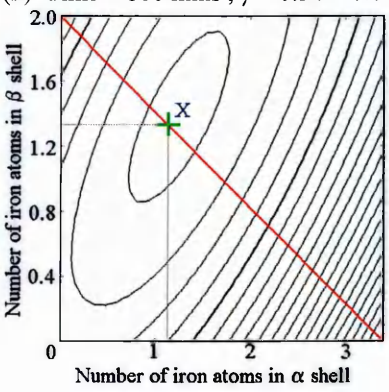

(j) Time = 952 mins ; $\gamma = 0.67 \pm 0.05$

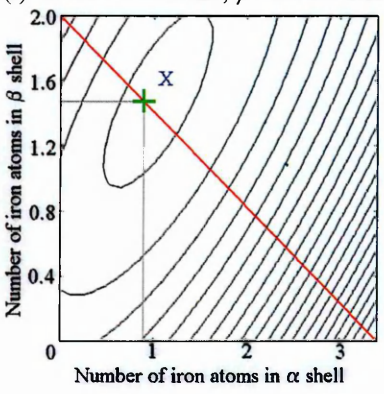

(k) Time = 1039 mins ; $\gamma = 0.74 \pm 0.06$

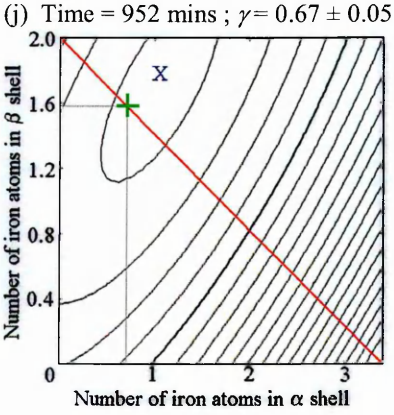

(l) Time = 1122 mins ; $\gamma = 0.79 \pm 0.06$

Figures 4.29g-l: Map contour plots relating to Fe K-edge EXAFS data recorded during the phase transition of ζ_α- to ζ_β-ferrosilicon at 855 K

The central contour indicating the likely composition of the sample can be seen to move from the bottom-right-hand corner (indicating 100 % ζ_α-ferrosilicon) towards the top-left corner (indicating 100 % ζ_β-ferrosilicon). The last contour plot indicates that the sample has not yet completely converted to ζ_β-ferrosilicon, which is in agreement with the data recorded by X-ray powder diffraction.

The values calculated for γ, the fraction of ζ_α-ferrosilicon converted to ζ_β-ferrosilicon, using the method described in Section 4.2.1.2 are plotted against time in Figure 4.30.

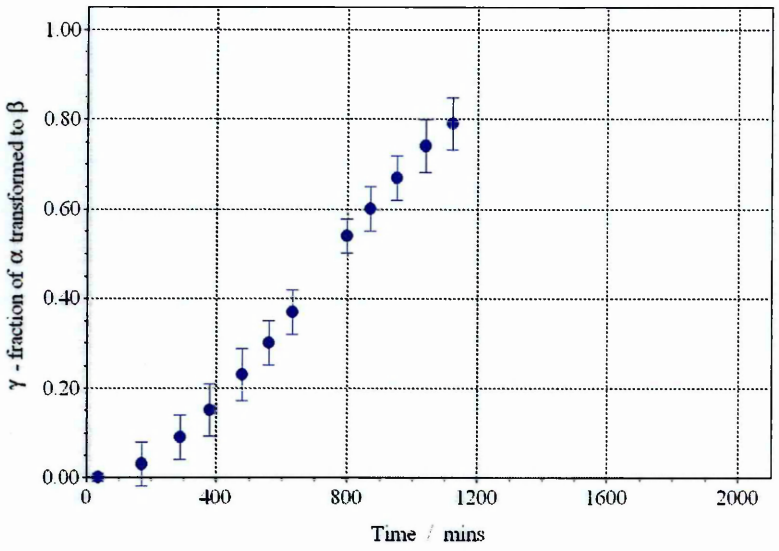

Figure 4.30: Fraction of ζ_α-ferrosilicon converted to ζ_β-ferrosilicon plotted against time for the experiment at 855 K

The analysis of these data is discussed in Section 4.2.4.

4.2.2.2 Experiment at 873 K

A three-dimensional plot of the X-ray powder diffraction patterns collected using λ = 1.779 Å during the heating at 873 K of undoped ζ_α-ferrosilicon, prepared as described in Sections 3.1.1.1(ii) and Section 3.3.1, is shown in Figure 4.31.

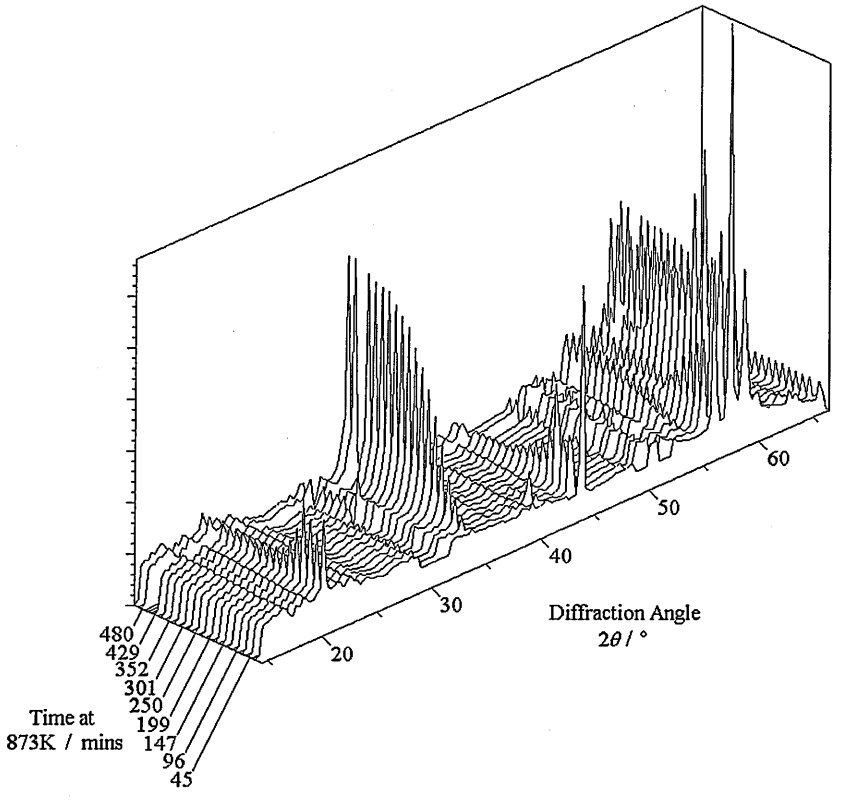

Figure 4.31: 3D view of the XRD patterns recorded during the phase transition of ζ_α- to ζ_β-ferrosilicon at 873 K

The peak characteristic of ζ_α-ferrosilicon at $2\theta = 44°$ is seen to decrease sharply in the first 5 patterns, and then decrease more slowly until the 11th pattern (time = 300 minutes) after which the intensity remains constant, as there is a minor peak characteristic of ζ_β-ferrosilicon at $2\theta = 43°$. Peaks characteristic of ζ_β-ferrosilicon are visible in the 2nd pattern (time = 45 minutes) and increase until the 11th pattern, after which they remain constant in intensity.

Figure 4.32 shows a three-dimensional plot of the Fourier transforms of the Fe K-edge EXAFS recorded during the same experiment. The shoulder to the right of the first shell peak, which is indicative of the second shell characteristic of ζ_α-ferrosilicon at d = 2.69 Å, decreases with time and is indistinct after 176 minutes, while the separate peak at about 3 Å characteristic of ζ_β-ferrosilicon becomes distinct at time = 227 minutes, and is seen to increase in intensity with increasing time.

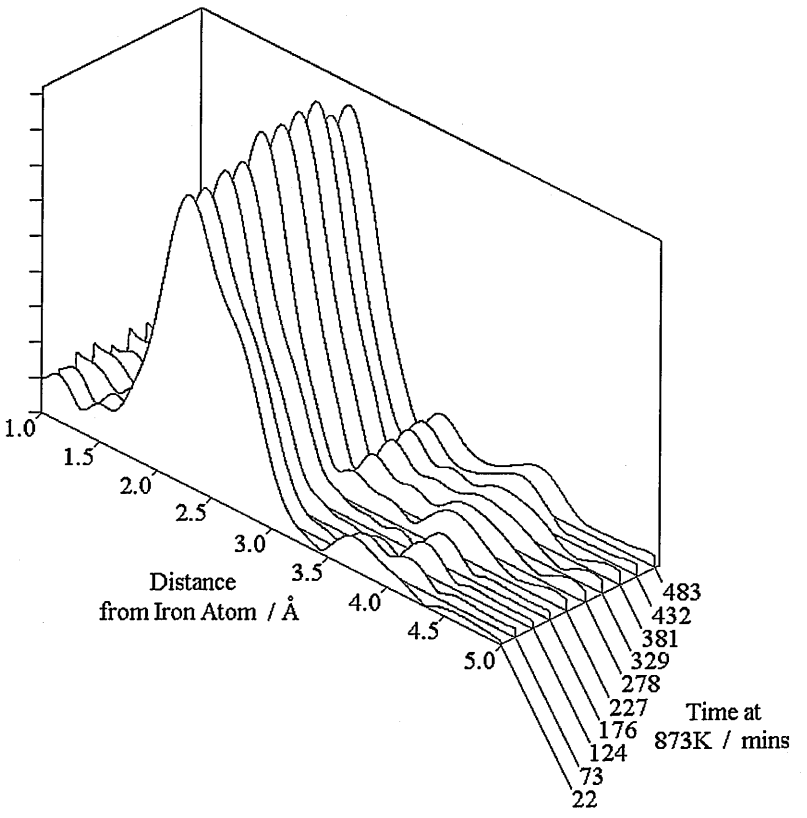

Figure 4.32: 3D view of the Fourier transforms of Fe K-edge EXAFS data recorded during the phase transition of ζ_α- to ζ_β-ferrosilicon at 873 K

Each EXAFS file was analysed using the method demonstrated in Section 4.2.1. The map contour plots for each EXAFS file are shown in Figures 4.33a-h.

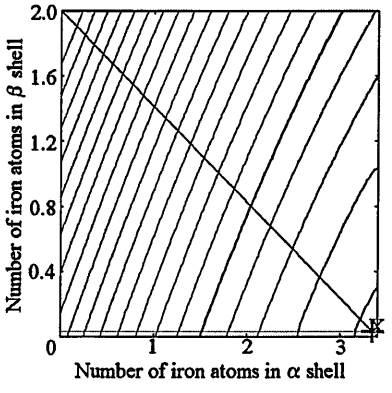

(a) Time = 22 mins ; $\gamma = 0.00 \pm 0.03$

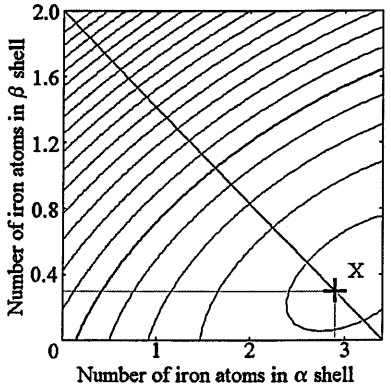

(b) Time = 73 mins ; $\gamma = 0.15 \pm 0.07$

Figures 4.33a-b: Map contour plots relating to Fe K-edge EXAFS data recorded during the phase transition of ζ_α- to ζ_β-ferrosilicon at 873 K

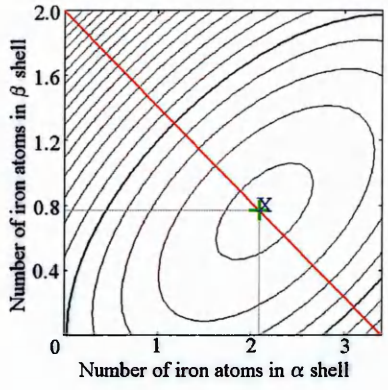

(c) Time = 124 mins ; $\gamma = 0.39 \pm 0.05$

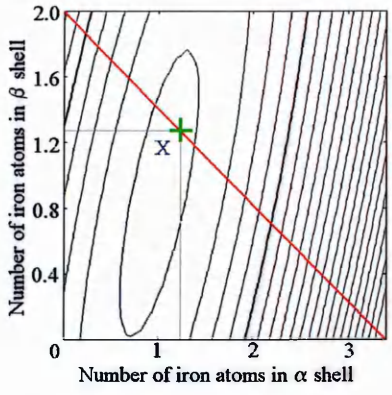

(d) Time = 176 mins ; $\gamma = 0.63 \pm 0.03$

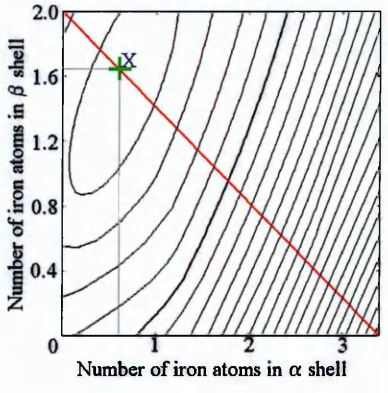

(e) Time = 227 mins ; $\gamma = 0.82 \pm 0.05$

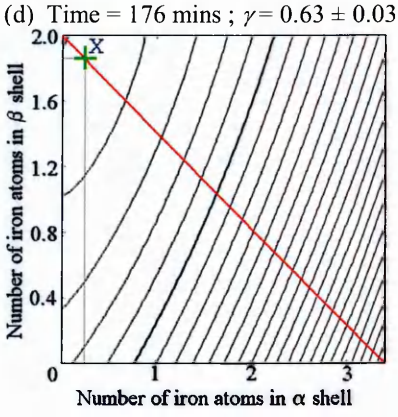

(f) Time = 278 mins ; $\gamma = 0.93 \pm 0.06$

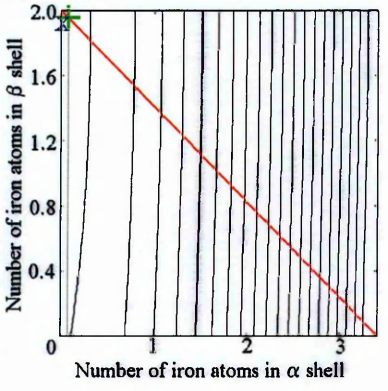

(g) Time = 329 mins ; $\gamma = 0.98 \pm 0.04$

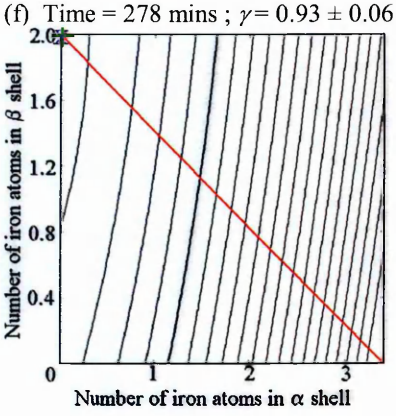

(h) Time = 381 mins ; $\gamma = 0.99 \pm 0.04$

Figures 4.33c-h: Map contour plots relating to Fe K-edge EXAFS data recorded during the phase transition of ζ_α- to ζ_β-ferrosilicon at 873 K

The long vertical contours in the plots shown in Figures 4.33g and 4.33h show that the corresponding EXAFS data indicate very strongly that the proportion of ζ_α-ferrosilicon is low, but that there is more uncertainty over the exact quantity of ζ_β-ferrosilicon present. The values for γ, the fraction of ζ_α-ferrosilicon converted to ζ_β-ferrosilicon, are therefore calculated using the coordination numbers for the ζ_α-ferrosilicon shell.

The values calculated for γ using the method described in Section 4.2.1.2 are plotted against time in Figure 4.34.

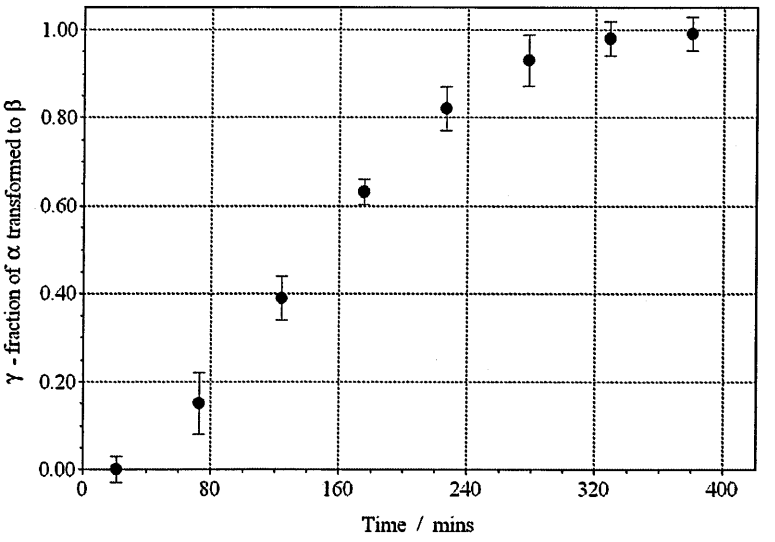

Figure 4.34: Fraction of ζ_α-ferrosilicon converted to ζ_β-ferrosilicon plotted against time for the experiment at 873 K

The analysis of these data is discussed in Section 4.2.4.

4.2.2.3 Experiment at 898 K

A three-dimensional plot of the X-ray powder diffraction patterns collected using λ = 1.779 Å during the heating at 898 K of undoped ζ_α-ferrosilicon, prepared as described in Sections 3.1.1.1(ii) and Section 3.3.1, is shown in Figure 4.35.

Due to the higher temperature (and thus faster progression of the phase transition) a shorter recording time was used for the collection of each pattern. This has caused a reduction in the intensity of each diffraction peak and thus increased the relative prominence of the background.

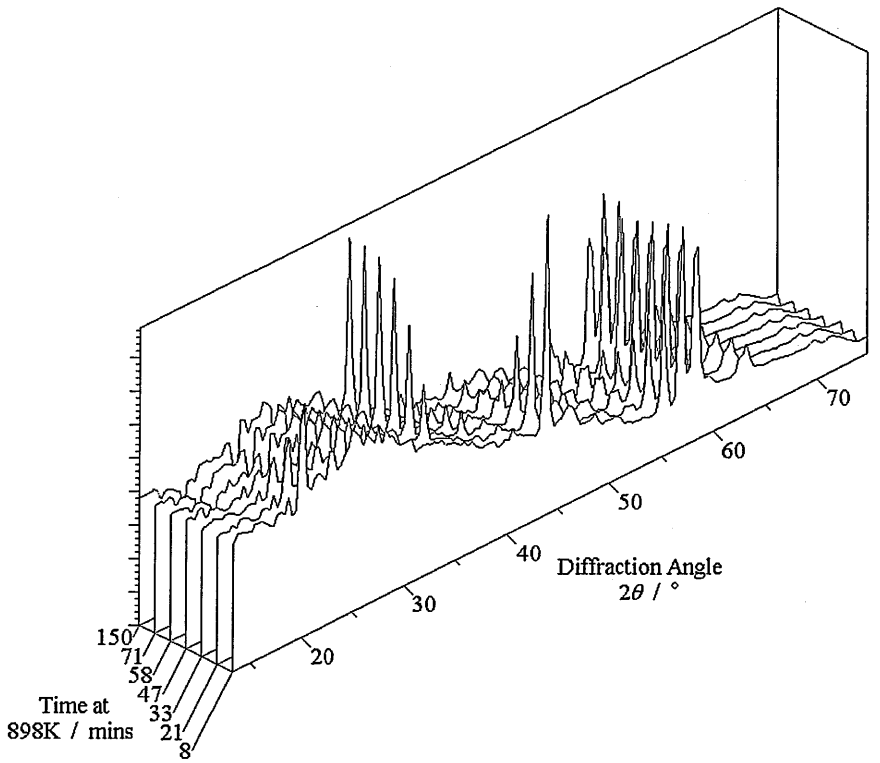

Figure 4.35: 3D view of the XRD patterns recorded during the phase transition of ζ_α- to ζ_β-ferrosilicon at 898 K

The peak characteristic of ζ_α-ferrosilicon at $2\theta = 44°$ is seen to decrease sharply in the first 3 patterns, and then decrease more slowly until the 5th pattern (time = 71 minutes) after which the intensity appears to remain constant, but this is due to the minor peak characteristic of ζ_β-ferrosilicon at $2\theta = 43°$. Peaks characteristic of ζ_β-ferrosilicon are visible in the 2nd pattern (time = 21 minutes) and increase until the 5th pattern, after which they remain constant in intensity.

Figure 4.36 shows a three-dimensional plot of the Fourier transforms of the Fe K-edge EXAFS recorded during the same experiment. The shoulder to the right of the first shell peak, indicative of the second shell characteristic of ζ_α-ferrosilicon, is seen to decrease sharply after 39 minutes, while the separate peak at about 3 Å, characteristic of ζ_β-ferrosilicon, becomes distinct after 64 minutes.

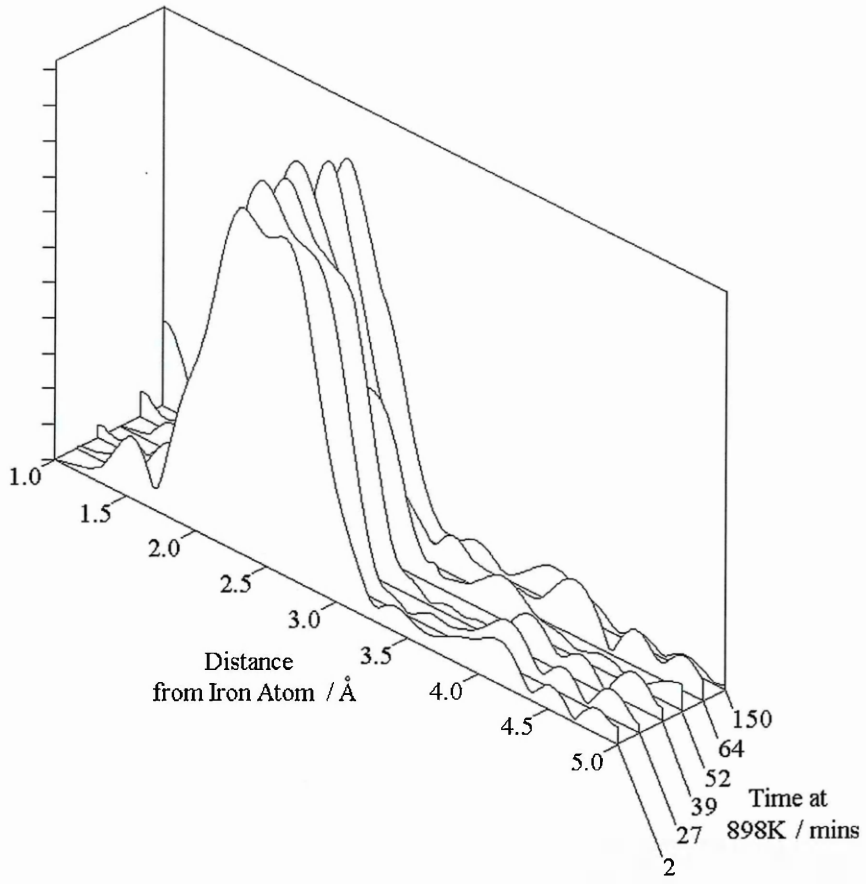

Figure 4.36: 3D view of the Fourier transforms of Fe K-edge EXAFS data recorded during the phase transition of ζ_{α}- to ζ_{β}-ferrosilicon at 898 K

Each EXAFS file was analysed using the method demonstrated in Section 4.2.1.2. The map contour plots for each EXAFS file are shown in Figures 4.37a-f.

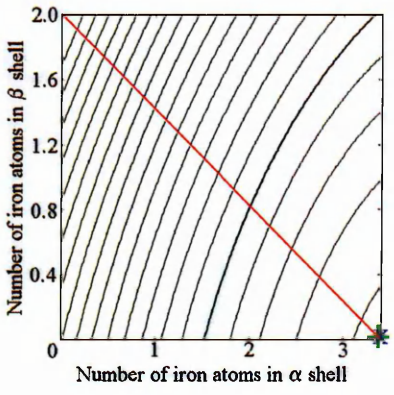

(a) Time = 2 mins ; $\gamma = 0$

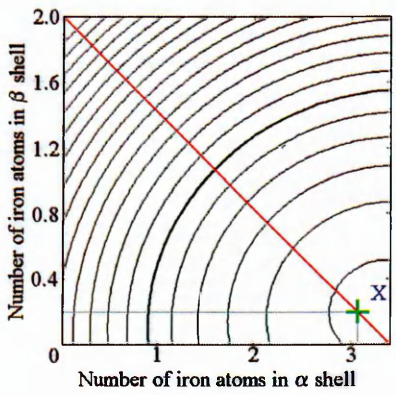

(b) Time = 27 mins ; $\gamma = 0.10 \pm 0.04$

Figures 4.37a-b: Map contour plots relating to Fe K-edge EXAFS data recorded during the phase transition of ζ_{α}- to ζ_{β}-ferrosilicon at 898 K

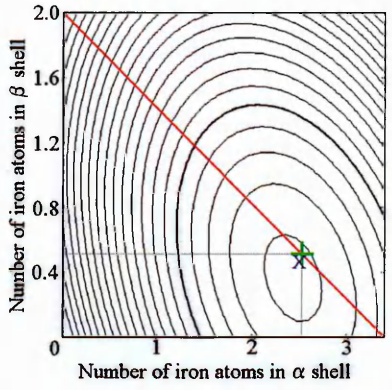

(c) Time = 39 mins ; $\gamma = 0.26 \pm 0.04$

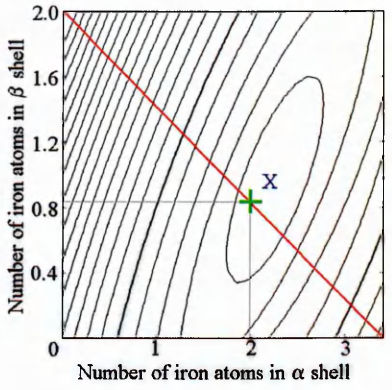

(d) Time = 52 mins ; $\gamma = 0.41 \pm 0.06$

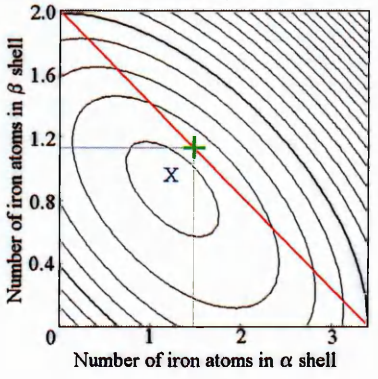

(e) Time = 64 mins ; $\gamma = 0.56 \pm 0.06$

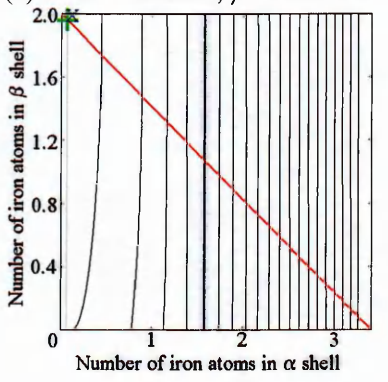

(f) Time = 150 mins ; $\gamma = 0.98 \pm 0.04$

Figures 4.37c-f: Map contour plots relating to Fe K-edge EXAFS data recorded during the phase transition of ζ_α- to ζ_β-ferrosilicon at 898 K

The EXAFS data collected during the latter half of the experiment were less amenable to fitting as the SRS beam strength decreased and noise levels increased. The final plot shown above is calculated from the sum of five EXAFS scans recorded after the XRD patterns indicated that the phase transition was complete. The values calculated for γ using the method described in Section 4.2.1.2 are plotted against time in Figure 4.34.

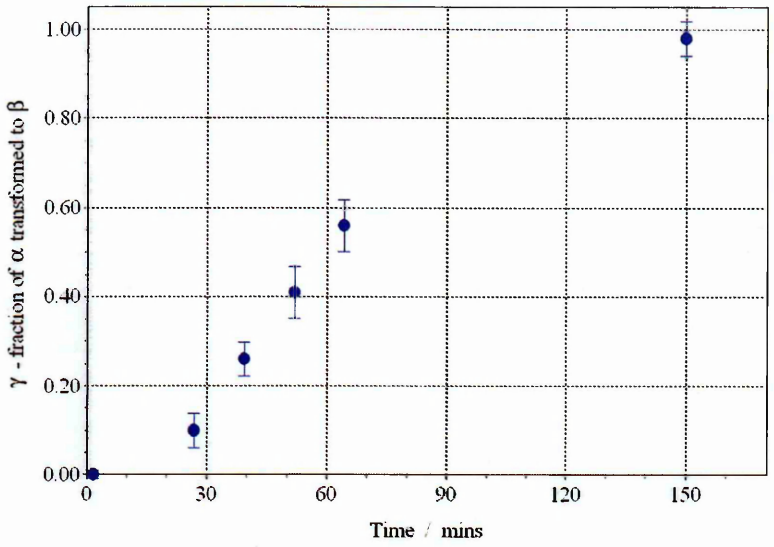

Figure 4.38: Fraction of ζ_{α}-ferrosilicon converted to ζ_{β}-ferrosilicon plotted against time for the experiment at 898 K

The analysis of these data is discussed in Section 4.2.4.

4.2.2.4 Experiment at 923K

A three-dimensional plot of the X-ray powder diffraction patterns collected using λ = 1.779 Å during the heating at 923 K of undoped ζ_{α}-ferrosilicon, prepared as described in Sections 3.1.1.1(ii) and Section 3.3.1, is shown in Figure 4.39.

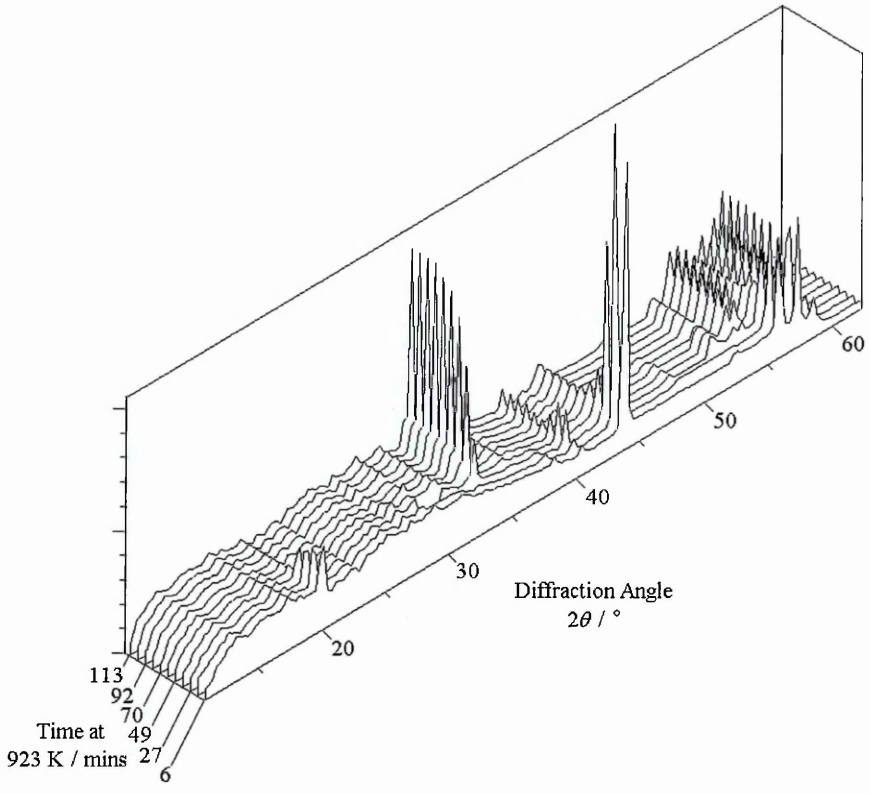

Figure 4.39: 3D view of the XRD patterns recorded during the phase transition of ζ_α- to ζ_β-ferrosilicon at 923 K

The peak characteristic of ζ_α-ferrosilicon at $2\theta = 44°$ is seen to decrease sharply in the first 3 patterns. It then decreases more slowly until the 7th pattern (time = 70 minutes) after which the intensity appears to remain constant, because of the minor peak characteristic of ζ_β-ferrosilicon at $2\theta = 43°$. Peaks characteristic of ζ_β-ferrosilicon at 2θ = 33, 53 and 55° are visible in the 2nd pattern (time = 17 minutes) and increase in intensity until the 7th pattern, after which they remain constant in intensity.

Figure 4.40 shows a three-dimensional plot of the Fourier transforms of the Fe K-edge EXAFS recorded during the same experiment. The shoulder to the right of the first shell peak, which is indicative of the second shell characteristic of ζ_α-ferrosilicon at 2.69 Å, is seen to decrease in intensity. It is barely present in the curves corresponding to data recorded after the sample has been held at 923 K for 33 minutes. The separate peak indicative of the

second shell characteristic of ζ_β-ferrosilicon at about 3 Å is first seen in the curve corresponding to data recorded when the sample had been held at 923 K for 33 minutes.

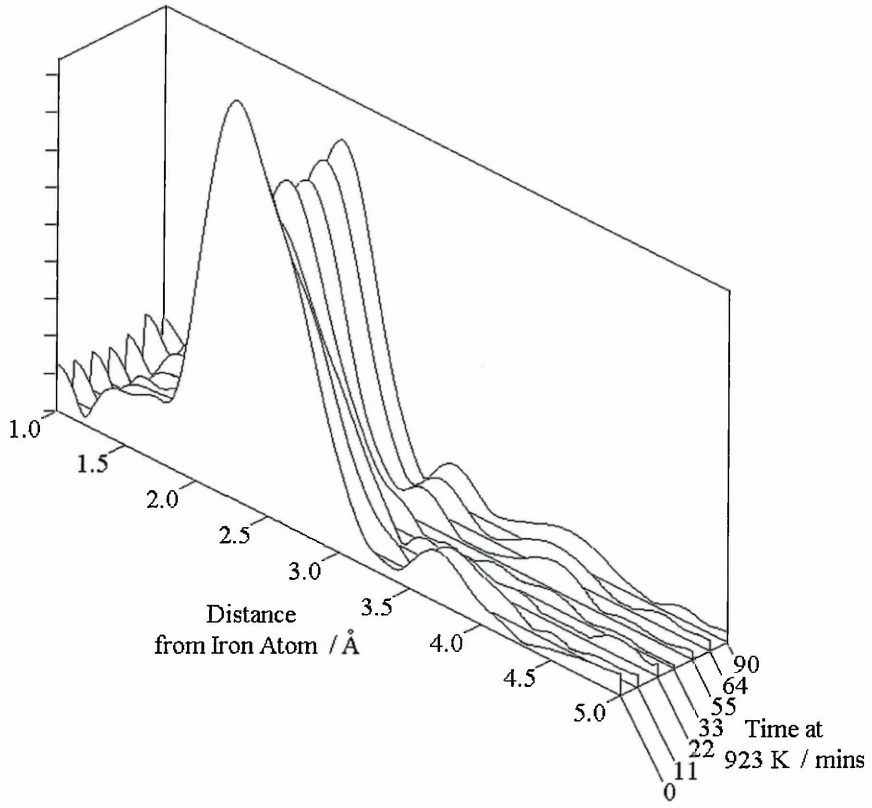

Figure 4.40: 3D view of the Fourier transforms of Fe K-edge EXAFS data recorded during the phase transition of ζ_α- to ζ_β-ferrosilicon at 923 K

Each EXAFS file was analysed using the method demonstrated in Section 4.2.1.2. The map contour plots for each EXAFS file are shown in Figures 4.41a-e.

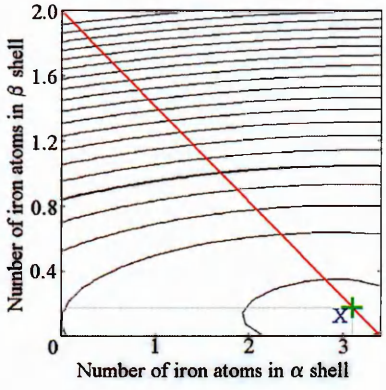

(a) Time = 11 mins ; $\gamma = 0.10 \pm 0.07$

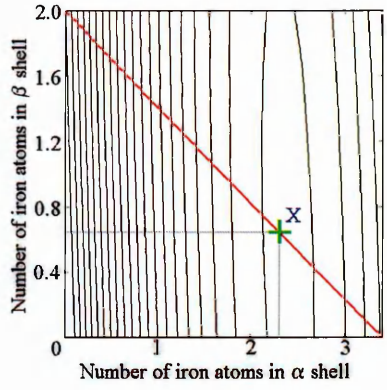

(b) Time = 22 mins ; $\gamma = 0.32 \pm 0.05$

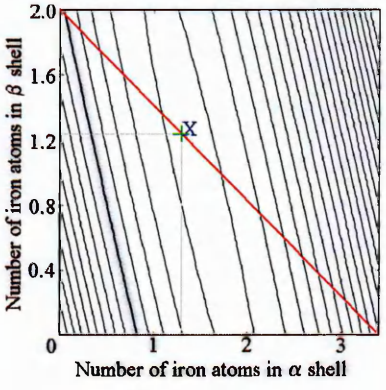

(c) Time = 33 mins ; $\gamma = 0.62 \pm 0.05$

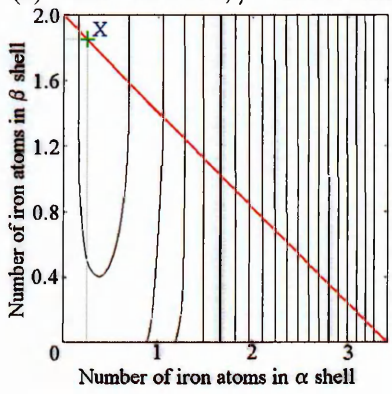

(d) Time = 55 mins ; $\gamma = 0.92 \pm 0.06$

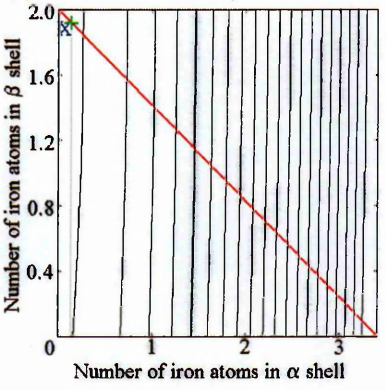

(e) Time = 64 mins ; $\gamma = 0.97 \pm 0.05$

Figures 4.41a-e: Map contour plots relating to Fe K-edge EXAFS data recorded during the phase transition of ζ_α- to ζ_β-ferrosilicon at 923 K

The values thus calculated for γ, the fraction of ζ_α-ferrosilicon converted to ζ_β-ferrosilicon, are plotted against time in Figure 4.42. These contour plots seem to indicate that the data are more unreliable than for experiments carried out at lower temperatures – as evidenced by the long thin contours indicating that the best fit for the coordination numbers of the ζ_β-ferrosilicon shell could not be calculated. This is to be

expected as the data quality would be reduced both by the necessarily shorter scan time and by the higher temperature leading to more disorder in the structure. However, the reduction in data quality does not prevent analysis. Values of γ were calculated from the coordination numbers of the ζ_α-ferrosilicon shell at 2.69 Å only.

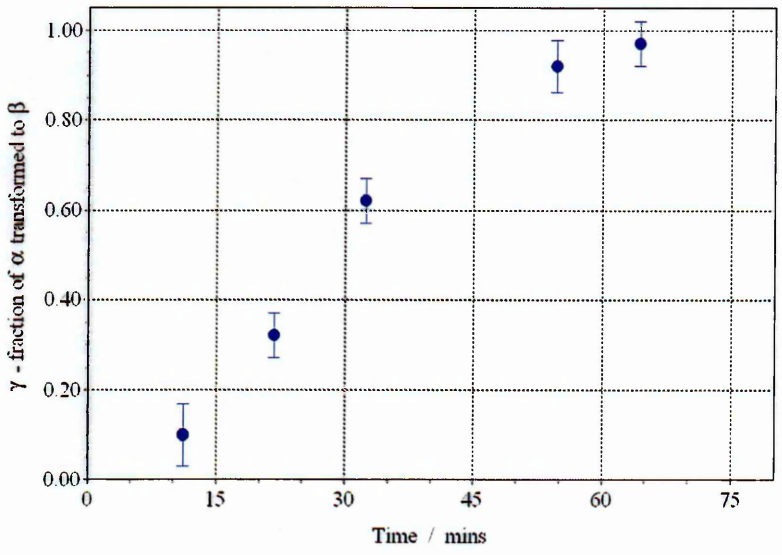

Figure 4.42: Fraction of ζ_α-ferrosilicon converted to ζ_β-ferrosilicon plotted against time for the experiment at 923 K

The analysis of these data is discussed in Section 4.2.4.

4.2.3 High-temperature time-resolved combined X-ray powder diffraction and Fe K-edge EXAFS recorded from the 1 % Al-doped phase transition of ζ_α- to ζ_β-ferrosilicon.

4.2.3.1 Experiment at 855 K

A three-dimensional plot of the X-ray powder diffraction patterns collected using λ = 1.779 Å during the heating at 855 K of 1 % Al-doped ζ_α-ferrosilicon, prepared as described in Sections 3.1.1.1(ii) and Section 3.3.1, is shown in Figure 4.43.

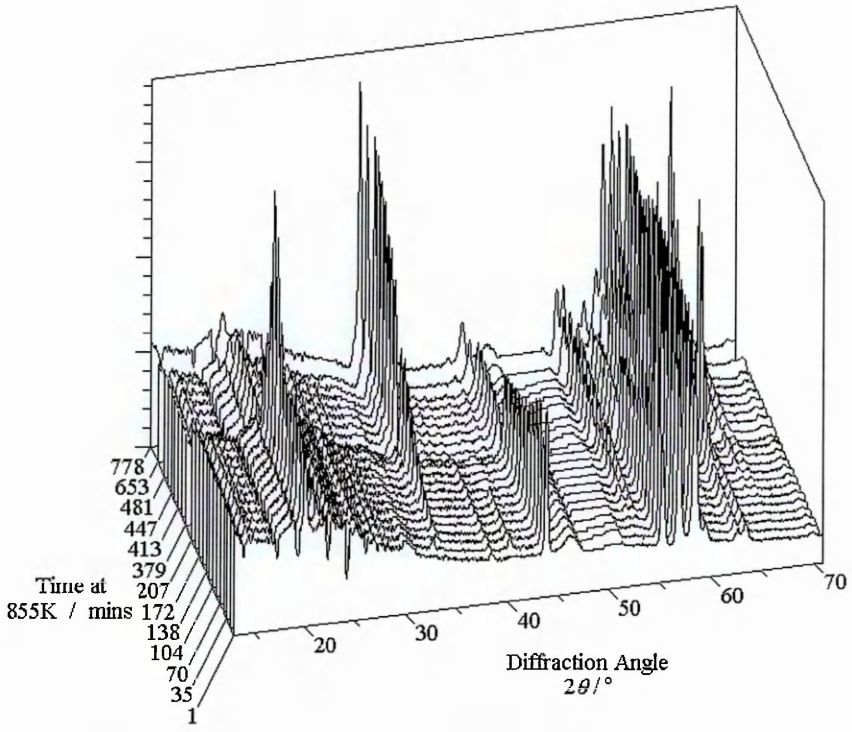

Figure 4.43: 3D view of the XRD patterns recorded during the phase transition of 1 % Al-doped ζ_α- to ζ_β-ferrosilicon at 855 K

The peak characteristic of ζ_α-ferrosilicon at $2\theta = 44°$ is seen to decrease slowly throughout the experiment. Peaks characteristic of ζ_β-ferrosilicon are just visible in the 4th pattern (time = 87 minutes) and increase until the final pattern. Note that the time axis is not a continuum in the above Figure – there were breaks in data recording when the synchrotron beam was restarted.

Figure 4.44 shows a three-dimensional plot of the Fourier transforms of the Fe K-edge EXAFS recorded during the same experiment. Each curve is the sum of three consecutively recorded spectra. The shoulder to the right of the first shell peak, which is indicative of the second shell characteristic of ζ_α-ferrosilicon, is intense in the Fourier transform relating to the first spectra, and overall appears to decrease in intensity. However, this feature is less clearly defined in the Fourier transform relating to the spectra recorded at time = 387 minutes. The separate peak at about 3 Å, characteristic of

ζ_β-ferrosilicon, is distinct in spectra recorded at times greater than 438 minutes.

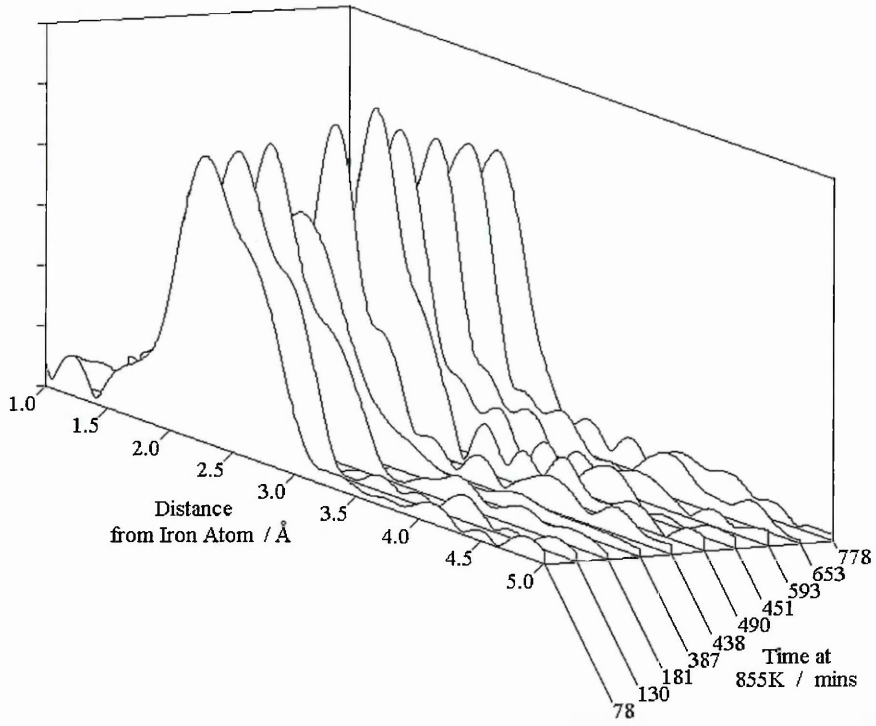

Figure 4.44: 3D view of the Fourier transforms of Fe K-edge EXAFS data recorded during the phase transition of 1 % Al-doped ζ_α- to ζ_β-ferrosilicon at 855 K

Each EXAFS file was analysed using the method demonstrated in Section 4.2.1.2. The map contour plots for each EXAFS file are shown in Figures 4.45a-j.

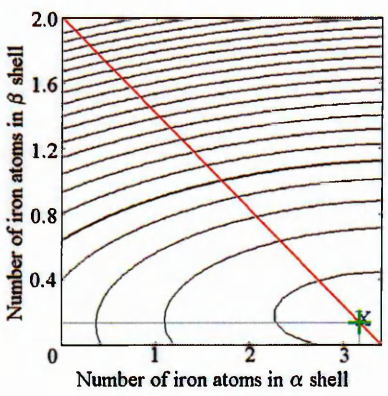

(a) Time = 78 mins ; $\gamma = 0.07 \pm 0.05$

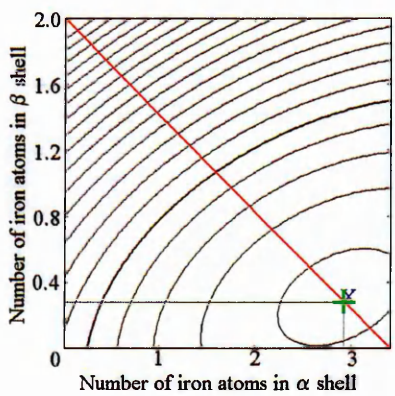

(b) Time = 130 mins ; $\gamma = 0.14 \pm 0.06$

Figures 4.45a-b: Map contour plots relating to Fe K-edge EXAFS data recorded during the phase transition of 1 % Al-doped ζ_α- to ζ_β-ferrosilicon at 855 K

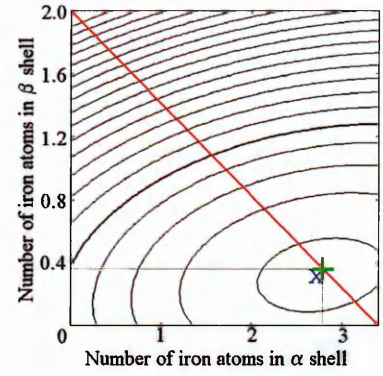

(c) Time = 181 mins ; $\gamma = 0.18 \pm 0.04$

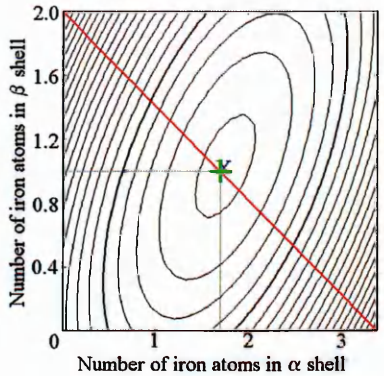

(d) Time = 387 mins ; $\gamma = 0.50 \pm 0.03$

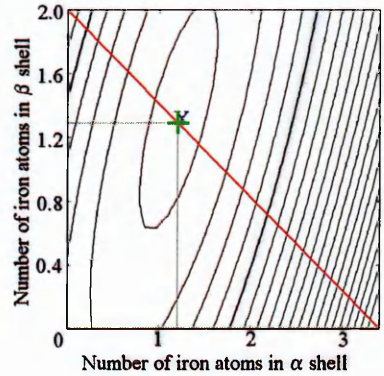

(e) Time = 438 mins ; $\gamma = 0.65 \pm 0.04$

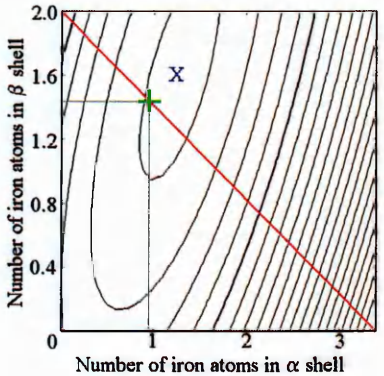

(f) Time = 490 mins ; $\gamma = 0.72 \pm 0.05$

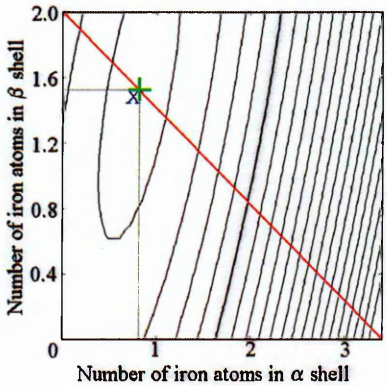

(g) Time = 541 mins ; $\gamma = 0.76 \pm 0.05$

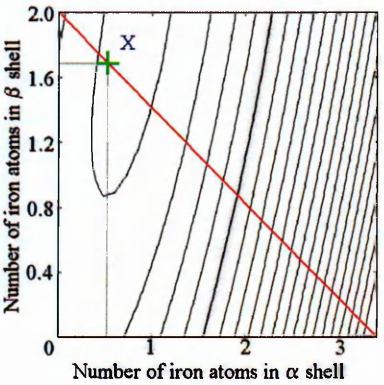

(h) Time = 593 mins ; $\gamma = 0.84 \pm 0.05$

Figures 4.45c-h: Map contour plots relating to Fe K-edge EXAFS data recorded during the phase transition of 1 % Al-doped ζ_{α}- to ζ_{β}-ferrosilicon at 855 K

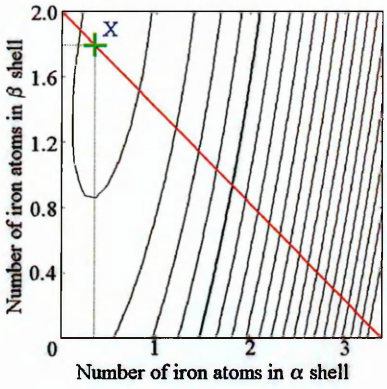

(i) Time = 652.6 mins ; $\gamma = 0.90 \pm 0.05$

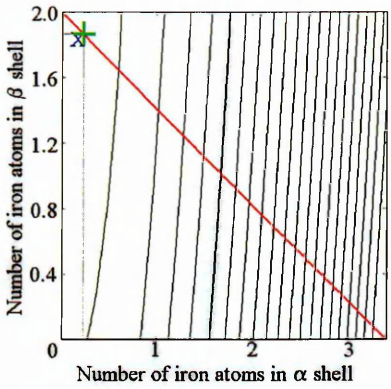

(j) Time = 778.4 mins ; $\gamma = 0.93 \pm 0.04$

Figures 4.45i-j: Map contour plots relating to Fe K-edge EXAFS data recorded during the phase transition of 1 % Al-doped ζ_α- to ζ_β-ferrosilicon at 855 K

The values calculated for γ, the fraction of ζ_α-ferrosilicon converted to ζ_β-ferrosilicon, are plotted against time in Figure 4.46.

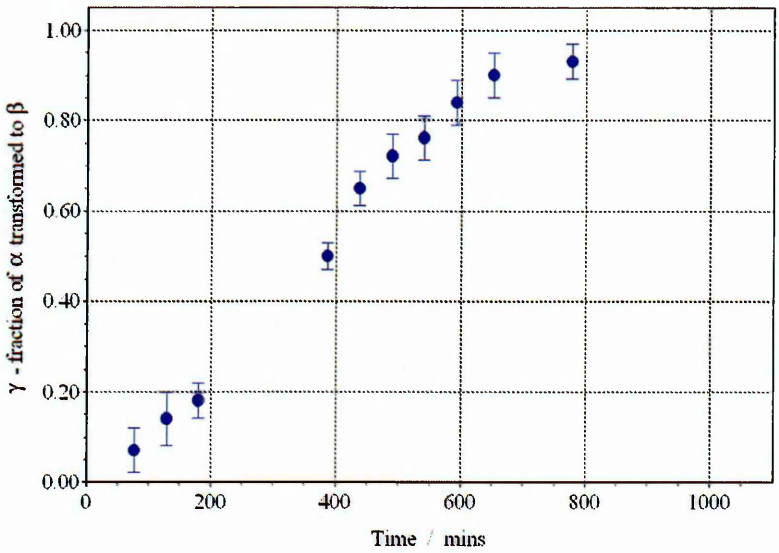

Figure 4.46: Fraction of ζ_α-ferrosilicon converted to ζ_β-ferrosilicon plotted against time for the 1 % Al-doped experiment at 855 K

The analysis of these data is discussed in Section 4.2.4.

4.2.3.2 Experiment at 873 K

A three-dimensional plot of the X-ray powder diffraction patterns collected using $\lambda = 1.779$ Å during the heating at 873 K of 1 % Al-doped ζ_α-ferrosilicon, prepared as described in

Sections 3.1.1.1(ii) and Section 3.3.1, is shown in Figure 4.47.

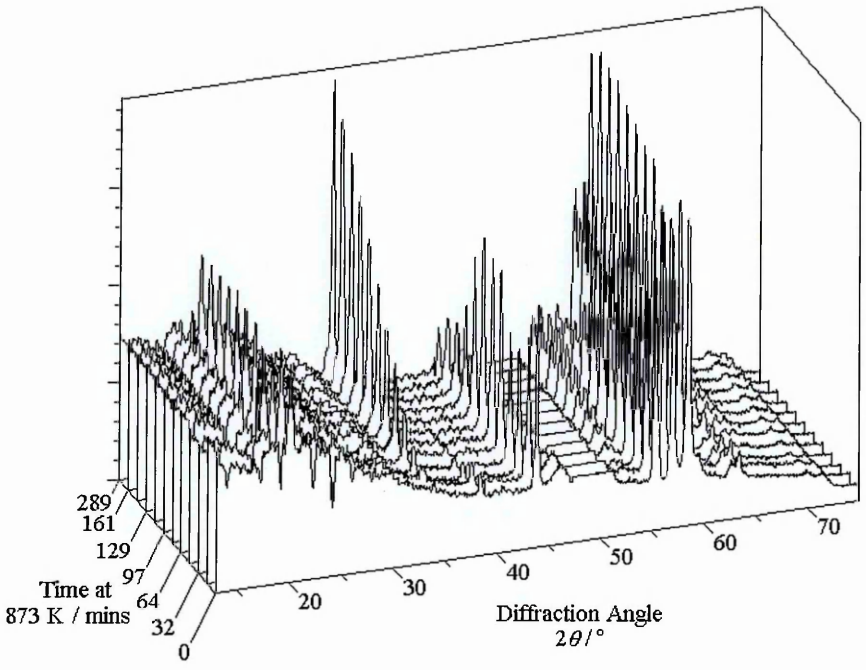

Figure 4.47: 3D view of the XRD patterns recorded during the phase transition of 1 % Al-doped ζ_α- to ζ_β-ferrosilicon at 873 K

The intensity of the peak characteristic of ζ_α-ferrosilicon at $2\theta = 44°$ does not vary in a consistent manner until after the pattern recorded at time = 129 minutes, when it is seen to decrease with time. Peaks characteristic of ζ_β-ferrosilicon are just visible in the 2nd pattern (time = 16 minutes) and increase until the 11th pattern, after which they remain constant in intensity.

Figure 4.48 shows a three-dimensional plot of the Fourier transforms of the Fe K-edge EXAFS recorded during the same experiment. The last two curves in the series are the result of a sum of two spectra, in an attempt to improve data quality. In this experiment, the change from curves characteristic of ζ_α-ferrosilicon to curves characteristic of ζ_β-ferrosilicon is not as clear as has been observed in other time-resolved experiments, due

to the inferior data quality inherent in the significantly shorter recording time.

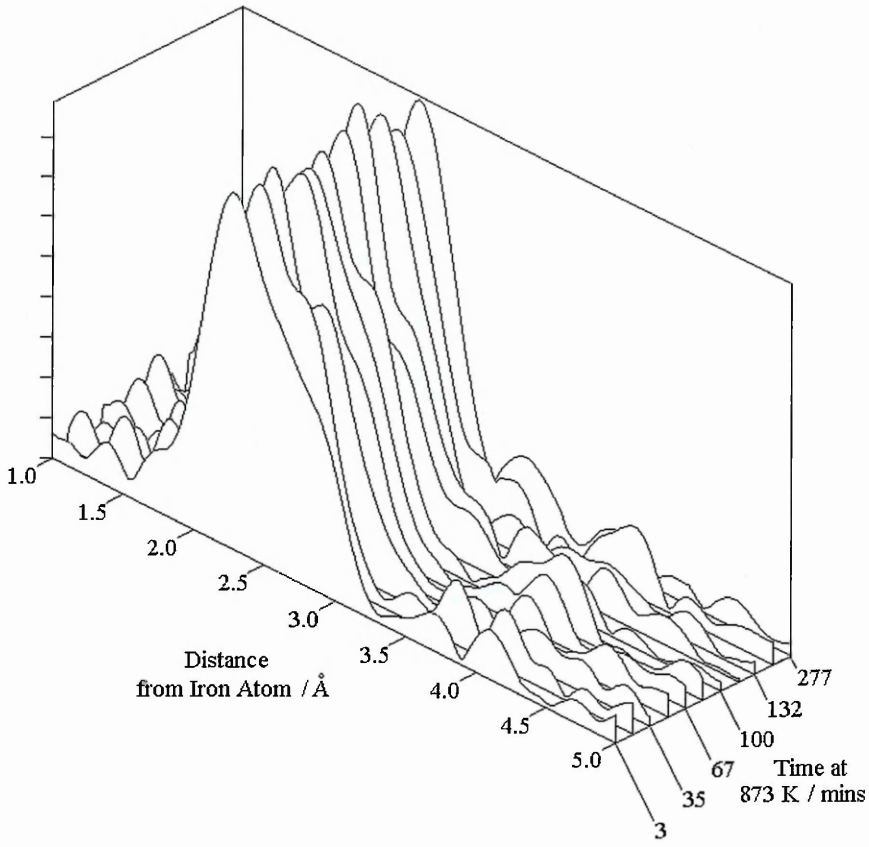

Figure 4.48: 3D view of the Fourier transforms of Fe K-edge EXAFS data recorded during the phase transition of 1 % Al-doped ζ_{α}- to ζ_{β}-ferrosilicon at 873 K

Each EXAFS file was analysed using the method demonstrated in Section 4.2.1.2. The map contour plots for each EXAFS file are shown in Figures 4.49a-k.

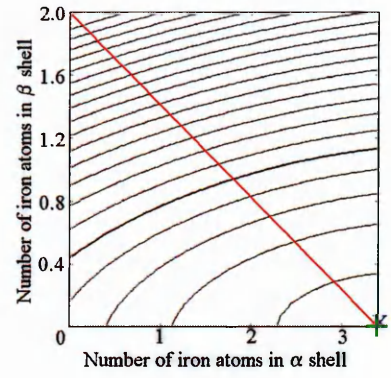

(a) Time = 3 mins ; $\gamma = 0.0$

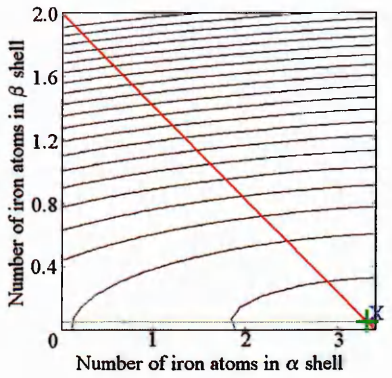

(b) Time = 19 mins ; $\gamma = 0.02 \pm 0.05$

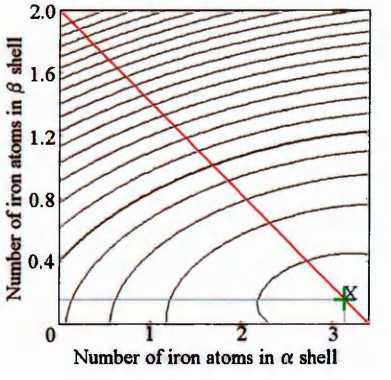

(c) Time = 35 mins ; $\gamma = 0.08 \pm 0.05$

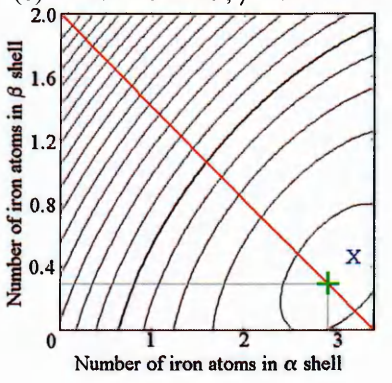

(d) Time = 51 mins ; $\gamma = 0.15 \pm 0.05$

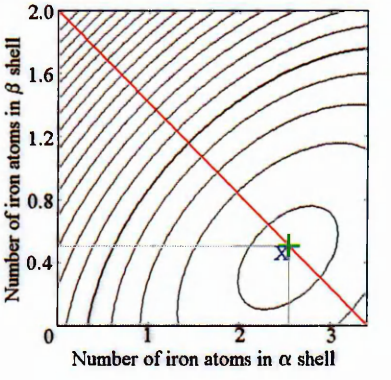

(e) Time = 67 mins ; $\gamma = 0.25 \pm 0.04$

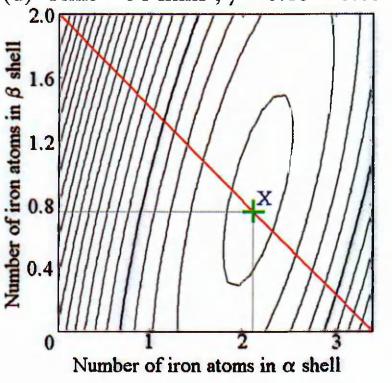

(f) Time = 84 mins ; $\gamma = 0.38 \pm 0.04$

Figures 4.49a-f: Map contour plots relating to Fe K-edge EXAFS data recorded during the phase transition of 1 % Al-doped ζ_{α}- to ζ_{β}-ferrosilicon at 873 K

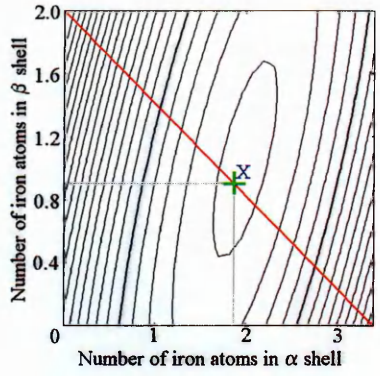

(g) Time = 100 mins ; $\gamma = 0.45 \pm 0.04$

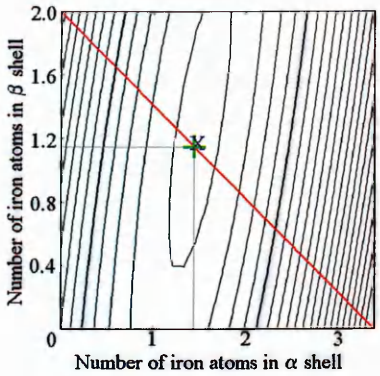

(h) Time = 116 mins ; $\gamma = 0.57 \pm 0.04$

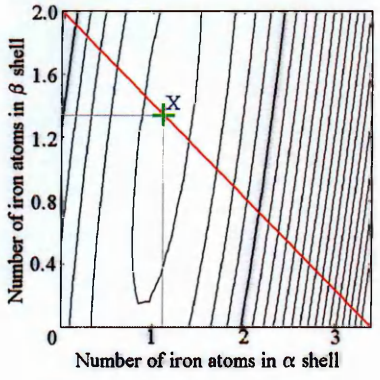

(i) Time = 132 mins ; $\gamma = 0.67 \pm 0.04$

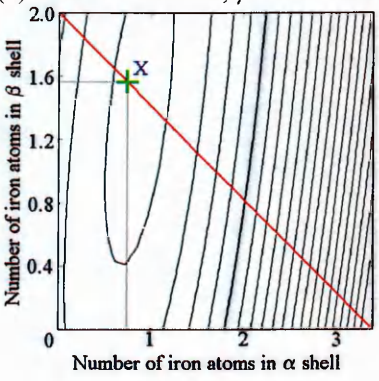

(j) Time = 156 mins ; $\gamma = 0.78 \pm 0.05$

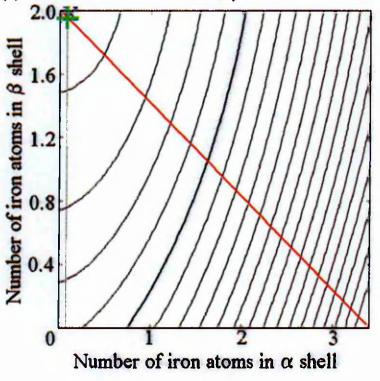

(k) Time = 277 mins ; $\gamma = 0.98 \pm 0.05$

Figures 4.49g-k: Map contour plots relating to Fe K-edge EXAFS data recorded during the phase transition of 1 % Al-doped ζ_α- to ζ_β-ferrosilicon at 873 K

The values calculated for γ, the fraction of ζ_α-ferrosilicon converted to ζ_β-ferrosilicon, are plotted against time in Figure 4.50.

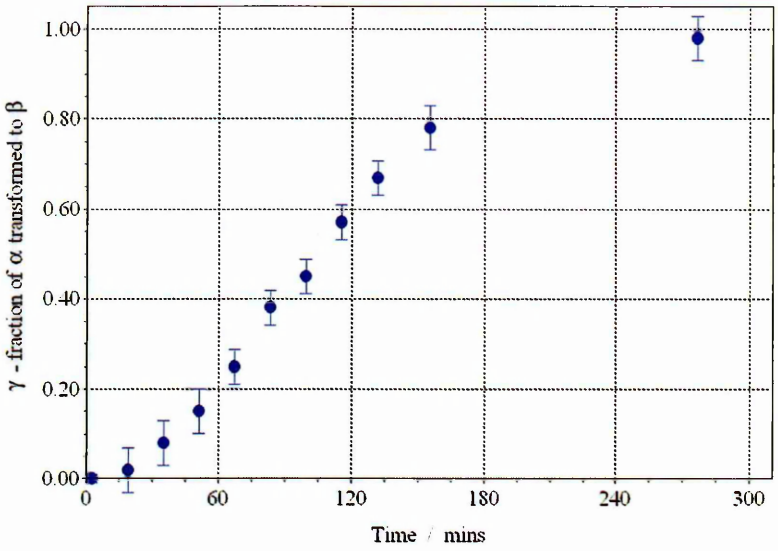

Figure 4.50: Fraction of ζ_{α}-ferrosilicon converted to ζ_{β}-ferrosilicon plotted against time for the 1 % Al-doped experiment at 873 K

The analysis of these data is discussed in Section 4.2.4.

4.2.3.3 Experiment at 898 K

A three-dimensional plot of the X-ray powder diffraction patterns collected using λ = 1.779 Å during the heating at 898 K of 1 % Al-doped ζ_{α}-ferrosilicon, prepared as described in Sections 3.1.1.1(ii) and Section 3.3.1, is shown in Figure 4.51.

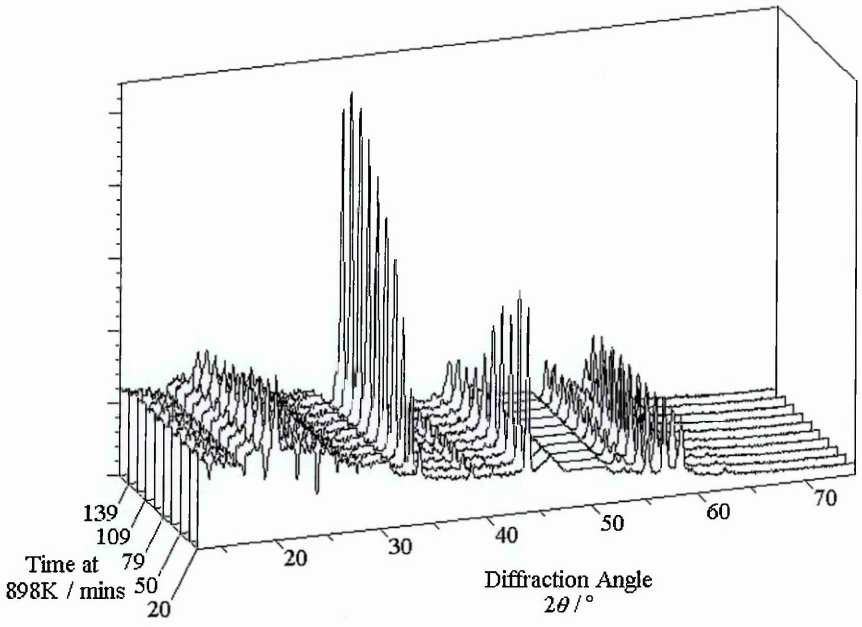

Figure 4.51: 3D view of the XRD patterns recorded during the phase transition of 1 % Al-doped ζ_α- to ζ_β-ferrosilicon at 898 K

The peak characteristic of ζ_α-ferrosilicon at $2\theta = 44°$ is seen to decrease significantly in the pattern recorded after 79 minutes at 898 K, and then continue to decrease until the pattern recorded after 124 minutes at 898 K after which little reduction is seen. Peaks characteristic of ζ_β-ferrosilicon are visible in the 1st pattern (time = 20 minutes) and increase in intensity until the last pattern. The peak intensities do not appear to stay constant in the last two patterns, suggesting that the phase transition may not have been complete at the end of the experiment.

Figure 4.52 shows a three-dimensional plot of the Fourier transforms of the Fe K-edge EXAFS recorded during the same experiment. The shoulder to the right of the first shell peak, indicative of the second shell characteristic of ζ_α-ferrosilicon, is seen to decrease during the first three spectra, is less distinct in the fourth and fifth spectrum, but is apparent albeit at low intensity in the sixth spectrum, after which it is no longer observed. The separate peak at about 3 Å, characteristic of ζ_β-ferrosilicon, becomes distinct after the fifth spectrum.

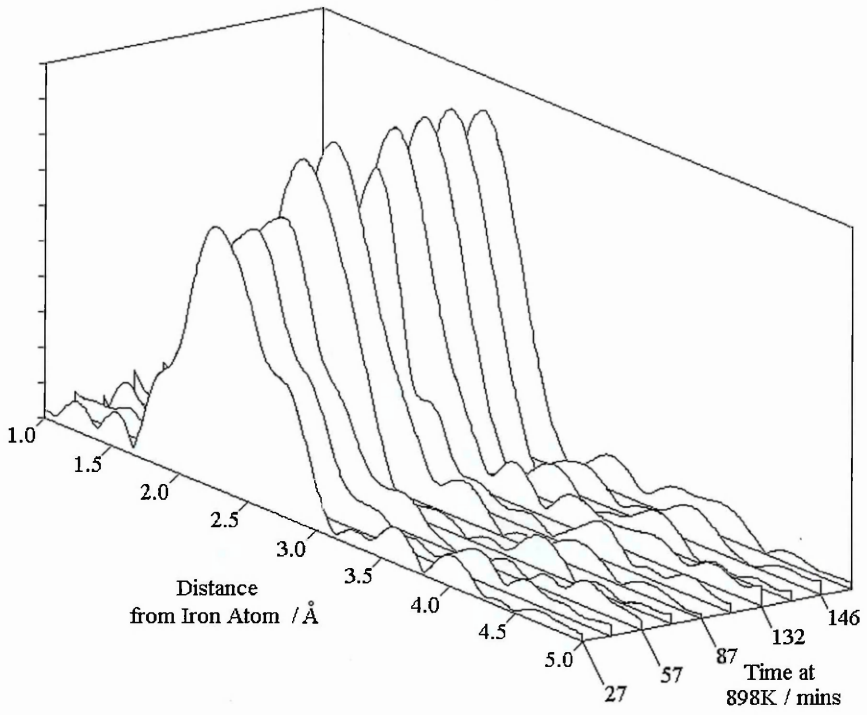

Figure 4.52: 3D view of the Fourier transforms of Fe K-edge EXAFS data recorded during the phase transition of 1 % Al-doped ζ_{α}- to ζ_{β}-ferrosilicon at 898 K

Each EXAFS file was analysed using the method demonstrated in Section 4.2.1.2. The map contour plots for each EXAFS file are shown in Figures 4.53a-j.

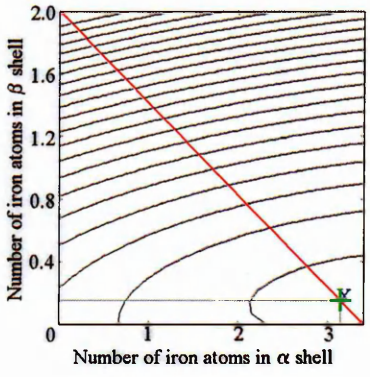

(a) Time = 27 mins ; $\gamma = 0.08 \pm 0.05$

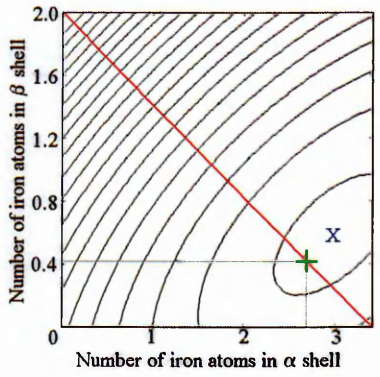

(b) Time = 42 mins ; $\gamma = 0.21 \pm 0.05$

Figures 4.53a-b: Map contour plots relating to Fe K-edge EXAFS data recorded during the phase transition of 1 % Al-doped ζ_{α}- to ζ_{β}-ferrosilicon at 898 K

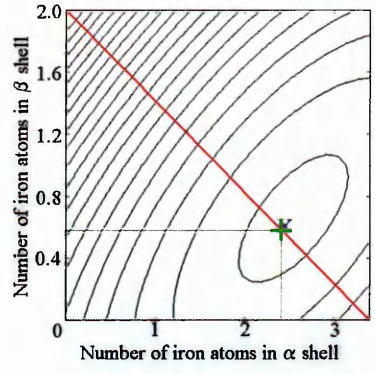

(c) Time = 57 mins ; $\gamma = 0.29 \pm 0.04$

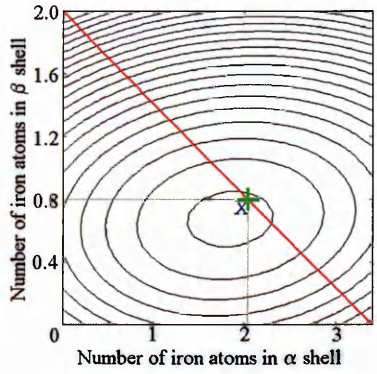

(d) Time = 72 mins ; $\gamma = 0.40 \pm 0.04$

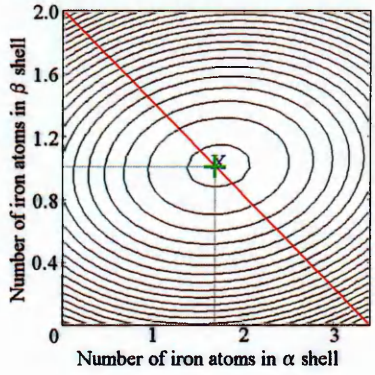

(e) Time = 87 mins ; $\gamma = 0.50 \pm 0.03$

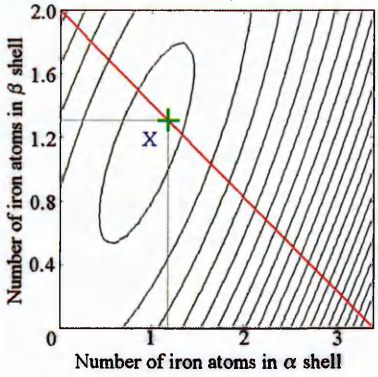

(f) Time = 102 mins ; $\gamma = 0.65 \pm 0.05$

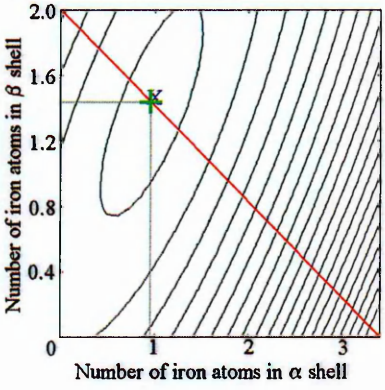

(g) Time = 117 mins ; $\gamma = 0.72 \pm 0.05$

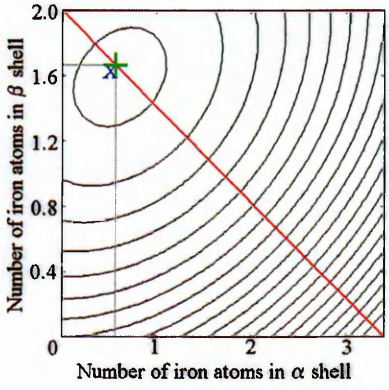

(h) Time = 132 mins ; $\gamma = 0.83 \pm 0.05$

Figures 4.53c-h: Map contour plots relating to Fe K-edge EXAFS data recorded during the phase transition of 1 % Al-doped ζ_{α}- to ζ_{β}-ferrosilicon at 898K

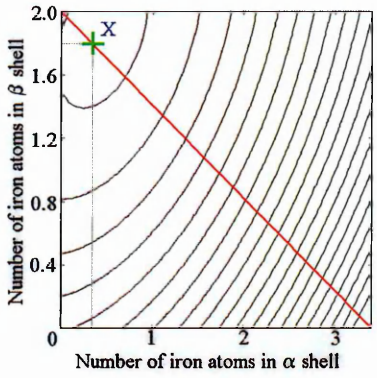

(i) Time = 146 mins ; $\gamma = 0.90 \pm 0.05$

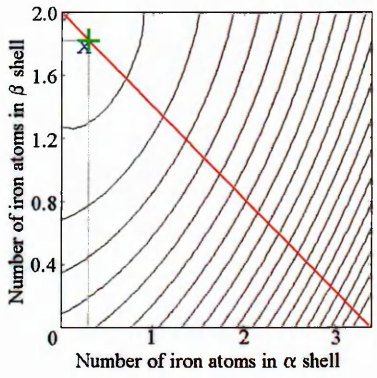

(j) Time = 161 mins ; $\gamma = 0.91 \pm 0.06$

Figures 4.53i-j: Map contour plots relating to Fe K-edge EXAFS data recorded during the phase transition of 1 % Al-doped ζ_α- to ζ_β-ferrosilicon at 898 K

The values thus calculated for γ, the fraction of ζ_α-ferrosilicon converted to ζ_β-ferrosilicon, are plotted against time in Figure 4.54.

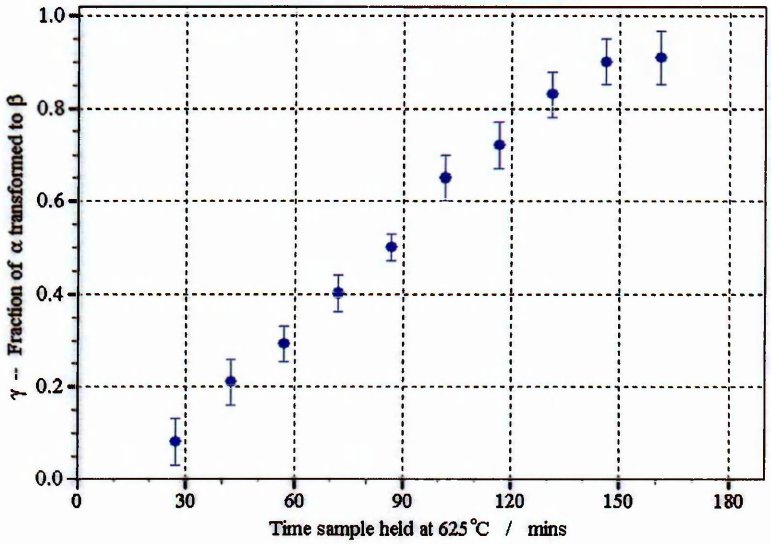

Figure 4.54: Fraction of ζ_α-ferrosilicon converted to ζ_β-ferrosilicon plotted against time for the 1 % Al-doped experiment at 898 K

The analysis of these data is discussed in Section 4.2.4.

4.2.3.4 Experiment at 923 K

Because the experiment at 923 K using undoped ferrosilicon yielded EXAFS data which were less amenable to fitting using the contour plot method than other experiments, in

this experiment the recording time for the X-ray diffraction data was reduced to 100 seconds and the collection time for the EXAFS data increased to 8.5 minutes in order to improve data quality.

A three-dimensional plot of the X-ray powder diffraction patterns collected using λ = 1.779 Å during the heating at 923 K of 1 % Al-doped ζ_α-ferrosilicon, prepared as described in Sections 3.1.1.1(ii) and Section 3.3.1, is shown in Figure 4.55.

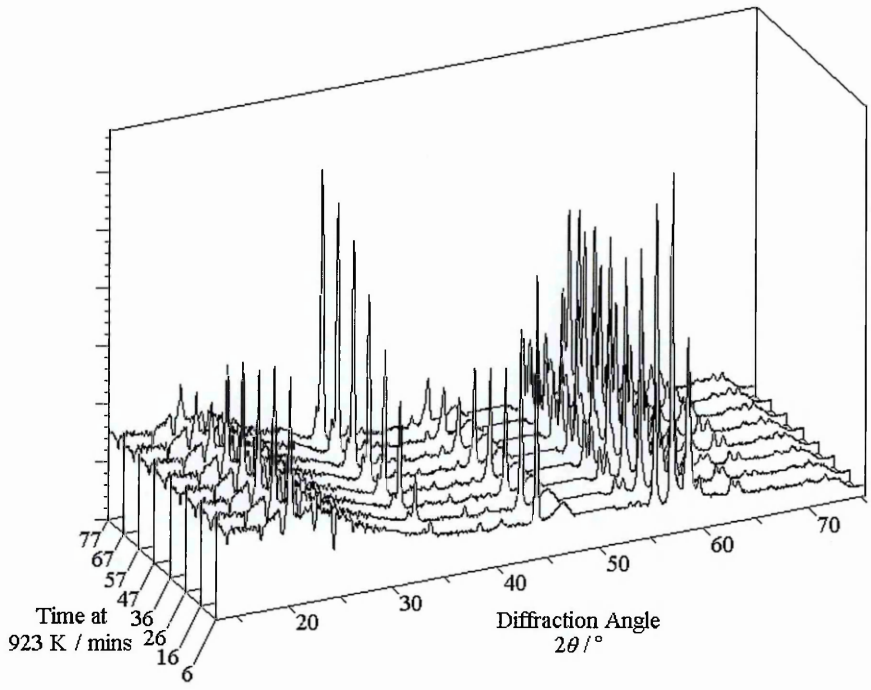

Figure 4.55: 3D view of the XRD patterns recorded during the phase transition of 1 % Al-doped ζ_α- to ζ_β-ferrosilicon at 923 K

The major peak characteristic of ζ_α-ferrosilicon at $2\theta = 44°$ is seen to decrease sharply in the first two patterns, and then decrease more slowly until the last pattern (time = 77 minutes). Peaks characteristic of ζ_β-ferrosilicon are visible in the 2nd pattern (time = 16 minutes) and increase until the final pattern. The peak intensities do not appear to stay constant in the last two patterns, suggesting that the phase transition was not complete at the end of the experiment.

Figure 4.56 shows a three-dimensional plot of the Fourier transforms of the Fe K-edge EXAFS recorded during the same experiment. The shoulder to the right of the first shell peak, indicative of the second shell characteristic of ζ_{α}-ferrosilicon, is seen to decrease and is no longer distinct after the Fourier transform relating to the spectrum recorded at time = 41 minutes. The separate peak at about 3 Å, characteristic of ζ_{β}-ferrosilicon, is visible in the Fourier transforms relating to the spectra recorded at time = 41, 62 and 72 minutes.

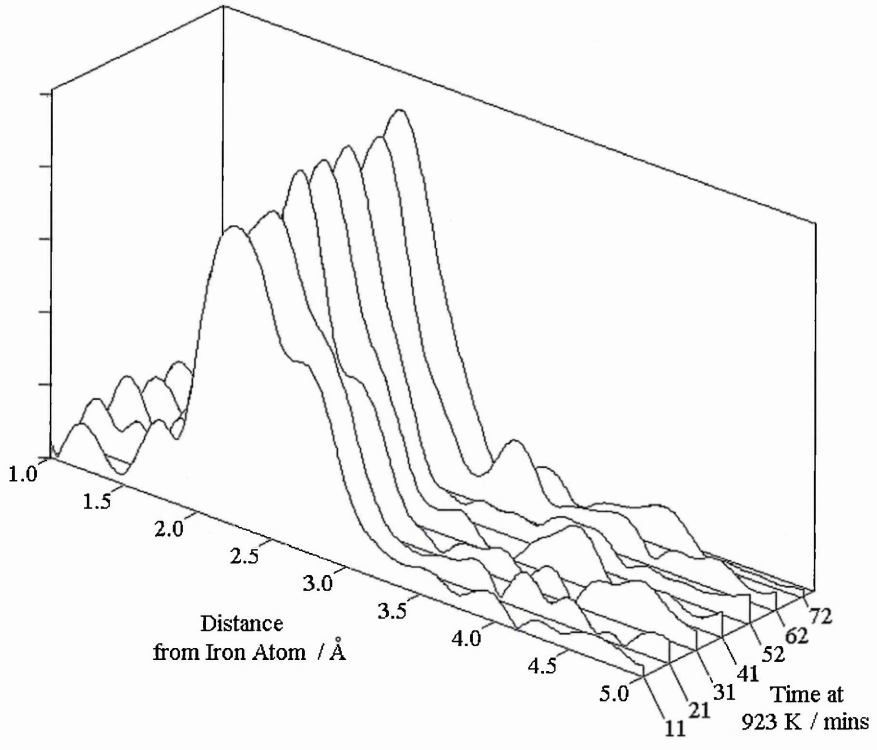

Figure 4.56: 3D view of the Fourier transforms of Fe K-edge EXAFS data recorded during the phase transition of 1 % Al-doped ζ_{α}- to ζ_{β}-ferrosilicon at 923 K

Each EXAFS file was analysed using the method demonstrated in Section 4.2.1.2. The map contour plots for each EXAFS file are shown in Figures 4.57a-g. The contour plots shown in Figures 5.57 indicate a much greater degree of certainty of fit compared with the equivalent plots in Figures 4.41, due to the increased data collection time for the EXAFS data.

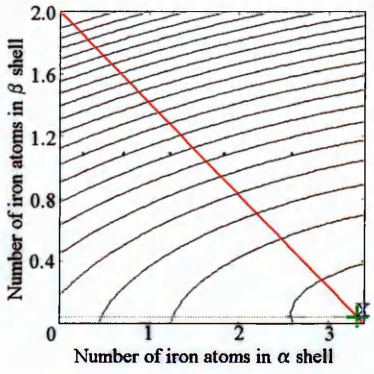

(a) Time = 11 mins ; $\gamma = 0.02 \pm 0.05$

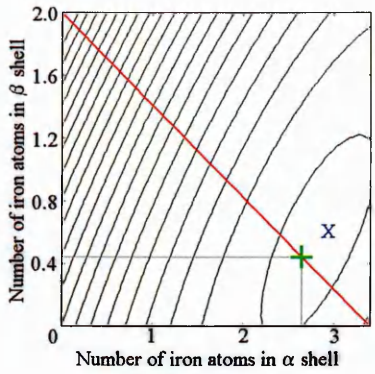

(b) Time = 21 mins ; $\gamma = 0.22 \pm 0.06$

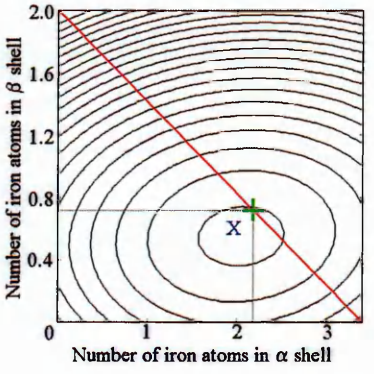

(c) Time = 31 mins ; $\gamma = 0.36 \pm 0.04$

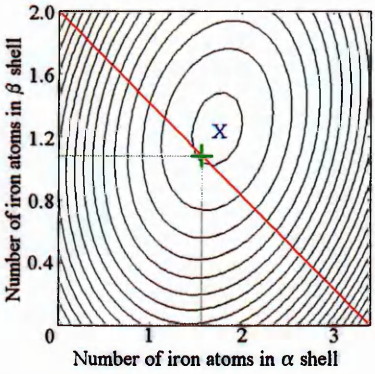

(d) Time = 41 mins ; $\gamma = 0.54 \pm 0.03$

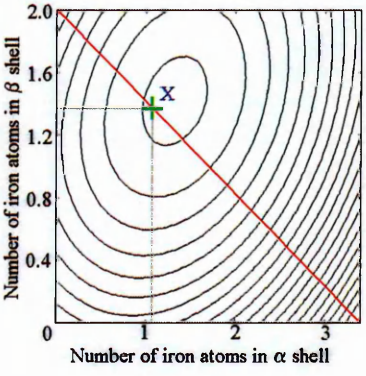

(e) Time = 52 mins ; $\gamma = 0.69 \pm 0.04$

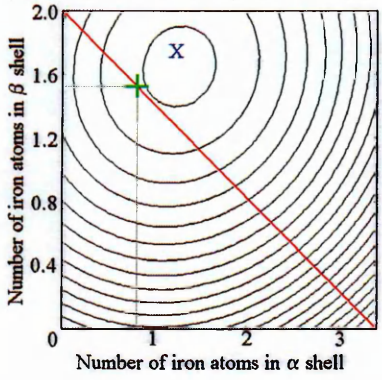

(f) Time = 62 mins ; $\gamma = 0.76 \pm 0.05$

Figures 4.57a-f: Map contour plots relating to Fe K-edge EXAFS data recorded during the phase transition of 1 % Al-doped ζ_{α}- to ζ_{β}-ferrosilicon at 923 K

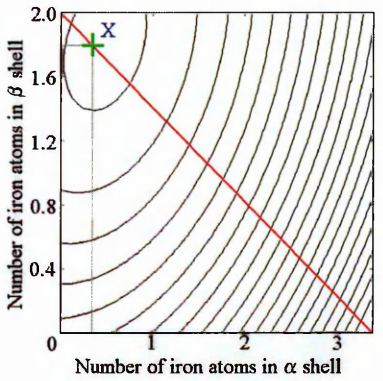

(g) Time = 72 mins ; $\gamma = 0.90 \pm 0.05$

Figure 4.57g: Map contour plots relating to Fe K-edge EXAFS data recorded during the phase transition of 1 % Al-doped ζ_α- to ζ_β-ferrosilicon at 923 K

The contour plot shown in Figure 4.58f is unusual as the only such plot in any of the experiments reported in this work where the central contour indicating the best fit for the EXAFS data does not intersect with the line indicating the composition where the proportion of ζ_α-ferrosilicon plus the proportion of ζ_β-ferrosilicon equals 100%. The significance of this is unknown.

The values thus calculated for γ, the fraction of ζ_α-ferrosilicon converted to ζ_β-ferrosilicon, are plotted against time in Figure 4.58.

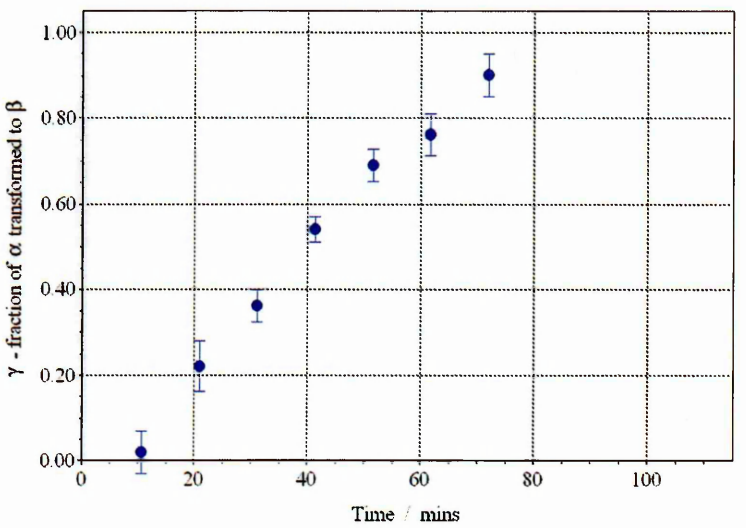

Figure 4.58: Fraction of ζ_α-ferrosilicon converted to ζ_β-ferrosilicon plotted against time for the 1 % Al-doped experiment at 923 K

The analysis of these data is discussed in Section 4.2.4.

4.2.4 Analysis of results

4.2.4.1 The Avrami-Erofe'ev Model

The data presented in Sections 4.2.2 and 4.2.3 for the time-resolved conversion of ζ_α- to ζ_β-ferrosilicon were fitted using the CurveExpert 1.3 software[19] (which calculates a best fit using the Levenberg-Marquardt algorithm for nonlinear regression) to the Avrami-Erofe'ev equation described in Section 1.3.4 (Equation 1.12)

$$k.t = N[-\ln(1-\gamma)]^{1/N}$$

The values for the rate constant k and the nucleation constant N thus calculated are given in Table 4.16. The data presented in Figures 4.30, 4.34, 4.38, 4.42, 4.46, 4.50, 4.54 and 4.58 are plotted in Figures 4.59a-h along with the sigmoid curves of these fits.

	Experiment Temperature / K	k / min^{-1}	N	Correlation Coefficient	Standard Deviation
Conversion of ζ_α- to ζ_β-ferrosilicon	855	0.0023 ± 0.0006	2.12 ± 0.28	0.9999	0.0029
	873	0.012 ± 0.003	2.11 ± 0.35	0.9999	0.0065
	898	0.031 ± 0.008	2.17 ± 0.32	0.9995	0.0130
	923	0.061 ± 0.004	2.07 ± 0.10	0.9994	0.0153
Conversion of 1 % Al-doped ζ_α- to ζ_β-ferrosilicon	855	0.0042 ± 0.0004	1.88 ± 0.09	0.9963	0.0300
	873	0.016 ± 0.002	1.96 ± 0.12	0.9996	0.0103
	898	0.019 ± 0.001	1.94 ± 0.09	0.9974	0.0227
	923	0.0386 ± 0.002	1.85 ± 0.08	0.9964	0.0293

Table 4.16: Values of k and N derived from the experiments presented in Sections 4.2.2 and 4.2.3 using the Avrami-Erofe'ev theory

It is clear from the graphs shown in Figures 4.59 as well as the low values of standard deviation and high values of correlation coefficient given in Table 4.16 that this model is a good fit to the data.

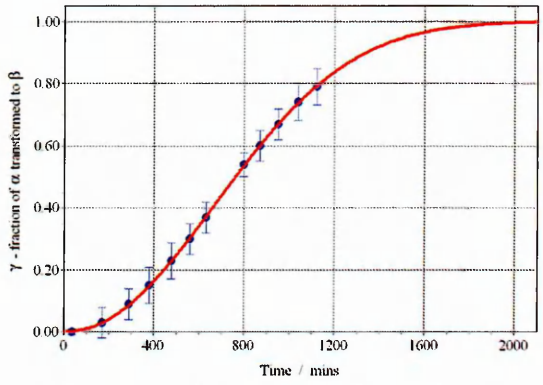

(a) Conversion of ζ_α- to ζ_β-ferrosilicon at 855 K

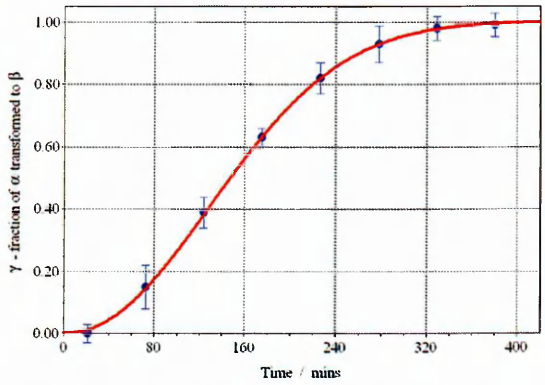

(b) Conversion of ζ_α- to ζ_β-ferrosilicon at 873 K

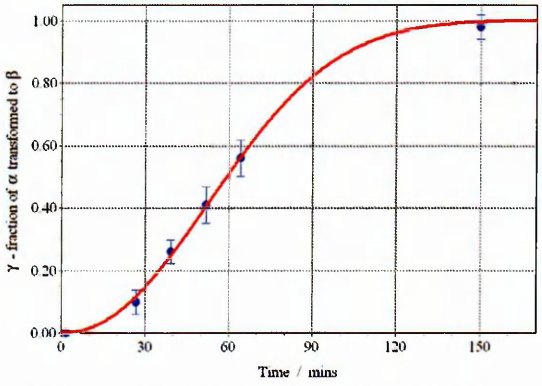

(c) Conversion of ζ_α- to ζ_β-ferrosilicon at 898 K

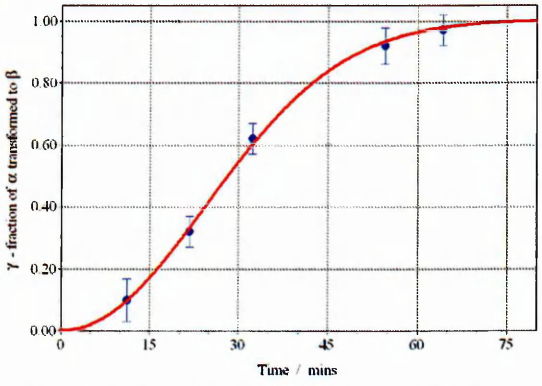

(d) Conversion of ζ_α- to ζ_β-ferrosilicon at 923 K

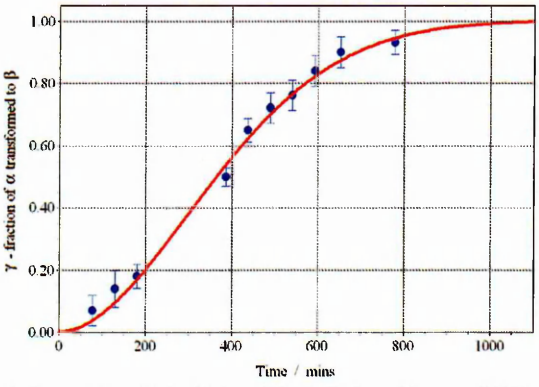

(e) Conversion of 1 % Al-doped ζ_α- to ζ_β-ferrosilicon at 855 K

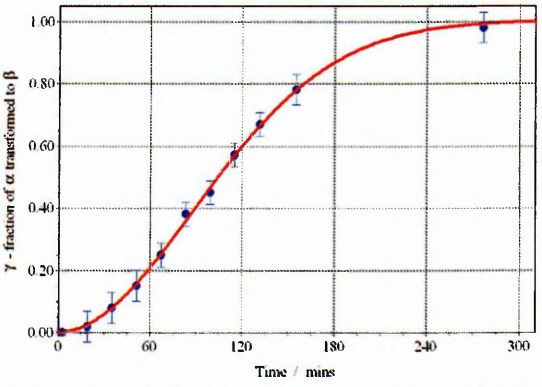

(f) Conversion of 1 % Al-doped ζ_α- to ζ_β-ferrosilicon at 873 K

Figures 4.59a-f: Data from Sections 4.2.2 and 4.2.3 fitted to the Avrami-Erofe'ev model with rate constants as displayed in Table 4.16

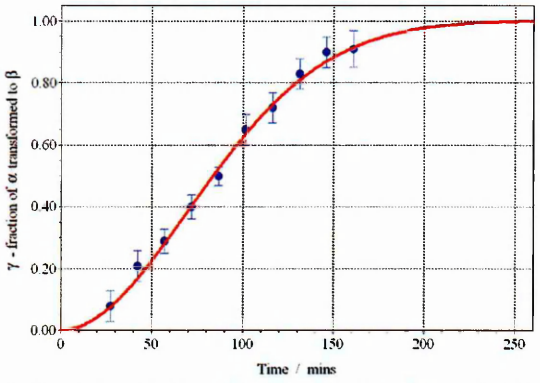

(g) Conversion of 1 % Al-doped ζ_{α}- to ζ_{β}-ferrosilicon at 898 K

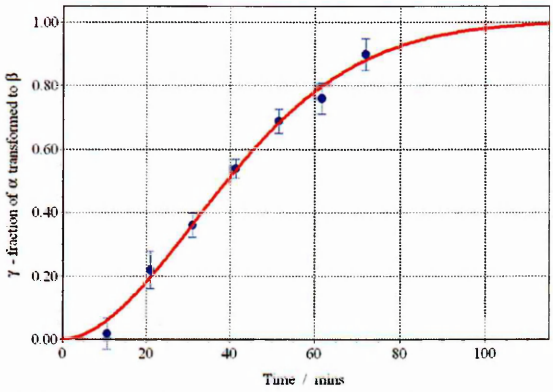

(h) Conversion of 1% Al-doped ζ_{α}- to ζ_{β}-ferrosilicon at 923 K

Figures 4.59g-h: Data from Sections 4.2.2 and 4.2.3 fitted to the Avrami-Erofe'ev model with rate constants as displayed in Table 4.16

4.2.4.2 The Prout-Tompkins Model

The data presented in Sections 4.2.2 and 4.2.3 were also fitted using the CurveExpert 1.3 software to the Prout-Tompkins equation described in Section 1.3.7 (Equation 1.22)

$$\ln\left[\frac{\gamma}{(1-\gamma)}\right] = k_B t + c$$

	Experiment Temperature / K	k_B / min^{-1}	c	Correlation Coefficient	Standard Deviation
Conversion of ζ_{α}- to ζ_{β}-ferrosilicon	855	0.0050 ± 0.0002	-3.90 ± 0.09	0.9913	0.0392
	873	0.0231 ± 0.0015	-3.52 ± 0.07	0.9973	0.0308
	898	0.0737 ± 0.0012	-4.25 ± 0.08	0.9940	0.0434
	923	0.112 ± 0.009	-3.20 ± 0.09	0.9984	0.0243
Conversion of 1 % Al-doped ζ_{α}- to ζ_{β}-ferrosilicon	855	0.0078 ± 0.0006	-2.94 ± 0.08	0.9982	0.0210
	873	0.0347 ± 0.0018	-3.70 ± 0.11	0.9931	0.0406
	898	0.0335 ± 0.0015	-2.87 ± 0.07	0.9975	0.0224
	923	0.0703 ± 0.0028	-2.82 ± 0.14	0.9891	0.0509

Table 4.17: Values of k_B and c derived from the experiments presented in Sections 4.2.2 and 4.2.3 using the Prout-Tompkins theory

The values for the rate constants k_B and the time-correction constant c thus calculated are given in Table 4.17. The data presented in Figures 4.30, 4.34, 4.38, 4.42, 4.46, 4.50,

4.54 and 4.58 are plotted in Figures 4.60a-h along with the sigmoid curves of these fits.

The graphs indicate that this model gives a reasonable fit to the data, but the figures for standard deviation and correlation coefficient indicate that the fit is not as good as that obtained using the Avrami-Erofe'ev model as described in the previous Section.

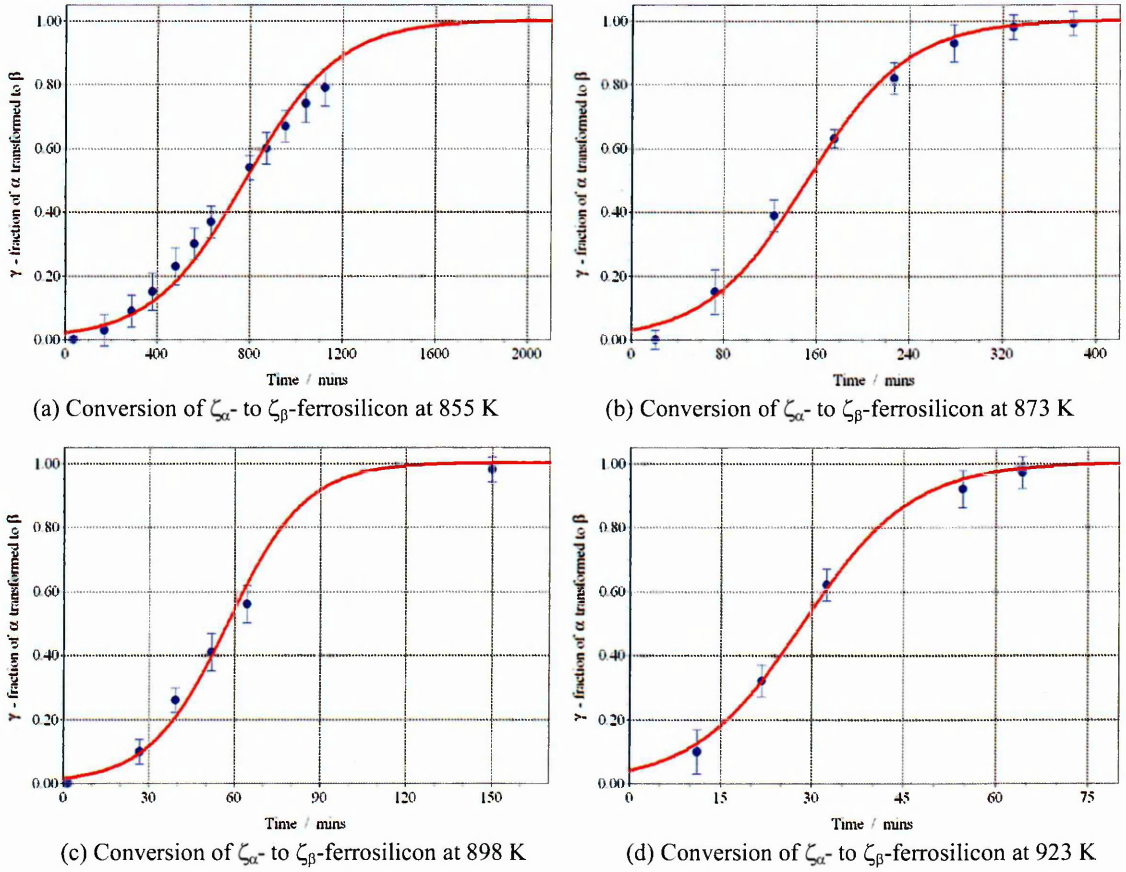

(a) Conversion of ζ_{α}- to ζ_{β}-ferrosilicon at 855 K

(b) Conversion of ζ_{α}- to ζ_{β}-ferrosilicon at 873 K

(c) Conversion of ζ_{α}- to ζ_{β}-ferrosilicon at 898 K

(d) Conversion of ζ_{α}- to ζ_{β}-ferrosilicon at 923 K

Figures 4.60a-d: Data from Sections 4.2.1 and 4.2.2 fitted to the Prout-Tompkins model with rate constants as displayed in Table 4.17

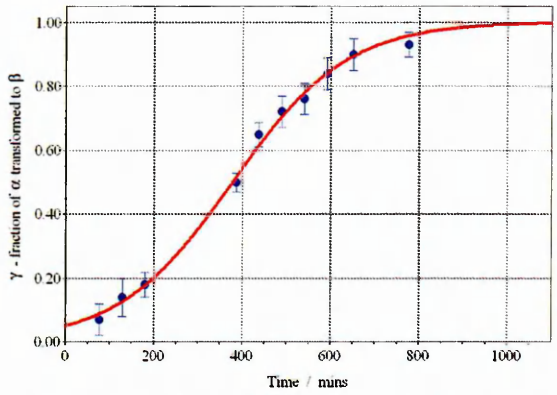

(e) Conversion of 1 % Al-doped ζ_{α}- to ζ_{β}-ferrosilicon at 855 K

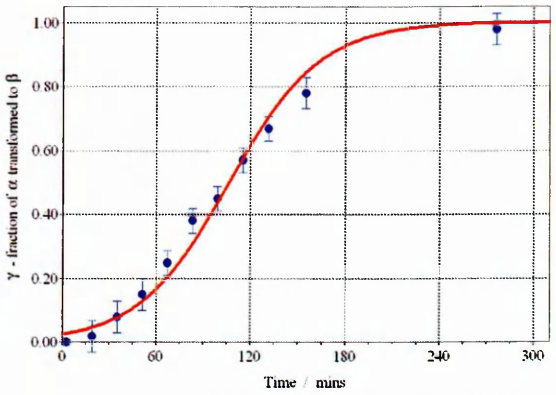

(f) Conversion of 1 % Al-doped ζ_{α}- to ζ_{β}-ferrosilicon at 873 K

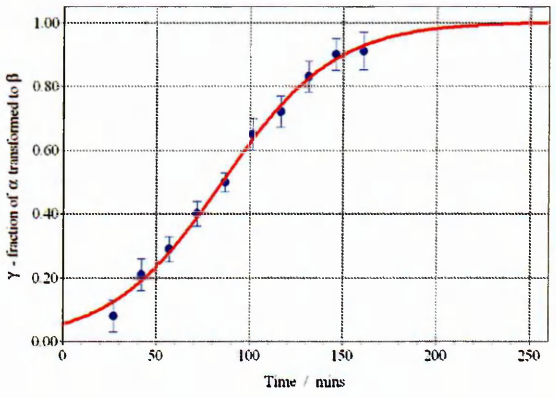

(g) Conversion of 1 % Al-doped ζ_{α}- to ζ_{β}-ferrosilicon at 898 K

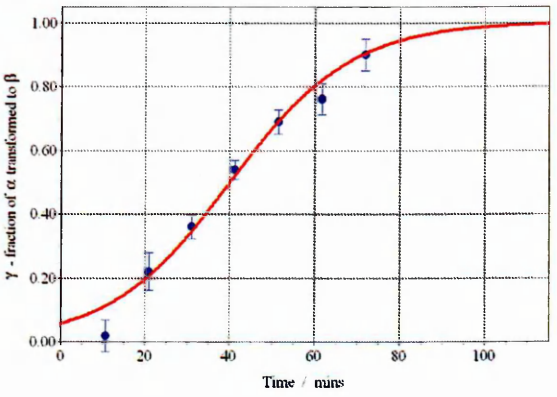

(h) Conversion of 1% Al-doped ζ_{α}- to ζ_{β}-ferrosilicon at 923 K

Figures 4.60e-h: Data from Sections 4.2.2 and 4.2.3 fitted to the Prout-Tompkins model with rate constants as displayed in Table 4.17

4.2.4.3 Comparison of the Avrami-Erofe'ev model and the Prout-Tompkins model

The values of correlation coefficient and standard deviation given in Tables 4.16 and 4.17 indicate that the phase transformation is better represented by the Avrami-Erofe'ev model than the Prout-Tompkins model. Deviations from these models can be more readily seen in the linearised models, *i.e.* by plotting the values of $\ln[-\ln(1-\gamma)]$ against $\ln(t)$ to demonstrate conformance to the Avrami-Erofe'ev model, and plotting the values of $\ln[\gamma/(1-\gamma)]$ against t to demonstrate conformance to the Prout-Tompkins model.

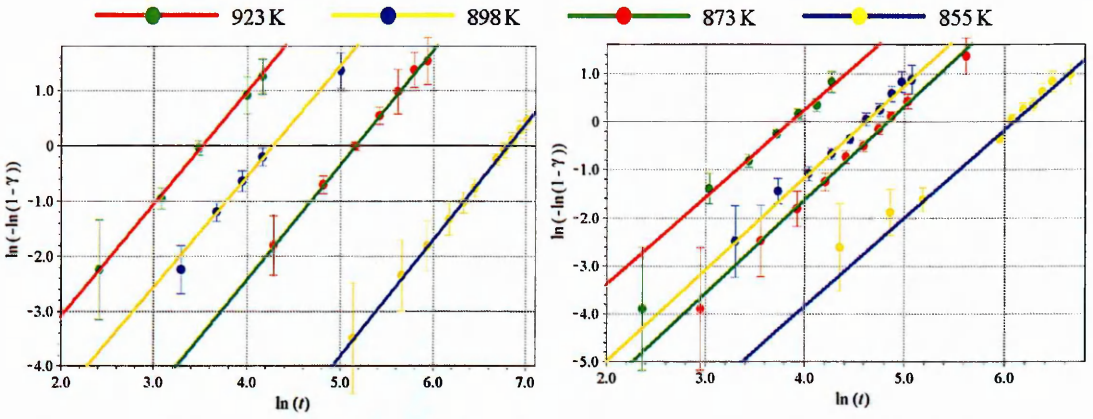

(a) Conversion of ζ_α- to ζ_β-ferrosilicon (undoped) (b) Conversion of 1 % Al-doped ζ_α- to ζ_β-ferrosilicon

Figures 4.61a-b: Data from Sections 4.2.2 and 4.2.3 fitted to straight lines based on the Avrami-Erofe'ev model

The data presented in Sections 4.2.2 and 4.2.3 are shown in Figures 4.61a-b in the form $\ln[-\ln(1-\gamma)]$ against $\ln(t)$ which should give a straight line according to the Avrami-Erofe'ev model. Data points with γ-values of zero have not been plotted. The data for each experiment have been fitted to a straight line using the CurveExpert 1.3 software. By manipulation of Equation 1.12, the gradients of these straight lines will be equal to N, the nucleation constant, and the intercept with the vertical axis will be equal to $N.\ln(k/N)$.

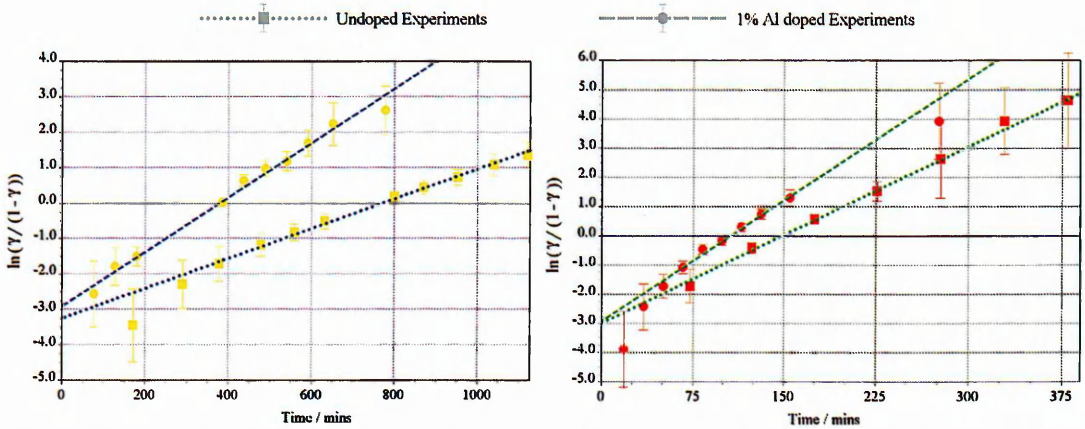

(a) Conversion of ζ_α- to ζ_β-ferrosilicon at 855 K (b) Conversion of ζ_α- to ζ_β-ferrosilicon at 873 K

Figures 4.62a-b: Data from Section 4.2.2 fitted to straight lines based on the Prout-Tompkins model

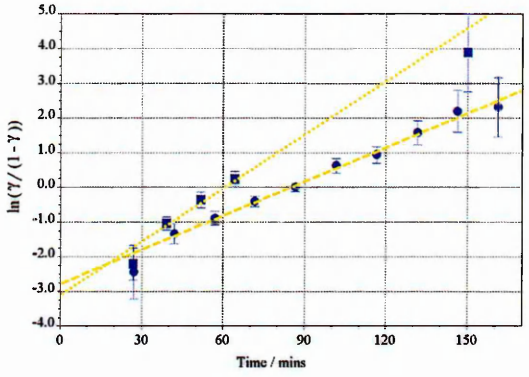

(c) Conversion of ζ_α- to ζ_β-ferrosilicon at 898 K

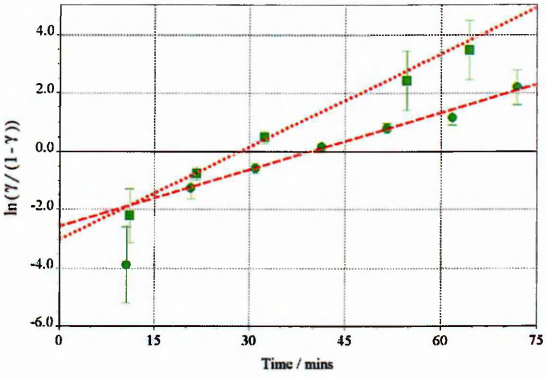

(d) Conversion of ζ_α- to ζ_β-ferrosilicon at 923 K

Figures 4.62c-d: Data from Section 4.2.3 fitted to straight lines based on the Prout-Tompkins model

The data presented in Sections 4.2.2 and 4.2.3 are shown in Figures 4.62a-d in the form $\ln[(\gamma/1-\gamma)]$ against t which should give a straight line according to the Prout-Tompkins model. Data points with γ-values of zero have not been plotted. The data for each experiment have been fitted to a straight line using the CurveExpert 1.3 software. In accordance with Equation 1.22, the gradients of these straight lines will be equal to k_B, the rate constant, and the intercept with the vertical axis will be equal to c, the time correction constant.

The data in Figures 4.61a-b conform more closely to a straight line than the data in Figures 4.62a-d, which further supports the conclusion that the phase transition is better represented by the Avrami-Erofe'ev model rather than the Prout Tompkins model.

The values of the Avrami constants N are all in the region of 2. Assuming that the transition is interface-controlled rather than diffusion controlled, Table 1.1 indicates that an integer value of $N = 2$ can suggest either that the growth is one-dimensional and the nucleation rate is constant, or that the growth is two-dimensional and the nucleation rate is zero (*i.e.* instant saturation). Non-integer values of N are more likely where the

nucleation rate is decreasing, in which case a value of under 2.0 indicates one-dimensional growth and a value of over 2.0 indicates two-dimensional growth[20]. The uncertainty in the values of N given in Table 4.16 are such that it cannot be determined with confidence which of these possibilities is most likely.

Related recent research examining a similar phase transition in ferrosilicon alloys $Fe_{30.7}Mn_{2.5}Si_{66.7}Cu_{0.1}$ and $Fe_{24.7}Mn_{2.5}Si_{70}Cu_{0.1}$ (not using any *in situ* method but annealing unpowdered samples at various temperatures and times and examining at room temperature using X-ray powder diffraction) concluded[21] that both the rate constant k and the Avrami constant N can vary significantly – values of k were calculated between 2.1×10^{-13} and 3.3×10^{-3} and values of N between 0.7 and 3.1 for experiments all carried out at 973 K. These variances were linked to the method of sample preparation, and were attributed to differing grain sizes within the bulk material. Therefore the values presented in Section 4.2.4.1 must be treated with caution.

4.3 High-temperature time-resolved Mössbauer spectroscopy recorded during the phase transition of ζ_α- to ζ_β-ferrosilicon.

4.3.1 Experiment at 855 K

The ^{57}Fe Mössbauer spectra recorded whilst heating ζ_α-ferrosilicon, prepared as described in Section 3.1.1.1(ii), at 855 K using the apparatus described in Section 2.5.6 are shown in Figures 4.63a-g. Each spectrum was fitted using the MFIT software[22], with the combined parameters characteristic of ζ_α-ferrosilicon (as presented in Section 4.1.1.4 and given in Table 4.2) and ζ_β-ferrosilicon (as presented in Section 4.1.4.6 and given in Table 4.13).

The value for γ, the proportion of ζ_α-ferrosilicon transformed into ζ_β-ferrosilicon, was calculated by the MFIT software using least-squares regression to refine the intensities of the two sets of doublets until the fit-index was optimised. The relative proportions of ζ_α- to ζ_β-ferrosilicon in the sample can be taken as the same as the relative proportions of the areas of the doublets in the Mössbauer spectra because the Debye temperatures of the two phases are similar[23].

The time given in minutes under each spectrum is the midpoint in time elapsed since the target temperature was achieved between when the data collection commenced and when data collection ended for that spectrum.

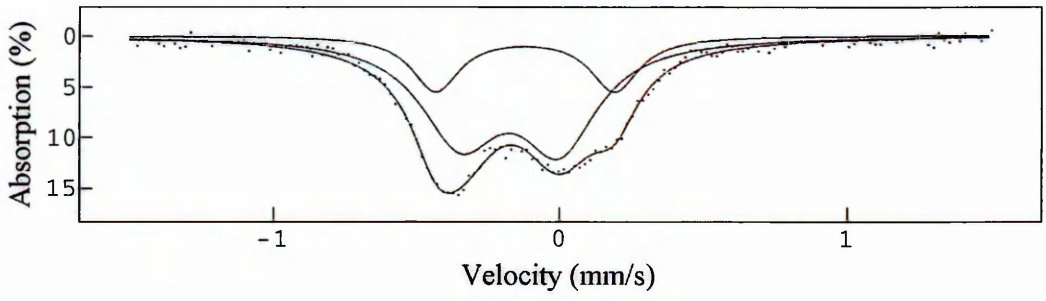

(a) Time = 105 mins ; $\gamma = 0.00 \pm 0.03$

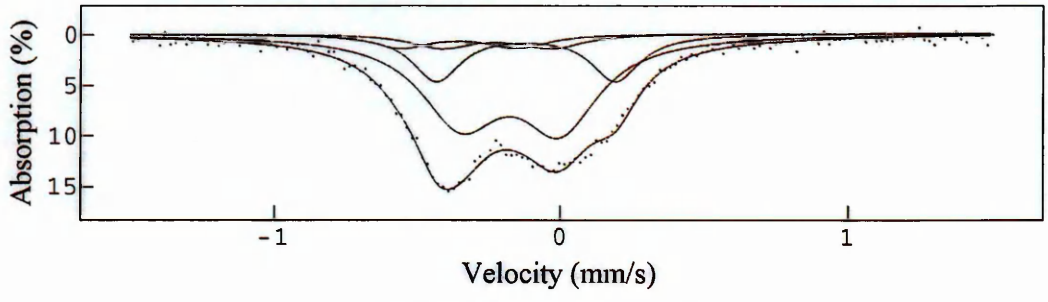

(b) Time = 595 mins ; $\gamma = 0.15 \pm 0.04$

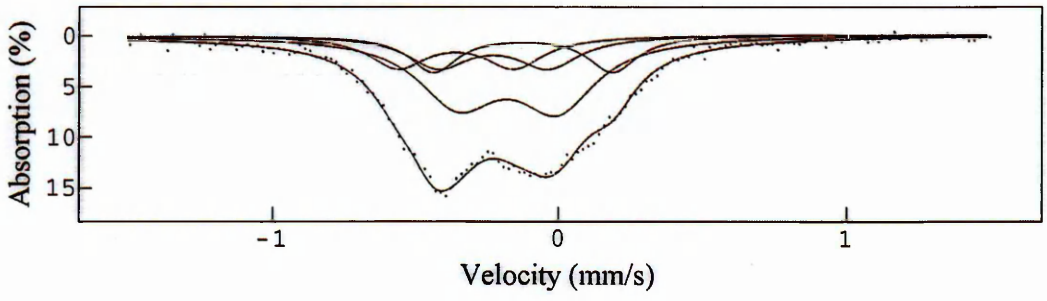

(c) Time = 955 mins ; $\gamma = 0.35 \pm 0.04$

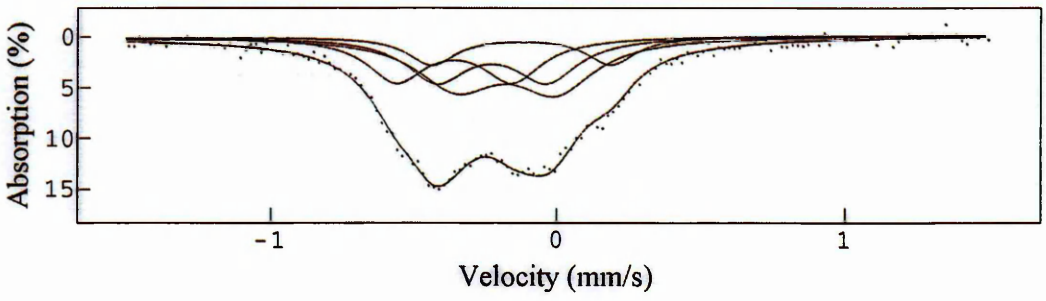

(d) Time = 1195 mins ; $\gamma = 0.50 \pm 0.03$

Figures 4.63a-d: Mössbauer spectra recorded at 855 K during the conversion of ζ_α- to ζ_β-ferrosilicon

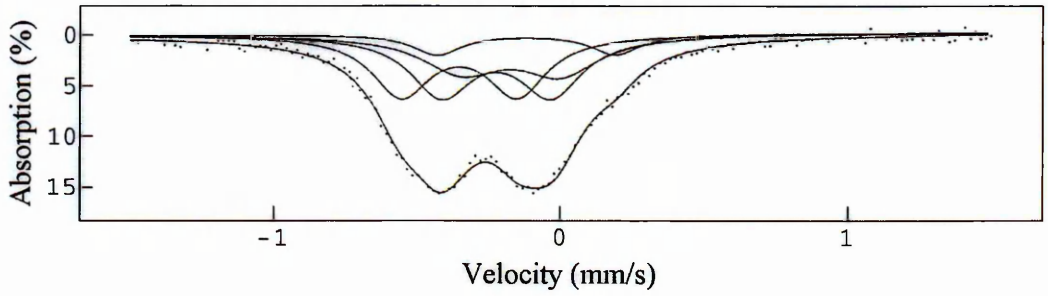

(e) Time = 1495 mins ; $\gamma = 0.65 \pm 0.04$

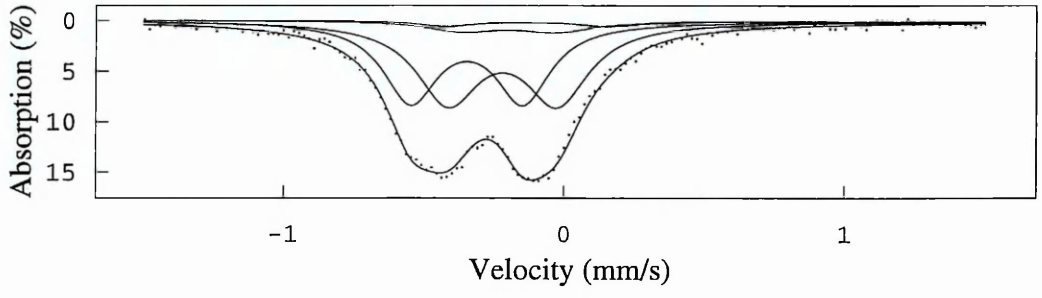

(f) Time = 2090 mins ; $\gamma = 0.85 \pm 0.03$

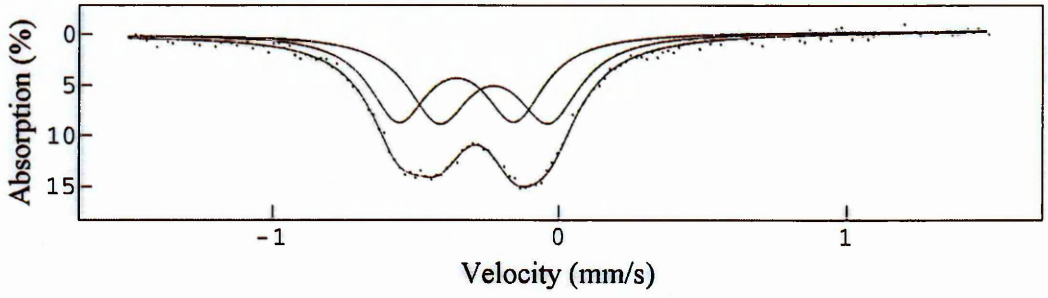

(g) Time = 3770 mins ; $\gamma = 1.00 \pm 0.03$

Figures 4.63e-g: Mössbauer spectra recorded at 855 K during the conversion of ζ_α- to ζ_β-ferrosilicon

4.3.2 Experiment at 873 K

The ^{57}Fe Mössbauer spectra recorded whilst heating ζ_α-ferrosilicon, prepared as described in Section 3.1.1.1(ii), at 873 K using the apparatus described in Section 2.5.6 are shown in Figures 4.64a-g. Each spectrum was fitted using the technique described above in Section 4.3.1 to calculate values for γ, the proportion of ζ_α-ferrosilicon transformed into ζ_β-ferrosilicon.

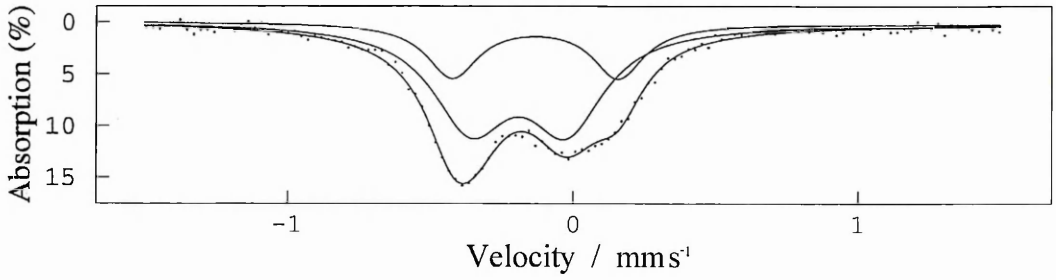

(a) Time = 60 mins ; $\gamma = 0.00 \pm 0.03$

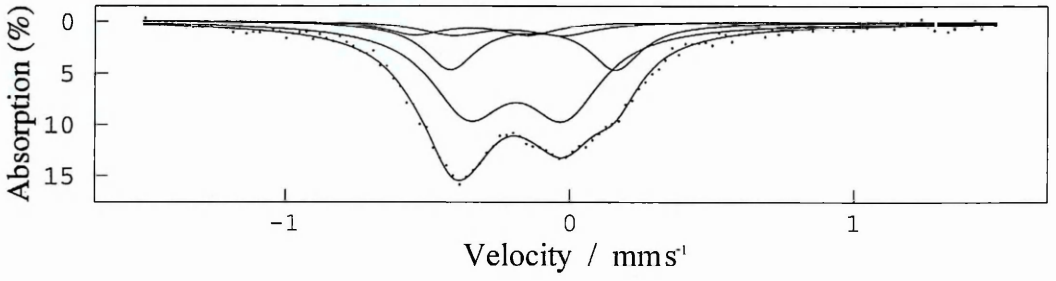

(b) Time = 174 mins ; $\gamma = 0.13 \pm 0.03$

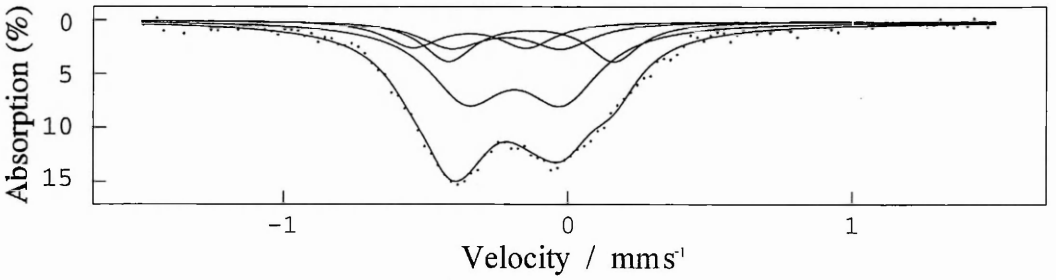

(c) Time = 280 mins ; $\gamma = 0.27 \pm 0.04$

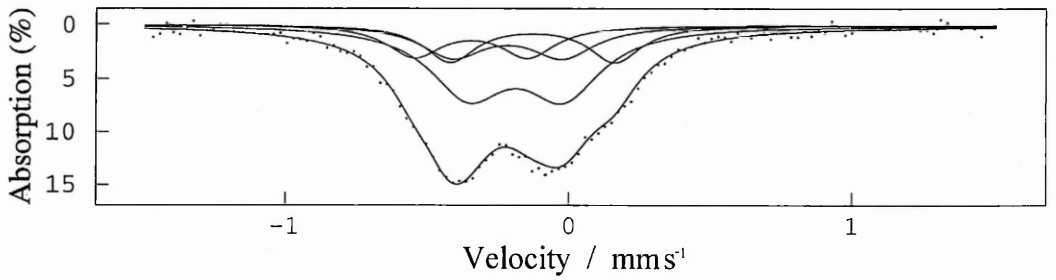

(d) Time = 385 mins ; $\gamma = 0.38 \pm 0.06$

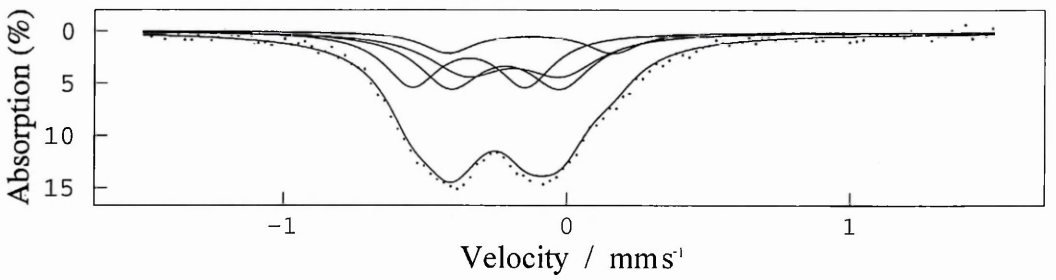

(e) Time = 550 mins ; $\gamma = 0.62 \pm 0.07$

Figures 4.64a-e: Mössbauer spectra recorded at 873 K during the conversion of ζ_{α}- to ζ_{β}-ferrosilicon

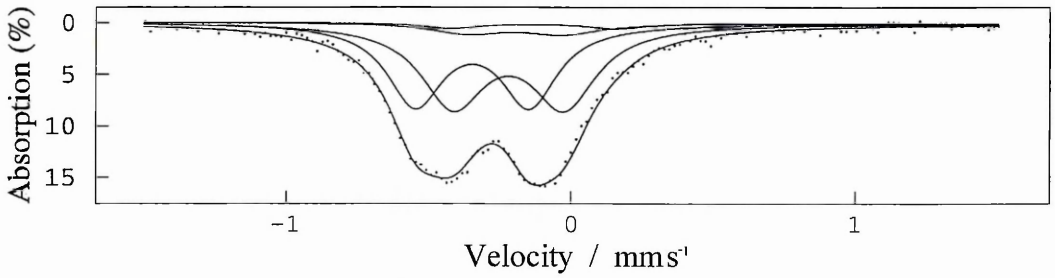

(f) Time = 982 mins ; $\gamma = 0.87 \pm 0.05$

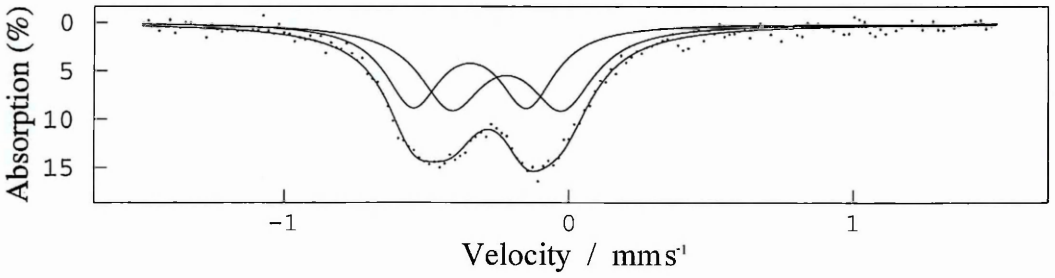

(g) Time = 1750 mins ; $\gamma = 1.00 \pm 0.04$

Figures 4.64f-g: Mössbauer spectra recorded at 873 K during the conversion of ζ_α- to ζ_β-ferrosilicon

4.3.3 Analysis of high Temperature Mössbauer spectroscopy experiments

The values for γ, the fraction of ζ_α-ferrosilicon transformed into ζ_β-ferrosilicon, in the experiment at 855 K are plotted against time in Figure 4.65. The values for γ in the experiment at 873 K are plotted against time in Figure 4.66. In each case the data were fitted using the CurveExpert1.3 software package to the Avrami-Erofe'ev model outlined in Section 1.3 and identified as the most appropriate to this phase transition in Section 4.2.4.3.

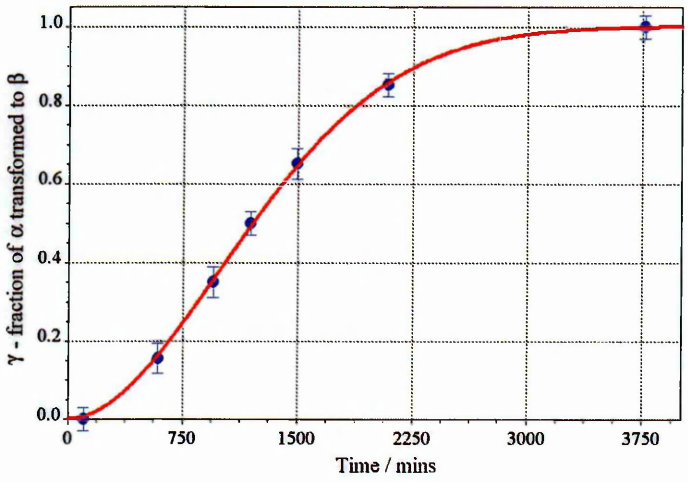

Figure 4.65: Fraction of ζ_α-ferrosilicon transformed into ζ_β-ferrosilicon during the experiment at 855 K measured by Mössbauer spectroscopy and plotted against time

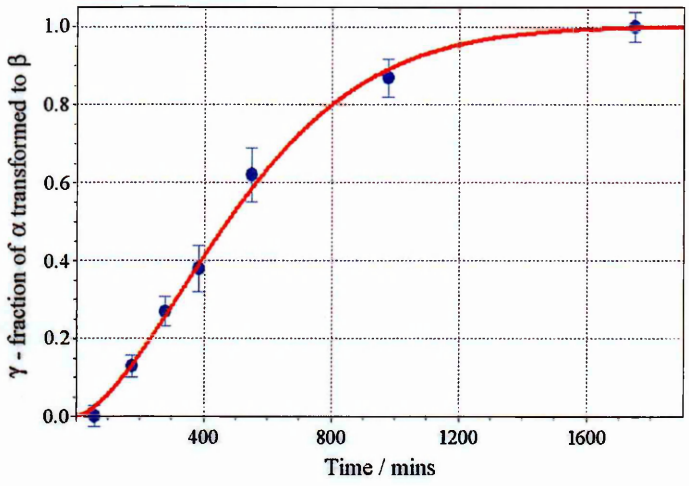

Figure 4.66: Fraction of ζ_α-ferrosilicon transformed into ζ_β-ferrosilicon during the experiment at 873 K measured by Mössbauer spectroscopy and plotted against time

The constants thus derived are shown in Table 4.18:

Experiment Temperature / K	k / min^{-1}	N	Correlation Coefficient	Standard Deviation
855	0.0013 ± 0.0001	1.90 ± 0.04	0.99896	0.0485
873	0.0027 ± 0.0004	1.60 ± 0.06	0.99851	0.0225

Table 4.18: Values of k and N derived from the experiments presented in Sections 4.3.1 and 4.3.2 using the Avrami-Erofe'ev theory

These values are significantly different from those calculated from the data recorded at 855 K and 873 K using simultaneous X-ray powder diffraction and Fe K-edge EXAFS (see Table 4.16). As expected from the different k and N values, the timescales in Figures 4.65 and 4.66 are very different from the equivalent graphs in Figures 4.59a and 4.59b.

A possible reason for the observed differences is that they are associated with the significant differences in grain size in the two experiments. The high-temperature Mössbauer spectroscopy experiments were carried out before the combined XRD/EXAFS experiments. In the Mössbauer spectroscopy experiments the sample was ground to a

powder, the grain size of which was not measured at the time but has subsequently been estimated to be of the order of 100 μm. In the XRD/EXAFS experiments which were carried out later, a very fine grain size is required for making the sample pellets in order to ensure the sample is uniform. The grain size used in the XRD/EXAFS experiments was estimated to be <10 μm as individual grains were not resolvable when viewed under a microscope at 50x magnification.

It was not feasible to repeat the Mössbauer spectroscopy experiments using a smaller grain size to provide more readily comparable results. However, the variance in the rate of the phase transformation with differing grain sizes is investigated qualitatively in Section 4.5.

4.4 Kinetics and mechanisms of the phase transition of ζ_α- to ζ_β-ferrosilicon

4.4.1 Kinetics and mechanisms of the phase transition of ζ_α- to ζ_β-ferrosilicon as observed by high-temperature time-resolved combined X-ray powder diffraction and Fe K-edge EXAFS

Table 4.19 shows the values of the rate constant k and Avrami mechanism constant N calculated from the results of the high-temperature time-resolved combined X-ray powder diffraction and Fe K-edge EXAFS experiments using undoped ferrosilicon.

Temperature / K	k / min^{-1}	N
855	0.0023 ± 0.0006	2.12 ± 0.28
873	0.012 ± 0.003	2.11 ± 0.35
898	0.031 ± 0.008	2.17 ± 0.32
923	0.061 ± 0.004	2.07 ± 0.10

Table 4.19: Constants derived from the results of time-resolved combined Fe K-edge EXAFS and XRD measurements during the phase transition of ζ_α- to ζ_β-ferrosilicon as presented in Section 4.2.2

All the values of N in the above table are in the region of a value of 2.1. As discussed in Section 4.2.4.3, this could mean that either that the growth is one-dimensional and the nucleation rate is constant, or that the growth is two-dimensional and the nucleation rate is zero or decreasing (c.f. Table 1.1).

The values of the rate constant k are plotted against temperature in Figure 4.67.

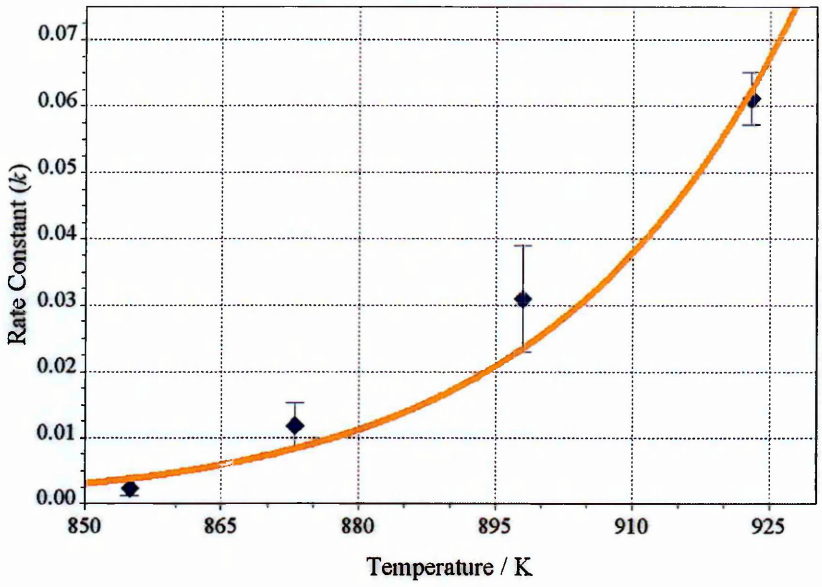

Figure 4.67: Values of rate constant k calculated from the results of time-resolved combined Fe K-edge EXAFS and XRD measurements during the conversion of ζ_α- to ζ_β-ferrosilicon, plotted against temperature

The data were fitted using the CurveExpert 1.3 software package to the Arrhenius equation,

$$k = C.\exp\left(-\frac{\varepsilon}{RT}\right)$$

the relevance of which is described in Section 1.3.4.4. A best fit line to these data was found with a value for constant C of $1.28\text{x}10^{14}$ and activation energy ε equal to 271 kJmol^{-1}. The correlation coefficient was 0.9815 with a standard deviation in k of 0.0062. However, acceptable fits to these data were possible over a wide range of values for C and ε, due to the small number of data points, and the statistical interdependence of the two parameters, with values for C between $3\text{x}10^{9}$ and $3\text{x}10^{16}$ and values for ε between 190 kJmol^{-1} and 310 kJmol^{-1}. A more extensive study would be required in order to calculate the value of activation energy ε with more confidence.

In general terms, the calculated activation energy is comparable to values for activation energies of other phase transitions in iron-containing materials obtained by other experimental methods. For example, a study examining a phase transition in Fe_3Al determined[24] an activation energy of 185 – 263 kJmol^{-1}, and in a study examining a phase transition in

stainless steel alloys (containing iron at *ca.* 72 at% and varying proportions of chromium, nickel, silicon and manganese) determined[25] an activation energy of 366 – 462 kJmol^{-1}.

4.4.2 Kinetics and mechanisms of the phase transition of 1 % Al-doped ζ_α- to ζ_β-ferrosilicon as observed by high-temperature time-resolved combined X-ray powder diffraction and Fe K-edge EXAFS

Table 4.20 shows the values of the rate constant k and Avrami mechanism constant N calculated from the results of the high-temperature time-resolved combined X-ray powder diffraction and Fe K-edge EXAFS experiments using 1% Al-doped ferrosilicon.

Temperature / K	k / min^{-1}	N
855	0.0042 ± 0.0004	1.88 ± 0.09
873	0.016 ± 0.002	1.96 ± 0.12
898	0.019 ± 0.001	1.94 ± 0.09
923	0.0386 ± 0.002	1.85 ± 0.08

Table 4.20: Constants derived from the results of time-resolved combined Fe K-edge EXAFS and XRD measurements during the conversion of 1 % Al-doped ζ_α- to ζ_β-ferrosilicon as presented in Section 4.2.3

The values of N in the above table are more variable than those shown in Table 4.15 for the experiments using undoped ferrosilicon. However, there is no trend in the variance. The values are all slightly below 2.0. According to the kinetic theory outlined in Section 1.3, this probably implies that the growth of the new phase is one dimensional, and that the nucleation rate is decreasing. It is also possible that the growth of the new phase is two dimensional with a zero nucleation rate (that is, instant saturation of nucleation sites), or that the growth of the new phase is one dimensional, and that the nucleation rate is constant, but in these cases the value of N will theoretically not fall below 2.0 (see Table 1.1). Within experimental uncertainty the values of N in Table 4.20 do encompass the value of 2.0 therefore

these possibilities cannot be discounted.

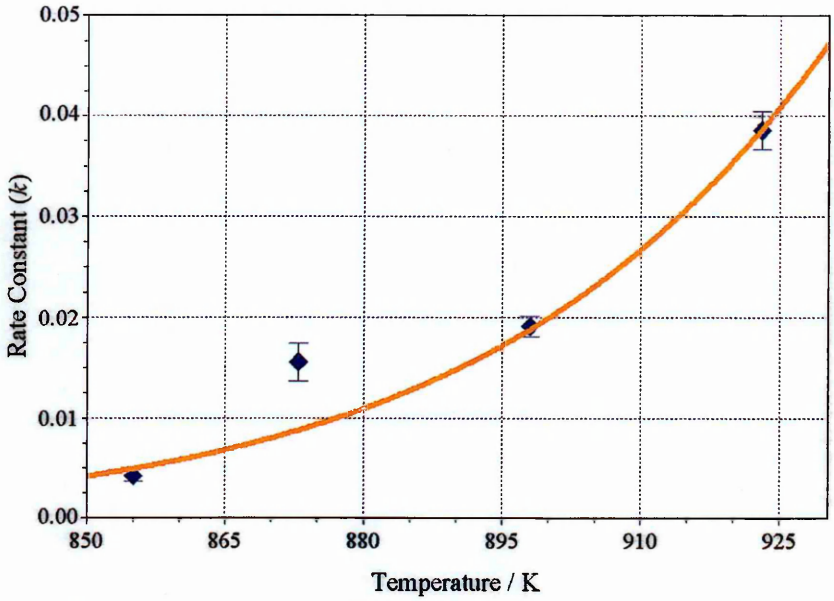

Figure 4.68: Values of rate constant k calculated from the results of time-resolved combined Fe K-edge EXAFS and XRD measurements during the conversion of 1 % Al-doped ζ_{α}- to ζ_{β}-ferrosilicon, plotted against temperature

The values of the rate constant k shown above are plotted against temperature in Figure 4.68. The data were fitted using the CurveExpert 1.3 software package to the Arrhenius equation,

$$k = C.\exp\left(-\frac{\varepsilon}{RT}\right).$$

The software could not initially find an acceptable fit. Therefore, the point representing the experiment carried out at 873 K was excluded as it lies significantly off the trend line of the other experiments. This enabled an acceptable fit to be identified. A best fit line to these data was found with a value for constant C of 7.11×10^{9} and a value for activation energy ε equal to 199 kJmol^{-1}. The correlation coefficient was 0.9995 with a standard deviation in k of 0.00077. However, as was found in the case of the undoped experiments presented in the previous Section, acceptable fits to these data were possible over a wide range of values for C and ε. Values for C were found between 5×10^{7} and 9×10^{15}, and values for ε between 160 kJmol^{-1} and 305 kJmol^{-1}.

4.5 Phase evolution of heated ferrosilicon of varying grain size

The results presented in Section 4.3 showed that the time-resolved measurements performed using Mössbauer spectroscopy were not directly comparable to the time-resolved measurements performed using combined XRD and EXAFS. It was suggested that this could be attributable to the difference in grain sizes, as the pellets in the XRD/EXAFS experiments used a more finely ground powder than is generally used in a Mössbauer Spectroscopy experiment. Ideally, the Mössbauer Spectroscopy experiment would be repeated with a much smaller grain size or a combined XRD/EXAFS experiment would be carried out with a larger grain size. Unfortunately, neither of these options was practicable.

The following sections describe the results of some basic experiments aimed at gaining a qualitative appreciation of the effect of grain size on the phase transition. Samples were prepared as described in Section 3.1.1.3(i). X-ray diffraction patterns were recorded using the techniques described in Section 2.2.7.

The data quality for this type of measurement is insufficient for quantitative methods of analysis such as Rietveld refinement. In all cases a figure for γ, the fraction of ζ_α-ferrosilicon converted to ζ_β-ferrosilicon, has been estimated by comparing the intensities of the major peaks characteristic of ζ_α-ferrosilicon with the intensities of the major peaks characteristic of ζ_β-ferrosilicon. This operational approach gives only a rough appreciation of the actual proportions of ζ_α- and ζ_β-ferrosilicon in the sample, but this is sufficient for the purpose of these experiments.

4.5.1 Conversion of ζ_α- to ζ_β-ferrosilicon with large grain size

The X-ray powder diffraction patterns recorded from undoped ζ_α-ferrosilicon with a silicon content of 54.0 % and with a grain size between 125 and 250 μm heated at 898 K

for 120, 240, 360, 540 and 1260 minutes are shown in Figure 4.69.

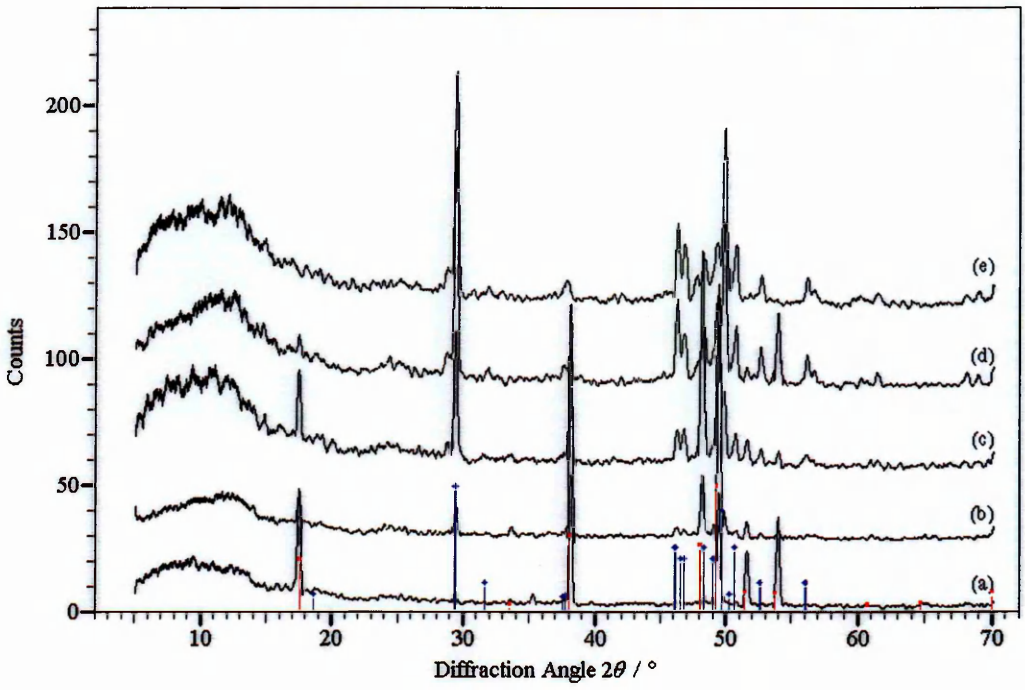

Figure 4.69: The X-ray powder diffraction patterns recorded from samples of ζ_α-ferrosilicon with a silicon content of 54.0 % and grain size between 125 and 250 μm heated at 898 K for (a) 120 mins (b) 240 mins (c) 360 mins (d) 540 mins and (e) 1260 mins.

Examination of the major peaks characteristic of ζ_α-ferrosilicon at 2θ = 17.5 and 38°, and the major peak characteristic of ζ_β-ferrosilicon at 2θ = 29.3°, indicate the following estimates of values for γ, the fraction of ζ_α-ferrosilicon converted to ζ_β-ferrosilicon:

Time at 898 K / mins	Extent of the phase transition	Estimate of γ
120	Just started, ζ_β-$FeSi_2$ peak barely visible	0.03
240	ζ_β-$FeSi_2$ peak has over doubled in intensity	0.10
360	Phase transition about 50% complete	0.50
540	Phase transition almost complete	0.90
1260	Phase transition complete	1.00

Table 4.21: Estimates of the extent of the phase transition of ζ_α- to ζ_β-ferrosilicon in samples with grain size between 125 and 250μm

4.5.2 Conversion of ζ_α- to ζ_β-ferrosilicon with medium grain size

The X-ray powder diffraction patterns recorded from undoped ζ_α-ferrosilicon with a silicon content of 54.0 % and with a grain size between 70 and 125 μm heated at 898 K for 120, 240, 360, 540 and 1260 minutes are shown in Figure 4.70.

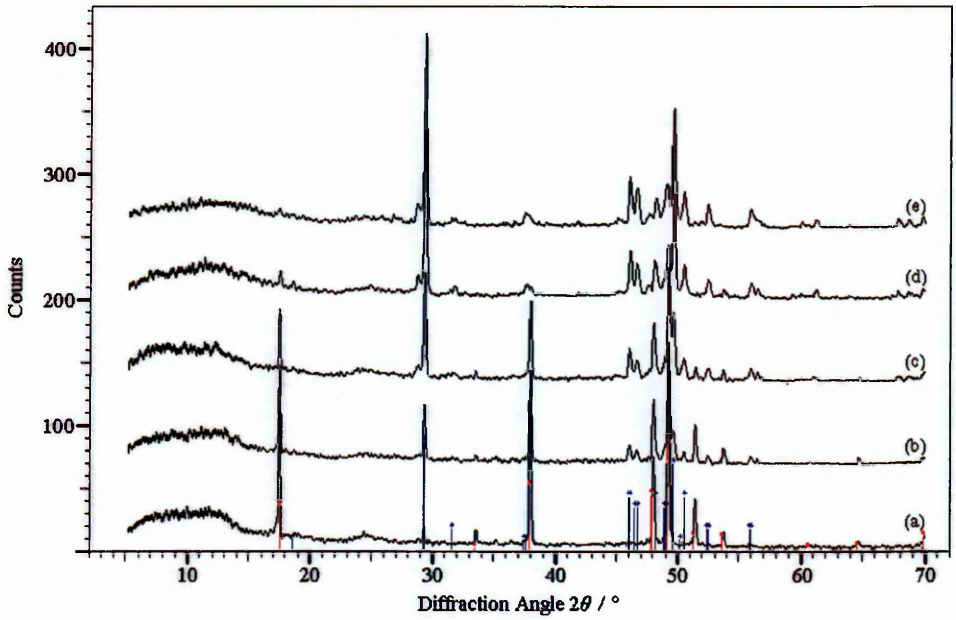

Figure 4.70: The X-ray powder diffraction patterns recorded from samples of ζ_α-ferrosilicon with a silicon content of 54.0 % and grain size between 70 and 125 μm heated at 898 K for (a) 120 mins (b) 240 mins (c) 360 mins (d) 540 mins and (e) 1260 mins.

Examination of the major peaks characteristic of ζ_α-ferrosilicon at 2θ = 17.5 and 38°, and the major peak characteristic of ζ_β-ferrosilicon at 2θ = 29.3°, indicate the following estimates of values for γ, the fraction of ζ_α-ferrosilicon converted to ζ_β-ferrosilicon:

Time at 898K / mins	Extent of the phase transition	Estimate of γ
120	Just started, ζ_β-$FeSi_2$ peak barely visible	0.05
240	ζ_β-$FeSi_2$ peak about quadrupled in intensity	0.20
360	Phase transition somewhat over 50% complete	0.60
540	Phase transition complete	1.00
1260	Phase transition complete	1.00

Table 4.22: Estimates of the extent of the phase transition of ζ_α- to ζ_β-ferrosilicon in samples with grain size between 70 and 125 μm

4.5.3 Conversion of ζ_α- to ζ_β-ferrosilicon with small grain size

The X-ray powder diffraction patterns recorded from undoped ζ_α-ferrosilicon with a silicon content of 54.0 % and with a grain size less than 70 μm heated at 898 K for 120, 240, 360, 540 and 1260 minutes are shown in Figure 4.71.

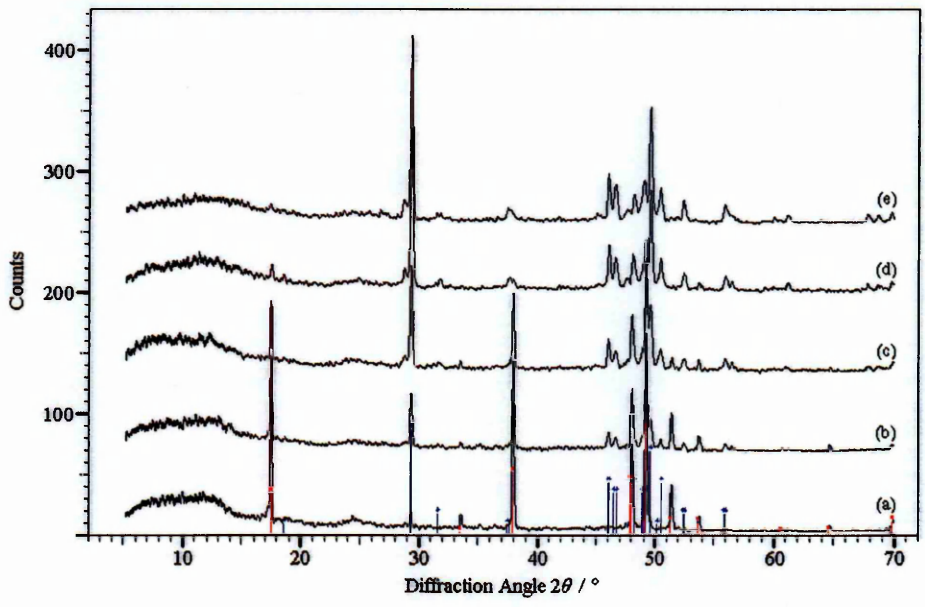

Figure 4.71: The X-ray powder diffraction patterns recorded from samples of ζ_α-ferrosilicon with a silicon content of 54.0 % and grain size less than 70 μm heated at 898 K for (a) 120 mins (b) 240 mins (c) 360 mins (d) 540 mins and (e) 1260 mins.

Examination of the major peaks characteristic of ζ_α-ferrosilicon at 2θ = 17.5 and 38°, and the major peak characteristic of ζ_β-ferrosilicon at 2θ = 29.3°, indicate the following estimates of values for γ, the fraction of ζ_α-ferrosilicon converted to ζ_β-ferrosilicon:

Time at 898K / mins	Extent of the phase transition	Estimate of γ
120	Just started, ζ_β-$FeSi_2$ peak visible but small	0.08
240	Phase transition somewhat over 50% complete	0.55
360	Phase transition almost complete	0.80
540	Phase transition complete	1.00
1260	Phase transition complete	1.00

Table 4.23: Estimates of the extent of the phase transition of ζ_α- to ζ_β-ferrosilicon in samples with grain size less than 70 μm

4.5.4 Effect of grain size on the phase transition

The estimates for the extent of the phase transition given above are shown plotted against time in minutes in Figure 4.72.

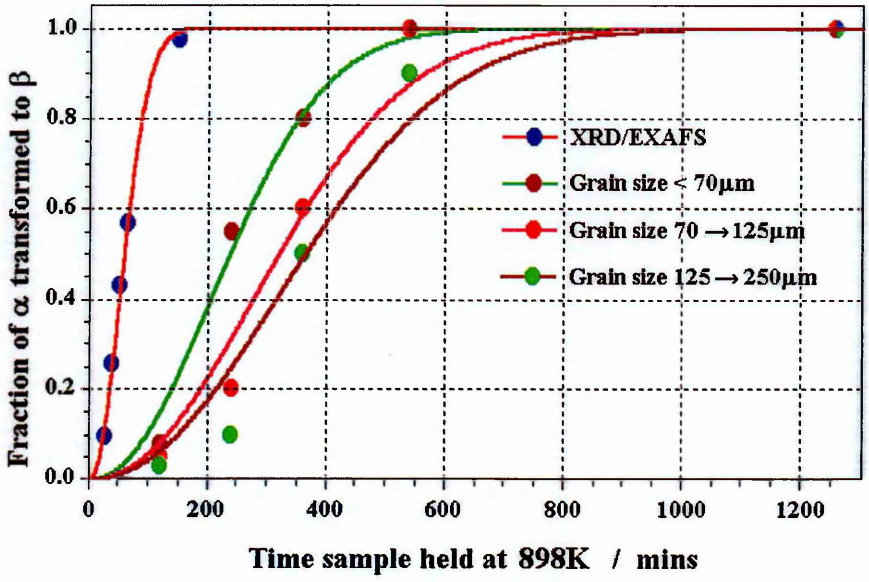

Figure 4.72: Fraction of ζ_α-ferrosilicon transformed to ζ_β-ferrosilicon for experiments at 898 K with various grain sizes

The data obtained by time-resolved combined X-ray powder diffraction and Fe K-edge EXAFS, as described in Section 4.2.2.3 (for which experiments the sample was very finely powdered and formed into a pellet with boron nitride at high pressure) are also shown. These data were fitted using the CurveExpert1.3 software package to the Avrami model outlined in Section 1.3:

$$k.t = N\left[-\ln(1-\gamma)\right]^{1/N}$$

the nucleation constant N was constrained to 2.1, the value typical of the results obtained from the combined X-ray powder diffraction and Fe K-edge EXAFS experiments described in Section 4.2.2.3.

The values of k for each curve are shown below.

Experiment	k / min^{-1}
XRD/EXAFS	0.031
Grain < 70μm	0.008
Grain 70 → 125μm	0.006
Grain 125 → 250μm	0.005

Table 4.24: Values of rate constant k

The large variation in the constant k for the different grain sizes indicates that the grain size used influences the experimental results. This result implies that experiments using different grain sizes cannot be meaningfully compared.

In the Arrhenius equation governing the value of rate constant k

$$k = C.\exp\left(-\frac{\varepsilon}{RT}\right)$$

the quantity C is often regarded as having empirical rather than theoretical significance[26], as it is the solid-state equivalent of the frequency factor, *i.e.* the frequency of occurrence of the reaction configuration. It seems likely that in this phase transition the value of C must depend in some way on particle size. This is an area for further work.

References for Chapter Four

1 JCPDS reference for ζ_α-ferrosilicon 35-0822.

2 JCPDS reference for ε-FeSi 79-0619.

3 ICSD reference for ζ_α-ferrosilicon 42561 (54380). F.A. Sidorenko, P.V. Gel'd, L.B. Dubrovskaya, *Fizika Metallov i Metallovedenie* 1959 **8** 88.

4 CRAD software on xrsserv1 © Daresbury Laboratory.

5 Ö. Helgason, Th. Magnusson, Th.I. Sigfusson *Hyperfine Interactions* 1998 **111** 215.

6 C. Blaauw, F. van der Woude, G.A. Sawatzky *J. Phys. C: Solid State Phys.* 1973 **6** 2371.

7 JCPDS reference for metallic silicon 27-1402.

8 A.V. Sabirzyanov, M A Shumilov, P V Gel'd, G.V. Ozhgikhina *Fiz. Metal. Metalloved* 1961 **12** 714.

9 JCPDS reference for ζ_β-$FeSi_2$ 20-0532.

10 ICSD reference for ζ_β-$FeSi_2$ 9119 (3440). Y. Dusausoy, J. Protas *Acta Cryst. B* 1971 **27** 1209.

11 ICSD reference for α-SiO_2 74529 (39330). D.J. Lacks, R.G. Gordon *Phys. Rev. 3B* 1993 **48** 2889.

12 J. van den Boomgaard *J. Iron and Steel Institute* 1962 p.1024.

13 ICSD reference for metallic silicon 41979 (54014). C. Filippi, D.J. Singh, C.J. Umrigar, *Phys. Rev. 3B* 1994 **50** 14947.

14 JCPDS reference for metallic iron 87-0721.

15 R.W. Joyner, K.J. Martin, P. Meehan *J. Phys. C: Solid State Phys.* 1987 **20** 4005.

16 A. Filipponi *J. Phys.: Condens. Matter* 1995 **7** 9343.

17 O. Helgason, B.J. Jóhannesson, B. Purser, F.J. Berry *Mössbauer Spectroscopy in Material Science* 1999 **66** 13.

18 F.J. Berry, B. Purser, R.I Bilsborrow, A.J. Dent, Ö. Helgason, B. Jóhannesson *Synchrotron Radiation Department Annual Report* 1997-1998 p366.

19 CurveExpert Software © Hyams Development – http://curveexpert.webhop.net/

20 C. H. Bamford, C. F. H. Tipper (eds.) *Comprehensive Chemical Kinetics vol. 22: Reactions in the Solid State* 1st ed. Elsevier Scientific Publishing 1980 The Netherlands p71.

21 T. J. Zhu, X. B. Zhao, L. Lü *Philosophical Magazine* 2003 **83** 2865.

[22] MFIT Software © Science Institute, University of Iceland. Author K. Jónsson.

[23] Th. I. Sigfusson, Ö. Helgason *Hyperfine Interactions* 1990 **54** 861.

[24] G. Frommeyer, C. Derder, and J. A. Jiménez *Materials Science and Technology* 2002 **18** 981.

[25] B. Boubeker, J.P. Eymery, P. Auric, M. Rahmoune *Nuclear Instruments and Methods in Physics Research B* 1995 **101** 267.

[26] C. H. Bamford, C. F. H. Tipper (eds.) *Comprehensive Chemical Kinetics vol. 22: Reactions in the Solid State* 1st ed. Elsevier Scientific Publishing 1980 The Netherlands p92.

Chapter Five: Results and Discussion – Mullite

5.1 Phase analysis of mullite precursors and related materials

5.1.1 Phase analysis of the gel formed by hydrothermal processing of aluminium acetate

The flat-plate X-ray powder diffraction pattern recorded using Cu-K_α radiation (λ = 1.54 Å) at *ca.* 295 K from the gel made by hydrothermal processing of aluminium acetate as described in Section 3.1.2.1 is shown in Figure 5.1. The red lines indicate the positions of the peaks characteristic of boehmite[1].

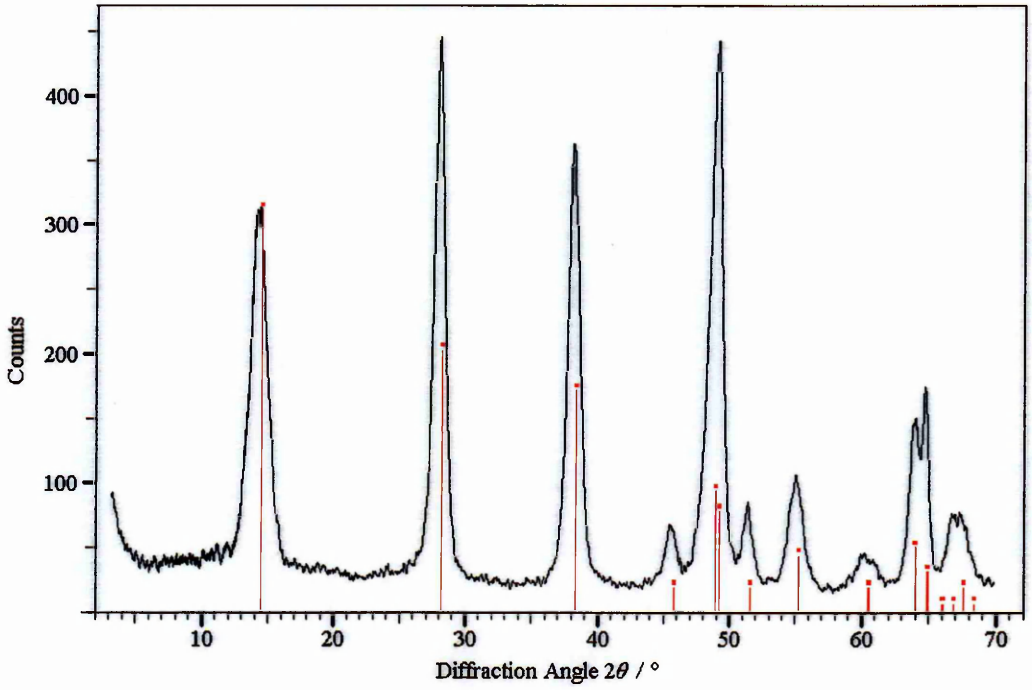

Figure 5.1: X-ray powder diffraction pattern recorded from the gel made by hydrothermal processing of aluminium acetate as described in Section 3.1.2.1

The peak widths are relatively broad, which suggests that the particle size may be small or the sample may be poorly crystalline. The recorded peaks are at a slightly lower angle than those in the literature. This could be attributable to increased interatomic distances due to the presence of intercalated water molecules. This would indicate that the sample is pseudoboehmite rather than boehmite (see Section 1.2.2.5).

5.1.2 Phase analysis of the gel formed by hydrothermal processing of silicon acetate.

The flat-plate X-ray powder diffraction pattern recorded using Cu-K_α radiation (λ = 1.54 Å) at *ca.* 295 K from the gel made by hydrothermal processing of silicon acetate as described in Section 3.1.2.1 is shown in Figure 5.2. The red line indicates the position of the single broad peak at $2\theta = 22°$ characteristic of poorly-crystalline silica[2], corresponding to a value of $d = 4.04$ Å.

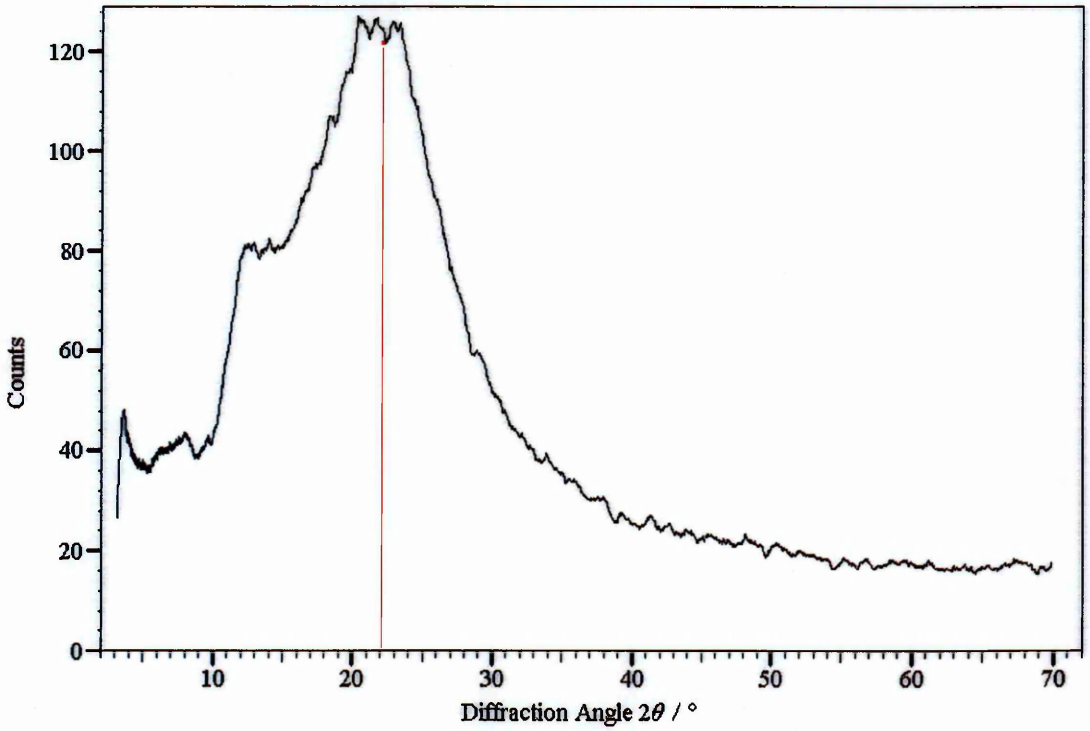

Figure 5.2: X-ray powder diffraction pattern recorded from the gel made by hydrothermal processing of silicon acetate as described in Section 3.1.2.1

5.1.3 Phase analysis of the gel formed by hydrothermal processing of iron(II) acetate

The flat-plate X-ray powder diffraction pattern recorded using Cu-K_α radiation (λ = 1.54 Å) at *ca.* 295 K from the gel made by hydrothermal processing of iron(II) acetate as described in Section 3.1.2.1 is shown in Figure 5.3. The blue lines indicate the positions of the peaks characteristic of hematite[3] (α-Fe_2O_3).

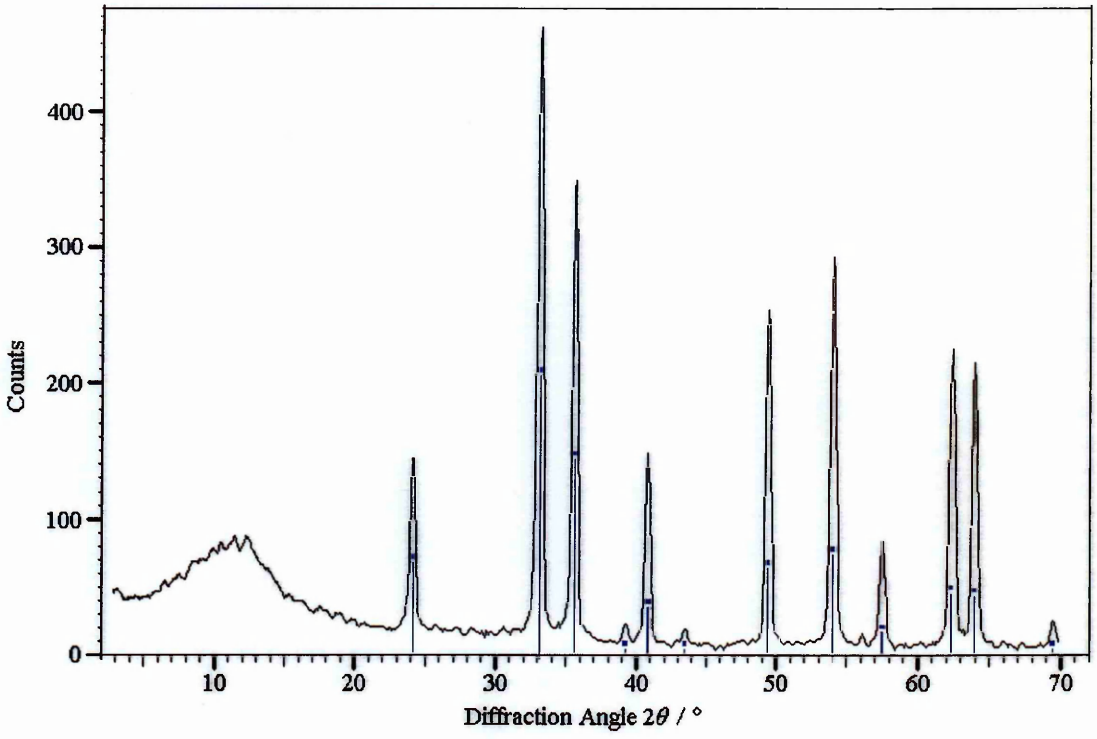

Figure 5.3: X-ray powder diffraction pattern recorded from the gel made by hydrothermal processing of iron(II) acetate as described in Section 3.1.2.1

5.1.4 Phase analysis of the gel formed by hydrothermal processing of vanadium(III) acetylacetonate

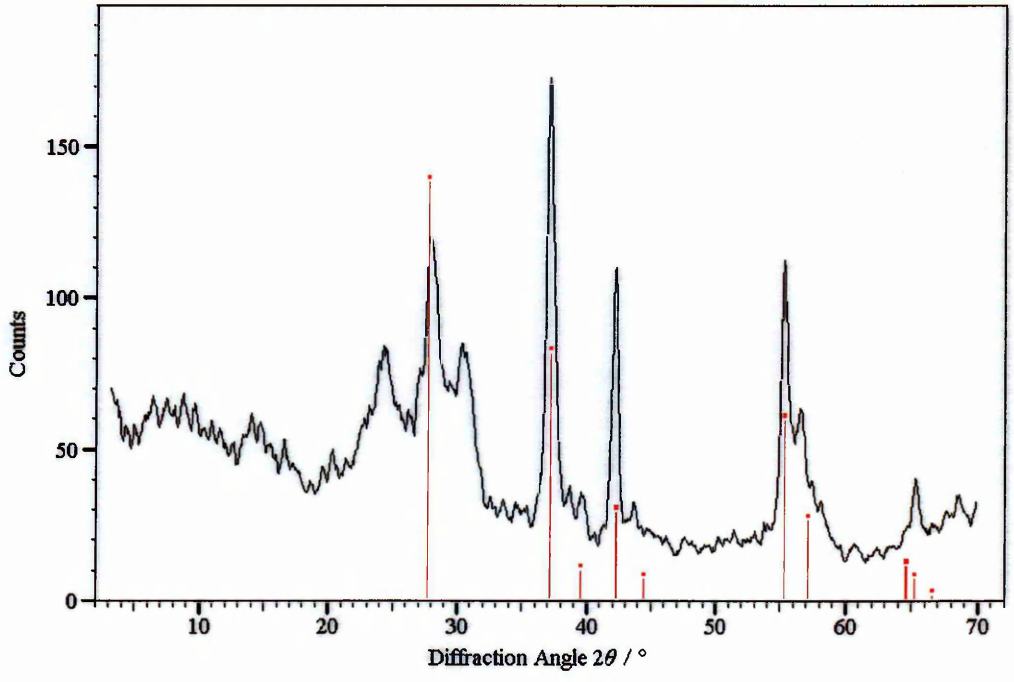

Figure 5.4: X-ray powder diffraction pattern recorded from the gel formed by hydrothermal processing of vanadium(III) acetylacetonate as described in Section 3.1.2.1

The flat-plate X-ray powder diffraction pattern recorded using Cu-K_α radiation (λ = 1.54 Å)

at *ca.* 295 K from the gel formed by hydrothermal processing of vanadium acetylacetonate as described in Section 3.1.2.1 is shown in Figure 5.4. The red lines indicate the positions of the peaks characteristic of vanadium(II) oxide[4].

5.1.5 Phase analysis of the gel formed by hydrothermal processing of undoped aluminium- and silicon-acetates.

5.1.5.1 X-Ray powder diffraction

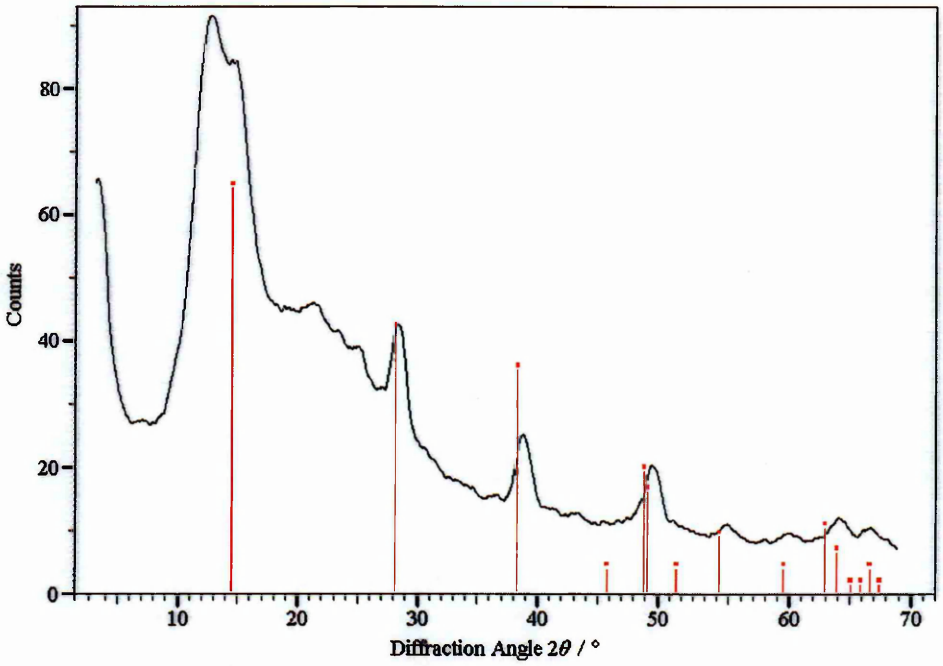

Figure 5.5: X-ray powder diffraction pattern recorded from the gel formed by hydrothermal processing of undoped aluminium- and silicon-acetates as described in Section 3.1.2.1

The flat-plate X-ray powder diffraction pattern recorded using Cu-K_α radiation (λ = 1.54 Å) at *ca.* 295 K from the gel made by hydrothermal processing of undoped aluminium- and silicon-acetates as described in Section 3.1.2.1 is shown in Figure 5.5. The red lines indicate the positions of the peaks characteristic of boehmite[1].

The very broad peak widths and very low count rates indicate a highly disordered structure. It is interesting to compare this pattern to that presented in Section 5.1.1, the X-ray powder

diffraction pattern recorded from the gel made by hydrothermal processing of aluminium acetate. Both patterns indicate a structure characteristic of pseudoboehmite (*i.e.* boehmite with intercalated water as described in Section 1.2.2.5). However, the pattern shown in Figure 5.5 indicates a significantly lower degree of crystallinity than that shown in Figure 5.1.

The peaks in the pattern shown in Figure 5.5 are generally at a slightly higher angle than those characteristic of boehmite. This indicates a decrease in unit cell size so cannot be explained by the presence of intercalated water, which would tend to increase the unit cell dimensions.

The silicon—oxygen bond length[5], 1.53 Å, is slightly lower than the aluminium—oxygen bond length[6], 1.62 Å. If a significant proportion of silicon is occupying aluminium positions in a pseudoboehmite-type structure, interatomic distances would decrease and diffraction angles would therefore be expected to increase by a small amount in the region of 1-3° in 2θ. This model could also explain the broader diffraction peaks and lower peak intensity seen in Figure 5.5 as compared to Figure 5.1. If neighbouring octahedral positions in the gel formed by hydrothermal processing of undoped aluminium- and silicon-acetates are occupied by a mixture of aluminium and silicon, the differing bond lengths would lead to distortions in unit cell sizes and, in turn, this would lead to both broader diffraction peaks and lower peak intensity.

There is an increased amorphous background in the region of $2\theta = 10°$ to 30°, which is similar to the broad peak shown in Figure 5.2. This indicates that some of the silicon has formed a separate highly disordered silica phase.

5.1.5.2 Magic-angle-spinning nuclear magnetic resonance spectroscopy

The ^{27}Al MAS NMR spectrum recorded at 104.3 MHz at *ca.* 295 K from a gel formed by hydrothermal processing of undoped aluminium- and silicon-acetates as described in

Section 3.1.2.1 is shown in Figure 5.6.

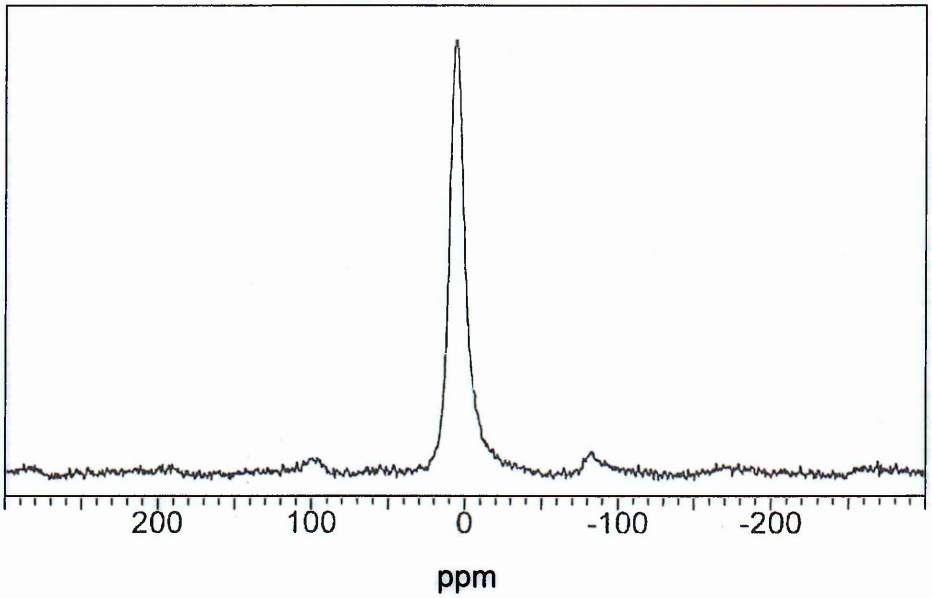

Figure 5.6: ^{27}Al MAS NMR spectrum recorded at *ca.* 295 K from of the gel formed by hydrothermal processing of undoped aluminium- and silicon-acetates as described in Section 3.1.2.1

The spectrum is consistent with the presence of aluminium in octahedral coordination[7] as would reasonably be expected for a pseudoboehmite-related structure.

5.1.6 Phase analysis of the gel formed by hydrothermal processing of aluminium-, silicon- and iron(II)-acetates

5.1.6.1 X-Ray powder diffraction

The flat-plate X-ray powder diffraction pattern recorded using Cu-K_α radiation (λ = 1.54 Å) at *ca.* 295 K from the gel formed by hydrothermal processing of aluminium-, silicon- and iron(II)-acetates as described in Section 3.1.2.1 is shown in Figure 5.7. The red lines indicate the positions of the peaks characteristic of boehmite[1]. The blue lines indicate the positions of the peaks characteristic of hematite[3]. The green lines indicate the positions of the peaks characteristic of maghemite[8] (γ-Fe_2O_3).

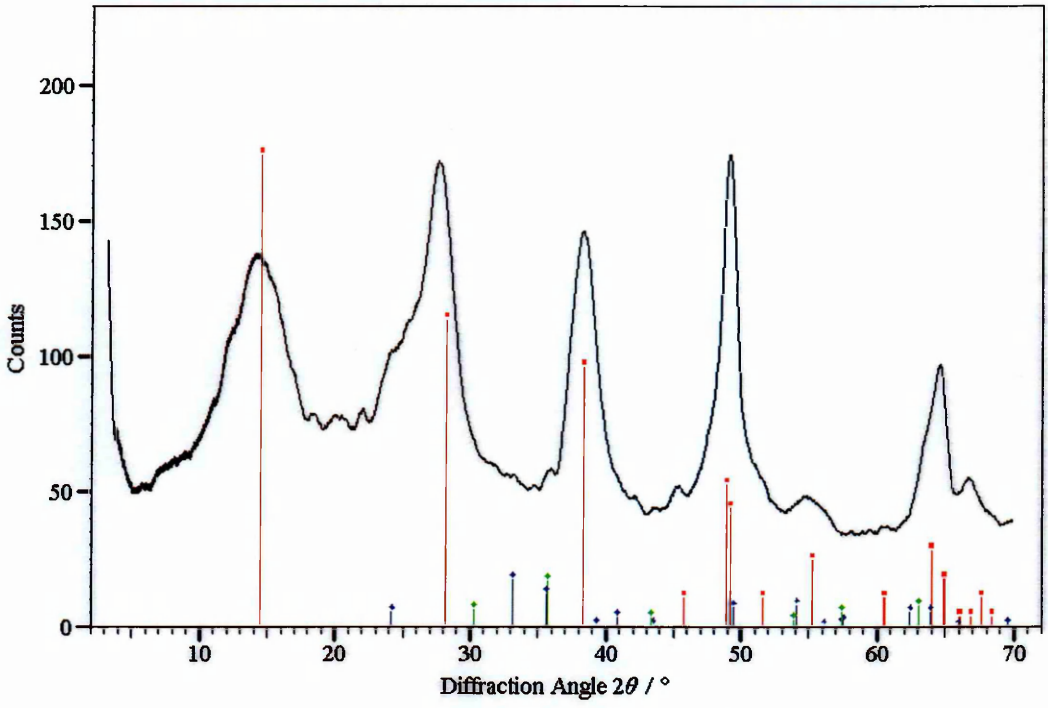

Figure 5.7: X-ray powder diffraction pattern recorded from the gel formed by hydrothermal processing of aluminium-, silicon- and iron(II)-acetates as described in Section 3.1.2.1

The pattern indicates that the material has a structure similar to that of pseudoboehmite (*i.e.* boehmite with intercalated water as described in Section 1.2.2.5). There is no evidence of the presence of hematite or maghemite. However, the X-ray powder diffraction pattern characteristic of lepidocrocite, FeOOH[9], which is isostructural with boehmite, is almost identical. It is therefore not possible to discern from X-ray powder diffraction data alone whether the iron is occupying Al sites in a pseudoboehmite structure or whether the iron has formed a separate lepidocrocite phase. It can be noted that the X-ray powder diffraction pattern recorded from the gel made by hydrothermal processing of iron acetate alone, presented in Section 5.1.3, indicated that the iron acetate formed hematite during hydrothermal processing, not lepidocrocite. This suggests that it is more likely that the iron is occupying aluminium sites in a pseudoboehmite structure.

The peak widths are broad, and the peak intensities are low indicating a disordered structure. This is consistent with the view that the octahedral sites in the pseudoboehmite

structure are occupied by a mixture of aluminium, silicon and iron atoms, the differing bond lengths would lead to distortions in unit cell sizes and, in turn, this would lead to both broader diffraction peaks and lower peak intensity.

5.1.6.2 Magic-angle-spinning nuclear magnetic resonance spectroscopy

The ^{27}Al MAS NMR spectrum recorded at 104.3 MHz at *ca.* 295 K from the gel formed by hydrothermal processing of aluminium-, silicon- and iron(II)-acetates as described in Section 3.1.2.1 is shown in Figure 5.8.

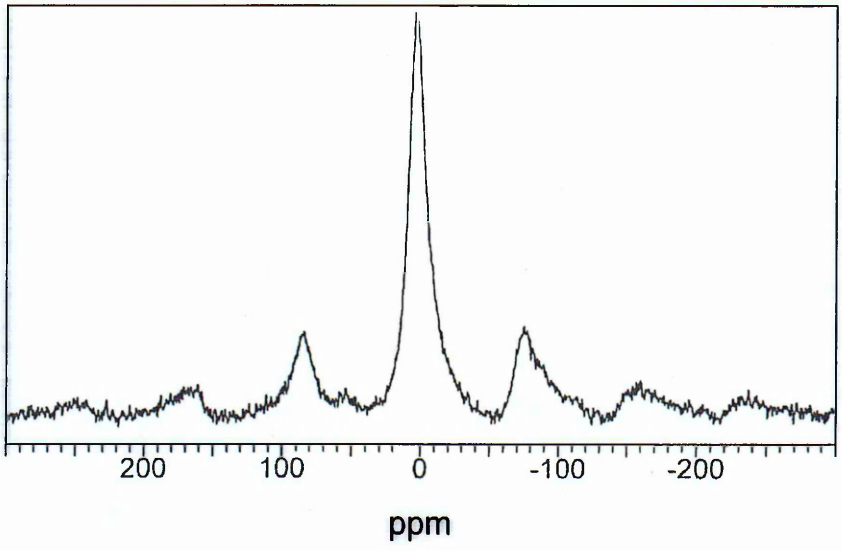

Figure 5.8: ^{27}Al MAS NMR Spectrum recorded from the gel formed by hydrothermal processing of aluminium-, silicon- and iron(II)-acetates as described in Section 3.1.2.1

The spectrum is broader than that recorded from the gel formed by hydrothermal processing of undoped aluminium- and silicon-acetates shown in Figure 5.6. There is a sideband manifold which is enhanced in intensity. Not all of the aluminium was detectable in this sample, as indicated by the significant increase in the number of scans required (3220 compared to 280) to obtain a signal-to-noise ratio comparable to that for Figure 5.6 under the same NMR experimental conditions. Overall, this behaviour is typical for materials containing magnetic centres[10 11]. This would mean that some of the aluminium atoms are in an environment within

~10 Å of iron atoms, in order to be in dipolar contact. This supports the suggestion that iron has been directly incorporated into the structure of the pseudoboehmite-type phase[12].

5.1.6.3 Mössbauer spectroscopy

The Mössbauer spectrum recorded at *ca.* 295 K from the gel formed by hydrothermal processing of aluminium-, silicon- and iron (II)-acetates as described in Section 3.1.2.1 is shown in Figure 5.9.

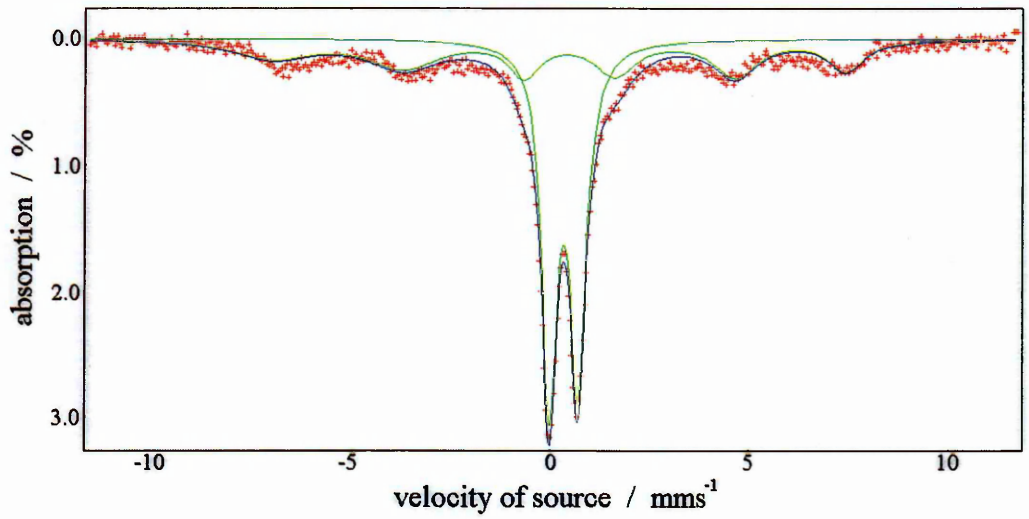

Figure 5.9: Mössbauer spectrum recorded from the gel formed by hydrothermal processing of aluminium-, silicon- and iron(II)-acetates as described in Section 3.1.2.1

The was best fitted to a doublet with isomer shift 0.33 mms^{-1} and quadrupole splitting 0.72 mms^{-1}, partially superimposed by a sextet with magnetic field of 44.8 T and an isomer shift of 0.33 mms^{-1}.

These data are consistent with a small amount of the iron in the sample being present as an oxide of iron exhibiting hyperfine splitting. The sextet seen in Figure 5.9 is similar to that characteristic of maghemite[13], γ-Fe_2O_3. The remainder of the iron is located within a hydrated oxide. There are numerous oxides and oxy-hydroxides of iron which exhibit Mössbauer spectra similar to the doublet seen in Figure 5.9, so firm conclusions cannot be drawn. The spectrum

is not inconsistent with the suggestion that iron may be incorporated into the pseudoboehmite-type structure, but could also be characteristic of a separate iron-containing phase.

5.1.6.4 Iron K-edge EXAFS

The background subtracted k^3 weighted Fe K-edge EXAFS and Fourier transform data recorded at *ca.* 295 K on Station 7.1 at Daresbury Laboratory from the gel formed by hydrothermal processing of aluminium-, silicon- and iron(II)-acetates as described in Section 3.1.2.1 is shown in Figures 5.10.

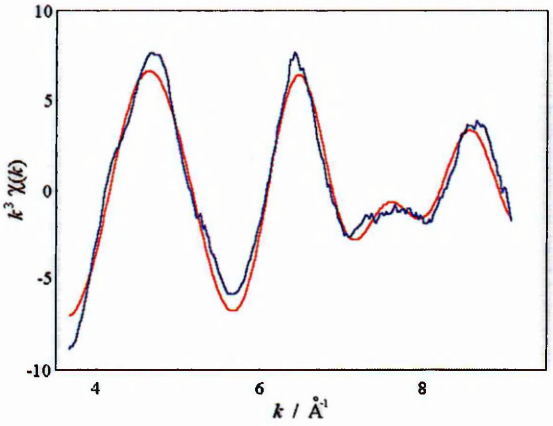

Figure 5.10a: k^3 weighted Fe K-edge EXAFS recorded from a dried hydrothermally processed mixture of aluminium-, silicon-, and iron(II)-acetates

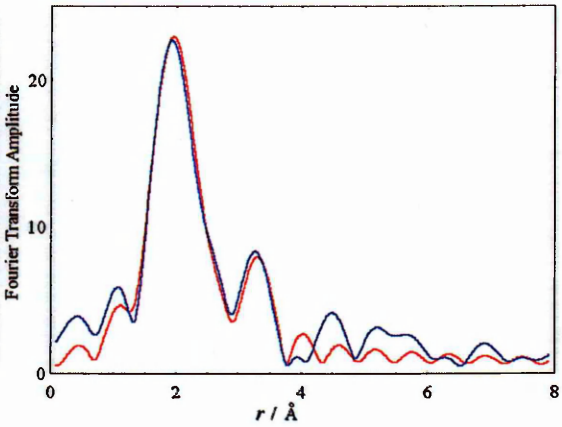

Figure 5.10b: Fourier Transform of Fe K-edge EXAFS recorded from a dried hydrothermally processed mixture of aluminium-, silicon-, and iron(II)-acetates

The blue lines show the experimental data; the red lines show the fitted model.

The data were fitted using the structure of boehmite given in the literature[14] to predict the position and occupancy of shells surrounding iron occupying an aluminium site in a pseudoboehmite structure. The model consists of 4 shells, detailed in Table 5.1. This fit carries a fit index of 0.00025 and an *R*-factor of 19.77. Aluminium and silicon cannot be distinguished in an EXAFS fit, therefore the shells given as containing aluminium should be taken as containing a mixture of aluminium and silicon.

Detailed Theoretical Model Calculated by CRAD[15] from ICSD data[14]			Simplified Theoretical Model Average of Detailed Theoretical Model			Fitted Model		
Coord. Number	Atom Type	Distance / Å	Coord. Number	Atom Type	Distance / Å	Coord. Number	Distance / Å	Debye-Waller $2\sigma^2$ / Å^2
2	Oxygen	1.885	6	Oxygen	1.900	6 ± 0.3	1.99 ± 0.01	0.02
4	Oxygen	1.908						
4	Aluminium	2.854	6	Aluminium	2.859	6 ± 0.6	2.91 ± 0.01	0.03
2	Aluminium	2.868						
4	Oxygen	3.432	6	Oxygen	3.433	6 ± 0.5	3.44 ± 0.01	0.02
2	Oxygen	3.434						
2	Aluminium	3.694	2	Aluminium	3.694	2 ± 0.3	3.62 ± 0.02	0.03

Table 5.1: EXAFS fit of data shown in Figures 5.10

The fit shows no evidence of the presence of any oxide or hydroxide of iron, which would be indicated by the presence of iron atoms in the second shell. This EXAFS measurement is consistent with iron occupying the aluminium sites in the pseudoboehmite-related structure. As would be expected, most of the interatomic distances are larger than the theoretical distances calculated from the structure of pseudoboehmite, as the iron atom is larger than aluminium.

5.1.7 Phase analysis of the gel formed by hydrothermal processing of aluminium- and silicon- acetates and vanadium(III) acetylacetonate

The flat-plate X-ray powder diffraction pattern recorded using Cu-K_α radiation (λ = 1.54 Å) at *ca.* 295 K from the gel formed by hydrothermal processing of aluminium- and silicon-acetates and vanadium(III) acetylacetonate as described in Section 3.1.2.1 is shown in Figure 5.11. The red lines indicate the positions of the peaks characteristic of boehmite[1].

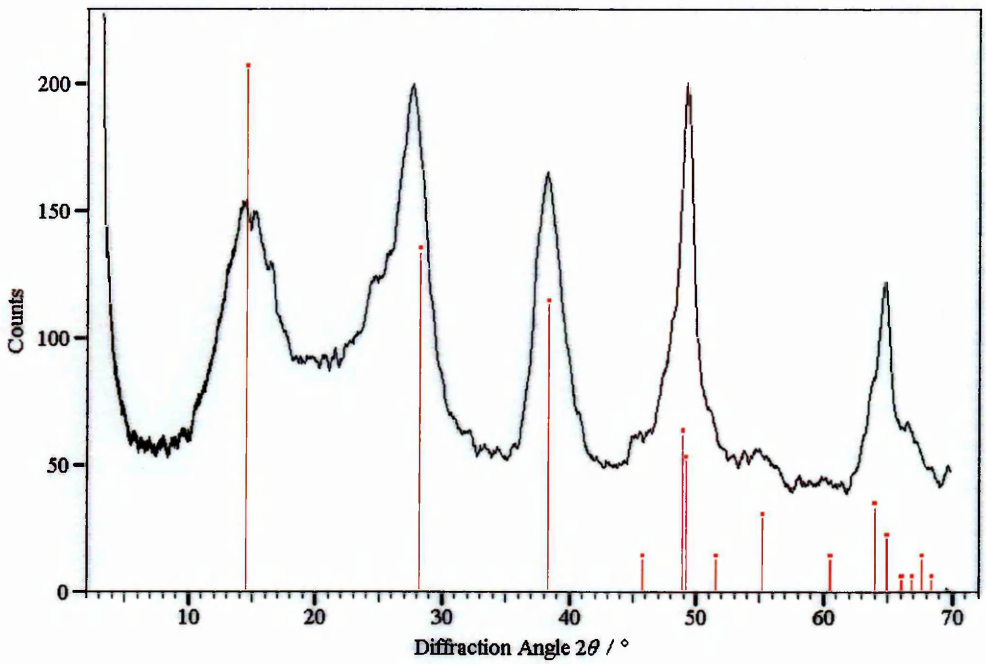

Figure 5.11: X-ray powder diffraction pattern recorded from the gel formed by hydrothermal processing of aluminium- and silicon- acetates and vanadium(III) acetylacetonate as described in Section 3.1.2.1

The pattern indicates that the sample has a structure similar to that of pseudoboehmite. There is no evidence of the presence of a separate crystalline vanadium- or silicon- containing phase.

The peak widths are broad, and the peak intensities are low indicating a disordered structure as was seen for the iron-doped sample in Section 5.1.6.1. This is consistent with the view that the octahedral sites in the pseudoboehmite structure are occupied by a mixture of aluminium, silicon and vanadium atoms.

5.2 Phase Evolution Studies.

5.2.1 Phase evolution on heating the gel made by hydrothermal processing of aluminium acetate

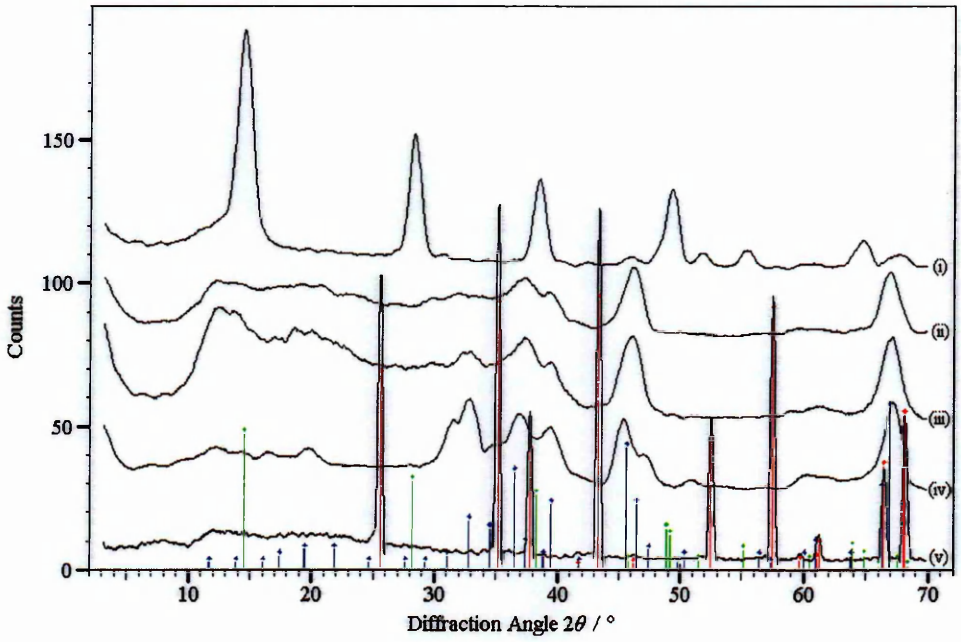

Figure 5.12: X-ray powder diffraction patterns recorded from the gel made by hydrothermal processing of aluminium acetate as described in Section 3.1.2.1 heated for 3 hours at (i) 623 K (ii) 873 K (iii) 1173 K (iv) 1273 K (v)1623 K

The flat-plate X-ray powder diffraction patterns recorded using Cu-K_α radiation (λ = 1.54 Å) at *ca.* 295 K from the gel made by hydrothermal processing of aluminium acetate as described in Section 3.1.2.1, following heating as described in Section 3.1.2.5, are shown in Figure 5.12. The green lines indicate the positions of peaks characteristic of boehmite[1]. The blue lines indicate the positions of peaks characteristic of γ-alumina[16]. The red lines indicate the positions of the peaks characteristic of α-alumina, corundum[17].

(i) Sample heated at 623 K

The pattern shows peaks characteristic of boehmite similar to that recorded from the unheated material as shown in Figure 5.1.

(ii) - (iv) Samples heated at 873, 1173 and 1273 K

These patterns all show peaks indicative of a disordered alumina structure, characteristic of the transitional alumina phases, collectively known as γ-alumina. The peaks appear more well-defined in the patterns recorded from samples heated at higher temperatures.

(v) Sample heated at 1623 K

The pattern shows peaks characteristic of α-Al_2O_3. There is no evidence of the presence of any remaining γ-alumina-type structure.

5.2.2 Phase evolution on heating the gel made by hydrothermal processing of silicon acetate

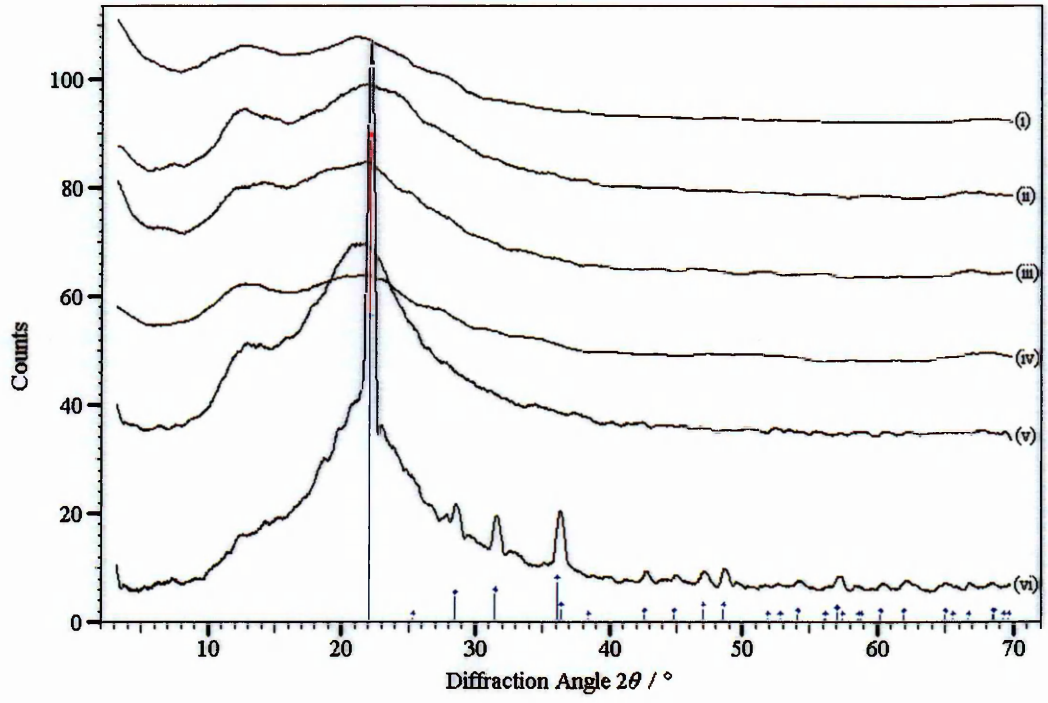

Figure 5.13: X-ray powder diffraction patterns recorded from the gel made by hydrothermal processing of silicon acetate as described in Section 3.1.2.1 heated for 3 hours at (i) 623 K (ii) 873 K (iii) 973 K (iv) 1173 K (v) 1373 K (vi)1623 K

The flat-plate X-ray powder diffraction patterns recorded using Cu-K_α radiation (λ = 1.54 Å) at *ca.* 295 K from the gel made by hydrothermal processing of silicon acetate as

described in Section 3.1.2.1, following heating as described in Section 3.1.2.5, are shown in Figure 5.13. The red line indicates the position of the single peak characteristic of non-crystalline silica[2] as seen in Section 51.2. The blue lines indicate the positions of peaks characteristic of the high temperature crystalline phase of silicon oxide[18], cristobalite.

(i) Sample heated at 623 K

The pattern indicates a highly disordered structure with little crystallinity. The very broad peak at $2\theta \approx 20°$ indicates the presence of amorphous silica.

(ii) - (iv) Samples heated at 873, 973 and 1173 K

These patterns show no significant difference from pattern (i) and indicate an amorphous silica structure.

(v) Sample heated at 1373 K

The broad peak at $2\theta \approx 20°$ is more intense and less broad in this pattern, which indicates that the crystallinity of the sample has increased.

(vi) Sample heated at 1623 K

This pattern shows peaks characteristic of the high temperature phase of SiO_2, cristobalite. This result is unexpected as the region of stability for cristobalite is between 1740 and 1985 K[19]. However, cristobalite can form at 1475 K at elevated pressure[20]. It is possible that the small particle size characteristic of materials formed by hydrothermal processing was conducive to the formation of cristobalite at a lower temperature, and that it was quenched to a metastable form at room temperature. The elevated background below the peak at $2\theta = 22°$ also indicates that a portion of the material is still in an amorphous phase.

5.2.3 Phase evolution of undoped mullite formed by heating the gel formed by hydrothermal processing of aluminium- and silicon-acetates

The flat-plate X-ray powder diffraction patterns recorded using Cu-K_α radiation (λ = 1.54 Å) at *ca.* 295 K from the gel formed by hydrothermal processing of undoped aluminium- and silicon-acetates as described in Section 3.1.2.1, following heating as described in Section 3.1.2.4, are shown in Figure 5.14.

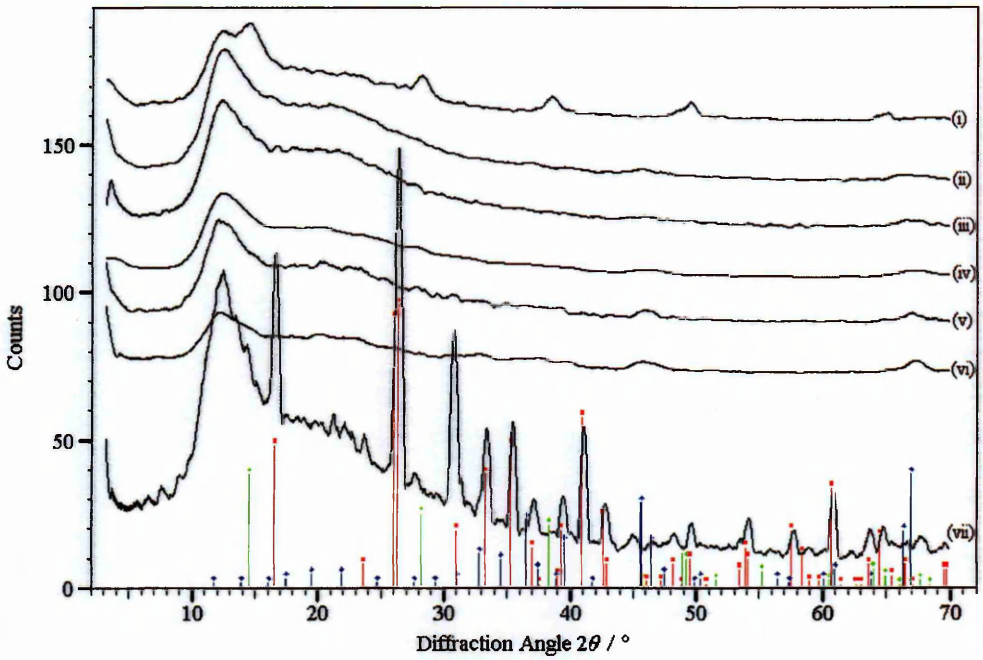

Figures 5.14: X-ray powder diffraction patterns recorded from the gel formed by hydrothermal processing of undoped aluminium- and silicon-acetates heated for 3 hours at (i) 623 K (ii) 723 K (iii) 873 K (iv) 973 K (v) 1173 K (vi) 1423 K (vii)1623 K

The green lines indicate the positions of the peaks characteristic of boehmite[1]. The blue lines indicate the positions of the peaks characteristic of γ-alumina[16]. The red lines indicate the positions of the peaks characteristic of mullite[21].

(i) Sample heated at 623 K

The structure of the material is similar to that of pseudoboehmite, but the peaks are less intense than those recorded from the unheated sample, shown in Figure 5.5.

(ii) Sample heated at 723 K

The second pattern indicates a highly disordered structure, with little crystallinity. However, broad peaks are seen in positions similar to those characteristic of γ-alumina. The very broad peak $2\theta \approx 12°$ does not correspond to any crystalline material in the JCPDS database which might reasonably be expected to be present in the sample. However, this feature is also seen to a lesser extent in Figures 5.13 (i)-(v) and may indicate the presence of an amorphous silica phase.

(iii) - (vi) Samples heated at 873, 973, 1173 and 1373 K

These patterns also showed evidence of these disordered γ-alumina and amorphous silica phases. There is little discernible difference between these patterns, but the broad peaks do appear to be slightly more intense in the patterns recorded from samples heated at the higher temperatures.

(vii) Sample heated at 1623 K

The final pattern shows peaks characteristic of mullite. There is no evidence of the presence of γ-alumina. However, the broad peak at $2\theta \approx 12°$ and the increased background level at $2\theta \approx 20°$, indicative of a highly disordered silica phase, as well as the disordered nature of the phases indicated in patterns (i) to (vi) suggest that it is likely that some of the material remains in a non-crystalline phase.

5.2.4 Phase evolution of iron-doped mullite formed by heating the gel formed by hydrothermal processing of aluminium-, silicon- and iron(II)-acetates

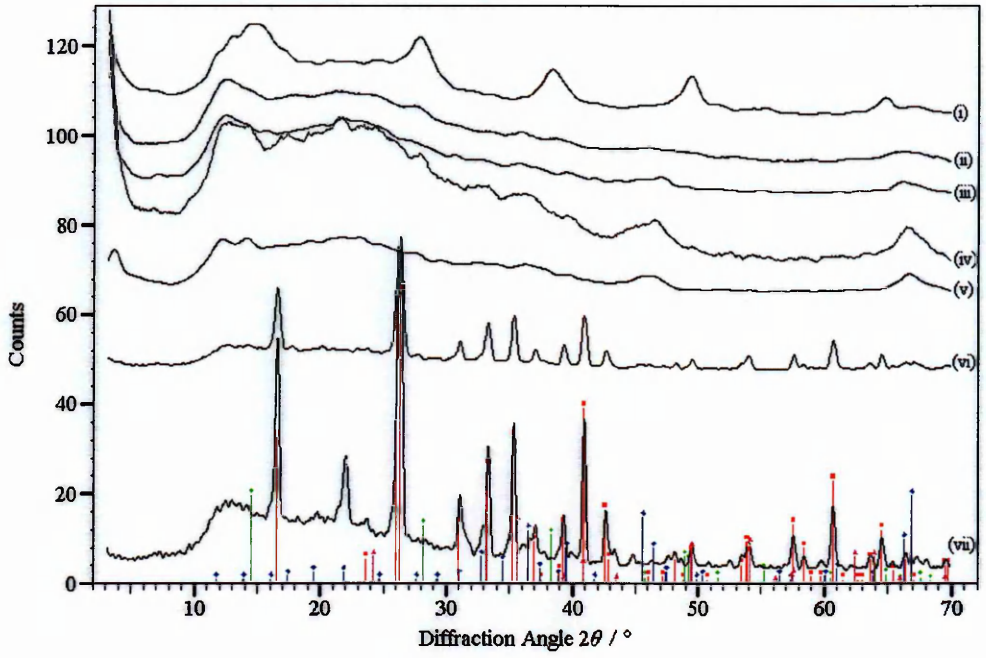

Figures 5.15: XRD patterns recorded from the gel formed by hydrothermal processing of aluminium-, silicon-, and iron(II)-acetates heated for 3 hours at (i) 623 K (ii) 723 K (iii) 873 K (iv) 973 K (v) 1173 K (vi) 1423 K (vii)1623 K

The flat-plate X-ray powder diffraction patterns recorded using Cu-K_α radiation (λ = 1.54 Å) at *ca.* 295 K from the gel formed by hydrothermal processing of aluminium-, silicon- and iron(II)-acetates as described in Section 3.1.2.1, following heating as described in Section 3.1.2.4, are shown in Figure 5.15. The green lines indicate the positions of the peaks characteristic of boehmite[1]. The red lines indicate the positions of the peaks characteristic of mullite[21]. The blue lines indicate the positions of the peaks characteristic of γ-alumina[16]. The pink lines indicate the positions of the peaks characteristic of hematite[3]. The brown lines indicate the positions of peaks characteristic of the high temperature crystalline phase of silicon oxide[18], cristobalite.

i) Sample heated at 623 K.

The pattern shows peaks similar to those characteristic of pseudoboehmite,

and is similar to that recorded from the unheated material, shown in Figure 5.7. The peaks are less intense, which may indicate that some of the pseudoboehmite has transformed to an amorphous material.

(ii) – (v) Samples heated at 723, 873, 973 and 1173 K

These patterns show very little crystallinity. The broad peaks at $2\theta \approx 47°$ and 67°, which appear to be slightly more intense in patterns recorded from samples heated at the higher temperatures, may be evidence of a highly disordered γ-alumina structure. The increased background level at low angle, particularly noticeable in pattern (iv), may indicate the presence of highly disordered silica.

(vi) Sample heated at 1423 K

This pattern shows peaks characteristic of mullite. Mullite did not form at this temperature from the gel prepared by the hydrothermal processing of aluminium- and silicon-acetates. This suggests that the presence of iron has lowered the temperature at which mullite can be formed.

(vii) Sample heated at 1623 K

This pattern shows peaks characteristic of mullite. The peaks are more intense in this pattern than in pattern (vi). This may suggest that not all the material has transformed to mullite in the sample heated at 1423 K, or that mullite formed at a higher temperature exhibits a greater degree of crystallinity.

The pattern also shows a peak characteristic of crystalline silica at $2\theta \approx 22°$. This suggests that the broad peak at this angle shown in patterns (ii) – (v) was indeed

indicative of the presence of disordered silica. It is possible that some silica is present as a separate phase due to silicon being replaced by iron in mullite.

5.2.5 Phase evolution of iron-doped mullite formed by heating the gel formed by hydrothermal processing of aluminium- and silicon-acetates and mixed with iron(III) oxide

The flat-plate X-ray powder diffraction patterns recorded using Cu-K_α radiation (λ = 1.54 Å) at *ca.* 295 K from the gel formed by hydrothermal processing of aluminium- and silicon-acetates and mixed with iron(III) oxide as described in Section 3.1.2.2, following heating as described in Section 3.1.2.4, are shown in Figure 5.16.

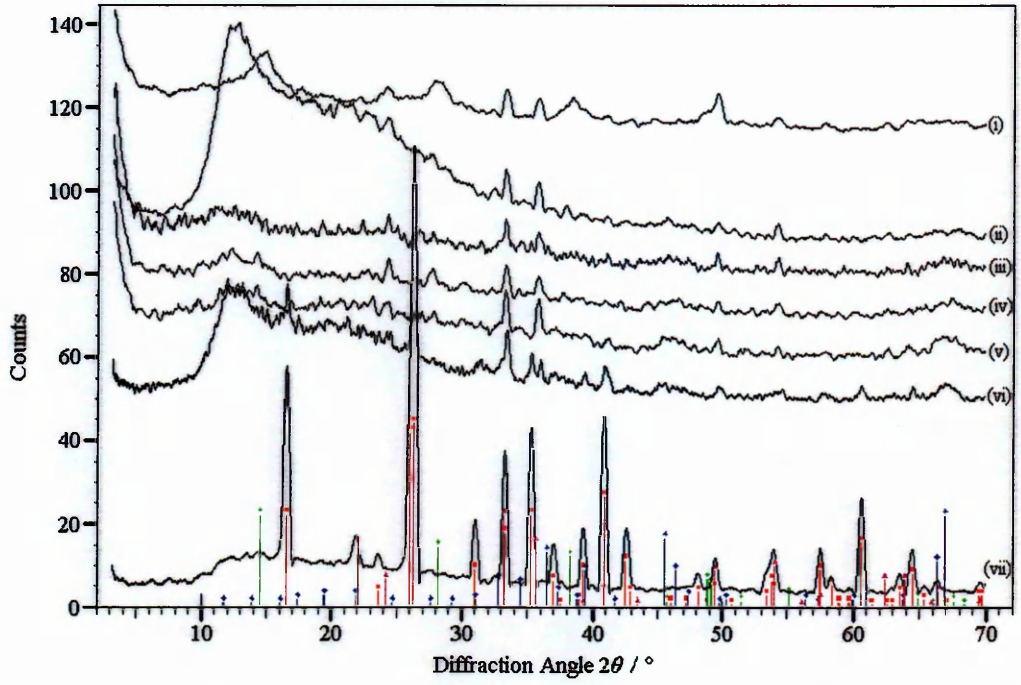

Figures 5.16: X-ray diffraction patterns recorded from the gel formed by hydrothermal processing of aluminium- and silicon-acetates and mixed with iron(III) oxide heated for 3 hours at (i) 623 K (ii) 723 K (iii) 873 K (iv) 973 K (v) 1173 K (vi) 1423 K (vii) 1623 K

The green lines indicate the positions of the peaks characteristic of boehmite[1]. The red lines indicate the positions of the peaks characteristic of mullite[21]. The blue lines indicate the positions of the peaks characteristic of γ-alumina[16]. The pink lines indicate the positions of the peaks characteristic of hematite[3]. The brown lines indicate the positions of peaks

characteristic of the high temperature crystalline phase of silicon oxide[18], cristobalite.

(i) Sample heated at 623 K

The pattern shows broad peaks in positions similar to those characteristic of pseudoboehmite, and very small peaks characteristic of hematite α-Fe_2O_3.

(ii) Sample heated at 723 K

The pattern shows very small peaks characteristic of hematite. Small broad peaks at positions similar to those characteristic of pseudoboehmite are discernible. The structure is otherwise non-crystalline, with evidence of an amorphous silica phase as seen in Figure 5.13.

(iii) - (v) Samples heated at 873, 973, 1173 K

These patterns show evidence of a highly disordered γ-alumina structure. Peaks characteristic of hematite are also evident. There is little discernible difference between these patterns, though the peaks characteristic of γ-alumina appear more intense in patterns recorded from samples heated at higher temperatures.

(vi) Sample heated at 1423 K.

This pattern shows peaks characteristic of mullite and peaks characteristic of hematite. A small broad peak at $2\theta \approx 67°$ and the shape of the background at $2\theta \approx 12°$ may also indicate that some γ-alumina and silica remains present.

(vii) Sample heated at 1623 K.

This pattern shows peaks characteristic of mullite. There is no evidence of the presence of γ-alumina, however, the disordered nature of the material indicated by the earlier patterns suggests that a non-crystalline phase may still be present in

this sample. Peaks characteristic of hematite and cristobalite are also evident. The presence of peaks characteristic of cristobalite may be evidence that some of the iron has replaced silicon in the mullite structure. However, some has also formed a separate hematite phase.

5.2.6 Phase evolution of vanadium-doped mullite made by heating the gel formed by hydrothermal processing of aluminium- and silicon- acetates and vanadium(III) acetylacetonate

The flat-plate X-ray powder diffraction patterns recorded using Cu-K_α radiation (λ = 1.54 Å) at *ca.* 295 K from the gel formed by hydrothermal processing of aluminium- and silicon- acetates and vanadium(III) acetylacetonate as described in Section 3.1.2.1, following heating as described in Section 3.1.2.4, are shown in Figure 5.17.

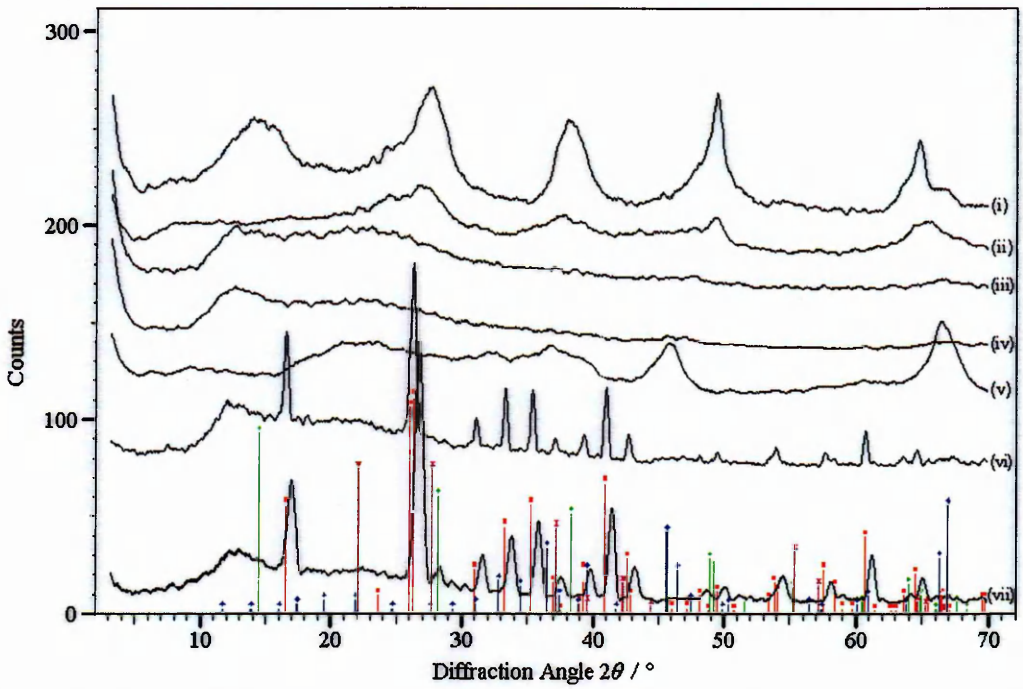

Figure 5.17: X-ray powder diffraction patterns recorded from the gel formed by hydrothermal processing of aluminium- and silicon- acetates and vanadium(III) acetylacetonate heated for 3 hours at (i) 623 K (ii) 723 K (iii) 873 K (iv) 973 K (v) 1173 K (vi) 1423 K (vii) 1623 K

The green lines indicate the positions of the peaks characteristic of boehmite[1]. The red lines indicate the positions of the peaks characteristic of mullite[21]. The blue lines indicate the

positions of the peaks characteristic of γ-alumina[16]. The pink lines indicate the positions of the peaks characteristic of vanadium(II) oxide[4]. The brown lines indicate the positions of peaks characteristic of the high temperature crystalline phase of silicon oxide[18], cristobalite.

(i) Sample heated at 623 K.

The pattern shows peaks characteristic of pseudoboehmite, and is similar to the pattern recorded from the unheated material, shown in Figure 5.10.

(ii) Sample heated at 723 K.

The pattern shows peaks characteristic of pseudoboehmite, although these are less intense than those shown in pattern (i). This may indicate that the presence of vanadium impedes the process by which the pseudoboehmite dehydrates to alumina.

(iii) - (v) Samples heated at 873, 973 and 1173 K.

These patterns indicate a highly disordered amorphous material with broad peaks in positions similar to those characteristic of γ-alumina. Patterns (iii) and (iv) show evidence of the presence of an amorphous silica phase as seen in Figure 5.13, but there is little other discernible difference between these patterns. The γ-alumina peaks appear more intense in patterns recorded from samples heated at higher temperatures.

(vi) Sample heated at 1423 K.

This pattern shows peaks characteristic of mullite. Mullite did not form at this temperature from the gel prepared by the hydrothermal processing of undoped aluminium- and silicon-acetates. This suggests that the presence

of vanadium has lowered the temperature at which mullite can be formed.

(vii) Sample heated at 1623 K.

This pattern shows peaks characteristic of mullite. The peaks are more intense in this pattern than in pattern (vii). This may suggest that not all the material has transformed to mullite in the sample heated at 1423 K, or that mullite formed at a higher temperature exhibits a greater degree of crystallinity. There is no evidence of the presence of crystalline silica, as was seen in Figures 5.15(vii) and 5.16(vii). However, the shape of the background at $2\theta \approx 12°$ may indicate that some amorphous silica may be present.

5.2.7 Phase evolution of vanadium-doped mullite formed by heating the gel formed by the hydrothermal processing of aluminium- and silicon- acetates and mixed with vanadium(V) oxide

The flat-plate X-ray powder diffraction patterns recorded using Cu-K_α radiation ($\lambda = 1.54$ Å) at *ca.* 295 K from the gel made by the hydrothermal processing of aluminium- and silicon- acetates mixed with vanadium(V) oxide as described in Section 3.1.2.2, following heating as described in Section 3.1.2.4, are shown in Figure 5.18. The green lines indicate the positions of the peaks characteristic of boehmite[1]. The red lines indicate the positions of the peaks characteristic of mullite[21]. The blue lines indicate the positions of the peaks characteristic of γ-alumina[16]. The pink lines indicate the positions of the peaks characteristic of vanadium(V) oxide[22]. The brown lines indicate the positions of peaks characteristic of the high temperature crystalline phase of silicon oxide[18], cristobalite.

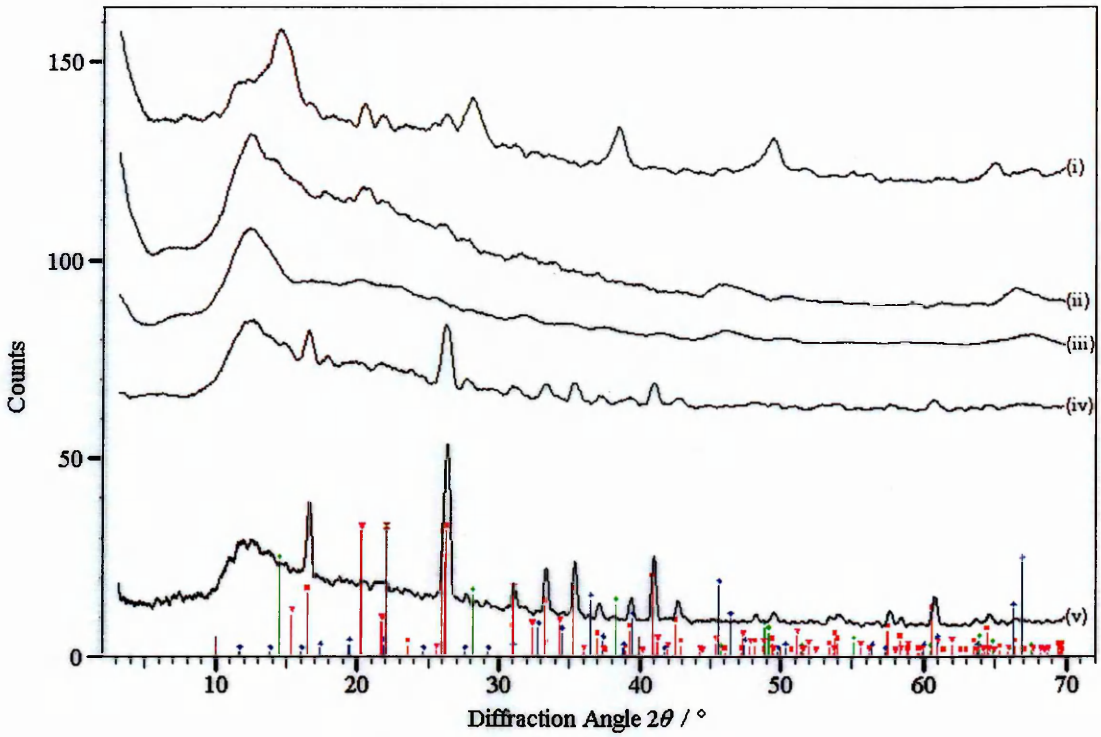

Figure 5.18: X-ray powder diffraction patterns recorded from samples of the mixture of a gel made by the hydrothermal processing of aluminium- and silicon- acetates and vanadium(V) oxide heated for 3 hours at (i) 623 K (ii) 873 K (iii) 973 K (iv) 1173 K (v) 1623 K

(i) Sample heated at 623 K

The pattern shows peaks characteristic of pseudoboehmite and peaks characteristic of vanadium(V) oxide. The widths of the peaks characteristic of pseudoboehmite are large, and the intensities are low indicative of a highly disordered structure.

(ii) Sample heated at 873 K

The pattern shows no distinct peaks, indicating that no crystalline phase is present. Very broad peaks of very low intensity are seen near the positions characteristic of γ-alumina, and there is evidence of the presence of an amorphous silica phase as seen in Figure 5.13. There may be a small peak characteristic of vanadium(V) oxide visible at $2\theta \approx 20°$, but this is uncertain due to a poor signal-to-noise ratio.

(iii) Sample heated at 973 K

The pattern shows no distinct peaks, which indicates that there is no crystalline phase present. Very broad peaks of low intensity are seen near the positions characteristic of γ-alumina, and there is evidence of the presence of an amorphous silica phase as seen in Figure 5.13. There is no indication of the presence of vanadium(V) oxide.

(iv) Sample heated at 1173 K

The pattern shows peaks characteristic of mullite. Very broad peaks of very low intensity are also seen near the positions characteristic of γ-alumina. Mullite did not form at this temperature from the undoped gel made by the hydrothermal processing of aluminium- and silicon- acetates, nor from either of the iron-doped materials, nor from the gel formed by the hydrothermal processing of aluminium- and silicon- acetates and vanadium acetylacetonate. This indicates that the presence of vanadium added to the precursor as oxide decreases the temperature at which mullite can be formed, and that this method of vanadium doping is more effective than adding vanadium acetylacetonate to the mixture for hydrothermal processing.

(v) Sample heated at 1623 K

The pattern shows peaks characteristic of mullite. The peaks are more intense in this pattern than in pattern (iv). This suggests that not all the material has transformed to mullite in the sample heated at 1173 K, or that mullite formed at a higher temperature exhibits a greater degree of crystallinity. The shape of the background at $2\theta \approx 12°$ may indicate the presence of some remaining amorphous silica, but there is no indication of the presence of γ-alumina or vanadium(V) oxide.

5.3 High-temperature time-resolved experiments

5.3.1 High-temperature time-resolved X-ray powder diffraction and EXAFS recorded from the transformation of the gel formed by hydrothermal processing of aluminium-, silicon- and iron(II)-acetates to iron-doped mullite

A pellet containing the gel formed by hydrothermal processing of aluminium-, silicon- and iron(II)-acetates was prepared and heated to 1323 K using the method described in Section 3.3.1 on Station 9.3 at Daresbury Laboratory.

5.3.1.1 X-Ray powder diffraction

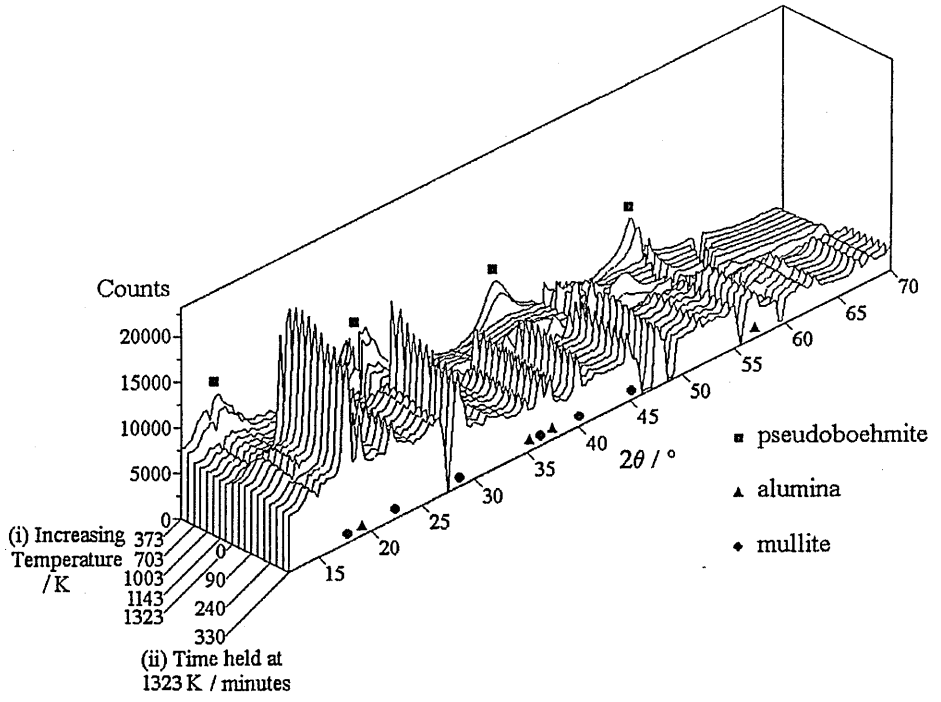

Figure 5.19: 3D view of the X-ray powder diffraction patterns recorded at high temperature from the reaction of the gel formed by hydrothermal processing of aluminium-, silicon- and iron(II)-acetates to form iron-doped mullite.

A three-dimensional plot of the X-ray powder diffraction patterns recorded during the course of the experiment is shown in Figure 5.19. During this experiment the furnace used to heat the sample was not achieving its expected performance and the rate of increase of temperature was slow. The first eight X-ray powder diffraction patterns were

recorded while the sample was being heated to 1323 K. These show that the peaks characteristic of pseudoboehmite gradually diminished and then disappeared as the temperature was increased to 773 K over a period of 2 hours. The patterns recorded at temperatures between *ca.* 773 K and 1273 K contained broad peaks characteristic of a small particle, highly defective γ-alumina type structure. The patterns were similar to those observed in Section 5.2.4, Figure 5.15(ii)-(v) which were recorded from samples which had been heated at temperatures between 723 and 1173 K. The ninth pattern in Figure 5.19 corresponds to the time when the temperature reached 1323 K. This pattern showed peaks characteristic of mullite, as well as a small peak characteristic of α-Al_2O_3. These peaks increased in intensity in the next two patterns and then remained constant for the remainder of the experiment.

5.3.1.2 Iron K-edge EXAFS

(i) Fe K-edge EXAFS recorded during the experiment

The Fe K-edge EXAFS data recorded in situ while the sample was at high temperature was complex with a poor signal-to-noise ratio, and was not amenable to confident fitting. A first shell coordination of six oxygen atoms consistent with iron occupying sites in the aluminium containing phase could be resolved, and the data indicated the outer shells to be highly disordered.

(ii) Fe K-edge EXAFS recorded after the experiment

After the experiment, when the sample had cooled to *ca.* 350 K, EXAFS data were recorded to a quality sufficient to allow for fitting. The background subtracted k^3 weighted Fe-K edge EXAFS and Fourier transform data is shown in Figures 5.20.

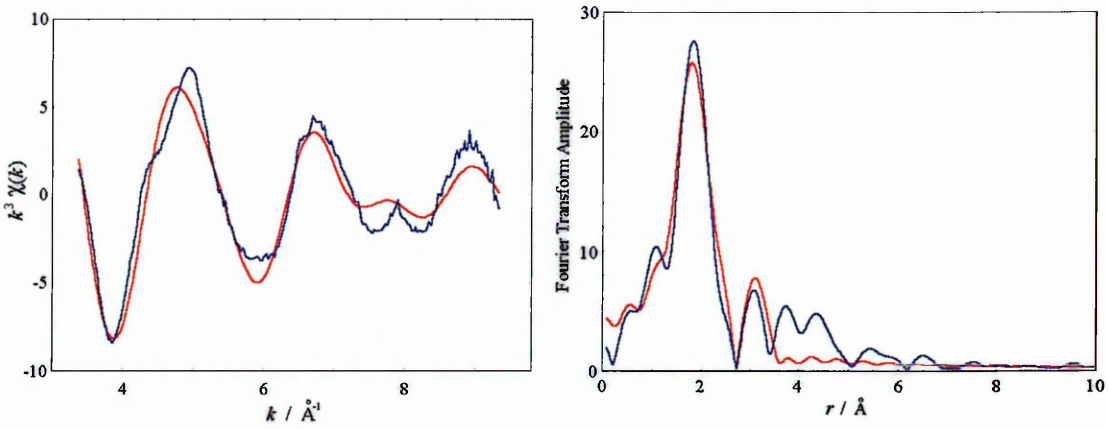

Figures 5.20 (a) k^3 weighted Fe K-edge EXAFS and (b) Fourier transform of Fe K-edge EXAFS; both recorded from a dried hydrothermally processed mixture of aluminium-, silicon-, and iron(II)-acetates heated at 1323 K for 10 hours and cooled to 350 K. The blue lines show the experimental data; the red lines show the fitted model.

The data were fitted using the structure of mullite given in the literature[23] to predict the position and occupancy of shells surrounding iron occupying an octahedral aluminium site in the mullite structure. Alternative attempts to fit the data to models for iron occupying a tetrahedral aluminium- or silicon- site in the mullite structure, or for Fe_3O_4, γ-Fe_2O_3 or α-Fe_2O_3 were not successful. This model assumes that all the iron in the sample is located in octahedral sites. As 0.07 mol iron was added for each 1.0 mol aluminium (see Section 3.1.2.1), this implies that 15% of the octahedral sites are occupied by iron. As EXAFS cannot readily distinguish between aluminium and silicon atoms the model assumes all such atoms are aluminium but should be taken as being a mixture of aluminium and silicon. The fitted model consists of three shells, as described in Table 5.2. This fit carries a fit index of 0.00044 and an *R*-factor of 29.0%.

Detailed Theoretical Model Calculated by CRAD[15] from ICSD data[23]			Simplified Theoretical Model Average of Detailed Theoretical Model			Fitted Model		
Coord. Number	Atom Type	Distance / Å	Coord. Number	Atom Type	Distance / Å	Coord. Number	Distance / Å	Debye-Waller $2\sigma^2$ / Å^2
4 2	Oxygen Oxygen	1.891 1.941	6	Oxygen	1.908	6	1.92 ± 0.02	0.032
0.30	Iron	2.884	0.3	Iron	2.884	0.3	2.83 ± 0.02	0.017
1.70 0.47	Aluminium Al/Si	2.884 2.915	2.17	Aluminium	2.890	2.17	2.83 ± 0.02	0.017
2.78 0.40 2.10	Al/Si Aluminium Aluminium	3.194 3.225 3.257	5.28	Aluminium	3.221	5.28	3.19 ± 0.04	0.049

Table 5.2: Best fit for the Fe K-edge EXAFS recorded from a gel made by the hydrothermal processing of aluminium-, silicon- and iron(II)-acetates heated at 1323K for 10 hours then cooled to 350 K

The fractional coordination numbers are due to the fact that many of the sites in the structure of mullite are partially occupied (see Section 1.2.2.3). The fit is in good agreement with the theoretical model, which supports the suggestion that iron is incorporated into the mullite structure occupying octahedral aluminium sites.

(iii) Fe K-edge EXAFS recorded from a sample of mullite prepared by heating the gel formed by hydrothermal processing of aluminium-, silicon- and iron(II)-acetates at 1623 K for 3 hours

The background subtracted k^3 weighted Fe K-edge EXAFS and Fourier transform data recorded at *ca.* 295 K from the gel formed by hydrothermal processing of aluminium-, silicon- and iron-acetates heated at 1623 K for 3 hours (as used in Section 5.2.4) is shown in Figures 5.21.

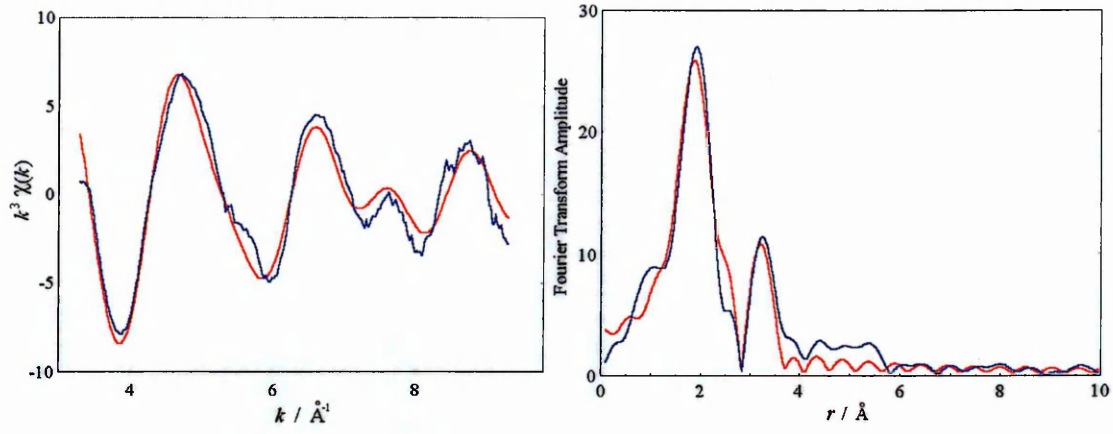

Figures 5.21 (a) k^3 weighted Fe K-edge EXAFS and (b) Fourier transform of Fe K-edge EXAFS; both recorded from a dried hydrothermally processed mixture of aluminium-, silicon-, and iron(II)-acetates heated at 1623 K for 3 hours. The blue lines show the experimental data; the red lines show the fitted model

The data were fitted using the same model as used above for shells surrounding iron occupying an octahedral aluminium site in a mullite structure. This fit carries a fit index of 0.00033 and an *R*-factor of 25.9%.

Detailed Theoretical Model Calculated by CRAD[15] from ICSD data[23]			Simplified Theoretical Model Average of Detailed Theoretical Model			Fitted Model	
Coord. Number	Atom Type	Distance / Å	Coord. Number	Atom Type	Distance / Å	Distance / Å	Debye-Waller $2\sigma^2$ / Å^2
4	Oxygen	1.891	6	Oxygen	1.908	1.94 ± 0.02	0.033
2	Oxygen	1.941					
0.30	Iron	2.884	0.3	Iron	2.884	2.90 ± 0.02	0.013
1.70	Aluminium	2.884	2.17	Aluminium	2.890	2.91 ± 0.02	0.013
0.47	Al/Si	2.915					
2.78	Al/Si	3.194	5.28	Aluminium	3.221	3.24 ± 0.04	0.029
0.40	Aluminium	3.225					
2.10	Aluminium	3.257					

Table 5.3: EXAFS fit of gel made by the hydrothermal processing of aluminium-, silicon- and iron- acetates heated at 1623 K for 3 hours recorded at *ca.* 295 K

An alternative attempt to fit the data to a model consistent with iron occupying a tetrahedral aluminium- or silicon-site in the mullite structure was not successful. There is no indication of the presence of any separate phase of an oxide of iron, which would be shown by a much greater presence of iron in the second shell. This fit demonstrates that data are in good agreement with the view that iron is occupying an octahedral aluminium site in the mullite structure.

5.3.2 High-temperature time-resolved X-ray powder diffraction recorded from the gel formed by hydrothermal processing of undoped aluminium- and silicon-acetates

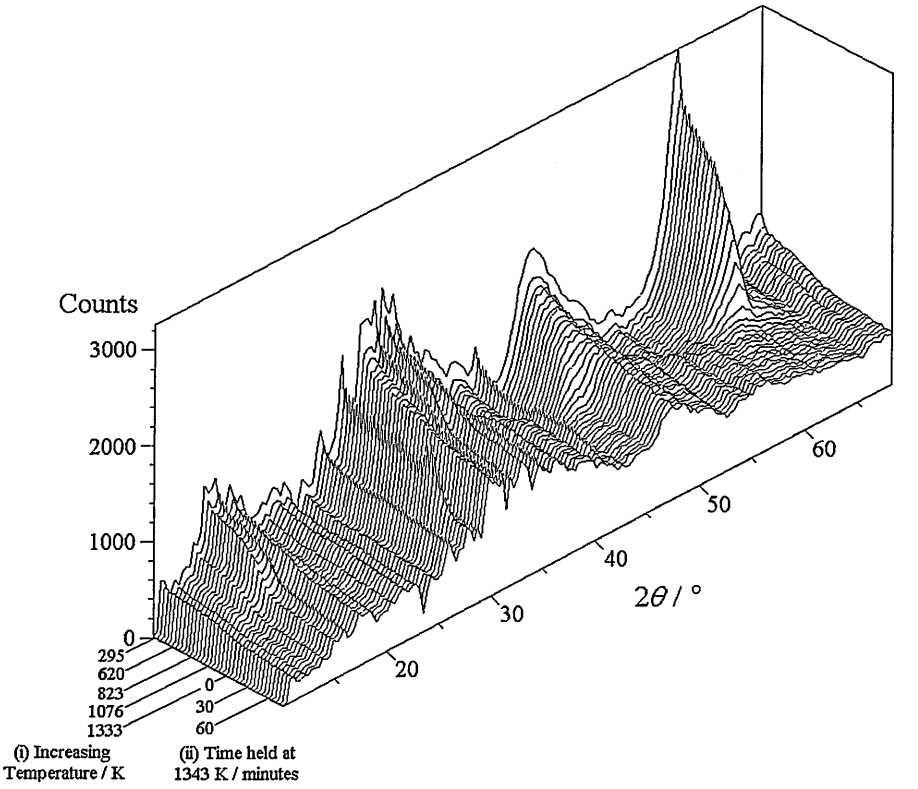

Figure 5.22: 3D view of the X-ray powder diffraction patterns recorded at high temperature from the gel formed by hydrothermal processing of undoped aluminium- and silicon-acetates

A three-dimensional view of the X-ray powder diffraction patterns recorded from the gel formed by hydrothermal processing of undoped aluminium- and silicon-acetates, while heating to 1333 K and while held at that temperature for 90 minutes on Station 9.3 at

Daresbury Laboratory is shown in Figure 5.22.

The results presented in Section 5.2.3 indicated that mullite was unlikely to form at this temperature. However, this was the maximum temperature obtainable with the apparatus available. It should be noted that the count rate is much lower than that seen in Figure 5.19, and the sharper peaks at $2\theta = 30°$ to $40°$ are most probably not diffraction peaks but fluctuations in the noise level due to glitches in the sensor array. Patterns were recorded while the sample was held at 1333 K for 10 hours. These patterns showed no further changes and are therefore not shown here.

The broad peaks characteristic of pseudoboehmite were seen to decrease in intensity as the sample temperature increased. The intensity of the peaks decreased by *ca.* 50 % in the pattern recorded when the furnace was at 723 K and peaks were no longer detectable in the patterns recorded after the furnace reached 1273 K. Subsequent patterns were indicative of a non-crystalline structure with no diffraction peaks evident. No significant changes were observed in the X-ray powder diffraction patterns recorded after the furnace reached 1333 K.

It is interesting to note that peaks characteristic of pseudoboehmite are observed in patterns recorded when the sample was at 1173 K and had been at temperatures exceeding 673 K for 1.5 hours. In the previous experiments reported in Section 5.2.3, peaks characteristic of pseudoboehmite were observed in the XRD pattern recorded from a sample which had been held at 623 K for 3 hours but were not observed in the XRD pattern recorded from a sample which had been held at 723 K for 3 hours.

5.3.3 High-temperature time-resolved X-ray powder diffraction recorded from the mixture of the gel formed by hydrothermal processing of aluminium- and silicon-acetates with iron(III) oxide

A three-dimensional plot of the X-ray powder diffraction patterns recorded on Station 9.3 at Daresbury Laboratory during the heating of a pellet containing the gel formed by hydrothermal processing of aluminium- and silicon-acetates mixed with iron(III) oxide (as described in Section 3.1.2.2) to 1343 K and while held at that temperature for 5 hours is shown in Figure 5.23. The results presented in Section 5.2.5 suggested that mullite may form at this temperature given enough time, as peaks characteristic of mullite were seen in the XRD pattern recorded from a sample of the same mixture heated at 1423 K for 3 hours.

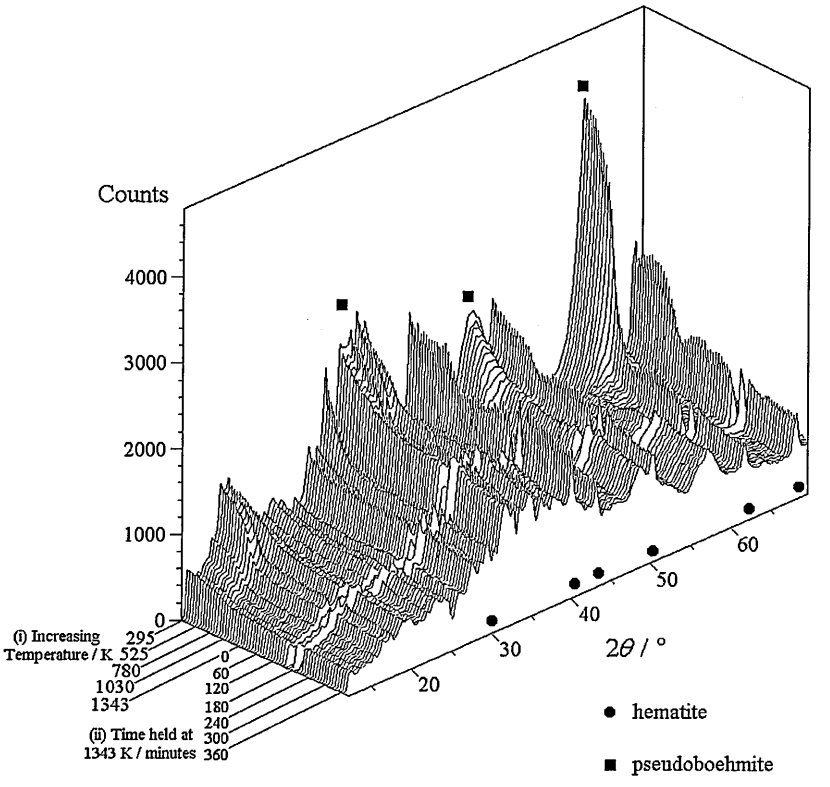

Figure 5.23: 3D view of the X-ray powder diffraction patterns recorded during the heating of a mixture of the gel formed by hydrothermal processing of aluminium- and silicon-acetates with iron(III) oxide

The initial patterns showed peaks characteristic of pseudoboehmite and peaks characteristic

of α-Fe_2O_3 (hematite). The peaks characteristic of pseudoboehmite decreased in intensity as the sample temperature increased. The intensity had decreased by *ca.* 50 % in the pattern recorded when the furnace was at 673 K and peaks were no longer detectable in the patterns recorded after the furnace reached 1073 K. The subsequent patterns indicated a non-crystalline phase and hematite. The peaks characteristic of hematite were also seen to decrease in intensity. This could be due to a reaction taking place between the iron and the non-crystalline aluminium- and silicon- containing phase. There is no evidence of mullite formation after 5 hours at 1343 K.

Fe K-edge EXAFS data recorded during this experiment was of insufficient quality for any useful information to be gained from the analysis.

References for Chapter Five

1 JCPDS reference for boehmite 21-1307.

2 JCPDS reference for silica 29-0085.

3 JCPDS reference for hematite 33-0664.

4 JCPDS reference for vanadium(II) oxide 44-0253.

5 J. A. Dean *Lange's Handbook of Chemistry* 4th ed. McGraw Hill USA 1992 p. 4-23.

6 J. A. Dean *Lange's Handbook of Chemistry* 4th ed. McGraw Hill USA 1992 p. 4-22.

7 M. B. Smith *Appl. Magn. Reson.* 1993 **4** 1.

8 JCPDS reference for maghemite 39-1346.

9 JCPDS reference for lepidocrocite 44-1415.

10 E. Oldfield, R. A. Kinsey, K. A. Smith, J. A. Nichols, R. J. Kirkpatrick *J. Magn. Reson.* 1983 **51** 325.

11 H. D. Morris, S. Bank, P. D. Ellis *J. Phys. Chem.* 1990 **94** 3121.

12 F. J. Berry, R. L. Bilsborrow, A. J. Dent, M. Mortimer, C. B. Ponton, B. J. Purser, K. R. Whittle *Polyhedron* 1999 **18** 1083.

13 G J Long (Ed) *Mössbauer Spectroscopy Applied to Inorganic Chemistry* Plenum Press USA 1983 Vol. 2 p. 518.

14 ICSD reference for boehmite 27865 (12984). P.P. Reichertz & W.J. Yost *J. Chem. Phys.* 1946 **14** 495.

15 CRAD software on xrsserv1 © Daresbury Laboratory.

16 JCPDS reference for γ-alumina 16-0394.

17 JCPDS reference for α-alumina 10-0173.

18 JCPDS reference for cristobalite 39-1425.

19 A. F. Wells *Structural Inorganic Chemistry* 5th ed. O.U.P. 1984 p.1004.

20 R. Lide (Ed) *CRC Handbook of Chemistry and Physics* 84th ed. CRC USA 2003 p. 12-203.

21 JCPDS reference for mullite 15-0776.

22 JCPDS reference for vanadium(V) oxide 41-1426.

23 ICSD reference for mullite 74008 (38582). D. Balzar, H. Ledbetter *Am. Mineral.* 1993 **78** 1192.

Chapter Six: Conclusions

The structures of ferrosilicon in the ζ_α and ζ_β phases both with and without a doping of 1 wt% aluminium have been examined by X-ray powder diffraction, Fe K-edge EXAFS, Si K-edge EXAFS and Mössbauer spectroscopy. High-temperature time-resolved measurements by combined X-ray powder diffraction and Fe K-edge EXAFS, using a novel technique for data analysis, and also by Mössbauer spectroscopy have been used to follow in detail the transition of the ζ_α phase to ζ_β phase at four temperatures.

The structures of mullite, mullite doped with iron, and mullite doped with vanadium, as well as various related precursor materials have been examined by X-ray powder diffraction, and, where possible, MAS-NMR and Fe K-edge EXAFS. High-temperature time-resolved measurements by combined X-ray powder diffraction and Fe K-edge EXAFS have been used to follow the formation of iron-doped mullite.

6.1 Structure of ferrosilicon phases

The work reported in this thesis shows that the structures of ferrosilicon in the ζ_α and ζ_β phases conforms to the structure reported in the literature. It was noted that:

- As discussed in Section 4.1.2.1, ζ_α-ferrosilicon with a silicon content of 54.0 wt% doped with 1 wt% aluminium showed evidence of the presence of metallic silicon, whereas ζ_α-ferrosilicon with a silicon content of 53.4 wt% doped with 1 wt% aluminium showed no evidence of the presence of metallic silicon. This indicates that the presence of aluminium may reduce the range of silicon content over which the ζ_α-ferrosilicon phase is stable.

- As discussed in Sections 4.1.2 and 4.1.5, it is not possible to deduce the position of the aluminium atoms within the structure of either ζ_α- or ζ_β-ferrosilicon using EXAFS or high-resolution X-ray powder diffraction within the sensitivity of the techniques used.
- As discussed in Section 4.1.4, ζ_β-ferrosilicon with a silicon content of 54.0 wt% (*i.e.* ζ_β-$FeSi_{2.33}$) shows evidence, when examined by Fe K-edge EXAFS, that some of the silicon is located at an average distance of 2.71 Å from the iron atoms in the ζ_β-$FeSi_2$ structure. This is further supported by examination using Si K-edge EXAFS, as shown in Section 4.1.4.5. The detailed structure of metastable ζ_β-$FeSi_{2.xx}$ has previously been unknown, as described in Section 1.2.1.4. These measurements demonstrate that the excess silicon may be located in large spaces at the (±0.25, ±0.25, ±0.25) positions in the unit cell. Precipitation from these sites results in the rods observed by Boomgaard[1]. Such rods were not observed in this work, but the presence of a small proportion of metallic silicon in some samples of ζ_β-$FeSi_{2.33}$, especially when examined some time after heating, supports this view. Further work, for example recording higher quality Fe K-edge EXAFS data using more intense radiation either at ESRF or the new Diamond facility would be worthwhile in confirming this conclusion.

6.2 Examination by simultaneous X-ray powder diffraction and EXAFS of the ζ_α- to ζ_β-ferrosilicon phase transition

Simultaneous high-temperature time-resolved X-ray powder diffraction and Fe K-edge extended X-ray absorption fine structure (EXAFS) was used to investigate *in situ* the kinetics and mechanisms of the phase transition of ζ_α- to ζ_β-ferrosilicon at temperatures of

855, 873, 898, and 923 K. These measurements enabled calculations of the extent of the phase transition against time to be made using a new method of analysis of EXAFS data to identify the proportion of iron in an environment characteristic of ζ_α-ferrosilicon with respect to the proportion of iron in an environment of ζ_β-ferrosilicon.

The data were analysed using both the Avrami-Erofe'ev and the Prout-Tompkins models for phase transitions. In Section 4.2.4.3, it was shown that the Avrami-Erofe'ev model gave the most satisfactory fit. The experiments indicated that the value of the nucleation constant N is close to 2.1. The experiments were repeated using ferrosilicon doped with 1 wt% aluminium. In these experiments, the results indicated that the value of the nucleation constant N is close to 1.9.

The values for the rate constants were observed to increase exponentially with temperature, and were fitted to the Arrhenius equation. Values for the activation energies of the undoped phase transition of ζ_α- to ζ_β-ferrosilicon and the phase transition of ζ_α- to ζ_β-ferrosilicon doped with 1 wt% aluminium were calculated to be both between *ca.* 160 $kJmol^{-1}$ and 310 $kJmol^{-1}$, the high uncertainty being due to a small number of data points in both cases. More extensive experiments at a wider range of temperatures would be worthwhile to allow accurate calculations of these values.

6.3 Examination by Mössbauer spectroscopy of the ζ_α- to ζ_β-ferrosilicon phase transition

Mössbauer spectroscopy was used to investigate *in situ* the kinetics of the phase transition of ζ_α- to ζ_β-ferrosilicon at 855 and 873 K. The results were significantly different from

those obtained by the combined X-ray powder diffraction and Fe K-edge EXAFS technique, as a result of the different grain sizes used in the two types of experiments. The conclusion that this was the cause of the differences was confirmed in Section 4.5 and is summarised in Section 6.4 below.

It would be worthwhile to repeat these experiments using samples with a grain size comparable to that used for the experiments performed using simultaneous X-ray powder diffraction and Fe K-edge EXAFS. However, the apparatus used for the Mössbauer spectroscopy measurements requires a minimum collection time of around 2 hours for each spectrum in order to obtain data of good quality. The faster rates associated with the smaller grain size would make observation with this technique unfeasible. Much faster collection of Mössbauer spectroscopy data is possible using synchrotron radiation instead of a radioactive source, and using this would allow comparable experiments to be performed.

6.4 Investigation of the effect of grain size

A qualitative analysis of the effect of grain size on the ζ_α- to ζ_β-ferrosilicon phase transition demonstrated that experiments performed using different techniques cannot be usefully compared unless samples with identical grain size are examined. A more quantitative examination of this effect would be worthwhile for the purposes of applying experimental results to the industrial uses of ferrosilicon.

6.5 Examination of the structures of mullite precursors

The hydrothermal processing of aluminium- and silicon- acetates produces a gel with low crystallinity and a structure similar to pseudoboehmite. Where dopants are added to the mixture prior to hydrothermal processing, they appear to be primarily incorporated into the pseudoboehmite, occupying octahedral sites within the structure, although there is some evidence that a small proportion of the dopant forms a separate phase.

6.6 Formation of mullite at various temperatures

X-ray powder diffraction patterns recorded from mullite precursors heated at a variety of temperatures (discussed in Section 5.2) showed that:

- the undoped mullite precursor gel will form mullite if heated at 1623 K for 3 hours but will not form mullite if heated at 1423 K for 3 hours
- the mullite precursor gel doped with iron by means of addition of iron(II) acetate prior to hydrothermal processing will form mullite if heated at 1423 K for 3 hours, therefore the presence of iron incorporated into the pseudoboehmite structure by means of hydrothermal processing reduces the temperature at which mullite will form.
- the mullite precursor doped with iron by means of mixing iron (III) oxide with the hydro-thermally processed gel begins to form mullite on heating at 1423 K for 3 hours, and under-goes complete transformation to mullite on heating at 1623 K for 3 hours. Therefore the presence of iron which is not incorporated into the pseudoboehmite structure by means of hydrothermal processing is less efficient at reducing the temperature at which mullite forms.
- the mullite precursor gel doped with vanadium by means of addition of vanadium acetylacetonate prior to hydrothermal processing will form mullite if heated at 1373 K

for 3 hours, therefore the presence of vanadium incorporated into the boehmite structure by means of hydrothermal processing reduces the temperature at which mullite forms.

- The mullite precursor doped with vanadium by means of mixing vanadium(V) oxide with the hydrothermally processed gel will have begun to form mullite if heated at 1173 K for 3 hours, and undergoes complete transformation to mullite if heated at 1623 K for 3 hours. Therefore the presence of vanadium which is not incorporated into the pseudoboehmite structure reduces the temperature at which mullite will form.

The gel prepared by the hydrothermal processing of aluminium-, silicon-, and iron(II)-acetates observed at high temperature by time-resolved X-ray powder diffraction and Fe K-edge EXAFS became amorphous on calcination at 673 K. A small particle highly defective γ-Al_2O_3-type structure develops as the temperature is increased. No evidence for a discrete crystalline silicon-containing phase was observed. The first evidence of mullite formation is observed at 1323 K. Analysis of the Fe K-edge EXAFS data indicated that the iron is incorporated into the mullite structure accommodated in octahedral sites.

References for Chapter Six

[1] J. van den Boomgaard *J. Iron and Steel Institute* 1962, 1024.